IAEA-TECDOC-1708

Integrated Approach to Dense Magnetized Plasmas Applications in Nuclear Fusion Technology

Report of a coordinated research project
2007-2011

IAEA
International Atomic Energy Agency

INTEGRATED APPROACH TO DENSE MAGNETIZED PLASMAS APPLICATIONS IN NUCLEAR FUSION TECHNOLOGY

The following States are Members of the International Atomic Energy Agency:

AFGHANISTAN
ALBANIA
ALGERIA
ANGOLA
ARGENTINA
ARMENIA
AUSTRALIA
AUSTRIA
AZERBAIJAN
BAHRAIN
BANGLADESH
BELARUS
BELGIUM
BELIZE
BENIN
BOLIVIA
BOSNIA AND HERZEGOVINA
BOTSWANA
BRAZIL
BULGARIA
BURKINA FASO
BURUNDI
CAMBODIA
CAMEROON
CANADA
CENTRAL AFRICAN REPUBLIC
CHAD
CHILE
CHINA
COLOMBIA
CONGO
COSTA RICA
CÔTE D'IVOIRE
CROATIA
CUBA
CYPRUS
CZECH REPUBLIC
DEMOCRATIC REPUBLIC OF THE CONGO
DENMARK
DOMINICA
DOMINICAN REPUBLIC
ECUADOR
EGYPT
EL SALVADOR
ERITREA
ESTONIA
ETHIOPIA
FIJI
FINLAND
FRANCE
GABON
GEORGIA
GERMANY
GHANA
GREECE
GUATEMALA
HAITI
HOLY SEE
HONDURAS
HUNGARY
ICELAND
INDIA
INDONESIA
IRAN, ISLAMIC REPUBLIC OF
IRAQ
IRELAND
ISRAEL
ITALY
JAMAICA
JAPAN
JORDAN
KAZAKHSTAN
KENYA
KOREA, REPUBLIC OF
KUWAIT
KYRGYZSTAN
LAO PEOPLE'S DEMOCRATIC REPUBLIC
LATVIA
LEBANON
LESOTHO
LIBERIA
LIBYA
LIECHTENSTEIN
LITHUANIA
LUXEMBOURG
MADAGASCAR
MALAWI
MALAYSIA
MALI
MALTA
MARSHALL ISLANDS
MAURITANIA
MAURITIUS
MEXICO
MONACO
MONGOLIA
MONTENEGRO
MOROCCO
MOZAMBIQUE
MYANMAR
NAMIBIA
NEPAL
NETHERLANDS
NEW ZEALAND
NICARAGUA
NIGER
NIGERIA
NORWAY
OMAN
PAKISTAN
PALAU
PANAMA
PAPUA NEW GUINEA
PARAGUAY
PERU
PHILIPPINES
POLAND
PORTUGAL
QATAR
REPUBLIC OF MOLDOVA
ROMANIA
RUSSIAN FEDERATION
RWANDA
SAUDI ARABIA
SENEGAL
SERBIA
SEYCHELLES
SIERRA LEONE
SINGAPORE
SLOVAKIA
SLOVENIA
SOUTH AFRICA
SPAIN
SRI LANKA
SUDAN
SWAZILAND
SWEDEN
SWITZERLAND
SYRIAN ARAB REPUBLIC
TAJIKISTAN
THAILAND
THE FORMER YUGOSLAV REPUBLIC OF MACEDONIA
TOGO
TRINIDAD AND TOBAGO
TUNISIA
TURKEY
UGANDA
UKRAINE
UNITED ARAB EMIRATES
UNITED KINGDOM OF GREAT BRITAIN AND NORTHERN IRELAND
UNITED REPUBLIC OF TANZANIA
UNITED STATES OF AMERICA
URUGUAY
UZBEKISTAN
VENEZUELA
VIETNAM
YEMEN
ZAMBIA
ZIMBABWE

The Agency's Statute was approved on 23 October 1956 by the Conference on the Statute of the IAEA held at United Nations Headquarters, New York; it entered into force on 29 July 1957. The Headquarters of the Agency are situated in Vienna. Its principal objective is "to accelerate and enlarge the contribution of atomic energy to peace, health and prosperity throughout the world''.

IAEA-TECDOC-1708

INTEGRATED APPROACH TO DENSE MAGNETIZED PLASMAS APPLICATIONS IN NUCLEAR FUSION TECHNOLOGY

Report of a Coordinated Research Project
2007 – 2011

INTERNATIONAL ATOMIC ENERGY AGENCY
VIENNA, 2013

For further information on this publication, please contact:

Physics Section
International Atomic Energy Agency
Vienna International Centre
PO Box 100
1400 Vienna, Austria
Email: official.mail@iaea.org

Printed by the IAEA in Austria
April 2013

IAEA Library Cataloguing in Publication Data

Integrated approach to dense magnetized plasmas applications in nuclear fusion technology : report of a coordinated research project 2007-2011. – Vienna : International Atomic Energy Agency, 2013.
p. ; 30 cm. – (IAEA-TECDOC series, ISSN 1011-4289 ; no. 1708)
ISBN 978-92-0-142810-3
Includes bibliographical references.

1. Plasma (Ionized gases) – Research. 2. Dense plasma focus. I. International Atomic Energy Agency. II. Series.

IAEAL 13-00805

FOREWORD

Through its coordinated research activities, the IAEA promotes the development and application of nuclear technologies in Member States. The scientific and technical knowledge required for the construction and operation of large nuclear fusion research facilities, including ITER and the Laser Mégajoule in France, and the Z machine and the National Ignition Facility in the United States of America, necessitates several accompanying research and development programmes in physics and technology. This is particularly true in the areas of materials science and fusion technology. Hence, the long standing IAEA effort to conduct coordinated research projects (CRPs) in these areas is aimed at: (i) the development of appropriate technical tools to investigate the issue of materials damage and degradation in a fusion plasma environment; and (ii) the emergence of a knowledge based understanding of the various processes underlying materials damage and degradation, thereby leading to the identification of suitable candidate materials fulfilling the stringent requirements of a fusion environment in any next step facility.

Dense magnetized plasma (DMP) devices serve as a first test bench for testing of fusion relevant plasma facing materials, diagnostic development and calibration, technologies and scaling to conceptual principles of larger devices while sophisticated testing facilities such as the International Fusion Materials Irradiation Facility (IFMIF) are being designed. The CRP on Integrated Approach to Dense Magnetized Plasmas Applications in Nuclear Fusion Technology described herein was initiated in 2007 with the participation of 12 research institutions in 8 Member States and was concluded in 2011. It was designed with specific research objectives falling into two main categories: support to mainstream fusion research and development of DMP technology. This publication is a compilation of the individual reports submitted by the 12 CRP participants. These reports discuss and present results of the research work undertaken as well as further expected, important spin-off applications of DMP devices.

The IAEA officers responsible for the publication were R. Kamendje and T. Desai of the Division of Physical and Chemical Sciences.

EDITORIAL NOTE

This publication has been prepared from the original material as submitted by the authors. The views expressed do not necessarily reflect those of the IAEA, the governments of the nominating Member States or the nominating organizations.

This publication has not been edited by the editorial staff of the IAEA. It does not address questions of responsibility, legal or otherwise, for acts or omissions on the part of any person.

The use of particular designations of countries or territories does not imply any judgement by the publisher, the IAEA, as to the legal status of such countries or territories, of their authorities and institutions or of the delimitation of their boundaries.

The mention of names of specific companies or products (whether or not indicated as registered) does not imply any intention to infringe proprietary rights, nor should it be construed as an endorsement or recommendation on the part of the IAEA.

The authors are responsible for having obtained the necessary permission for the IAEA to reproduce, translate or use material from sources already protected by copyrights.

CONTENTS

SUMMARY

The developments in the construction of the magnetic confinement fusion device ITER (France) as a joint undertaking between seven international partners, and three large Inertial Fusion Facilities, the Laser Mega Joule (LMJ, France), the Z-machine (United States of America) and the National Ignition Facility (NIF, United States of America) pave a clear path for the research activities leading to nuclear fusion energy. Supporting programmes to the mainstream research activities include, inter alia, developing physics and technology in the areas of material sciences and fusion technology requiring solutions for many of the existing and foreseen technological issues that the operation of these devices as well as future fusion demonstration power plant (DEMO) will pose.

Dense Magnetized Plasma (DMP) devices in general - Quasi-Steady-state Plasma Accelerators (QSPA) and Dense Plasma Focus (DPF) devices - can in principle be used to test, in an intermediate step, the materials, technologies and conceptual principles for larger devices while dedicated testing facilities such as the International Fusion Materials Irradiation Facility (IFMIF) are being designed. These research activities bear the advantage of being immediately implementable. Dense magnetized plasma devices can produce Deuterium-Deuterium (D-D) and Deuterium-Tritium (DT) fusion reactions, plasma streams, hard and soft X rays, and electron as well as positive ion beams up to the MeV range. The previous IAEA Coordinated Research Project (CRP) on this topic helped to build a network of DMP laboratories with improved technology and research capability that is ready to be applied in many topics of mainstream fusion research. The overall objective of the here described CRP was to utilize dense magnetized plasma devices that have been constructed over recent years to support mainstream fusion research contributing to several research topics relevant for the construction and operation of large fusion facilities including ITER, LMJ, the Z-machine and NIF. In particular, the CRP aimed at:

- Utilizing DMP devices to support mainstream fusion research on: i) material science and ii) fusion technology
- Developing DMP technology
- Elaborating spin-off applications based on DMP devices
- Establishing networking culture and lasting links with major fusion players
- Facilitating equipment sharing and expertise exchange.

The specific research objectives of this CRP fell into two categories:

1. Support of mainstream fusion research

- To design and provide representative tests for fusion candidate materials (first wall, divertor, others)
- To provide tests and calibration for fusion product diagnostics and MCNP codes
- To develop powerful soft and hard pulsed X ray sources for fusion applications
- To investigate basic processes in support of fusion technology (e.g. breeding blanket, plasma fuelling, etc.)
- To develop tools and methods of radiography utilizing X ray, neutron and proton Beams

2. Development of DMP technology

- To improve repetition rate and discharge optimization
- To develop diagnostics for characterization of impinging radiation on material test samples. Improve the measurements of transient phenomena (ps to ns range)
- Components improvement for utilization costs reduction
- Development of inherently safe low-cost technology to perform tritium-deuterium fusion discharges for utilization as a source of 14-MeV neutrons
- To improve characteristics of dense plasma sources used in high-energy ion accelerators for applications in large fusion devices

The network of DMP devices involved in this CRP has enabled a substantial level of collaboration between the various CRP members and has also served in (i) providing a framework for equipment sharing and exchange of expertise through regular visits, (ii) helping in manufacturing modern DMP devices in new countries and (iii) organizing joint experiments.

In terms of support to mainstream fusion research, properties of plasma-facing materials (tungsten, CFC, low-activated stainless steels) as well as functional (ceramics, optics) and structural/construction materials (stainless steel) for next step nuclear fusion devices (ITER, DEMO) have been investigated, both experimentally and theoretically, with significant results underpinning the capability of dense magnetised plasma devices.

During the CRP life time, many outstanding results have been accomplished to support the main stream fusion research and the development of DMP technology as described below. A wide number of materials samples preheated and at room temperature for first wall, divertor, have been tested including tungsten, various types of ceramics, different optical materials, low activated stainless steels, etc. Different irradiation regimes by hot plasma (T_{pl} ~ 0.05 - 1.0 keV) and fast ion (E_i ~ 0.1 - 1 MeV) streams with pulse durations from 10^{-7} to 10^{-3} s were realized in a broad range of power flux densities extending from 10^4 to 10^{12} W/cm^2. This experimental work was carried out with the help of plasma accelerators and DPF devices in Kharkov (Ukraine), Moscow (Russian Federation), Warsaw (Poland), St Petersburg (RF), Trieste (Italy) and Tallinn (Estonia).

- CRP participants from Poland, the Czech Republic, People's Republic of China and Singapore have carried out tests and calibration for fusion product diagnostics and related Monte Carlo N-Particle transport (MCNP) codes. Special attention was paid to high temporal resolution of neutron emission diagnostics up to the picosecond range to advance new activation detectors for neutrons (based on beryllium) and to improve angular and spatial resolution of fusion proton diagnostics. All these techniques yielded new results on the mechanisms of fusion reactions in DPF. Based on MCNP calculations the neutron energy spectrum from the PF-1000 device has been shaped by moderating media, to simulate the required spectrum at specific locations in JET. This enabled the validation of data on targets activation for the purpose of neutron diagnostics calibration.
- For the development of soft and hard pulsed X ray sources for fusion applications the CRP participants from Poland and the People's Republic of China have provided experiments in the field of DPF- and X-pinch-based sources. It was also demonstrated that MPC (IPP, Ukraine) can be used as a powerful source of EUV radiation. These sources also support investigations of plasma dynamics on the Z-machine with exploding wire arrays and for a number of spin-off applications.

- Several tools have been developed for studying radiography utilizing X ray, neutron and proton beams in Singapore, China and Poland using DPF-based and X-pinch sources of X rays. They were successfully applied for X ray radiography of an exploding double-wire configuration and for the goals of dynamic quality control technique. The Coded Aperture Imaging (CAI) technique was used to study the spatial distribution of fusion reactions. The nuclear track detector material CR-39 was employed to register the ~ 3-MeV fusion protons from the D(d,p)T reaction. A deconvolution algorithm was developed and applied to the (x,y) data for recognized proton tracks to obtain images of the DPF fusion source. Coded mask patterns based on Singer cyclic difference sets were derived. These mask patterns have a wider range of open fractions than the more commonly used Hadamard sets. This is advantageous for optimizing the signal-to-noise ratio (SNR) for semi-extended sources. Numerical Monte Carlo calculations were carried out to study the performance of the CAI imaging system, together with experimental simulations using Radium-226, Plutonium-239 and Polonium-210 alpha sources with brass stencils of varying shapes. The results demonstrate that the CAI system can achieve the resolution and SNR requirements necessary for imaging the fusion proton source.
- To investigate the basic processes in particular an efficient fuelling method based on a plasma accelerator (plasma gun) that can assist in efficient control of the discharge in a tokamak, St. Petersburg (RF) and Warsaw (Poland) teams provided several experimental support. Initial investigations showed that for two gun positions plasma density on the magnetic axis increases and the temperature drops within 50 μs of the start of the jet injection. Observation of jet radiation, density and temperature profile measurements in different cross sections show that the injected plasma spreads around the toroid also within $\leq$ 50 μs. Undisruptive fuelling of the spherical tokamak Globus-M (PTI, St-Petersburg) plasma core with the help of the developed plasma gun was achieved. A moderate density rise (up to 40%) in the central plasma region without plasma disruption was obtained. A DPF device working with a deuterium-tritium mixture for the production of 14-MeV neutrons was put into operation. Experiments related to the interaction of 14-MeV neutrons with fissile materials perspective for fusion-fission hybrid systems have been started.
- To improve repetition rate and discharge optimization CRP participants in Poland, RF, Italy, Singapore, Estonia and Bulgaria implemented several measures including elaboration of a new design of DPF chambers, the improvement of electrical circuit of the DPF discharge and the substitution of its components by modern ones, etc. With these modifications, large devices (QSPA Kh-50, and PF-1000) have attained a higher reliability and reproducibility of necessary particle and energy loads, whereas small and medium-sized DMP devices have acquired a repetition rate up to 16 Hz, long-pulse operation regimes and elimination of impurities to a great extent.
- Researchers from Poland, China and the RF have introduced three modern diagnostics techniques: 1-nanosecond (ns) self-luminescence 4-frame imaging camera, 16-frame laser interferometry and 0.3-2.0 ns scintillator-photomultiplier tube (S+PMT), and diamond photo-conducting detectors (PCD). By means of these methods they were able to investigate detailed mechanisms and characteristics of hot plasma streams and ion beams in DPF and X-pinch, the process of interaction of these plasma and fast ion streams with specimens, the production of secondary plasma near the specimens' surface and the dynamics of shock waves.
- CRP teams from the RF and Poland (along with the N.L. Dukhov All-Russia Research Institute of Automatics, RF) have developed safe and low-cost 14-MeV neutrons source

using tritium-deuterium fusion discharges. This technology is very cheap and safe compared large accelerators.

- A number of important advances include pseudo-spark (thyratron with cold cathode) switches for capacitor energy storage systems with a life-time of about 1 million "shots" and able to work at 50 Hz, newly designed DPF chambers, including those with a built-in D-T generators, 4-frame self-luminescence 1ns imaging cameras, 1ns 16-frames laser interferometry, time-resolved atomic spectroscopy, neutron/X ray detectors with 100-300 ps time resolution, various up-to-date analytical tools in the sphere of material sciences, etc.

During the lifetime this CRP participants have created 5 new DPF devices ("Bora", ICTP; NX-3, Singapore; PFZ-200, Czech Republic; PF-3, Bulgaria; and PF-12, Estonia), one table-top X-pinch (China) and 2 additional DPF devices in countries not participating in the CRP. All participants took part in joint experimental sessions and workshops devoted to the CRP goals at the premises of ICDMP, IPPLM (both Poland), ICTP (Italy) and IMET (RF).

Spin-off applications

There are several spin-off application from this CRP and the most important ones are:

- Dynamic quality control experiments performed jointly by RF, Poland and ICTP have shown that a single nanosecond X ray flash can produce high spatial resolution images of fast-moving object (fast rotating car tires, blades of a fan or turbine).
- Radiation enzymology (RF and Poland) have shown that radiation effect of nanosecond powerful X ray pulses can be obtained by using continuous isotope X ray source of 4-5 orders magnitudes less dose; it may be a foundation for a new radiation hygiene based on pulsed radiation sources where dose, product of dose and dose power are of key importance
- Experimental works in the field of neutron treatment of malignant tumors (RF and ICTP) where it has been shown that, at the presently achievable doses and dose powers of neutron generators and DPFs, it may be possible to substitute powerful, cumbersome and hazardous fission reactors by these compact, cheap and ecologically more acceptable devices
- Theoretical calculations using MCNP codes show (ICTP) that DPF-based source may be a very promising instrument in low-dose and effective boron-neutron-capture therapy of cancer.
- Experimental and theoretical work by Polish and Russian teams has demonstrated the ability of a single-shot Neutron Impulse Nanosecond System for detecting hidden objects like explosives, narcotics and fissile materials. This technique is useful in particular for interrogation of fast-moving objects like cars, trains, etc.
- As it was shown by the team from the University of Sofia (Bulgaria) the irradiation of the duckweed samples of Chlamydomonas reinhardtii by X rays generated in the DPF discharge with a dose of 11 mSv produces a considerable change of the parameters of photosynthesis
- Experimental work from China using the X-pinch has proved to be an ideal X ray source for phase-contrast imaging of small and weakly X ray absorbing biological object like mosquito which cannot be imaged by conventional X ray radiography.

Conclusion

In particular the CRP has been instrumental in stream-lining the contribution of small devices to mainstream nuclear fusion research, establishing functioning networks and contributing to capacity building. In addition the activities within this CRP have been conducive for the support of the involvement of developing and developed countries into nuclear fusion programmes of Member States where mainstream fusion facilities are under construction.

COUNTRY REPORTS

INVESTIGATION OF THE DENSE MAGNETIZED PLASMA CREATED BY PLASMA FOCUS DEVICE

A.B. BLAGOEV

Sofia University, Sofia, Bulgaria

Abstract

The experimental results with a device with a plasma–focus like geometry show the development of a planar surface ionization wave. In the pressure range, typical of PF machines the ionization process is supported by a photo-effect on the cathode part adjacent to the insulator. The FEM-PIC-MC model of the ignition process in this device shows a reasonable agreement with the observed optical measurements. A new version of the FEM-PIC-MC code is being tested. It will use PLASIMO platform. By a set of magnetic probes the velocity of the current sheath during the run-down axial phase is determined. In the last two thirds of the axial phase the current layer velocity is a constant. The data, derived from a series of shots at conditions: air, gas pressure (1 - 2) mbar, charging voltage 14 - 17 kV shows that between 1^{st} and 2.8^{th} μs of the discharge development the current sheet has almost equal constant velocity in range of 5 - 6.7 cm/μs. The irradiation of the duckweed samples by X ray produced by the PF discharge through 20 μm Al foil produces a considerable change of the photosynthesis parameters.

1. INTRODUCTION

As it is well known, the plasma focus device transforms the energy of the condenser bank into energy of the movement of the current sheath consisting of highly ionized plasma before the pinch phase. After the switching on of the spark gap the potential of the bank is applied on the coaxial electrodes, thus triggering a breakdown along the cylindrical insulator between the electrodes. The breakdown ends with a formation of an annular current sheath. In the second phase the current sheath is accelerated towards the open end of the electrodes under the force $j \times B$. In the third phase the current sheath is compressed and forms a small cylindrical column, consisting of high density plasma (pinch). At the pinch instabilities occur which are a source of various emissions and then with or without second pinch the plasma column expands. During the decades since the first papers dedicated to Plasma Focus (PF) appeared [1,2], the acceleration and the pinch phases have been thoroughly investigated both theoretically and experimentally, [3, 4]. At the same time the breakdown and the current sheath formation have been in some way neglected. Probably it is due to the difficulties posed by the fast transformation of neutral gas into the high ionized plasma. A better insight into the initial stage of the PF discharge is still needed in view of the increasing interest in these devices for the high temperature plasma investigations as well as for industrial and medical applications, [5, 6]. Especially interesting is the high neutron yield of this discharge, [7]. The specific applications require new constructions of the discharge chambers, with a change of the geometry and a new type of insulators.

In the literature there are not so many works considering the breakdown phase (for example see [8-11]). The theoretical description of the ignition in these papers uses the hydrodynamic models. However the hydrodynamic approach has some intrinsic limitations, when the ionisation process has to start from a few electrons in the volume. The stochastic approach seems to be more suitable [12, 13]. It allows the creation of an adequate model for the complicated case of the PF breakdown. It is well known [3] that this phase depends on several parameters namely, gas type and pressure, rate of voltage rise, dielectric material, geometry, possible modifications of the dielectric surface during the period of exploitation.

The aim of this project was to prove experimentally the existing model [13] by dedicated experiments and to construct more flexible and comprehensive description of the breakdown phase.

The second aim was to obtain experimental results with the plasma focus device in the University of Sofia, that starts operation in the beginning of the project.

As it was stated above the continuing interest towards the PF phenomenon is due to the unresolved problems of the discharge dynamics and the variety of possible applications of the DPF machines. One of these applications is a study of the impact of radiation emitted by the PF discharge on live microorganisms, living cells or other biologic objects. In the literature there are a few similar works, although that the PF radiation has some advantages over the conventional ionization sources. The PF discharge ensures in the pinch phase short (3.10^{-8} -10^{-7} s) and powerful X ray and particle pulses. In the works [14, 15, 16] medium and hard X rays of the PF discharge have been used for the needs of radiation enzymology. Different enzymes have been irradiated *in vitro* changing the conditions e.g. the X ray spectral range, doses, dose power, etc. The results obtained by the authors show huge difference in the enzyme activation/deactivation after it's irradiation by pulse X rays burst from PF and from conventional continuous radio isotope source (γ - source ^{137}Cs) and X ray tube. In particular the above effect is seen at doses five to six orders of magnitude lower for this radiation source than in the case of prolonged action of hard radiation having low intensity. The authors presume that the most adequate characteristic of the action is not dose but the product of the dose and the dose power.

In this report we present the results of the experiments with living micro organisms, irradiated by hard and soft X ray generated by the PF device. We tried to ensure predominant soft X ray radiation. The data is obtained with the 3 kJ PF machine of the Faculty of Physics at the University of Sofia.

2. INVESTIGATIONS OF SURFACE IONIZATION WAVE

2.1 Existing models

Both the hydrodynamic and the kinetic approaches used to tackle the breakdown mechanism until now assume direct electron impact ionization in the volume and losses of charged particles by diffusion towards the non-ionized parts and the walls [11, 12]. The results of these works show that additional ionization sources are required to get an adequate description. In the last years the breakdown models take into account the photoelectrons appearing at the cathode. As a result an ionization wave sliding above the cylindrical insulator surface was derived [13]. For the next step it was necessary to validate this model by experiments and further calculations. The correctness of the models in such a system can affect the design of a number of other devices where surface discharges are used as pre-ionizers, for example in excimer lasers or compact Z pinch plasmas for industrial applications.

2.2. Experimental observation of the surface wave

The breakdown in plasma focus devices starts with the propagation of an ionization wave along the cylindrical insulator. The electron density in this wave is of the order of 10^{11} – 10^{12} cm^{-3}, the number of excitations is small, therefore the light flux from the coresponding area is low. In order to record the sliding wave the optical camera has to operate at a high sensitivity mode. A current return stroke is expected to occur immediately after the gap

between the anode and cathode is closed by the weakly ionized plasma. The respective intensive light flux at this moment may damage the optical detector, adjusted to monitor the pre-ionization phase. Another obstacle to use a real PF is that the majority of the devices are constructed in a way that assures access to the most interesting point in the device, i.e. the area above the anode, where the plasma compression and the pinch take place, while the insulator section in which the breakdown occurs is in the screened part. Moreover the strong electromagnetic pulses from the plasma focus (PF) currents, that are in the range of 10^5-10^6 A, are dangerous for the delicate electronics of the optical camera.

For all these reasons a model device with flat parallel electrodes was created. The cathode is L-shaped, so that the short arm corresponds to the bottom part of the PF electrode's compartment. The electrodes of the discharge gap are aluminum plates separated with a flat acryl insulator with a thickness of 0.5 cm (see figure 1):

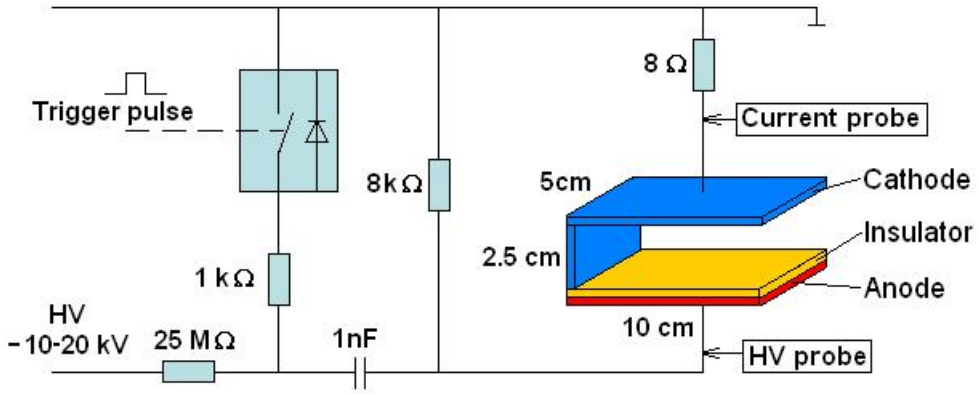

FIG. 1. Experimental scheme of the planar device for modeling of the PF breakdown.

The anode below the flat insulator is completely insulated in order to avoid transverse discharges and direct ohmic current that leads to a strong return stroke. The thickness of this extra insulation is gradually increased until the discharges, due to edge effects on anode boundaries, were not observed. In the pre-ionization study there is no need for considerable stored energies (like in Plasma Focus device), so a 1 nF capacitor charged up to 20 kV is used in the circuit. The parameters of this circuit ensure the rates of the voltage rise (dU/dt), in the range of (1 - 2) 10^{11} V/s. This corresponds to the typical rates in the PF device.

The 2D sectional view of the model device is similar to the sectional view of the PF bottom part. That is why the potential lines between the dielectric and the cathode are the same as in the plasma focus device despite the fact that the PF electrodes have cylindrical symmetry (See Figure 6).

The optical images of the discharges are recorded by an ICCD camera 4 Quick Edig using its maximal sensitivity at 2 ns exposure time. The direction of observation is normal to the plane of the L shaped cathode. The time delay τ of each picture taken is chosen by adjustment of the optical camera delay generator. It is determined from the moment of the sharp rise of the current. The device operation was controlled by a master generator, working in a single shot mode. The variable parameters in the experiment are: the gas pressure, the charging voltage, the gain of the optical camera. The investigations have been done in argon and in air. What is presented here is the data showing the results obtained in Ar in the pressure

range 7.5 - 90 mbar. Experimentally observed emission patterns of the ionization wave at 7.5 mbar are shown on Figure 2.

At the low pressures a plasma layer appears along the horizontal insulator. The length of the layer increases with time. But these pictures show also a glow in front of the cathode short leg (vertical layer). When the pressure increases the size of this plasma layer along the cathode decreases (Figure 3) and at 90 mbar it almost disappears (Figure 4). In contrast one can see that the maximal length of the ionization wave along the dielectric increases with the rise of the pressure.

The dependence of the dimensions of plasma layers (along the dielectric and the vertical cathode surface) on pressure shows that the development mechanism of the surface ionization wave is different at different pressures. At a pressure of several tens of mbar it is predominantly controlled by volume processes (see figure 4) as the classical streamer theory predicts. At the same time when the pressure is 7.5 mbar (which is a typical operational pressure for the PF machines), apart from the electron impact ionization, the role of the electron emission from the cathode is also substantial. In the case under consideration during several tens of nanoseconds only the photo-effect can be responsible for the ejection of electrons. In the first few nanoseconds after the application of the voltage on the electrodes the modest quantity of electrons near the cathode edge contacting the dielectric both ionize and excite the atoms of the filing gas.

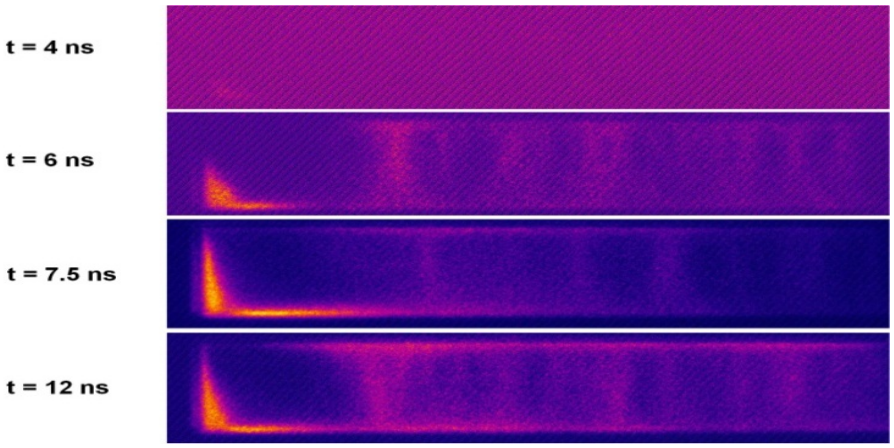

FIG. 2. Optical images of the discharge at 7.5 mbar Ar pressure.

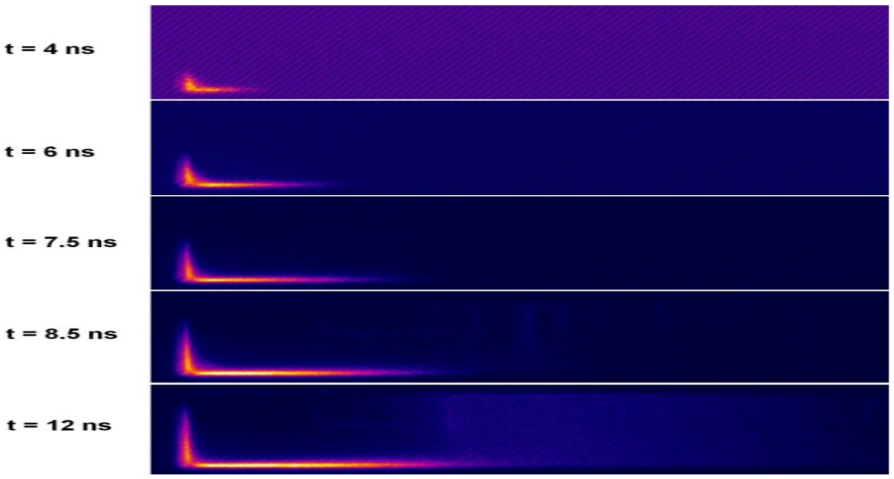

FIG. 3. Optical images of the discharge at 15 mbar Ar pressure.

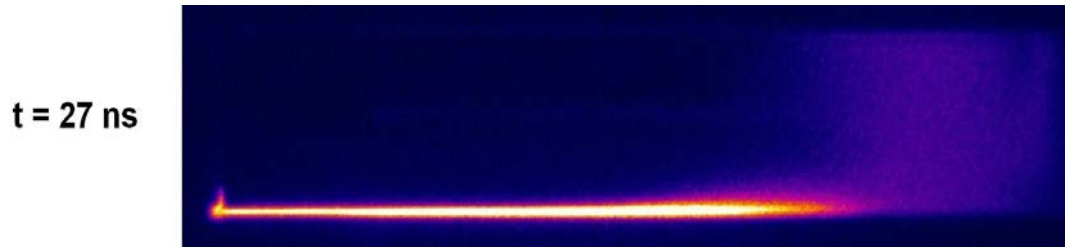

FIG. 4. Optical image of the discharge at 90 mbar Ar pressure.

We presume that the VUV photons emitted subsequently reach the bottom part of the cathode and eject new electrons that appear in the region with a large electric field. These secondary electrons create new avalanches supporting the appearance of an ionization wave. Without these avalanches the diffusion and drift losses will stop the development of the ionization process. Weak traces are observed between the upper horizontal cathode and the insulator surface (see figure 2). It is more difficult to observe these traces in the pressure range above 15 mbar and they cannot be seen at a pressure of 90 mbar (figure 4). These traces are probably due to avalanches. Such transverse discharges have been observed earlier in the PF breakdown experiments [3].

2.3. Model results

The experiment above has been simulated using a numerical Particle in Cell -- Monte Carlo model with Finite Element Method (FEM-PIC-MC) for solving the electric field equation. The model is well described in our previous works [13, 17]. For the current study changes were made in the model to conform to the geometry, filling gas and externally applied voltage on the anode [18]. Here we will only mention the most important modules of the model: "particle movement", "collisions", "weighting" and "field". The "collisions" module simulates the collision events applying the Monte Carlo method and using a set of cross sections for Ar given in ref. [19]. As in the model published before [13], here it is also assumed that when an electron excites an Ar atom to one of the resonance levels - $4s^1P_1$ or $4s\ ^3P_1$, this atom immediately emits a photon. This assumption is reasonable, because the life time of these levels is in the order of 2-3 ns. The corresponding VUV spectral lines Ar I 1048.2 and Ar I 1066.7, have the energy of the quanta 11.83 eV and 11.61 eV respectively. These are capable of ejecting photoelectrons from the Al plate with quantum efficiency γ above 1% [20]. In the calculations this coefficient is assumed to have constant value equal to 0.05. Upon the generation of a photon a ray is generated in a random direction. The ray originates from the place where the excited atom was created. At the place where the ray crosses the cathode a new photo electron is created with probability γ. The Penning ionization as an important ionization source is also taken into account using the following scheme. A very fine rectangular mesh is used for counting the number of metastable Ar $^3P_0$ and Ar^3P_2 atoms in each cell when they are created in a collision event. Using the calculated excited Ar atom density and rate coefficient for penning ionization [19], we obtain the number of Penning ionizations in each cell for the given time step. The electron and ion particle born in each penning ionization reaction are put in the particle code, while the number of corresponding excited atoms per cell is decreased respectively.

Quite a clear picture of the ionization growth is derived by a tracking of separate electrons during the inception of the wave in the first several nanoseconds, after the external

electric field is turned on [21]. The few free electrons, accidentally existing in the device volume, are accelerated by the field (see Figure 5 (a)).

However at this moment the field is not high enough to create a lot of electron avalanches and the average electron energy is not so high either. With the increase of the field at 10^{th} nanosecond the average energy of the electrons increases. As a result a higher number of exited atoms are created. According to our model the photons emitted from the exited atoms reach the device walls and ejects photo electrons. (See Fig. 5 (b)). The photoelectrons emitted from the cathode near the region with the high electric field creates for a short time a lot of small avalanches that can be seen on Figure 5 (c). The excited atoms in these avalanches also emit photons, but this time they are closer to the region with the higher electric field (see Figure 5 (d)).

The results for the electric potential and electron density obtained by the modeling are shown on Figure 6. Assuming that the light emission in a certain region is proportional to the local electron density, it is seen that the model results are consistent with the experimental data at pressure 7.5mbar. The first frame of the figure 6 ~ is showing the moment at 13^{th} ns after the turn-on of the external field. Before that, in the first 10--12 ns the potential rises linearly. The distribution of the potential lines has a form similar to the one presented on the first frame. However at 13^{th} ns the electric field in the corner between the cathode and the dielectric is large.

A single electron appearing in this area, due to photo-effect from photons emitted in the volume, creates one of the first avalanches. The UV photons emitted from the Ar atoms, excited by the fast electrons of the avalanche, can liberate photo-electrons from the cathode plate. These electrons appear in the same area with a high electric field. When enough of these chain reactions - electron multiplication and photo-effect events, take place, the density of the charged particles becomes high enough (~ 2.10^{11} cm $^{-3}$) to screen the external field in this place (see the second frame from the figure). Then a head of a streamer is formed, where the electric field is also very high (see the third frame in the figure). This electric field in front of the streamer head drives the ionization wave to slide along the dielectric. In the subsequent moment the field in front of the cathode is not so high, but the model and the optical frames show considerable density of electrons in the short plasma layer. Therefore one may expect that the processes of ejection of the photo-electrons and volume ionization continue, ensuring a conductive plasma media between the cathode and the streamer head.

The results show the development of a planar surface ionization wave. In the case of low pressures the ionization process is supported by photo-effect on the cathode part adjacent to the insulator. The FEM-PIC-MC model of the ignition process in this device shows reasonable agreement with observed optical measurements.

The tracking of the single electrons in the first several nanoseconds has shown that the photo-effect plays an important role for the creation of seed electrons in the region where the electric field is very high [21]. We presume that the electrons, whose images are pointed with arrows, are ejected by the cathode. It is seen that in the region with a high electric field (See Figure 6) the number of charged particles rapidly increases. In the last 2 frames (*e* and *f*) the weighting factor is 10000, e.g. 1000 electrons shown represent 10 millions electrons in the model.

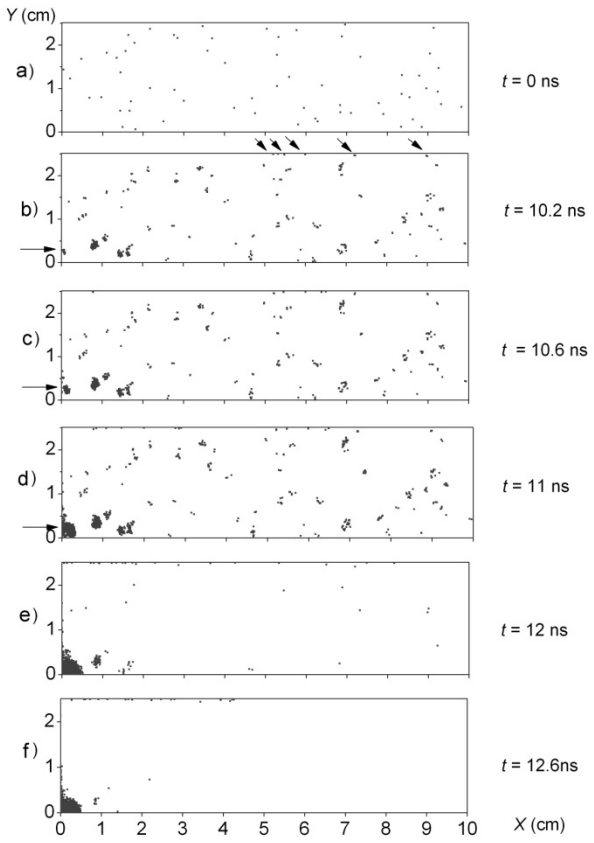

FIG. 5. Single electrons distributed in the device volume during the initial phase. Pressure p=10.5 mBar.

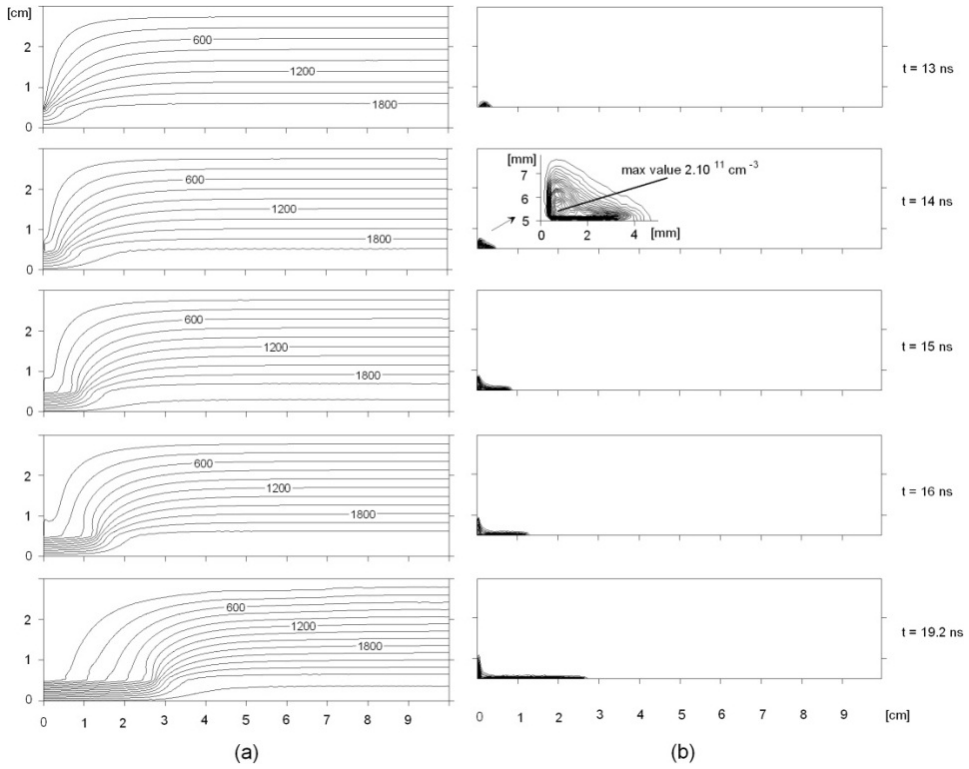

FIG. 6. Distribution of the potential (a) and charge particle density (b) in the model [22].

2.4. Code development

The results that have been published are calculated using our old Monte Carlo code [22]. One disadvantage of this code is that any change of the geometry or the type of the filling gas leads to a change of the source code. Such changes are related to the creation of different versions and braches of the code and make it difficult for maintenance.

The efficiency of the Plasma Focus device strongly depends on its geometry, the filling gas, the externally applied electric field, dielectric material, etc. For all these reasons we have developed a new more flexible and sophisticated code that can be configured runtime (not compile-time), using configuration files or graphical user interfaces (GUI).

This program is based on “Plasimo” framework [23]. It is composed of the following modules: Monte Carlo (MC), Particle in Cell (PIC) and The Finite Element Method (FEM) modules. For the MC module we have used the Plasimo MC module, while the PIC and FEM modules were developed from our group [17, 18]. The program has two different user interfaces: command line and GUI. Here we will present some results by the GUI version of the program. Figure (7) shows results for the electric potential obtained from simulation of a Plasma Focus device, while Figure (8) presents results for the electron density distribution in the device volume 10 ns after the electric field is applied.

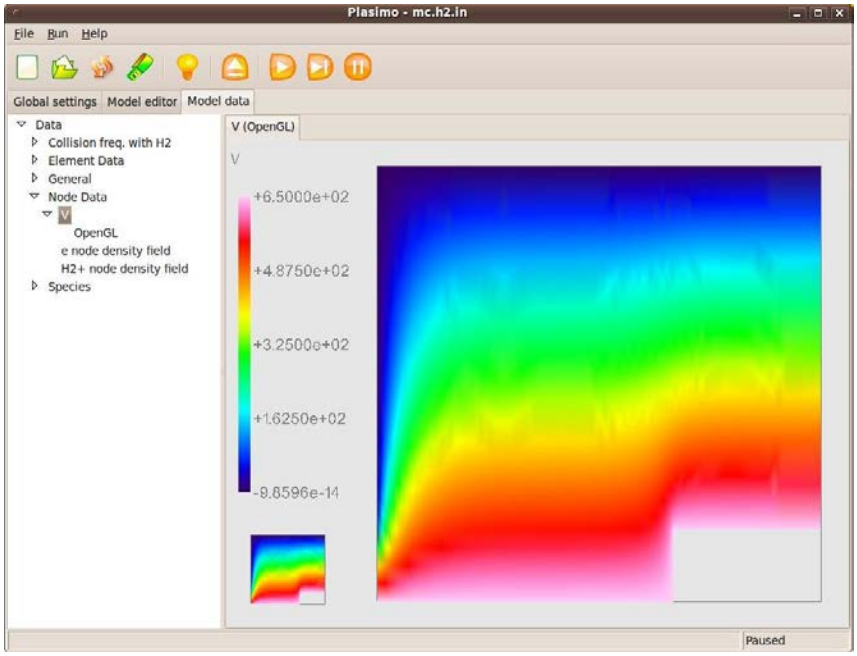

FIG. 7. Model data for electric potential in PF device.

These data are derived without accounting for the photo effect caused by the VUV photons on the walls. They are similar to the results obtained before in the fluid models [11].

In the present model we simulate the appearance of the resonance radiation in the volume by MC method, which results in single excitation acts. As a result we have to monitor the excited particles, to track their quenching and transport of single photons through the vessel volume.

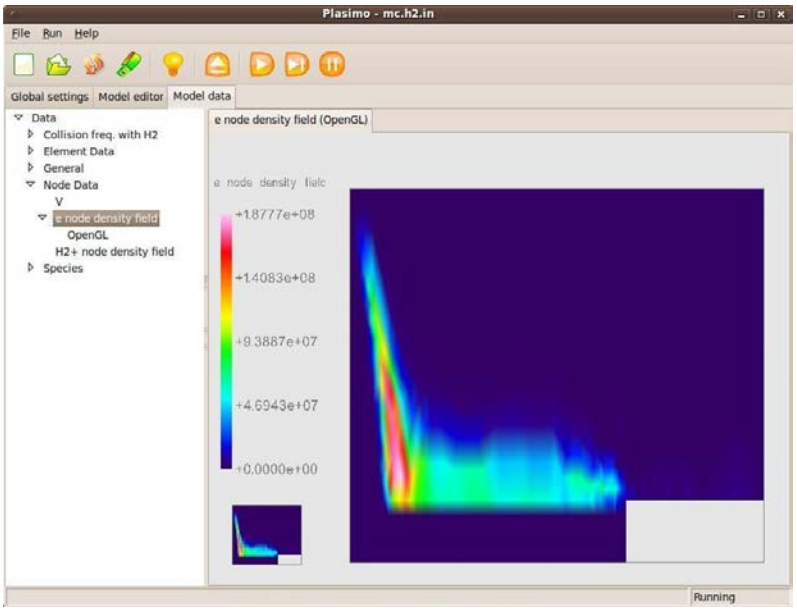

FIG. 8. Model data for electron density in the breakdown phase of the PF device.

In order to solve this problem we have created the following simple test model:

1. We put a number of excited molecules in the coordinate system's centre and start to monitor the movement and collisions (lifecycle) of the following particles: ground state molecules $H_2(X^1\Sigma^+_g)$, excited hydrogen molecules $H_2\,(B^1\Sigma^+)$, photons, etc as shown below.

2. We simulate the lifetime of the excited molecule by the Monte-Carlo method.

3. After this step spontaneous emission occurs:

$$H_2(B^1\Sigma^+) \rightarrow H_2(X^1\Sigma^+_g)+\text{photon (11,3 eV)}.$$

4. The appearing photon is generated with an arbitrary direction in space. Using MC method the photon travels a distance determined by its free path length - a function of the photon's energy.

5. After that the photon is absorbed by a ground state particle:|

$$H_2(X^1\Sigma^+_g)+ \text{photon} \rightarrow H_2\,(B^1\Sigma^+)$$

6. The procedure of this newly born excited molecule continues from step 2

Figure 9 shows the simulation of 1 million excited molecules placed in a small volume of the coordinate system. One can see how the radiation spreads in the volume 1 nanosecond after the start of the simulation. The same for the VUV quanta is presented by Figure 10.

These results show that the resonance quanta emitted from the ground vibration states of the electron excited singlet molecular states $H_2\,(B^1\Sigma^+)$ and $H_2\,(C^1\,\Pi_u)$ to the ground vibration state of the are reabsorbed in the volume and their path is not long enough to reach the metallic surfaces for the short time. However there are a lot of possible transition from the same electronic states to the ground electronic state $H_2(X^1\Sigma^+_g)$, but in higher vibration states (see Figure 11).

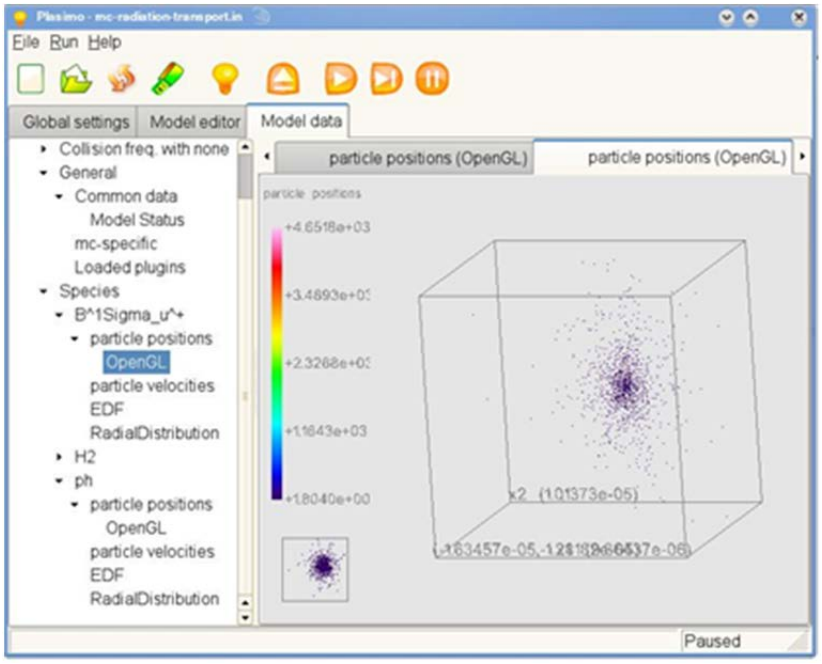

FIG. 9. Test of the model with excited particle swarm at 1st ns.

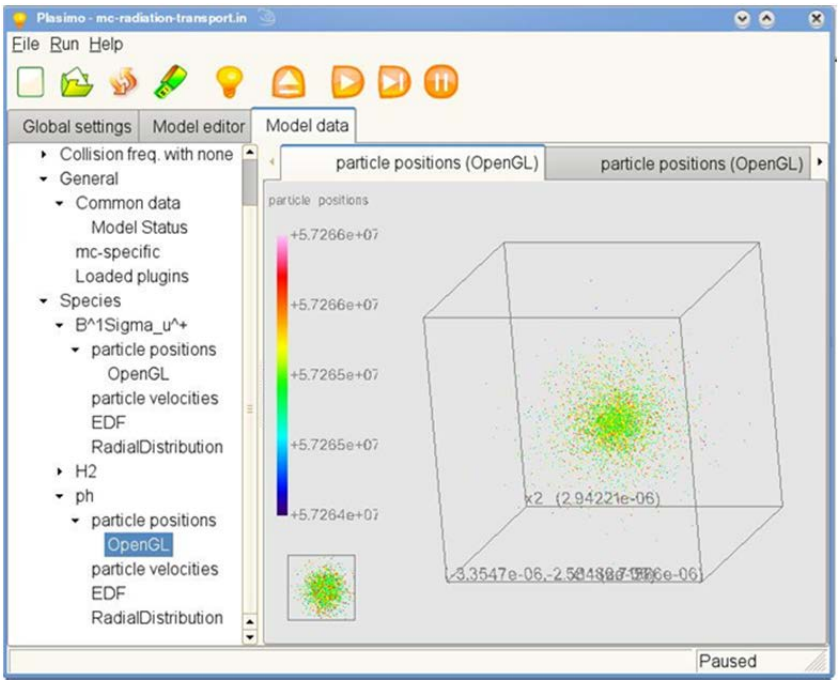

FIG. 10. Test of the model with photon's swarm at 1st ns.

In the initial period of the breakdown phase the gas in the vicinity of the insulator is neutral and at room temperature, with the exception of the thin plasma layer upon it. Therefore the vibration state with vibration numbers ν = (2 - 14) will not be populated; therefore they will not absorb VUV lines to these states. Thus a considerable numbers of VUV quanta, emitted from the plasma can reach the metal surface of the cathode and eject photoelectrons.

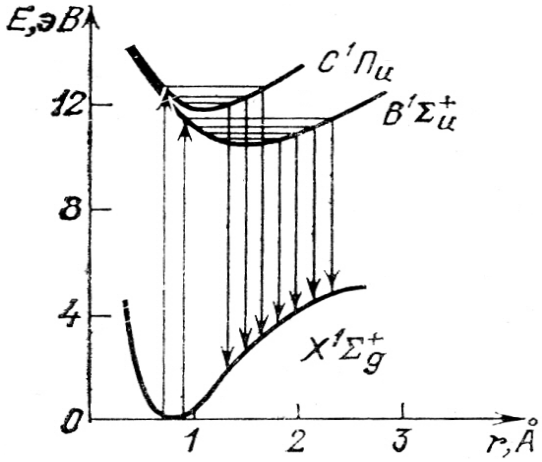

FIG. 11. Some energy terms and transitions in hydrogen molecule.

1. Lyman Band – 93 transition λ = (128,0 - 164,6 nm) λ max =161,0 nm.
2. Werner Band - 36 transitions λ = (109,8 - 127,0 nm) λ max =116,0.

3. PLASMA FOCUS EXPERIMENTS AT THE UNIVERSITY OF SOFIA

3.1. Experimental device

Here we briefly will outline the parameters of our Mather typa PF device. The condenser bank has capacitance of 20 μF, with the maximal voltage of 40 kV. The insulator is a quartz tube (2.6 mm in diameter, 30 mm length) the main switch is a vacuum spark gap. The anode is a hollow copper tube with 20 mm diameter and 145 mm length, the cathode consists of 6 copper rods (8 mm diameter, 160 mm length) mounted in the massive cathode bottom on a circle with a radius 35 mm. So far the experiments were conducted in air and the nominal pressure is in the range 1.0 - 1.7 mBar. The voltage operating range is chosen to be 15 - 18 kV. We are monitoring the discharge current, the current derivative, the soft X ray by PIN diodes and the hard X ray emission from the plasma. Thermo-luminescent dosimeters (TLD) were used to measure the full X ray dose in the stainless steel chamber of our DPF and to control the radiation outside the device.

A set of magnetic probes is inserted between the anode and one of the cathode rods. It allows us to determine the velocity of the current sheath, during the run-down phase.

Figure 1 shows schematically the PF electrodes and the set of magnetic probes. Each probe is formed by a twenty-turn, 2 mm diameter coil. The distance between the probes is 1 cm. The probes shown by one color are connected in series. So we have 4 “channels” of probes each one with 4 cm distance between the separate coils. A Pyrex tube with 5 mm external diameter serves as a container of the probes.

The data of all of the detectors mentioned above have been recorded by two 4 channel oscilloscopes (TDS 3034C, TDS 2004B).

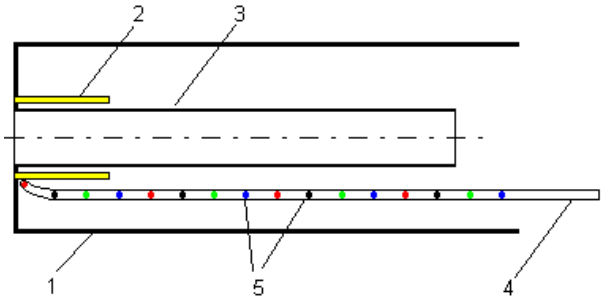

FIG. 12. Scheme of the PF electrodes and the Pyrex tube with the set of magnetic probes. 1 – cathode, 2 – insulator, 3 – anode, 4 – Pyrex tube, 5 – probe coils.

3.2. Results and discussions

3.2.1. Basic measurements.

The data, received by the diagnostic tools in the first several hundred shots fired so far, reveal the typical peculiarities known from the literature. The oscilloscope pictures give the moment of the initial breakdown of the gas, followed in a few microseconds by the occurrence of a pinch. A correlation between the observed one or more peaks of soft and hard X rays and the peculiarities of the dI/dt signal is established, the latter corresponding to the same number of pinches with the same mutual distance in time. Figure 11 presents oscilloscope traces of discharge current, soft and hard X ray signals. These measurements are essential and have to be done together with other measurement on order to be sure that the pinch exists at every counted shot.

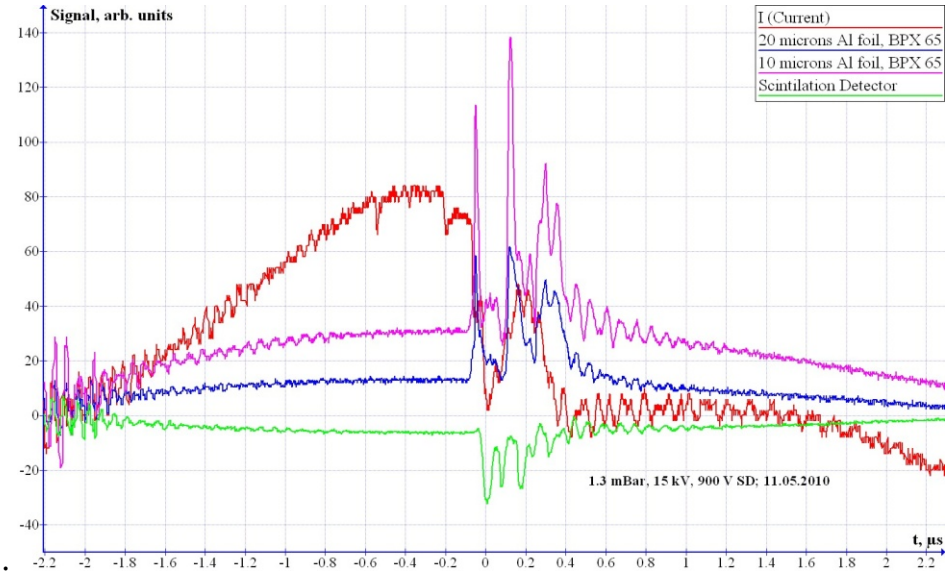

FIG. 13. The scope traces: PF current (red); soft X ray detectors signals (blue and violet) and hard X ray signal (green), respectively.

As it was stated above the optimization of the run-down phase of a specific plasma focus system is necessary in order to obtain high yield of radiation in the pinch phase. Thus the experimental study of this period is required. For this purpose monitoring of the light of the moving layer or magnetic probe measurements are used.

3.2.2. Magnetic probe measurements.

As it was already mentioned in this work we use a set of magnetic probes shown on Fig. 12. As output of the set are 4 "channels", consisting of connected probes with a distance of 4 cm between the coils of one such "channel".

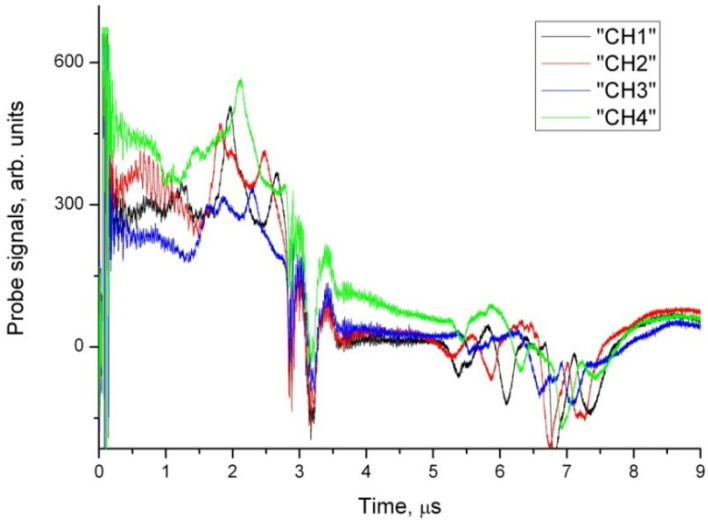

FIG. 14. Signals from the magnetic probe system for a single shot.

Figure 14 presents the experimental results derived with this system of probes. Using such system of probes we can determine the velocity and the acceleration of the current sheet as well as it's evolution during the run-down phase in a single shot. It is seen that in the frame of one probe "channel" the intensity of the peaks increases (see for example the behaviour of the red curve). This is due to the current density distribution of the layer [7].

The two sharp dips appearing simultaneously for all four channels near 2.8th and 3.2nd microsecond time moments correspond to the electromagnetic signals from the pinch detected by the probes. It is seen also that there are signals from the probes in the second half period of the discharge current too although that no pinch in this case is observed.

Figure 13 presents the axial positions of the probe peak maximums versus the time scale of the discharge evolution. The points at the beginning of the acceleration phase are determined with a considerable error. Nevertheless Figure 13 shows that after about 1 microsecond from the beginning of the discharge the forces, controlling the current layer established an equilibrium. It seems that the driving magnetic piston is balanced by the resistance of the compressed gas. That leads to constant velocity of the current layer. In our case between the 1st and 2.8th μs the layer velocity is constant. The values of the velocity of the current sheath were derived by processing of the data of a number of shots fired at different conditions. Before this time interval according to the figure, from 700 ns to 1 μs the layer is moving faster. Quite interesting is the period before 700 ns but it is impossible to say something for this time interval with the present probe set. For the purpose a radial set of probes has to be used [8,9]. Subtle details in the behavior of the current sheath can be obtained by a model, however this model should be complete enough in order to describe adequately the operation of the specific device (see for example [3]). Naturally constructing such a model is not a trivial task. In the paper [9] Bruzzone et al propose a simple model for the same lift-off stage that is intermediate between the breakdown and the axial phase the PF discharge.

The figure below shows the positions of the maxima recorded by the set of magnetic probe at different conditions.

FIG. 15. Axial positions of the maximums of the signal of magnetic probe set vs. time of the discharge evolution.

The data, derived from a series of shots at conditions: gas pressure 1 - 2 mbar, charging voltage 14 - 17 kV shows that between 1st and 2.8th µs the current sheet has almost equal constant velocity in range of 5 - 6.7 cm/µs.

The next picture presents the data obtained with different orientation of the magnetic probe, that allows determining the relative intensities of the different component of the magnetic field: B_φ , B_r and B_z

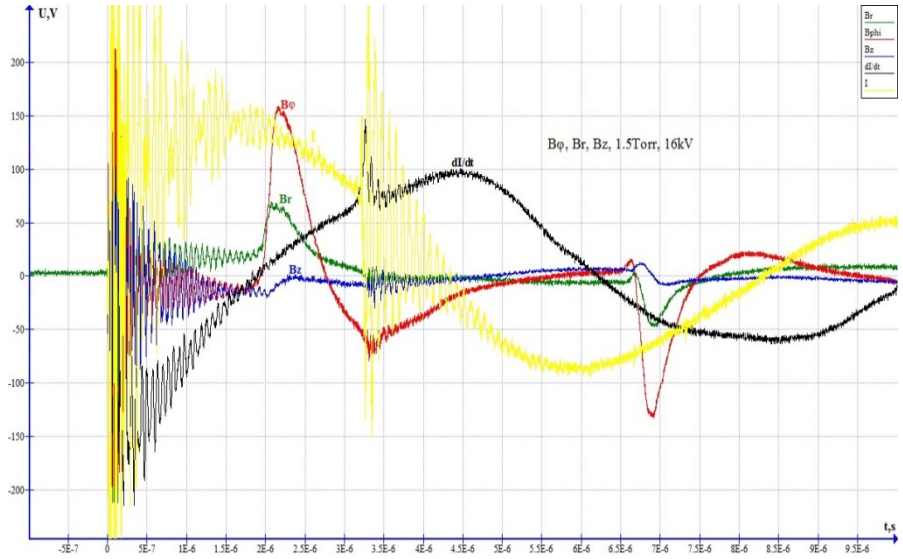

FIG. 16. Measurements of the different components of the magnetic field of the current layer in the rundown phase.

3.2.3. Influence of the Soft X ray Plasma Focus radiation on live micro organisms.

The aim of these first experiments is to examine some vital characteristics of live micro organisms exposed to the X ray radiation of the PF device.

Figure 15 represents the upper part of the PF chamber with the port on its top used for biological experiments. As it can be seen the port is formed like a shallow “dish” that can keep a certain amount of liquid substance. The bottom of the vessel is made from thin aluminium foil, supported from below with a stainless steel mesh. The water solution of the sample was poured in the vessel. The samples have been irradiated by soft X rays with different number of shots. For the control of the dose obtained Thermo Luminescent Detectors (TLD) were placed near the samples. An X ray film for additional control also was positioned there.

IRRADIATED OBJECTS:

1. Saccharomyces cerevisiae – (yeast):

A study of the fertile activity. Cells were grown in YPD medium, containing 2% w/v glucose, 2% w/v peptone, 1% yeast extract, to late exponential phase. Cells were washed twice and resuspended to final concentration of 10^7 cells/ml, and irradiated in a sealed thick plastic test for sterile conditions, by 14 shots through 100 μm Al foil. No difference of the fertility activity between the control probe and the sample is observed after irradiation. The total dose of the X ray radiation throughout these 14 shots observed by the TLD detectors placed upon the metal foil near the sample is 65 mSv.

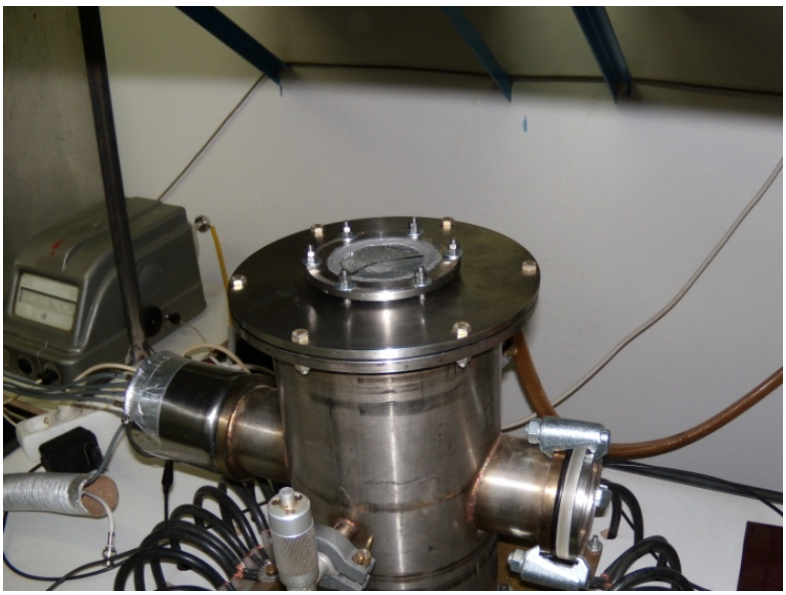

FIG. 17. View of the upper part of the plasma focus chamber. The port used for the biology experiments is seen.

Similar results have been obtained several months ago with another type of yeast - *Kluyveromyces marxiamus*, where no change of the survival enzyme activity was found after irradiation through a thick foil.

2. *Chlamydomonas reinhardtii* – (see weeds):

C. reinhardtii cells were grown photomixotrophically in a Tris-Acetate-Phosphate (TAP) medium with pH of 7.0, at a temperature of 25ºC. Cultures were first grown in 25 ml glass flaks, and were illuminated by luminescent light with a photon flux density (PFD) of 80 µmol photons m^{-2} s^{-1} 24 h/d at continuous shaking. The micrcroalgal suspension was cultivated during 7 days to achieve late exponential phase with cell density of about 4-6 × 10^6 cells/ml.

Chlorophyll fluorescence was measured using mPEA (multifunctional Plant Efficiensy Analyzer, Hansatech Ltd., Kings Lynn, UK) as reported before (Strasser et al. 2010).

First irradiation trough 20 µm Al foil and 10 µm plastic foil - 4 shots; dose ~ 11 mSv

Second irradiation trough 100 µm Al foil and 10 µm plastic foil – 14 shots; dose ~ 65 mSv

Study of the photosynthesis activity.

The method, used for analysis of photosynthetic activity in living system is given by Strasser et all [24]. According to the procedure given by these authors, the probe treated by ionizing radiation (soft X rays in this case) is illuminated afterwards with certain visible light pulses (627 ± 10nm) and then the prompt and the delayed fluorescence emission (735 ± 15 nm) of the sample is recorded *in vivo*. The changes of fluorescence intensity during dark to light transition, so called "induction curves" are derived and analyzed by the JIP-test [24].

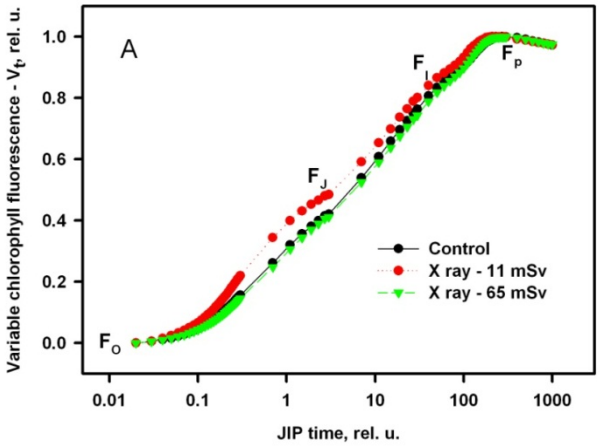

FIG. 18 A. Effect of X ray irradiation on photoinduced transients in suspension of Chlamydomonas reinhardtii. Typical induction curves (Relative Variable chlorophyll fluorescence vs. time (ms)) of the irradiated (red and green symbols) and control samples (black). V_t was calculated according relation: $V_t = (F(t) - F_o)/(F_p - F_o)$. Fluorescence values are normalized to minimal and maximal values.

Suspension of *C. reinhardtii* was dark adapted during 1 h and chlorophyll fluorescence transients was measured at actinic light intensity 5000 µmol.m^{-2}.s^{-1}. Testing of photosynthetic activity of algal cultures shows that X ray irradiation has strong effect on photosynthetic apparatus. The shape of the induction curves of was modified (Fig.16, A). The characteristic increasing of both J and I phases of fluorescence transients suggests a slowdown of electron transfer in acceptor sides of Photosystem II and I (PS II and PS I), respectively. For For visualization of the X ray effect data are presented as a differential curves (see Fig. 18 B).

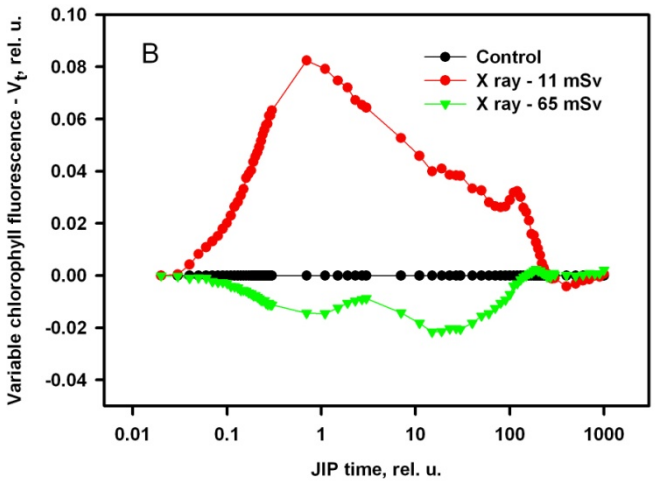

FIG. 18 B. Effect of X ray irradiation on photoinduced transients in suspension of Chlamydomonas reinhardtii. Differential curves of relative variable chlorophyll fluorescence, calculated as: V_t(treated sample) – V_t(control).

Most pronounced effect is at about 2 ms (phase J) when the stationary state of electron transfer reactions toward primary quione acceptor Q_A and from Q_A^- to Q_B is established. It means that during Test 1 the reoxidation reaction in PSII acceptor side was suppressed. The effect of X ray treatment during Test 2 can be explained as a weak stress. More detailed information concerning X ray effect on photosynthetic electron transfer chain is presented by JIP-test parameters that reflect quantum yields of primary photochemical reaction in PS II, φ_{Po}, reoxidation of PS II acceptors, φ_{Eo}, and photoinduced electron transfer through PS I to their terminal acceptors, φ_{Ro}.

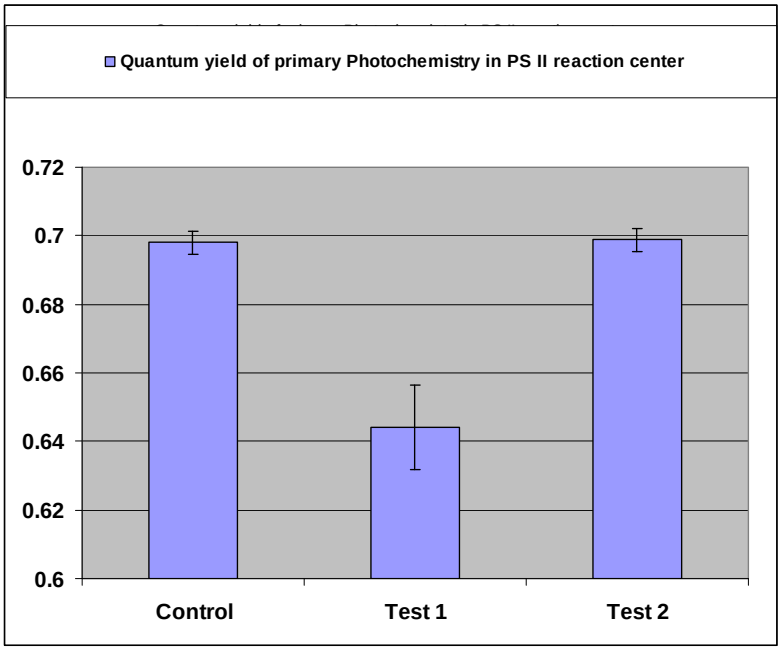

FIG. 19. Effect of X ray irradiation on Quantum Yield on the primary photochemical reaction in the Reaction Center of the PS II in suspension of Chlamydomonas reinhardtii.

Test 1 – Irradiation of the samples through 20 µm Al foil - 4 shots , Dose ~ 11 mSv.
Test 2 – Irradiation through 100 µm Al foil - 14 shots, Dose ~65 m.

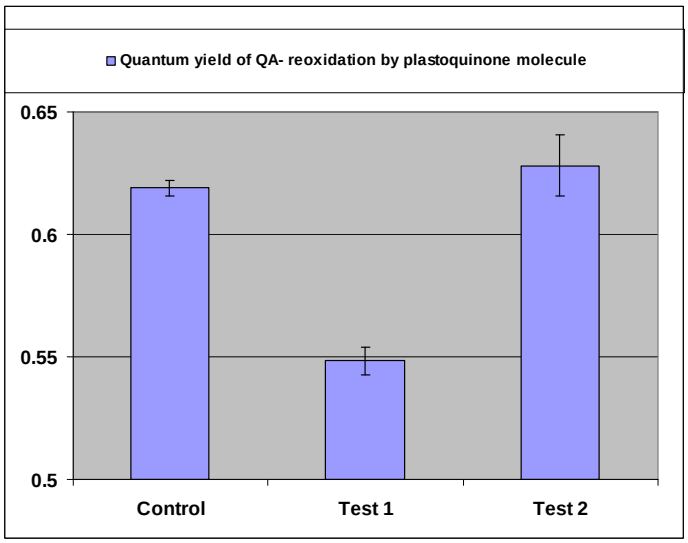

FIG. 20. Effect of X ray irradiation on Quantum Yield on re-oxidation of the quinone acceptor in PS II to the plastoquinone in suspension of Chlamydomonas reinhardtii.

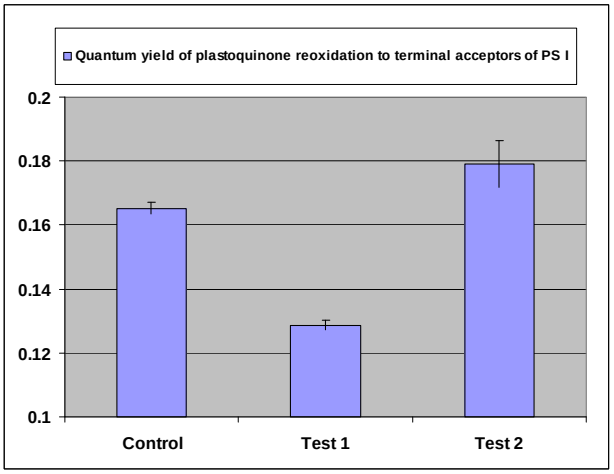

FIG. 21. Effect of X ray irradiation on Quantum Yield on re-oxidation of the plastoquinone to PS I terminal electron acceptors in suspension of Chlamydomonas reinhardtii.

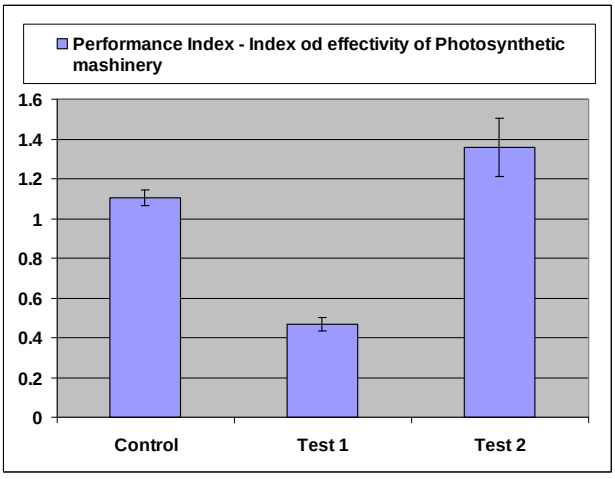

FIG. 22. Effect of X ray irradiation on Quantum Yield on Performance Index in suspension of Chlamydomonas reinhardtii.

The results obtained so far show that in the irradiated probe through 20 μm Al foil with a dose of 11 mSv the affects Photosynthetic electron transport chain at all investigated sites – in PS II, in PS I and between both photosystems. The Performance Index (it is an index quantified vitality of photosynthetic machinery and reflects both structure and functional characteristics of the total photosynthetic activity) decreases more than twice in comparison with the same value of the reference probe. In the same time a 20 percent increase of the efficiency of the electron transport increases is observed for the probe irradiated through 100 μm Al foil with a dose of 65 mSv.

SUMMARY

A progress is made in creating a comprehensive description of the plasma focus breakdown both by experimental observation and modelling of this complicated phenomenon.

Experiments with the new 3 kJ plasma focus devise in the University of Sofia gives some results about the plasma current sheath and permits to obtain data for the influence of the plasma focus X ray radiation on the photosynthesis of some living micro – organisms.

REFERENCES

[1] FILIPOV, N., FILIPOVA, T. and VINOGRADOV, V., "Dense, high-temperature plasma in a noncylindrical 2-pinch compression'"Nuclear Fusion **2** (1962) Suppl. 577.

[2] MATHER, J., Physics of Fluids **7** (1964) Suppl. 28.

[3] BERNARD, A., *et al*., "Scientific status of plasma focus research", Journal of Moscow Phys. Soc., **8** (1998) 93-170.

[4] SOTO, L., "New trends and future perspective on plasma focus research", Plasma Physics and Controlled Fusion, **47** (2005) A361 – A381.

[5] MORENO, M., BRUSONE, H., *et al.*, "Industrial applications of plasma focus radiation", Braz. Journ.. Phys. **32** (2002) 20.

[6] MORENO, M., *et al*., "0.2 Hz Plasma-Focus-based source of fast neutrons and hard x rays for applications", Plasma and Fusion Science: Proc. of the 16th IAEA Techn. Meeting on Res. with Small Fusion Devices, AIP Conference Series **875,** 2006, 23–26.

[7] VIKHREV, V., KOROLEV, V., "Neutron generation from Z-pinches", Plasma Physics Reports **33** (2007) 356 – 380.

[8] DONGES, A., HERZBERG, G., KROMPHOLZ, H., RUHL, F., SCHOMBAH, K., "The breakdown phase in a coaxial plasma gun", Phys. Lett. A **76** (1980) 391.

[9] KROMPHOLZ, H., NEFF, W., RUHL, F., SCHONBACH, K., HERZIGER, G., "Formation of the plasma layer in a plasma focus device", Phys. Lett. A **77** (1980) 246.

[10] FEUGEAS, J., "The influence of the insulator surface in the plasma focus behavior", J. Appl. Phys. **66** (1989) 3467.

[11] SHOLZ, M, IVANOVA-STANIK, I., "Initial stage in plasma focus device, model and computer simulation", Vacuum **58** (2000) 287.

[12] YORDANOV, V., GENOV, D., IVANOVA-STANIK, I., BLAGOEV, A., "Ionization growth in the breakdown of plasma focus discharge", Vacuum **76** (2004) 365-368.

[13] YORDANOV, V., IVANOVA-STANIK, I., BLAGOEV, A., "Development of the ionization wave in the breakdown of the plasma focus device", J. Phys. D: Appl. Phys. **40** (2007) 2522-2525.

[14] GRIBKOV, V., ORLOVA, M., "On various possibilities in pulsed radiation biochemistry and chemistry", Radiation Environmental Biophysics **43** (2004) 303−309.

[15] DUBROVSKY, A., GAZARYAN, I., GRIBKOV, V., IVANOV, Y., KOST, O., ORLOVA M., TROSHINA, N., "On the possible mechanism of activation changes of enzymes under pulsed irradiation", Journal of Russian Laser Research **24(**4) (2003) 289 – 300.
[16] GRIBKOV, V., *et al.*, "PF 6 – an effective plasma focus as a source of ionizing radiation and plasma streams", Nucleonika **51 (**2006) 55 – 66.
[17] YORDANOV, V., IVANOVA-STANIK, I., BLAGOEV, A., "The role of photo electrical effect in sustaining the preionization process in Plasma Focus device", J. Phys.: Conf. Ser. **63** (2007) 012022 (6 pp).
[18] YORDANOV, V., *et al*., "Surface ionization wave in a plasma focus-like model device", J. Phys. D: Appl. Phys.**41** (2008) 215208 (7 pp).
[19] HAYASHI, M., "Bibliography of electron and photon cross-section with atoms and molecules published in 20th century", NIFS-Data-72, Nat. Institute for Fus. Science of Japan, 2003.
[20] DOBRETSOV, L., GOMOYUNOVA, M., "Emisionnaya electronika", Nauka, M., 1966, *in Russian.*
[21] YORDANOV, V., BLAGOEV, A., Third International Workshop and Summer School on Plasma Physics, Kiten, Bulgaria, 2008, Abstracts.
[22] BLAGOEV, A., YORDANOV, V., "A modelling of the breakdown phase in the plasma focus discharge", PPCF **51**(12) (2009) Article Number: 124022.
[23] Plasimo web cite: http://plasimo.phys.tue.nl/
[24] STRASSER, R., TSIMILLI-MIHAEL, M., QIANG, S., GOLTSEV, V., "Simultaneous *in vivo* recording of prompt and delayed fluorescence and 820 nm reflection changes during drying and after rehydration of the resurrection plant *Haberlea rhodopensis"*, Biochimica et Biophysica Acta **1797** (2010)1313-26.

CREATION OF A DENSE PLASMA FOCUS DEVICE AND ITS APPLICATION IN RADIATION MATERIAL SCIENCES FOR THE GOALS OF THE MAINSTREAM FUSION RESEARCHES

E.V. DEMINA[*], V.A. GRIBKOV[*,**,***], A.V. DUBROVSKY[*,+], V.N. PIMENOV[*], S.V. MASLYAEV[*], M.D. PRUSAKOVA[*], I.P. SASINIVSKAYA[*], M. SCHOLZ[**], M. PADUCH[**], A. TARTARI.[++]

[*] A.A. Baikov Institute of Metallurgy and Material Science, Moscow, Russian Federation
[**] Institute of Plasma Physics and Laser Microfusion, Warsaw, Poland
[***] The Abdus Salam International Centre for Theoretical Physics, 34014 Trieste, Italy
[+] Moscow Physical Society, 119991 Moscow, Russian Federation
[++] Ferrara University, 9-44121 Ferrara, Italy

Abstract

The devices PF-5M elaborated by IMET in co-operation with Moscow Physical Society, PF-6 (IPPLM), PF-1000 (ICDMP) and "Bora" (ICTP) – all of them of the Dense Plasma Focus type – were used in irradiation experiments with different working gases and for testing of dissimilar materials perspective in the mainstream technology for fusion energy reactors. Among the materials under test with deuterium as a working gas tungsten and tungsten alloy as well as ceramics of CFC types were investigated. Experiments were provided with the use of the above devices in the range of power flux density of streams of hot plasma and fast ion beams $q = 10^6$-10^{12} W/cm^2 with irradiation pulses of about a hundred nanoseconds duration. Interaction of powerful pulsed streams of nitrogen high-temperature plasma and fast ions with low-activated austenitic steels 25Cr12Mn20W_2 and 03Cr10Mn33WV and ferritic steel 10Cr9WVTa was investigated. These experiments were provided for the aim of the surface layer modifications improving its characteristics. Specific features of the interaction of these streams of energy with the above-mentioned steels are discussed for two experimental regimes – with and without melting of the surface layer.

1. INTRODUCTION

Our investigations provided in the framework of the current Co-ordinated Research Project (CRP) of the International Atomic Energy Agency (IAEA) "Integrated Approach to Dense Magnetized Plasma Applications in Nuclear Fusion Technology" during the fulfilment of the 4-year activity of IMET entitled "Creation of a Dense Plasma Focus device and its application in radiation material sciences for the goals of the mainstream fusion researches" were concentrated in three principal directions:

1) Testing of a number of materials, counted as perspective ones for the contemporary fusion reactors (FR) of both types – with magnetic and inertial plasma confinements (MPC and IPC correspondingly) – by irradiation of specimens with powerful streams of hot plasma and fast ion beams. We used two sorts of materials: 1) intended for implementation in plasma facing components of the devices chambers (in the first wall and in the divertor elements – tungsten and some ceramics like CFC, alumina, etc.) and 2) in its construction systems (mainly different types of low activation stainless steels). The last ones were tested in our works in the same regimes as it was applied for plasma facing components because of two motivations: for the reasons of accident risks when plasma facing elements will be broken thus uncovering the FR constructions and due to possible future usage of them as plasma facing elements in the next generation of FR chambers.
2) Modification of surface layers of different materials with an aim to impart them improved characteristics like advanced corrosion and radiation resistance, higher hardness, and some others.
3) Providing a comprehensive and precise analysis of the irradiated specimens aimed to understand character and mechanisms of damageability of specimens, their resulting properties and modifications, and to elaborate recommendations on the future use of them in FR.

Dense Magnetized Plasmas (DMP) produced by a number of different devices (various plasma accelerators, pinch facilities, high-voltage/high-current fast energy storage systems of the water-line type with wire loads, etc.) occupies a niche between the inertial plasma fusion devices (e.g. of the laser-produced plasma types) and installations with the magnetic plasma confinement (for example, of the tokamak type) because of the characteristic times of their physical processes and their main plasma parameters.

Besides its own intrinsic fusion perspectives discussed in 50's and now re-emerging due to new concepts put forward during the last few years, installations based on plasma of this type can serve as very powerful sources of various types of ionizing radiation for a number of important applications. In this CRP we used the sub-class of DMP installations – the so-called Dense Plasma Focus (DPF) devices [1]. The DPF facility is a type of plasma accelerator that produces directed hot (T_{pl} ~ 1 keV) fast ($v_{pl} > 10^7$ cm/s) dense ($n_{pl} \approx 10^{16}$ to 10^{19} cm^{-3}) plasma streams, high energy ion ($E_i \approx 0.01$ to 100 MeV) and electron ($E_e \approx 0.01$ to 1.0 MeV) beams in addition to soft (E_{hv} ~ 0.1 to 10 keV) and hard (E_{hv} ~ 10 to 1000 keV) X rays and fusion neutrons (E_n ~ 2.45 and 14 MeV) [2].

These streams and beams have characteristic parameters that exist in present-day accelerators and space vehicles, but in particular, in thermonuclear fusion devices employing inertial and magnetic plasma confinement, e.g. at plasma facing components of future fusion pilot reactors such as Iter and NIF facilities. They can also be used for a large number of applications where one needs short powerful pulses of radiation of the above-mentioned types.

Dense Plasma Focus devices, compared with other thermonuclear devices, have a number of important advantages:

- These devices provide an opportunity to expose different materials and objects to pulsed directed beams of various types – ion, electron, plasma, X ray, neutron and shock wave – of high-power flux density (up to 10^{13} W/cm^2 for fast electrons, 10^{12} W/cm^2 for fast ions, plasma streams and X ray photons and up to 10^9 n/cm^2 for neutrons) with pulse duration in the range 10^{-9} to 10^{-6} s. Thermal loads in these devices produced by the above-mentioned streams and a discharge current may reach magnitudes up to 10^{10} MW/m^2 with the characteristic time of action up to about 10^{-4} s.
- Because all types of radiation generated by DPF are of penetrating nature these devices can produce important volumetric effects (in contrast to lasers).
- They enable the experimenter to choose the specific distribution of pulsed energy between all the above-mentioned types of ionizing radiation – soft and hard X rays, neutrons, electron, ion and plasma beams. It is so because energy flux density may be significantly different for each type of radiation depending on the mode of a device operation.
- These streams in DPF devices can be separated in time due to different velocities of their (quasi-)particles.
- These beams in DPF devices can also be separated in space due to different angular distributions and by application of a magnetic field as well as because of their dissimilar Linear Energy Transfer (LET).
- Very high brightness of radiation of the above types gives important opportunities for new and sometimes unusual applications in pulsed radiation physics and chemistry in general, and in different branches of material sciences (radiation material science, nano-technologies, dynamic quality control of machines and mechanisms during their operation, express neutron activation analysis, etc.) in particular.

- The physics of interaction of high-power pulses of radiation generated in different fusion devices with materials is especially important for study of damage produced in elements of these installations including the discharge chamber of the DPF itself, but specifically the plasma-facing walls of thermonuclear fusion installations with inertial (laser, wire-array Z-pinches and heavy ion fusion) and magnetic (tokamak and stellarator) plasma confinement. In the latter case DPF devices can simulate radiation loads, which are typical for the stressed regimes of the reactor's operation (ELMs, VDEs, disruption instability, etc.).

2. IRRADIATION EQUIPMENT AND ANALYTICAL METHODS USED IN THE EXPERIMENTS PROVIDED BY THE IMET TEAM

2.1. Equipment used in the irradiation experiments

2.1.1. The PF-5M device and its metrology

This device PF-5M (Fig. 1) was elaborated by IMET during the fulfilment of the current IAEA CRP in cooperation with the Moscow Physical Society (MPS), and it is based at the A.A. Baikov Institute of Metallurgy and Material Sciences, Russian Academy of Sciences (IMET RAS, Moscow, RF). General device's characteristics are presented in the Table 1.

a)

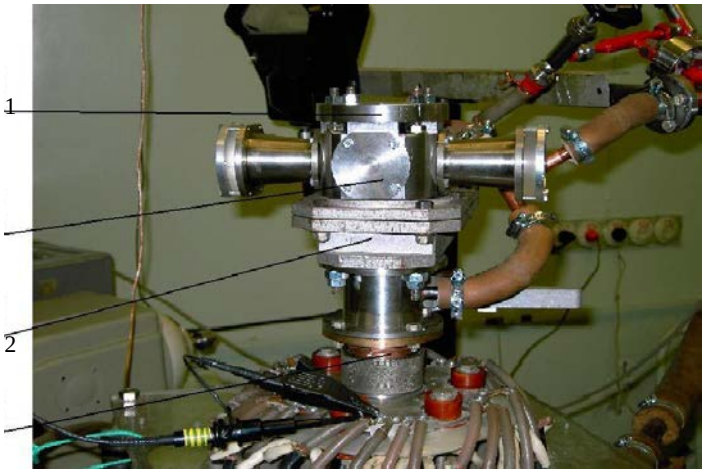

b)

FIG. 1. PF-5M device (a) with the DPF chamber and supplement parts (b) designed for experiments in the area of radiation material science: 1) small visible edge of DPF chamber, 2) vacuum gate valve, 3) target set, 4) target set cover with the sample holder (inside the chamber).

The works on this device was carried out by MPS and IMET in close collaboration with colleagues from other institutes-participants of the CRP (Institute of Plasma Physics and Laser Microfusion – IPPLM, and International Centre for Dense Magnetized Plasmas – ICDMP, both in Warsaw, Poland, and Tallinn University – TU, Tallinn, Estonia).

TABLE 1. MAIN PARAMETERS OF THE PF-5M DEVICE

Bank capacity	16 μF
Charging voltage	15 - 20 kV
Energy storage	1.8 - 3.2 kJ
Working gases	N, H_2, Ar, Xe, He, CH_4, or indoor air
DPF chamber type	The Mather configuration
Repetition rate	1 shot per 2 min
Life-time of the DPF systems	~ 10^4 shots

The PF-5M device now is in operational status. The main function of the device is connected with its use in radiation material science. The series of austenitic and ferrite samples, Al_2O_3, CFC, tungsten samples were irradiated by hot plasma jets (temperature T_{pl} ~ 300 eV, speed v_{pl} ~ 2×10^7 cm/s) and fast ions (energy E_i ~ 100 keV) under different irradiative conditions (the number of irradiative pulses was changed from 1 to 50, distances between the anode and a specimen were in the range 3…15 cm). In process of the experiments the following diagnostics were used for registration of:

- Oscilloscope traces of the discharge current (by the Rogowski coil) and voltage (by the resistive divider) (see Fig. 2).
- Oscilloscope traces of the time derivative of the discharge current *dI/dt* (by magnetic probes).
- Hard R-ray doses (by the gas ionization chamber).
- Temporal behaviour of X ray and visible light pulses (by detectors of the type E.CCDI38 based on the photomultiplier tubes (PMT) of the type SNFT18 (time resolution τ ~ 2.5 ns, linear output current I_{linear} ~ 5 A) equipped with plastic scintillators (S)).
- Thermal loads (based on thermocouple calorimeter method with the copper washer of precisely weighted mass as calorimetric detector. Digital thermocouple thermometer of *K*-type was used to measure a temperature difference between measuring and ballast elements directly after each DPF shot).

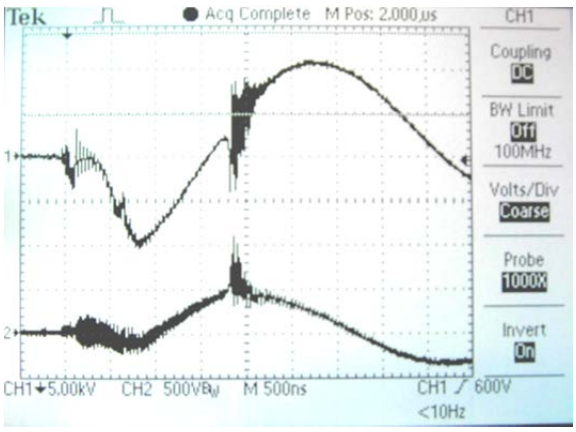

FIG. 2. Oscilloscope traces of the signals of high voltage (top) and current (bottom).

The new demountable stainless steel DPF chamber was designed and has been realized. It is fitted for works of testing of various new constructions as well as different metals in order to optimize the chamber design.

1.1.2. Other irradiation facilities and corresponding diagnostics

Besides of using the PF-5M device IMET continued its participation in mutual experiments on PF-6 device (7 kJ, IPPLM, Poland), PF-1000 facility (1.0 MJ, ICDMP, Poland) and "Bora" set-up (5 kJ, the Abdus Salam International Centre for Theoretical Physics – ICTP, Trieste, Italy) with colleagues from other institutes-participants of the CRP (IPPLM, ICDMP, ICTP, TU and Ferrara University, Ferrara, Italy).
The above-mentioned devices are equipped by some additional to the above-mentioned diagnostics giving opportunities to investigate the *process* of interaction of radiation with targets (material specimens) in more details (laser interferometry, plasma self luminescence, plasma spectroscopy, etc.) and with high temporal (~ 1 ns) and spatial (~ 10 μm).

2.2. Equipment used in the analysis of the irradiated specimens

For the instrumental analysis of the irradiated specimens we have used equipment as follows:

- Optical microscopes NU-2E and Neopot-32 with computerized image processing.
- Scanning multi-microscope VMM-2000.
- Focused beam microscope VEGA/SBU with a system of X ray energy dispersion microanalysis, Oxford Instruments.
- High precision X ray Diffractometer, Rigaku Ultima IV (III Thin-film).
- Optical emission spectrometer based on a glow discharge Leco GDS-850A.
- Automated micro- and macro-hardness meters 401/402-MVD and Digi-Testor 930N.
- Universal test instrumentation MicroTester 5848 and Electropuls E3000, Instron.
- Unit for measuring of nano-hardness NanoTest, Micro-Materials Ltd, et al.

3. DAMAGEABILITY OF THE SURFACE LAYER OF SAMPLES MADE OF W AND W-1LA_2O_3 ALLOY SUBJECTED TO THE ACTION OF POWERFUL PULSED STREAMS OF DEUTERIUM FAST IONS AND HOT PLASMA INSIDE THE DPF DEVICE

3.1. Introduction

Important problems of material sciences in the field of thermonuclear energy facilities are elaboration, selection and testing of materials intended for the most heat loaded parts of the device where the direct contact of hot plasma with a solid surface takes place. In particular, tungsten is proposed as one of the main materials for the divertor of the reactor Iter elaborated in the frame of the international program on this device that uses MPC. Practical impossibility of testing candidate materials inside real reactors of thermonuclear fusion of proper dimensions makes the task of simulation investigations of them under high energy density streams of hot plasma and fast ion beams to be pressing. Devices of the Dense Plasma Focus type show themselves as effective instruments for modelling of an action of pulsed thermal and radiative loads upon material surface [3 – 6]. In present work we investigated some features of radiative-thermal action of pulsed streams of fast deuterons and hot deuterium plasma produced in the PF-1000 facility [7] upon specimens manufactured of pure tungsten and tungsten with doping of lanthanum oxide.

3.2. Materials and experimental methods

For comparative experiments we selected two types of materials manufactured by a company PLANSEE: pure tungsten (W) and tungsten containing 1 mass percent (mass-%) of doping of lanthanum oxide – the W-1La_20_3 alloy. The materials were obtained by methods of powder metallurgy enclosing mixing of tungsten powder with lanthanum oxide, pressing, agglomerating and rolling.

Fig. 3 shows microstructure of the W-1La_2O_3 alloy where metallographic section is made in a plane perpendicular to the rolling direction. Lanthanum oxide inclusions are seen as dark strokes. Specimens were plates with sizes 20×25 mm. Plates of pure tungsten have thickness of 4 mm whereas plates of the W-1La_2O_3 alloy – 2 mm.

Irradiation experiments were provided at the PF-1000 device (IPPLM, Warsaw, Poland) [7] in a geometry shown in Fig. 4. Samples of materials were placed at the cathode part of the facility at a distance of 70 mm from the anode surface. Charging voltage was 24 kV, working gas – deuterium at the initial pressure equal to 2.1 Torr. We have irradiated 4 samples of pure tungsten and 5 samples of the W-1La_2O_3 alloy. Each sample was subjected to two successive sessions of irradiation with an interval of a few minutes. Durations of each pulse of hot plasma (acting first) and of fast ions (irradiating a sample later) were about 100 ns. These pulses acted upon specimens successively one after another. Power flux density changed from 10^{12} W/cm^2 at the centre of the sample (where we had both hot plasma and fast ion streams) down to 10^9 W/cm^2 at its periphery (where only the hot plasma stream was presented).

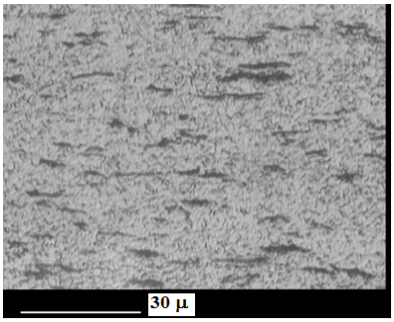

FIG. 3. Microstructure of the virgin sample of the alloy W-1La_20_3.

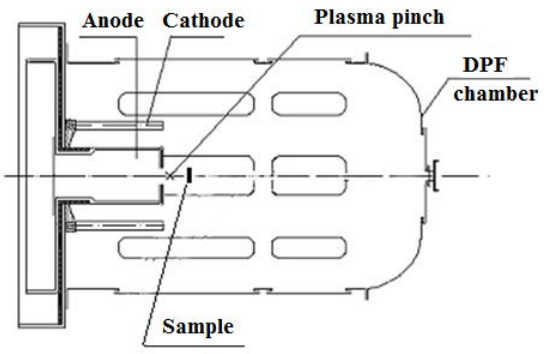

FIG. 4. Schematic of the irradiation geometry at the PF-1000 facility.

During the irradiation process we provided interferometric measurements of plasma dynamics both for primary pinch plasma and for secondary plasma produced on the surface of samples by hot primary plasma and fast ion streams generated inside the pinch.

Laser frame interferometry has temporal resolution (laser pulse duration) equal to 1 ns with time intervals between frames (1 frames in total during each DPF shot) equal to 10 or 20 ns. Fig 5 presents a typical interferometric picture of primary (pinch, on the left-hand side) and secondary (on the right side in front of the target of W-1La_2O_3) plasmas as they look at the moment very soon after an irradiation of the sample by hot plasma and fast ion streams. One may see that the cloud of secondary plasma is very well developed near the surface of the target. Its velocity of expansion is equal to ~ 10^7 cm/s and it is transparent for the laser light (second harmonic of Nd-glass laser). Both these facts mean that its temperature was high (several hundred eV). This secondary plasma cloud increases time of the sample's heating compared with the time of the action of fast ion/hot plasma streams from the pinch.

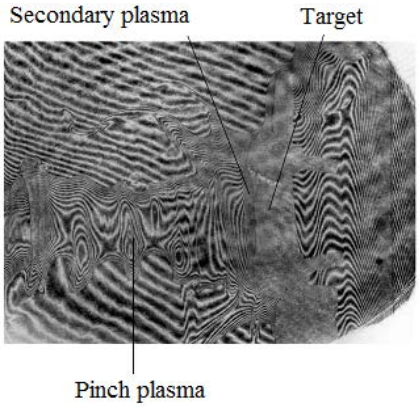

FIG. 5. Interferometric picture of plasma density distribution taken during the process of the irradiation of a sample manufactured of the alloy W-1La_20_3.

Structure of the surface relief of specimens before and after irradiation was investigated by methods of optical and scanning electron microscopy. Elemental content was determined by means of X ray spectral analysis. Micro-hardness was measured at the device PMT-3. Numerical modelling of thermal effects produced by powerful pulsed streams of fast deuterium ions (energy about 100 keV) and hot deuterium plasma (velocity about 2×10^7 cm/s, temperature $\leq$ 1 keV) upon materials under investigations was done according to a method described in [8].

3.3. Results

3.3.1. Formation of a surface relief

Analysis of the samples surfaces made after irradiation by method of optical microscopy has shown that an action of streams of hot plasma and fast ions together with the secondary plasma results in melting of a surface layer of tungsten. Fig. 6 and 7 present some parts of the surfaces of tungsten and of a W-1La_2O_3 alloy after a two-fold irradiation.

One may see that the aerodynamic action of streams of dense plasma and fast ions having velocities much higher compared with the sound velocity produced a formation of waves on the melted surface of samples. Besides a brunched structure of cracks is seen on the surface that was appeared in the conditions of fast cooling after crystallization of the melted layer. At this stage thermal stresses within the layer are created because compression of this thin hot layer is prevented by its strong coupling with the cold bulk of the specimen. Magnitude of these stresses very likely exceeded the ultimate strength of the material.

Fig. 8 shows a picture of the tungsten surface obtained in secondary electrons by means of a Scanning Electron Microscopy (SEM).

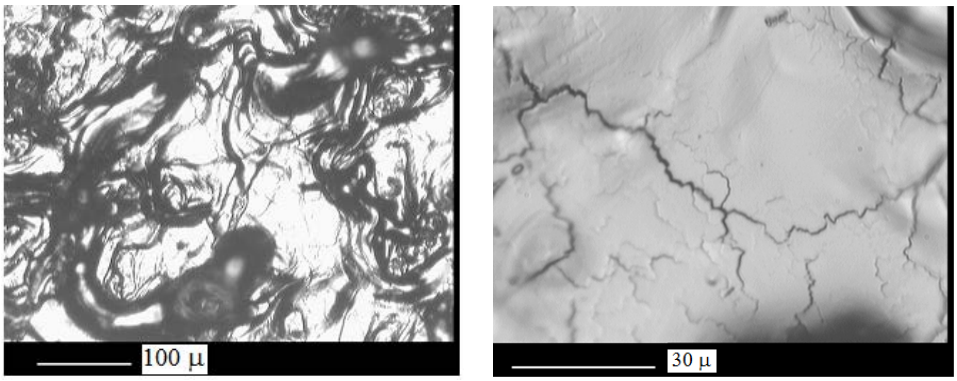

FIG. 6. Surface of a specimen of pure tungsten after its irradiation by hot dense plasma and fast ion streams (optical microscopy) shown here with different magnification.

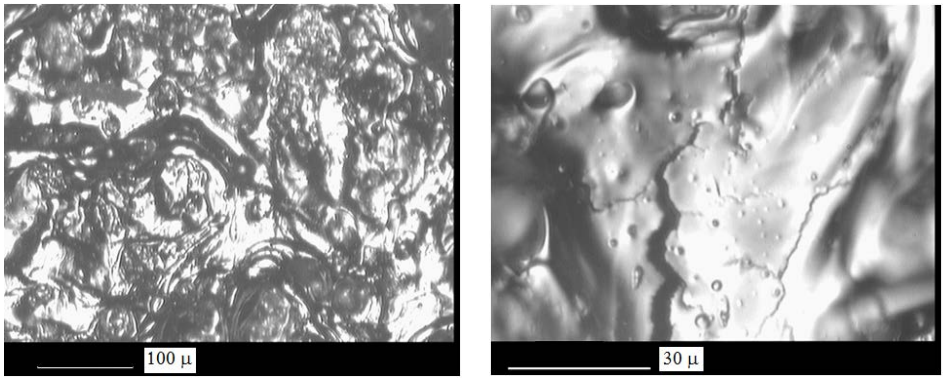

FIG. 7. Surface of the sample of W-1La_20_3 alloy after its irradiation by hot dense plasma and fast ion streams (optical microscopy).

3.3.2. Chemical composition of the surface layer

X ray spectral analysis of specimens of W and W-1La_2O_3 alloy has shown that some impurities are existed inside the surface layer of the irradiated samples. These impurities are typical for the elemental composition of construction components of Dense Plasma Focus chamber: Fe, Ni, Cr (entering into composition of stainless steel of cathode), and copper as well (anode of the chamber).

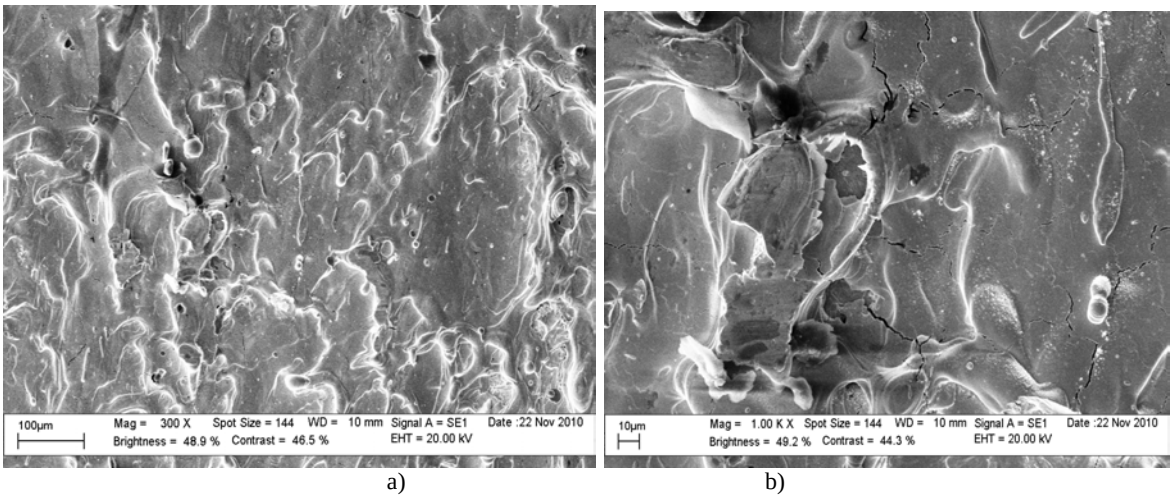

a) b)

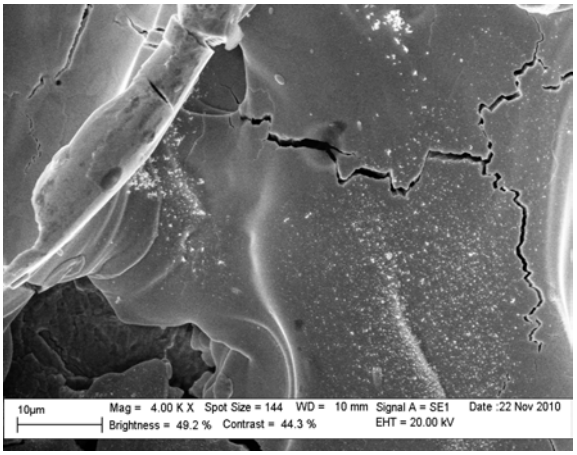

c)

FIG. 8. a), b) and c) are zones of the surface of a tungsten specimen irradiated by streams of fast ions and hot plasma of deuterium(SEM).

These elements were intensively evaporated from the chamber's electrodes and re-deposited onto the surface of samples under irradiation. Fig. 9 and 10 as well as corresponding Tables 1 and 2 present data on chemical composition of surface layers of the samples of tungsten and W-1La_2O_3 alloy in different zones of the irradiated surfaces.

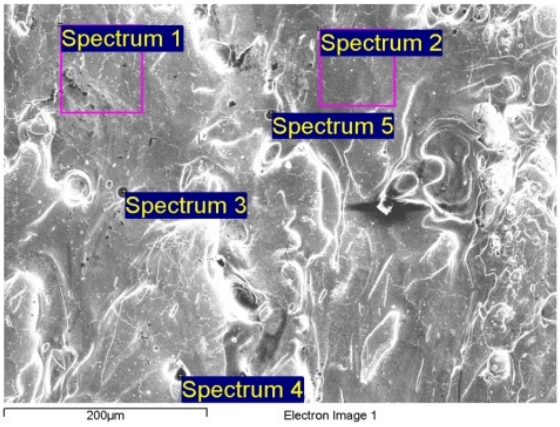

FIG. 9. Irradiated surface of pure W with marked zones where composition of a surface layer was determined (SEM).

TABLE 1. CHANGES IN ELEMENTAL COMPOSITION (AT.-%) OF THE SURFACE LAYER OF THE W-SAMPLE AFTER IRRADIATION

Zone\element	O	Cr	Fe	Ni	Cu	W	Total
Spectrum 1	19.95		6.56			73.48	100.00
Spectrum 2	21.01		6.35			72.64	100.00
Spectrum 3	4.78	9.75	73.27	10.24		1.95	100.00
Spectrum 4			18.13			81.87	100.00
Spectrum 5	3.40	0.92	4.15	1.33	89.12	1.08	100.00
Max.	21.01	9.75	73.27	10.24	89.12	81.87	
Min.	3.40	0.92	4.15	1.33	89.12	1.08	

To investigate the components distribution by depth a determination of elemental composition was performed along the cross section of the surface layer. Fig. 11 and corresponding to this figure Table 3 show results of X ray spectral analysis of the surface layer of a specimen of the W-1La_2O_3 alloy.

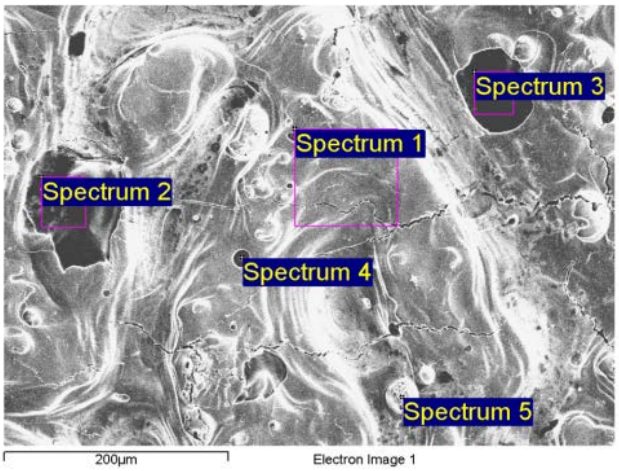

FIG. 10. Irradiated surface of the sample of W-1La_2O_3 alloy(SEM) with marked zones where composition of a surface layer was determined.

TABLE 2. CHANGES IN ELEMENTAL COMPOSITION (%) OF THE SURFACE LAYER OF THE W-1LA_2O_3 ALLOY SAMPLE AFTER IRRADIATION

Zone/element	O	Cr	Fe	Ni	Cu	La	W	Total
Spectrum 1	25.74		5.34			1.07	67.84	100.00
Spectrum 2	7.82	3.88	15.78		68.35	0.00	4.17	100.00
Spectrum 3	7.26	3.36	12.94	1.68	71.37	0.39	3.00	100.00
Spectrum 4	14.43	4.15	16.26		43.66	0.00	21.51	100.00
Spectrum 5							100.00	100.00
Max.	25.74	4.15	16.26	1.68	71.37	1.07	100.00	
Min.	7.26	3.36	5.34	1.68	43.66	0.00	3.00	

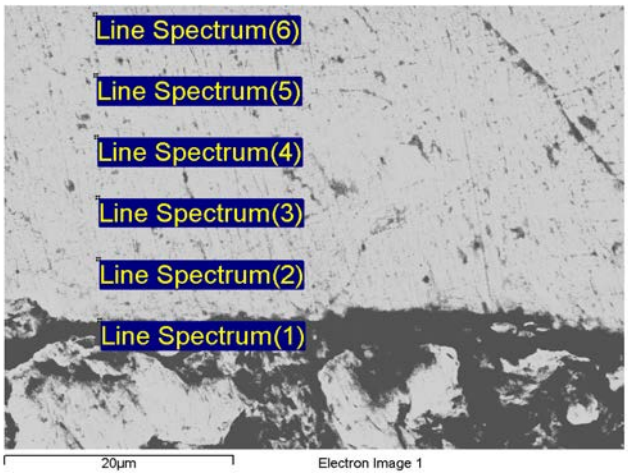

FIG. 11. Cross-section of the surface layer of the specimen of W-1La_2O_3 alloy with marked zones where composition of a surface layer was determined.

TABLE 3. CHANGES IN ELEMENTAL COMPOSITION (%) BY DEPTH WITHIN THE SURFACE LAYER OF THE W-1LA_2O_3 ALLOY SAMPLE AFTER IRRADIATION

Region/element	C	O	W	Total
Line Spectrum(1)	41.85	3.31	54.83	100.00
Line Spectrum(2)	31.29		68.71	100.00
Line Spectrum(3)	28.70		71.30	100.00
Line Spectrum(4)	24.94		75.06	100.00
Line Spectrum(5)	22.91		77.09	100.00
Line Spectrum(6)	20.02	1.89	78.09	100.00
Max.	41.85	3.31	78.09	
Min.	20.02	1.89	54.83	

Point marked as the “Line Spectrum (1)” corresponds to the position maximal close to the irradiated surface. All other points were selected with regular distances by depth equal to 5.5 μm. It was appeared somewhat unexpectedly that concentration of carbon in the layers of all samples under investigation was quite considerable. This concentration decreases monotonically from the surface to the depth (Fig. 12). Same picture was observed for pure tungsten.

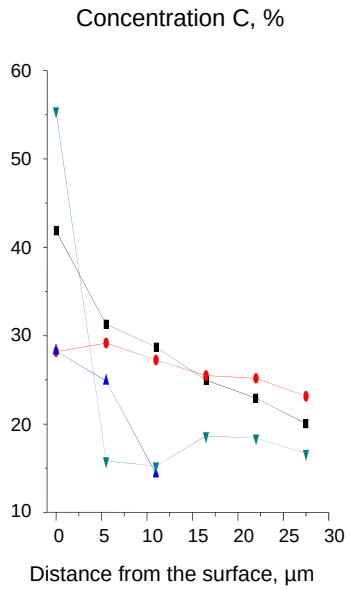

FIG. 12. Concentration of carbon versus distance from the surface.

3.3.3. Micro-hardness of the irradiated samples

Average values of micro-hardness inside the main bulk of the materials under investigation are equal to 6000 – 7000 MPa. After irradiation we observed a certain softening of the materials both from the irradiation side and from the back side of the samples within a thin near-surface layer (~ 250 μ). It can be seen in Fig. 13 where we present results of micro-hardness measurements along the cross-section of the specimen of W-1La_2O_3 alloy.

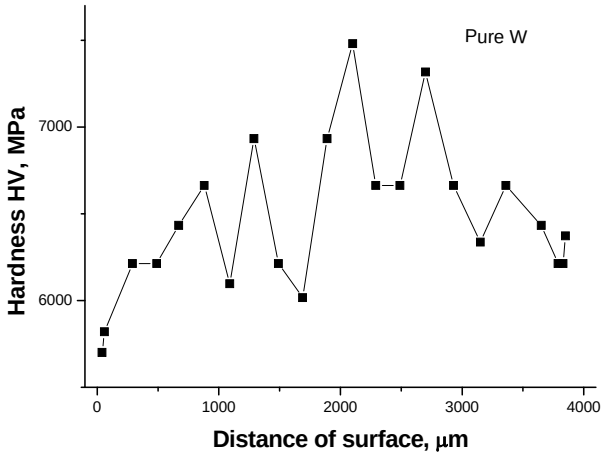

FIG. 13. Results of measurements of micro-hardness of samples of W-1La_2O_3 alloy along its cross-sections provided after its irradiation.

We must note here that our samples were relatively small by area and that our plasma stream ejected by the pinch was hot. So these plasma clouds enveloped the samples and might act upon the rear side of our samples with about the same effectiveness as from the front side.

3.3.4. Numerical modelling of thermal effects

Fig. 14 shows calculation graphs of distribution of temperature by depth of the surface layer of tungsten for different moments of time.

Numerical modelling of processes of tungsten heating and melting has shown that thickness of the layer of liquid phase δ changes in time by a complicated way. This behaviour results from variation of impacts of two competitive processes: melting and evaporation of the material. At the initial stage during an increase of the radiation intensity the value of δ enlarges up to 0.3 μm. Then the absorption of the high intensity radiation produces strong evaporation of the material and this thickness δ is decreased down to 0.04 μm.

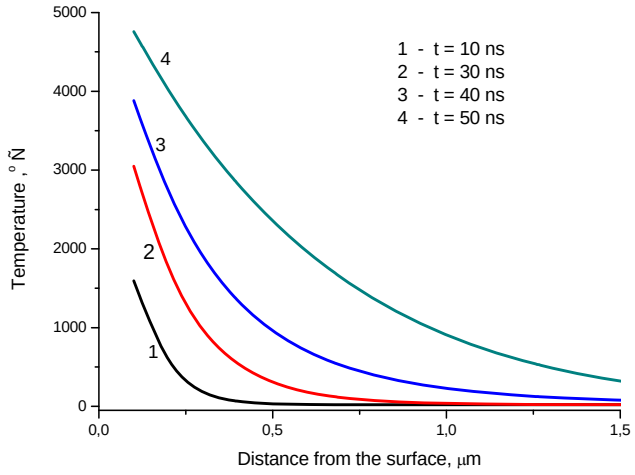

FIG. 14. Temperature distribution by depth of the surface layer of tungsten at the stage of its heating due to irradiation by streams of hot deuterium plasma and fast deuterons at q = 10^9 W/cm^2.

In the final stage of the heating pulse its intensity decreases and the dominating process appears to be again a movement of the border “liquid melt – solid body” because of intensive melting. Thickness of the melt reaches its maximal value: $\delta \approx 0.48$ μm. In about 205 ns after the beginning of irradiation action this melt is solidified completely.
In our experiments an erosion of a surface layer took place due to evaporation of material resulted in a decrease of its thickness. Calculations have shown that at the power flux density equal to $q = 10^9$ W/cm^2 this diminution of thickness is equal to ~ 1.6 μm.
Diagrams of temperature distributions at the cooling stage are presented in Fig. 15.

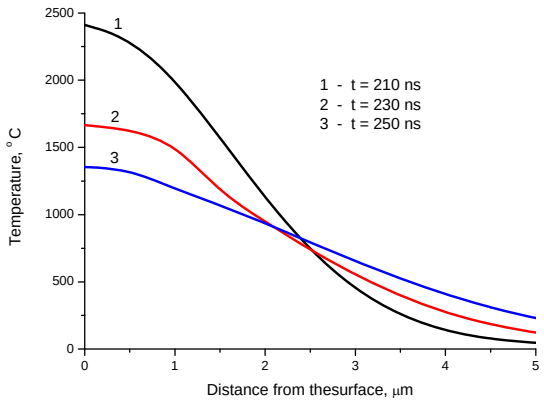

FIG. 15. Temperature distribution within the surface layer of tungsten by depth at the cooling stage after irradiation by powerful streams of hot deuterium plasma and fast deuterons at $q = 10^9$ W/cm^2.

Calculations has shown that cooling of crystallized and adjacent to it layers of material takes place in the conditions of a very high temperature gradient. Thus at $t = 250$ ns after the beginning of the action of irradiation pulses (graph 3 in Fig. 15) a magnitude of the *gradT* at the depth of a few micrometers from the surface is equal to $\approx 2\times10^6$ K/cm. Estimations show that such high values of temperature gradients result in thermal stresses within a surface layer of a sample in the cooling stage. Namely these stresses may exceed the breaking point of tungsten and result in formation of surface micro-cracks observed in metallographic pictures of Fig. 6 – 8.

3.4. CONCLUSIONS

1. Characteristics of radiation-thermal action of powerful pulsed streams of fast deuterium ions and hot deuterium plasma upon pure W and W-1La_2O_3 alloy (tungsten with doping of lanthanum oxides inclusions) were investigated by means of the PF-1000 facility. Irradiation provided in the selected regime (power flux density of the streams 10^{12} to 10^9 W/cm^2, heating pulse duration 200 ns) results in heating, melting and evaporation of thin surface layer of the materials.

2. It is shown experimentally that an action of the aerodynamic pressure of powerful streams of fast ions and hot plasma upon the thin melted layer of samples of tungsten and alloy W-1La_2O_3 results in a creation of wave-like relief that is preserved on the irradiated surface after solidification of the melt.

3. It is found that after pulsed action of the above mentioned energy streams a net of micro-cracks is produced in the irradiated surface layers. Calculations have shown that the surface crack formation may be connected with the high temperature gradients existed near the surface at the cooling stage.

4. Softening of the layers on both surfaces of samples (front and rear) of pure tungsten and W-1La_2O_3 alloy from the values of 6000 – 7000 MPa (typical for the bulk of the materials) till magnitudes of 4000 – 5000 MPa was observed. This loss of strength is connected with thermal treatment of the surface layers at pulsed heating of them by direct streams of hot dense plasma and by enveloping of samples by it.

5. All experiments provided for two materials under investigation – pure W and W-La_2O_3 alloy – gave close results. Taking into consideration that the above alloy can be machine working much easier compared with pure tungsten this alloy now can be considered as an alternative one for the divertor unite of the working chamber of thermonuclear reactors of the tokamak type (in particular for ITER).

5. STAINLESS STEEL MATERIALS UNDER THE ACTION OF HIGH-POWER STREAMS OF HOT NITROGEN PLASMA AND FAST NITROGEN IONS

5.1. Introduction

Processing of material by powerful pulsed streams of high-temperature plasma results in changes of structure-phase state of its surface layer (SL) and gives an opportunity to influence upon its physical-chemical, mechanical, radiation resistance and other characteristics [15–19]. Implantation of the working gas ions into material realized at this treatment can be or not be accompanied by melting of the SL. In both cases modification of the layer will take place but character of the structure changes as well as of its characteristics will be dissimilar.

Investigation of results of interaction of powerful pulsed streams of fast nitrogen ions (NI) and nitrogen hot plasma (NP) having duration in a nanosecond range and generated by Dense Plasma Focus (DPF) devices with low-activated austenitic and ferritic-martensitic stainless steels was the aim of this work. In particular characteristic features of damage and structure-phase changes were examined.

Behaviour of austenitic 25Cr12Mn20W2V and ferritic-martensitic 10Cr9WVTa steels as candidate materials for thermonuclear fusion reactor (TFR) under the action of powerful pulsed energetic streams was investigated previously [15, 17–19]. As working gas in these experiments hydrogen and deuterium were used. Researches of pulsed action on the above-mentioned steels produced by NI and NP are absent and they are of fundamental and applied interest.

5.2. Materials, irradiation conditions, methods of analysis

5.2.1. Materials

Chemical composition of steels under investigation is presented in Table 6. The steels under examination were different by their manufacturing technology and thermal treatment. Austenitic low-activated chromium-manganese steel 25Cr12Mn20W2V was investigated upon delivery: cold-rolled 1-mm sheet with 20% of cold deformation after finishing high-temperature annealing at 1050ºC, 30 min. Austenitic low-activated chromium-manganese steel 03Cr10Mn33WV appeared as a hot-forged bar with a rectangular cross-section 15×15 mm^2 with thermo-treatment by the regime: heating at 1000ºC, 30 min., water cooled. Ferritic-martensitic steel 10Cr9WVTa (cold-rolled 1-mm sheet) was subjected to thermal processing by the regime: normalization at 1050ºC, 30 min., with subsequent tempering at temperature

780ºC, 1 hour (main regime of thermal processing). Then it was kept to long mature at 600ºC during 600 hours.

Steels 25Cr12Mn20W2V and 03Cr10Mn33WV had austenitic structure with carbide of the types MC and $M_{23}C_6$. Ferritic-martensitic steel 0Cr9WVTa had structure of tempered martensite containing cementite Fe_3C (about 3%) and chromium carbide $Cr_{23}C_6$ (about 2%). Flat samples of the above-mentioned steels having dimensions 10×10×1 mm^3 were used in the experiments.

TABLE 6. CHEMICAL COMPOSITION OF STEELS UNDER INVESTIGATION

Steel	Elements, mass %									
	C	Cr	Mn	Si	W	V	Ta	N	P	S
25Cr12Mn20W2V [6]	0.25	11.57	20.75	0.02	2.01	0.1	-	0,003	0.04	0.01
03Cr10Mn33WV[7]	0.03	10.0	33.0	-	1.0	1.0	-	0,06	-	-
10Cr9WVTa[8]	0.11	9.2	0.65	0.3	1.0	0.15	0.1	0.03	0.02	0.007

Remarks: 1) Steel 25Cr12Mn20W2V was manufactured by Oak-Ridge National Laboratory, USA. It contains 0.006% of B. 2) Steel 03Cr10Mn33WV has been manufactured IMET, AS of Georgia.

5.2.2. Irradiation conditions

Two devices – PF-6 (energy 3 kJ, Institute of Plasma Physics and Laser Microfusion, Warsaw, Poland) and PF-5M (2 kJ, A.A. Baikov Institute of Metallurgy and Material Science RAS, Moscow, RF) were used for irradiation. Working gas was nitrogen. The harshest mode of operation at irradiation experiments resulting in sample's surface melting was realized with the PF-6 device. At the PF-5M the softer regime without such melting was produced. Scheme of the experiment provided with the PF-5M device is presented in Fig. 22. NP streams had a speed about 10^7 cm/s and density in the range 10^{15}…$10^{18}cm^{-3}$ (depending on the distance between the source – DPF pinch – and the target). Energy of fast ions was in the range 10…200 keV with the maximum around 80 keV). Power flux density of each stream also depends on the same distance and was in the limits 10^6…10^9 W/cm^2.

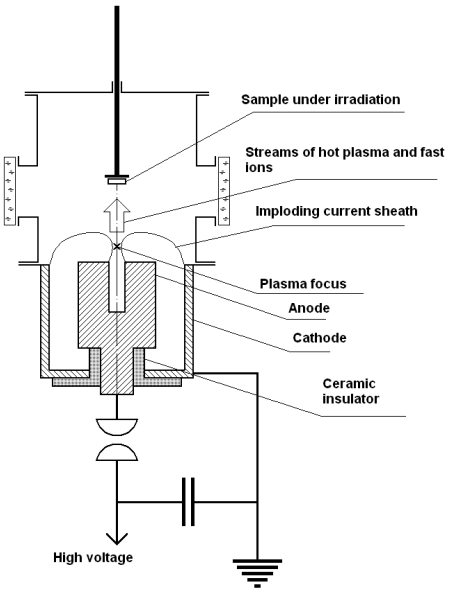

FIG. 22. Schematic of the device PF-5M.

5.2.3. Analytical methods

Microstructure of steel samples was investigated by methods of optical and scanning electron microscopy (OM and SEM), X ray structure and X ray spectrum analysis. X ray diffraction analysis was provided by a help of the device DRON-1 in cooperation with the electron data base PDF.

5.3. Results and discussion

5.3.1. Computing of thermal filed in the surface layer of the steels at the action of a single pulse

Fig. 23 and 24 present temperature distribution curves within the steel SL calculated by method of numerical modelling [8] for different time moments after their irradiation by streams of NI and NP in the regimes of melting (Fig. 23) and without it (Fig. 24). In these calculations we took into account that at the high power flux densities with $q \geq 10^8$ W/cm^2 streams of NI and NP produce secondary plasma by evaporation of metal under irradiation. Temperature of secondary plasma is close to that one for primary plasma (~ 1 keV) but later on after about 10^{-6} s it is decreased down to 2-3 eV (2...3×10^4 ^{0}C) and preserved on this level during 20-30 microseconds with density decrease by 2-3 orders of magnitude.

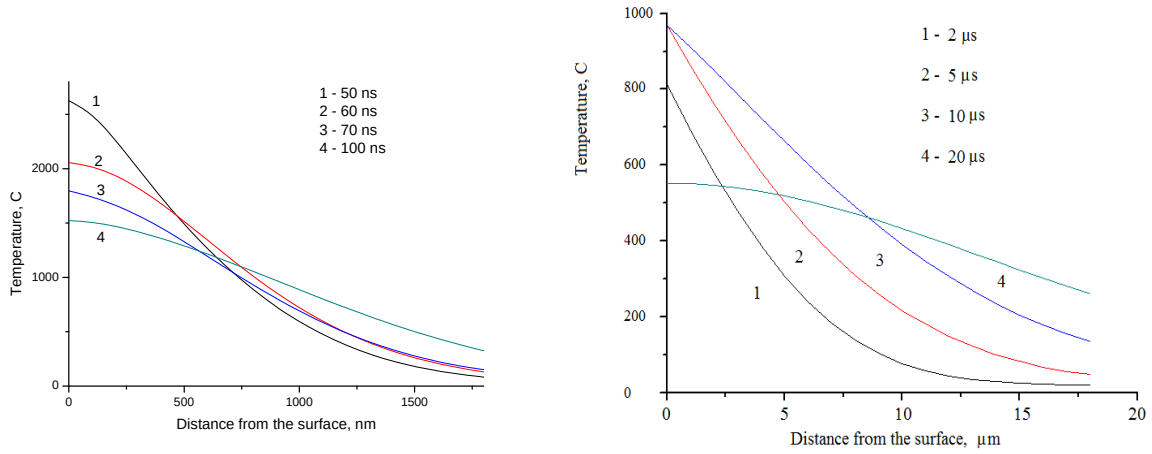

FIG. 23. Temperature distribution within the surface layer of steels irradiated by streams of NI and NP in the device PF-6 in the regime with melting of SL presented for different time moments after the irradiation pulse action ($q = 10^8$-10^9 W/cm^2, τ = 50 ns).

Secondary plasma helps in the increase of duration of thermal processes within the SL, and it was taken into account at the computing of the thermal field evaluation. Fig. 23 shows that the distance in which temperature changes in the range $T_{SL} > T_{melt} > T > T_{recrist}$ and where processes of structure changes could take place is equal to a few μm.

Energy of implanted ions in the irradiation regime realized (Fig. 24) was ruled by temperature of plasma stream ($T \approx 1$ keV) and by energy of fast ions from the stream of NI ($E_i \approx 100$ keV). Correspondingly their penetration depth h for irradiated steels' material (projective path depth) was in the range from a unit till ≈ 100 nanometers.

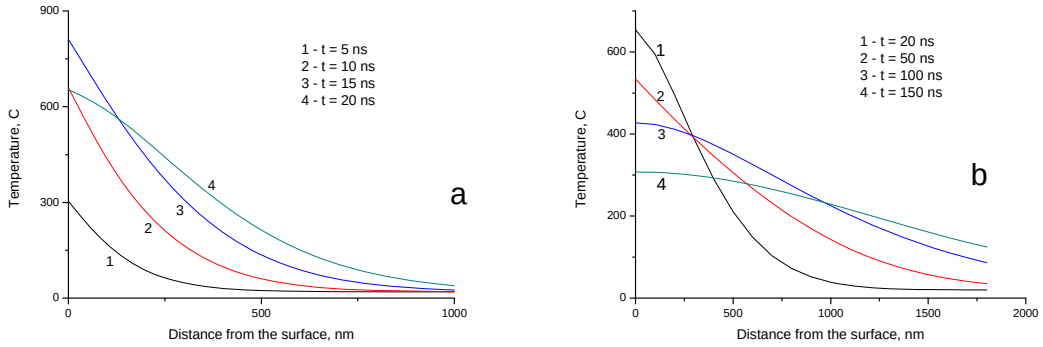

FIG. 24. Temperature distribution within the surface layer of steels irradiated at the PF-5M device: by streams of NI (q_i = 10^7 W/cm^2 ,τ_i = 20 ns) and b) by streams of NP ($q = 2\times10^6$ W/cm^2, τ = 100 ns).

5.3.2. Morphology and structural features of surface layer of irradiated steels (with and without SL melting)

Investigation of samples of austenitic steels after their harsh irradiation at $q = 10^8 - 10^9$ W/cm^2 (PF-6) has shown that in a course of interaction of NI and NP streams with material the processes of melting, evaporation and sometimes cracking of SL took place. Fused surface had always a wave-like relief and contained various types of structure defects: droplets, influxes, pores, open bubbles, micro-cracks. Fig. 25 and 26 present photomicrographs by of electron beam scanning of the irradiated parts of surfaces of 03Cr10Mn33WV and 25Cr12Mn20W2V steels.

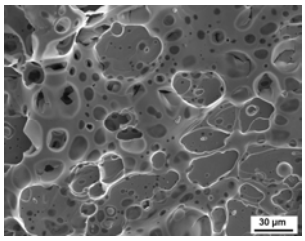

FIG. 25. Electron photomicrograph of the surface of 03Cr10Mn33WV steel irradiated by NP at q = 10^8- 10^9 W/cm^2, number of pulses N =10 (melting of SL). Pores and blisters on the surface.

Surface of steel 03Cr10Mn33WV subjected to 10 pulses of NP has higher developed porosity compared with steel 25Cr12Mn20W2V irradiated by 15 pulses of NP. It contains also “large” pores having characteristic size about 10 µm. Besides of these defects such an irradiation of samples of steel 03Cr10Mn33WV with $N > 1$ produces many bubbles with open “covers” on their surfaces, which are practically absent in samples of 25Cr12Mn20W2V steel. Marked dissimilarity is connected with higher concentration of volatile Mn in 03Cr10Mn33WV steel. As a rule manganese plays a remarkable role in production of surface defects of the type of pores and bubbles on chromium-manganese steels [20–23].

At the same time surface of samples of steel 25Cr12Mn20W2V has many micro-cracks (Fig. 26). Their appearance can be explained by high concentration of carbon and carbides in the type of steel as well as by high initial density of deformation defects resulting in development of stretching thermal strains in SL at fast steel’s solidification. Implantation of nitrogen ions and production of nitride phases at the material’s cooling creates additional deformation of grid of γ-phase.

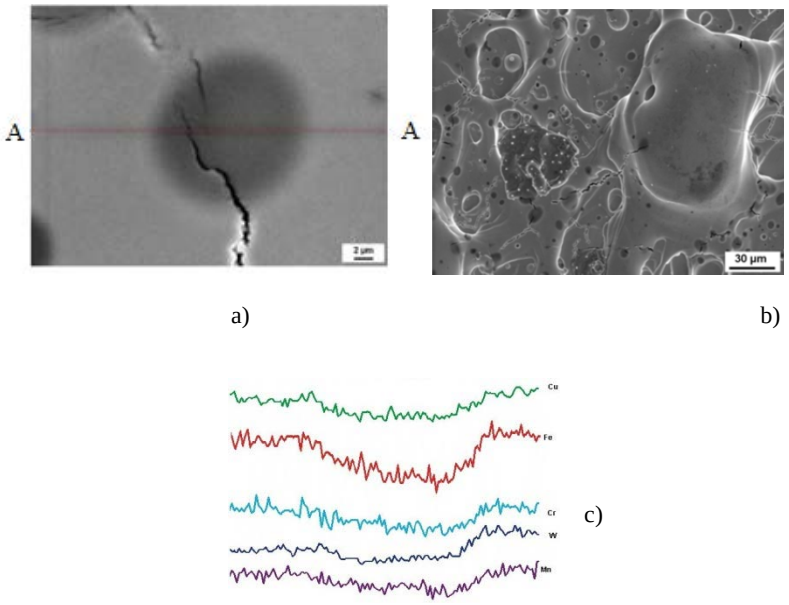

FIG. 26. Electron photomicrographs of the surface of the sample of 25Cr12Mn20W2V steel irradiated by NP at q = 10^8- 10^9 W/cm^2, N = 15 (melting of SL) taken with different magnifications (a) and (b). Micro-cracks and pores on the surface. Microelements distribution along the A – A line of (a).

As a result of it damaging thermal stresses $\sigma(T)$ overcome proof stress. In this connection it must be noted that irradiation of steel 25Cr12Mn20W2V by deuterium plasma (DP) and by fast deuterons which are lighter compared with nitrogen ions did not produce cracking of material at the analogous power flux density [24].

Irradiation of materials in the melting regimes results in erosion of SL producing mass loss and thickness decrease of samples compared with their initial state. For austenitic steel 03Cr10Mn33WV thickness of the layer *d* evaporated from the samples' surfaces for a single pulse was in the range 0.16 - 0.32 µm.

At irradiation of ferritic-martensitic 10Cr9WVTa steel and austenitic 03Cr10Mn33WV steel in the regime without melting of SL we haven't found a noticeable mass change of the samples. Buffed samples' surfaces having initially a metallic lustre was "painted" after irradiation in grey and brown colours. It is a visual characteristic of production of nitride phases in the irradiated SL during the process of nitrogen ion implantation. Photomicrographs of irradiated samples of 10Cr9WVTa and 03Cr10Mn33WV steels are presented in Fig. 27.

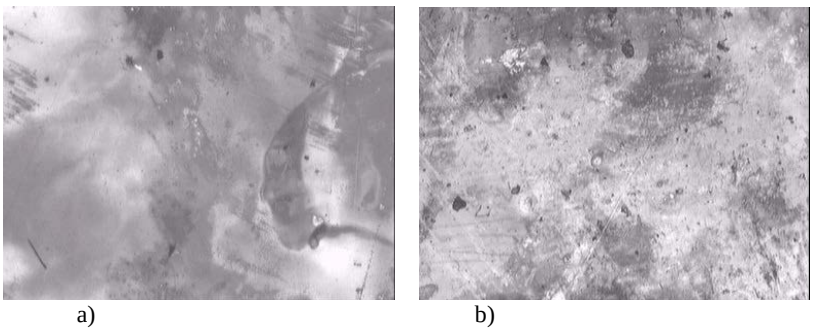

FIG. 27. Electron photomicrographs of the surface of the steels irradiated by NI at q = 10^7 W/cm^2 and by NP at q = 10^6 W/cm^2 (without melting of SL). Film of nitrides on the surface of the steels: a) steel 10Cr9WVTa, N = 10; b) steel 03Cr10Mn33WV, N = 6.

5.3.3. Nitride phases creation in surface layers of steels at their irradiation

Implantation of nitrogen into steel results in creation of more multifarious structures than in the case of carbon implantation. In this case nitrides as the phases of implantation have as a rule a metallic lattice dissimilar compared with it for metal-solvent [25, 26]. Interchange of implantation structures produced by a change of metalloid concentration defined by a term "concentration polymorphism" (by G.V. Kurdjumov). Conception of implantation phases as the result of concentration polymorphic transformations taking place at cooling of solid solutions of implants is also supported as for the system Fe-N so for the alloys based on Fe.
Table 7 presents types of nitride phases appeared within the SL of irradiated steels as well as a relative quantity of each phase in dependence on the number of pulses in every set of shots. For all three transition metals creating nitrides – Fe, Mn and Cr – the relation holds true:

$$r_N / r_{Me} < 0.59$$

where r_N and r_{Me} – radii of atoms of implanted nitrogen and metal correspondingly. Because of this according to the rule of H. Hagg [26] nitride phases created by these metals have simple structures, whereas nitrogen atoms are placed in octahedron internodes or in the centre of trigonal prisms.

TABLE 7. THE TYPES AND THE QUANTITY* OF NITRIDE PHASES APPEARED WITH THE SURFACE LAYER OF STEELS AT PULSED IRRADIATION BY NITROGEN IONS AND NITROGEN PLASMA

№	Nitride phase	Grid type	With SL melting				Without SL melting				
			Number of pulses *N*								
			25Cr12Mn20W	03Cr10Mn33WV			10Cr9WVA			03Cr10Mn33WV	
			15	1	5	10	10	30	50	3	6
1	$FeN_{0,0880}$	FCC	9.5	3.5	5.6	7.7	1.0	1.0	1.0	1.8	1.8
2	$FeN_{0,0939}$	BCT	3.8	1.0	1.6	1.6	1.0	2.0	2.5	1.8	2.6
3	Fe_3N	Hexagonal	3.8	1.7	1.7	1.6	-	-	-	2.7	3.5
4	Fe_2N	Ortho-rhombic (well-ordered)	2.5	1.7	2.4	1.6	1.0	1.0	1.7	-	-
5	Cr_2N	Hexagonal	-	-	-	-	-	-	-	1.0	1.0
6	(Cr,Mn)3N	FCC	4.5	1.0	1.0	1.6	-	-	-	-	-
7	CrN	FCC	-	-	-	-	2.0	2.7	2.5	1.0	1.8
8	$Cr_{0,62}C_{0,35}N_{0,03}$	Ortho-rhombic	-	-	-	-	-	-	-	1.8	1.8
9	Mn_3N_2	BCC	-	-	-	-	-	-	-	1.0	10

* Relative concentration of nitride phases within a surface micro-layer appears to be understated to some extent because at the X ray analysis a layer thickness under investigation is higher than the irradiated one.

Opportunity of carbonitrides creation in the investigated steels by irradiation may be explained by similarity of types of crystal structures of carbides and nitrides of transition metals as well as by conformity of their electronic structure.

Maximal quantity of nitride phases (about 25%) were created in austenitic steel 25Cr12Mn20W2V irradiated in the regime with melting (number of pulses N = 15). At that the main phase is the phase poor by nitrogen $FeN_{0.0880}$ (9.5 %) whereas the second place is taken by the phase more reach with nitrogen – chromium-manganese nitride $(CrMn)_3N$ (about 5 %). In the same conditions the number of nitride phases in the 03Cr10Mn33WV steel at N = 10 is almost two times less (14%) what explained by influence of evaporation process of its surface layer.

An increase of the quantity of shots in the set *N* results in an increase of the number of nitride phases in this steel mainly at the expense of the "poor" by nitrogen phase $FeN_{0.0880}$. However after the set with *N* = 5 a certain increase of the quantity of orthorhombic well-ordered *ξ*-phase Fe_2N (2.5%) was observed. In spite of a decrease of manganese within the SL of 03Cr10Mn33WVsteel the *α*-phase is not appeared what may be connected with the compensating influence of implanted nitrogen as *γ*-stabilizer. It can also be supported by data of the lattice parameter of *γ*-phase of the 03Cr10Mn33 WV steel at N>1 (see table 3 below).
In the regime of implantation without SL melting the quantity of nitride phases in the 03Cr10Mn33WV steel after sets with *N* = 3 and *N* = 6 is equal to 11% and 13.5% correspondingly what coincide practically with the quantity obtained in the regime with its melting. Main place is taken by the hexagonal phase Fe_3N (about 3.5%). And with that the other types of nitride phases are observed: carbonitride phase Cr0.62C035N0.03 having orthorhombic lattice, chromium nitride with hexagonal grid Cr_2N and manganese nitride Mn_3N_2 with BCC lattice.

Table 8 presents values of the parameter of FCC grid of austenitic 03Cr10Mn33WV steel after its irradiation in the regimes with and without melting of SL obtained at different number of shots *N* in a set. From the data presented one may see that the lattice parameter of γ-phase of a steel irradiated in the regime with melting at *N* = 5 and *N* = 10 is practically the same or higher than that for its non-irradiated state.

This fact may in particular show on preservation of some quantity of nitrogen directly in the grid of *γ*-phase what may help in its stabilization (that we have mentioned above). At irradiation of this steel in the regime without melting and with *N* = 3 and *N* = 6 a decrease of the lattice parameter is observed. It explained by creation of nitrides and carbonitrides of Cr. Escape of Cr from *γ*-solid solution as an element of substitution with a somewhat bigger atomic radius compared with Fe simultaneously with carbon and nitrogen may result in a decrease of the grid parameter of *γ*-phase. From the other side it may also indicate low concentration of "free" implanted nitrogen in the *γ*-phase solid solution.

TABLE 8. FCC LATTICE CONSTANT OF THE AUSTENITIC 03CR10MN33WV STEEL AFTER IRRADIATION IN THE REGIMES WITH AND WITHOUT MELTING OF SL AT DISSIMILAR NUMBER OF PULSES N IN A SET

№	Number of pulses, *N*	*a*, Å	*V*, Å^3
1	Before irradiation	3.6148	47.23
2	1 (SL melting)	3. 6085	46.99
3	5 (SL melting)	3.6152	47.25
4	10(SL melting)	3.6268	47.71
5	3 (without melting of SL)	3.6037	46.80
6	6 (without melting of SL)	3.6071	46.93

In the samples of ferritic-martensitic 10Cr9WVTa steel irradiated in the regime of implantation with the number of pulses in a set *N* = 10, 30 and 50 the number of nitride phases changes from set to set not much (in total from 5% till 8%).The main presented phase after each set of tests is the phase that is most enriched by nitrogen – chromium mononitride CrN (from 2% to 3%) as well as the poor by nitride phase body-centric tetragonal phase $FeN_{0.0939}$ (up to 2.5%). Particular feature of the irradiated ferritic-martensitic steel is an absence within the surface layer of cementite F_3C and chromium carbide $Cr_{23}C_6$ presenting in the bulk of the material.

Table 9 presents parameters of BCT lattice of ferritic-martensitic 10Cr9WVTa steel after pulsed irradiation in the implantation regime at different number of shots N in a set. These data show that at $N = 30$ and at $N = 30$ as well a decrease of the lattice parameters a and c is observed – similar to the 03Cr10Mn33WV steel irradiated in the regime of implantation (i.e. without melting). At $N = 50$ a rapprochement of the grid parameters a and c takes place due to an increase of a and a decrease of c at the continuing decrease of V (the lattice approaches to the correct cubic one, tetragonal distortions are decreased).

TABLE 9. CONSTANTS OF BCT LATTICE OF THE FERRITIC-MARTENSITIC 10CR9WVTA STEEL AFTER PULSED IRRADIATION IN THE REGIME WITHOUT MELTING OF SL AT DIFFERENT NUMBER OF PULSES N IN A SET

№	Number of pulses, N	a, Å	c, Å	V, Å^3	Δ (c-a), Å
1	Before irradiation	2.8665	2.8757	23.63	0.0092
2	10	2.8632	2.8748	23.57	0.0116
3	30	2.8626	2.8738	23.55	0.0112
4	50	2.8717	2.8729	23.53	0.0012

It must be noted that an interpretation of an influence of the number of pulses on the lattice parameters and creation of nitride phases in steels is rather complicated. Indeed each successive pulse of energy of plasma and ions may result in a complete or partial dissociation of nitrides appeared during cooling process at the previous cycle with subsequent creation of new phases during cooling of SL occurring with a high speed.

5.4. Conclusions

Experiments provided show a rather complicated character of structure changes and behaviour of nitrogen as well as processes of nitride phases' creation with its participation within the surface layers of steels having different lattice types taking place in the conditions of pulsed irradiation by nitrogen ions and plasma at the power flux density of radiation in the range $q = 10^6$-10^9 W/cm^2 and with nanosecond pulse duration.

At pulsed irradiation in the regime with melting of surface layer an important role is played by processes of vaporization, dissipation of energy due to blistering and porosity (in the case of the plastic state of steels) or appearance of micro-cracks (in the case of strengthened state of steels). Capture and confinement of nitrogen ions take place in the conditions of "exploding boiling" in a micro-layer (100 μm) with subsequent creation at the process of cooling of the nitride phases appeared within the micro-zones non-homogeneous by nitrogen concentration. Surface of the irradiated steels is changed and obeyed a wave-like micro-relief.

At the irradiation in the conditions of implantation (without melting of the surface layer) degradation of the surface does not happen, capture of nitrogen ions by elements of steel takes place at the depth up to 0.1 μm with appearance of nitride phases (mainly Fe and Cr) during cooling. Nitride phases are presented as a film on the irradiated surface of samples.

6. NANOSTRUCTURE SURFACE LAYERS PRODUCED BY POWERFUL PULSED IRRADIATION OF PLASMA FACING MATERIALS OF FUSION REACTORS AND THEIR INFLUENCE ON HYDROGEN ISOTOPE RETENTION

6.1. Introduction

Hydrogen isotope retention [28] is a very serious problem for materials used for manufacturing of the plasma-facing components (PFCs) intended for the chambers of large-scale modern thermonuclear fusion devices (like AUG and JET) and reactors of both types – with magnetic and inertial plasma confinement. These plasma-facing materials exploited or planned to use in the main-stream fusion devices are beryllium (Be), tungsten (W), carbon-fibre composites (CFC) and low-activated stainless steels (LASS).

In particular from the database available from tokamaks with carbon as the main PFCs, the important conclusion is that, assuming a retention to that obtained in carbon-dominated devices, the tritium (*T*) vessel inventory limit in *Iter* (established on the level of 350 g from the safety considerations) could be reached within about 100 discharges, unless efficient *T* removal processes are developed [28].

Moreover up to now, no significant influence on the global balance has been observed with increasing tungsten coverage (from 45% to 70% of *W* in *AUG*) of the carbon-based materials or tungsten itself.

6.2. Devices, irradiation conditions and analysis

In these sets of experiments we used three above-mentioned devices: PF-5M (IMET), PF-6 and PF-1000 (both IPPLM, Poland) facilities. We located the specimens in the centre of the chamber at the Z-axis of it as in previous cases (see e.g. Fig. 4 and 22).The most important feature of the irradiation conditions during these sets of shots was the maximal proximity of a target under irradiation to the source of HP and FI, i.e. to the anode of the particular device. In fact we placed our material samples in the region being away from the anode surface at a distance of the height of the pinch. It means that in the PF-5M and PF-6 devices it was at about 3 cm from the anode whereas at the PF-1000 facility this remoteness was approximately 10...14 cm. Analysis of samples surface was provided by scanning electron (SEM) and atomic force (ATM) microscopy.

6.3. Experiments and investigational results: self-assembly of nanostructured surfaces

First indications of the phenomena under this discussion was obtained during our works devoted to the problem of modelling of irradiation conditions realized on the first wall of the main-stream fusion reactors with magnetic (like tokamaks JET [29] and Iter [30]) or with inertial (like NIF [31]) plasma confinement. Namely in these experiments we observed specific features appeared in the surface layers of some plasma-facing materials subjected by irradiation with powerful nanosecond pulses of hot plasma and beams of fast ions (HP/FI). These 10…100 ns pulses of deuterium plasma with temperature of ~ 1 keV and speed of $>10^7$ cm/s and of beams of fast deuterons with energy ~ 100 keV are generated in our experiments within the devices known as Dense Plasma Focus (DPF) facilities [1]. Power flux densities on surfaces of samples under irradiation by HP/FI streams during this short stage may reach as it was mentioned above P ~ $10^{10\text{-}12}$ W/cm^2.

Namely, we found that these pulses produce very well developed nanostructures on the surface of the above materials like tungsten (used in tokamak's divertor – see Fig. 28), aluminum (used as a conductor for various coils inside a tokamak's chamber – see Fig. 29), iron (see Fig. 30) or low-activated stainless steels (used as plasma-facing elements in inertial fusion reactors or as construction materials in tokamaks) with characteristic sizes of hundred nanometers if $P \geq 10^{10}$ W/cm^2.

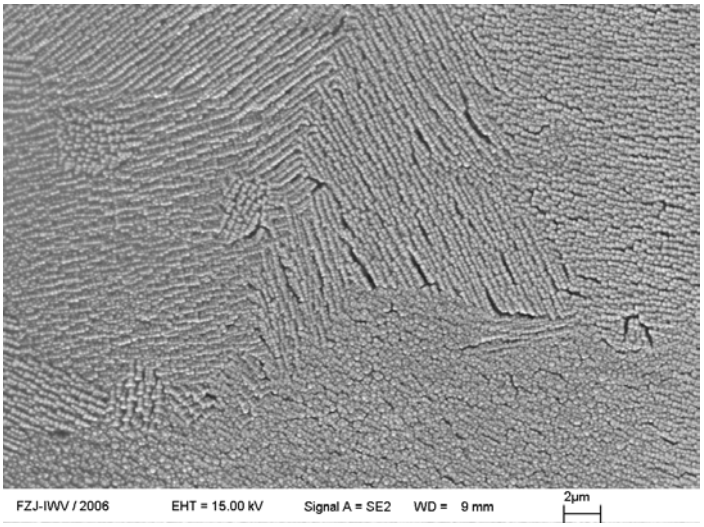

FIG. 28. Structure of the surface layer of W plate, 8 shots of PF-1000 device at P ~ 10^{12} W/cm^2(SEM).

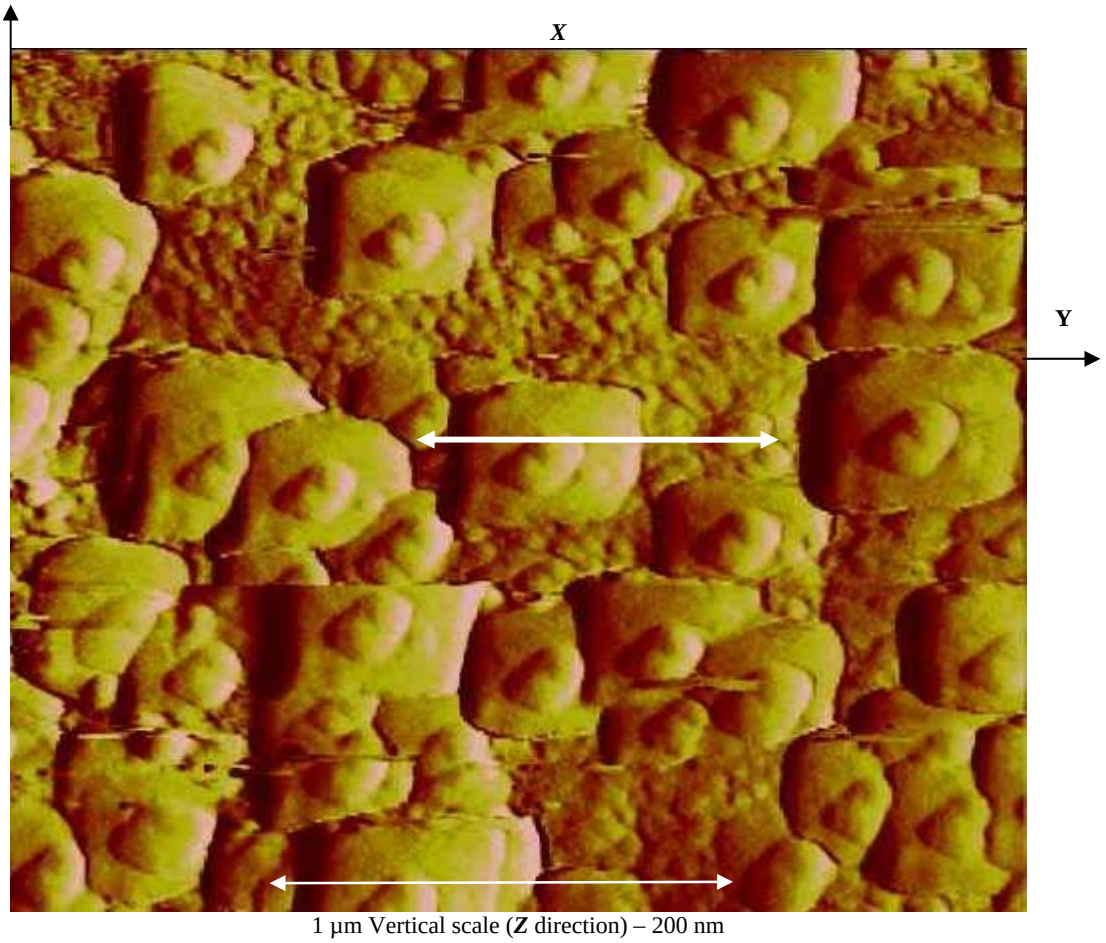

1 µm Vertical scale (**Z** direction) – 200 nm

FIG. 29. Structure of the surface layer of Al plate, 1 shot of PF-1000 device at P ≥ 10^{10} W/cm^2, AFM.

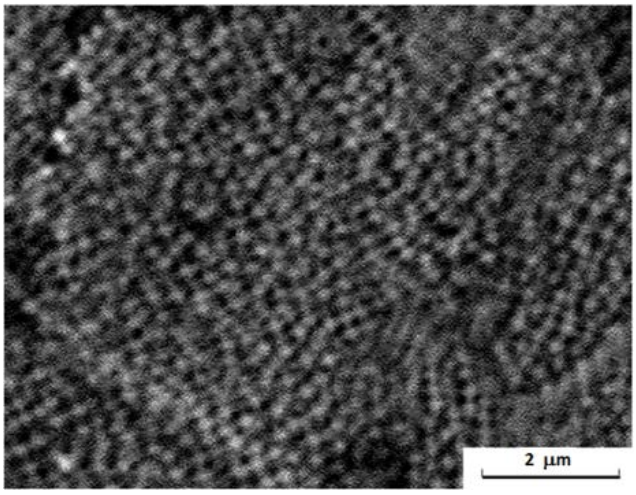

FIG. 30. Part of a surface of the irradiated sample manufactured of pure iron; a single-pulse irradiation at PF-5M device (IMET) with P ≥ 10^{10} W/cm^2, SEM.

As one may see the shapes of these nanostructures may be quite different. But their common feature is that the whole area of its local topography is strongly increased compared with a virgin smooth polished surface.

Such structures may appear regularly just in a single "shot" of the device in a certain range of irradiation parameters (e.g. at the power flux density of the above streams ≥ 10^{10} W/cm^2 on the target's surface). But with an increase of the number of such irradiations the above-mentioned relief becomes more profound.

This powerful irradiation of different samples has a couple of quite unexpected consequences. First we discovered in this very new field of DPF applications that the content of hydrogen isotopes that are implanted by force method into the bulk of material with concentration much higher compared with the solubility limit was decreased with an increase of the number of shots (see Fig. 31). This feature is of great importance for future fusion reactors in the context of hydrogen retention by plasma-facing elements.

We associate this phenomenon with a strong enlargement of the surface area of the samples due to the acquired nanostructures that results in an accelerated diffusion (release) of gas from solid materials back into the reactor's chamber.

In a view of this fact it seems quite reasonable to expect that such a kind of treatment of the PFC's surfaces by powerful streams of hot plasma/fast ions may help in resolving of the tritium retention problem.

Second effect discovered in these experiments is connected with the damageability of these materials. In particular, when our samples of tungsten (same as in Fig. 28) and pure iron (same as in Fig. 30) were irradiated by the above streams of rather lower power flux density – about P ~ 10^7…10^9 W/cm^2 (i.e. on the "border" of sample's surface melting or with low melting of it that was provided at the PF-5M device) we saw well-defined cracking and porosity of them correspondingly (see Fig. 32 and 33). These types of damage are not observed at P ≥ 10^{10} W/cm^2, when we have nano-structured surfaces (Fig. 28, 29, and 30).

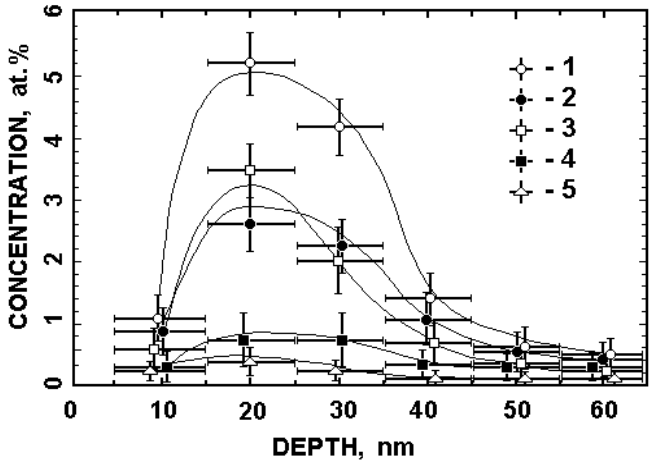

FIG. 31. Deuterium concentration distribution in the surface layer of austenitic 25Cr12Mn20W steel after irradiation by high powerful plasma jet and fast ion beam with P ~ 10^{10} W/cm^2; Elastic Recoil Detection Analysis – ERDA – processed with a Rutherford Universal Manipulation Program – RUMP: 1 - 1 pulse, 2 - 2 pulses, 3 - 4 pulses, 4 - 8 pulses, 5 - 16 pulses ("shots") of the PF-1000 facility.

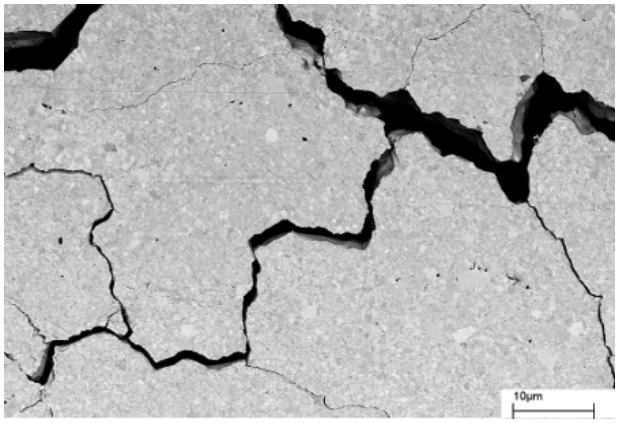

FIG. 32. Surface of tungsten irradiated by a single pulse of HP/FI at PF-1000 with P ~ 10^8 W/cm^2, SEM.

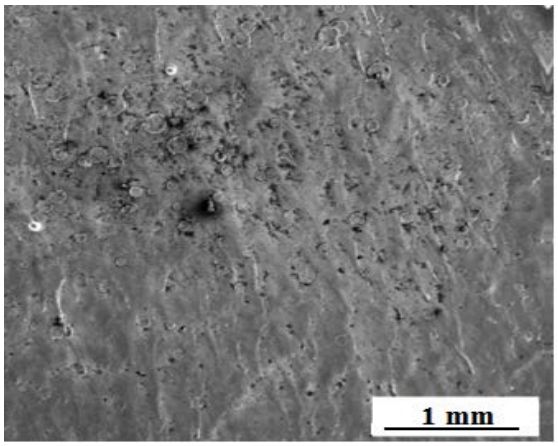

FIG. 33. Surface of pure iron irradiated by a single pulse of HP/FI at PF-5M with P ~ 10^9 W/cm^2, optical microscopy.

Reduction of grain sizes observed in these experiments of Fig. 28 through 30 and accompanied by a creation of a fine-meshed structure of sub-micron and nano-sized scales as a rule helps in improvement of mechanical, corrosion and radiation resistance of materials (see e.g. [4, 32]).

REFERENCES

[1] BERNARD, A., BRUZZONE, H., CHOI, P., *et al.*, "Scientific status of plasma focus research", J. Mosc. Phys. Soc. **8(**2) (1998) 93–170.

[2] a). GRIBKOV, V.A., BIENKOWSKA, B., BOROWIESKI, M., *et al.*, "Plasma dynamics in PF-1000 device under full-scale energy storage: I. Pinch dynamics, shock-wave diffraction, and inertial electrode", *J. Phys. D: Appl. Phys.* **40** (2007) 1977–1989.
b) GRIBKOV, V.A., BANASZAK, A., BIENKOWSKA, B., *et al.*, "Plasma dynamics in PF-1000 device under the full-scale energy storage: II. Fast electrons and ions characteristics versus neutron emission parameters, and the gun optimization properties", J. Phys. D: Appl. Phys. **40** (2007) 3592–3607.

[3] PIMENOV, V.N., GRIBKOV, V.A., IVANOV, L.I., SCHOLZ, M., *et al*., "On the new possibilities of application of Dense Plasma Focus devices for modification of surface layers of materials", Perspective materials #1 (2003) 13–23, *in Russian.*

[4] GRIBKOV, V.A., GRIGORIEV, F.I., KALIN, B.A., YAKUSHIN, V.L., Perspective radiation-beam technologies of materials treatment, Moscow, Kruglyj god (2001) 528 p., *in Russian*.

[5] MASLYAEV, S.A., PIMENOV, V.N., PLATOV, Yu.M., DEMINA E.V., *et al.*, "Action of deuterium plasma pulses upon materials of thermonuclear reactors in the Dense Plasma Focus device", Perspective materials #3 (1998) 39–46, *in Russian.*

[6] GRIBKOV, V.A., PIMENOV, V.N., IVANOV, L.I., DYOMINA E.V., *et al.*, "Interaction of High Temperature Deuterium Plasma Streams and Fast Ion Beams with Condensed Materials in Dense Plasma Focus Device", Journal of Physics D: Applied Physics **36** (2003) 1817–1825.

[7] SCHOLZ, M., MIKLASZEWSKI, R., GRIBKOV, V.A., MEZZETTI, F., "PF-1000 device", Nukleonika **45**(3) (2000) 155–158.

[8] MASLYAEV S.A., "Thermal effects at the pulsed irradiation of materials in the Dense Plasma Focus device", Perspective materials #5 (2007) 47–55, *in Russian.*

[9] BUTSEVA, T., HASSANEIN, A., OVCHINNKOV, I., TITOV, V., "Study of brittle and erosion mechanisms of carbon-based materials during plasma instabilities", J. Nucl. Mater. **290-293** (2001) 1059–1063.

[10] HASSANEIN, A., KONKASHBAEV, I., "Erosion of Plasma-Facing Materials During a Tokamak Disruption", Atomic and Plasma Material Interaction Date for Fusion (Supplement to the Nuclear Fusion) **5 (**1994) 193–224.

[11] LINKE, J., HIRAI, T., OGORODNIKOVA, O., PINTSUK, G., RÖDIG, M., "Thermal loads to plasma facing components in next step fusion devices" (Proceedings of the 1st Expert Meeting "Plasma streams interaction with materials", EURATOM/Institute of Plasma Physics and Laser Microfusion and IAEA, Warsaw, Poland, November 15-17) (2005).

[12] National Livermore National Laboratory website: https://lasers.llnl.gov/programs/nif.

[13] GRIBKOV, V.A., DEMINA, E.V., DUBROVSKY, A.V., *et al.*, "Effects of interaction of pulsed dense deuterium and hydrogen plasma streams with ferritic and austenitic steels in the Dense Plasma Focus device", Perspective materials, #1 (2008) 16–25, *in Russian*.

[14] PIMENOV, V.N., MASLYAEV, S.A., KOVTUN, A.V., *et al.*, "Interaction of powerful pulsed streams of energy with a surface of a tungsten sample in the Dense Plasma Focus device", Physics and chemistry of materials treatment, #3 (2008) 5–14, *in Russian.*

[15] PIMENOV, V.N., MASLYAEV, S.A., IVANOV, L.I., DYOMINA, E.V., *et al.*, "Surface and bulk processes in materials induced by pulsed ion and plasma beams at Dense Plasma Focus devices", Nukleonika **51**(1) (2006) 71.

[16] GRIBKOV, V.A., IVANOV, L.I., MASLYAEV, S.A., *et al.*, "On the nature of changes in the optical characterization produced in sapphire on its irradiation with a pulsed powerful stream of hydrogen ions", Nukleonika **49**(2) (2004) 43.
[17] GRIBKOV, V.A., PIMENOV, V.N., IVANOV, L.I., *et al.*, "Interaction of High Temperature Deuterium Plasma Streams and Fast Ion Beams with Condensed Materials in Dense Plasma Focus Device", Journal of Physics D: Applied Physics **36** (2003**)** 1817.
[18] IVANOV, L.I., PIMENOV, V.N., MASLYAEV, S.A., *et al.*, "Influence of dense deuterium plasma pulses on materials in Plasma Focus device", Nukleonika **45**(3) (2000) 203.
[19] PIMENOV, V.N., DYOMINA, E.V., IVANOV, L.I., *et al.*, "Damage of structural materials for fusion devices under pulsed ion and high temperature plasma beams", J. Nucl. Mater. **307-311** (Part 1) (2002) 95.
[20] KLUEH, R., KENIK, E.A., "Thermal stability of manganese-stabilized stainless steels", J. Nucl. Mater. **212-215** (1994) 437–441.
[21] GRICKUROV, G.N., GAGNIDZE, I.P., TAVADZE, P.N., In "Structure and physical and mechanical properties of nonmagnetic steels", Moscow, Nauka, 1986, 141–144, *in Russian.*
[22] SCHENKOVA, I.A., DEMINA, E.V., PLATOV YU.M., *et al*., "Low-activation 9% Cr Steel for Nuclear Applications", Perspective materials #2 (1996) 31–36, *in Russian.*
[23] GRIBKOV, V.A., DUBROVSKY, A.V., SCHOLZ, M., JEDNOROG, S., *et al.*, "PF-6 – an effective plasma focus as a source of ionizing radiation and plasma streams for application in material technology, biology and medicine", Nukleonika **51**(1) (2006) 55.
[24] GRIBKOV, V.A., DEMINA, E.V., DUBROVSKY, A.V., IVANOV, L.I., *et al*., "Effect of the deuterium pulsed irradiation in PF devices on the austenitic and ferritic-martensitic steels", Perspective materials #1 (2008) 16–25, *in Russian.*
[25] ANDRIEVSKYI, R.A., UMANSKYI, Ya.S., "Phase of the Intrusion", Moscow, Nauka (1977) 240 pp., *in Russian.*
[26] TOT, L., "Transition metal carbide and nitride", Moscow, Mir (1977) 295 pp., *in Russian.*
[27] CAUSEY, R.A., T.J. VENHAUS, T.J., "The use of tungsten in fusion reactors: a review of the hydrogen retention and migration properties", *Phys. Scr., T94,* (2001) pp. 9-15.
[28] T. LOARER, T., C. BROSSET, C., J. BUCALOSSI, J., COAD, P., *et al.* and JET EFDA contributors, "Gas balance and fuel retention in fusion devices", Nucl. Fusion **47** (2007) 1112–1120.
[29] European Fusion Development Agreement website: http://www.jet.efda.org/
[30] ITER website : http://www.iter.org/
[31] National Livermore National Laboratory website: http://www.llnl.gov/nif/
[32] YAKUSHIN, V.L., "Modifications of carbon and low-doped steels by streams of high-temperature plasma", Izvestia RAS: Metals, #2 (2005) 12–24, *in Russian.*

TECHNOLOGICAL DEVELOPMENT OF DENSE PLASMA FOCUS DEVICES, ELABORATION OF THE DEDICATED INTERFACE ISSUES AND APPLICATION THE DEVICES TO THE GOALS OF THE MAINSTREAM FUSION RESEARCHES

A.V. DUBROVSKY

Moscow Physical Society (MPS), Moscow, Russian Federation

Abstract

The CRP #14638 is the direct sequel of CRP #11942 (2001/12/01 – 2007/04/12), which lied on especially the design as well as launching of series of small-scale plasma focus devices. Three new DPF devices have been realized as a result of that CRP normal completion: PF-10.0, DPF-6.0, and PF-5M. This CRP principal activity was aimed at further development of listed devices. Furthermore design, realization, and application of the diagnostics, which makes possible to control the parameters of DPF discharge as well as to control the parameters of DPF plasma exerting influence upon the surface of test samples located at the cathode part of DPF chamber. This report describes the designed diagnostic techniques. The experiments carried out on small-scale DPF devices as well as on great PF-1000 installation are described here as well.

1. INTRODUCTION

During the period under report following improvements of small-scale DPF devices, which provide for considerable perfection of carrying out the irradiative experiment of fusion candidate materials had been realized by Moscow Physical Society CRP team:

- new demountable stainless steel DPF chamber was designed and realized,
- the moving target technique permissive to wide-range change of the irradiative conditions was designed, realized and tested,
- the experimental study of the energy of plasma-surface interaction using thermocouple calorimeter method was carried out,
- the measurement of flash duration from the surface of target sample induced by plasma jet incidence by using of fast photomultiplier technique is prepared.

2. ACTIVITY

2.1 Installation

The basic installation using for execution of the new experimental technique was PF-5M based on A.A. Baikov Institute of Metallurgy and Material Sciences – IMET (Moscow, RF). The main parameters of the device are presented in TABLE 1.

TABLE 1. Main parameters of PF-5M device

Battery capacity	16 μF
Actuating voltage	15 – 20 kV
Energy storage	1.8 – 3.2 kJ
Working gas	N, H_2, Ar, Xe, He, CH_4, or habitual indoor air
DPF chamber type	All types of chamber
Rep rate	Operation conditions of single shots
Life-time of the DPF systems	~ 10^4 shots

The works on this device is carried out by MPS in close collaboration with colleagues from other institutes-participants of the CRP (IPPLM, Warsaw, IMET, Moscow). PF-5M

device now is in operative status. The main destination of the device is the material science. The series of austenitic, ferrite SS samples, Al_2O_3, CFC samples were irradiated by nitrogen plasma jet and fast N – ions under different irradiative conditions (the number of irradiative pulses was changed from 3 to 50). In process of the experiment the next diagnostics were used:

- discharge current oscillogram registration;
- discharge high voltage oscillogram registration;
- time derivative of discharge function (di/dt) registration;
- hard R-ray dosimetry.
- for investigation of temporal characteristics of generated by DPF X ray radiation and light pulses (which are the shortest ones between all other used within the frame of the Project) we applied detectors of the type E.CCDI38 based on the photomultiplier tubes (PMT) of the type manufactured by NIIIT, (Moscow) on the base of photomultiplier of the type SNFT18 (time resolution $\tau < 1$ ns, linear output current Iline ≤ 1 A) equipped with plastic scintillators
- the thermocouple calorimeter method was applied. The copper washer of precisely weighted mass was used as calorimetric detector. Digital termocouple termometer of K-type was used to measure the temperature differential directly after each tested DPF shot. A special probe detector head able to insert into vacuum region not disturbing vacuum conditions has bean designed and realized. The moving target technique is used in calorimetric experiment. Photo of PF-5M device is presented in FIG. 1.

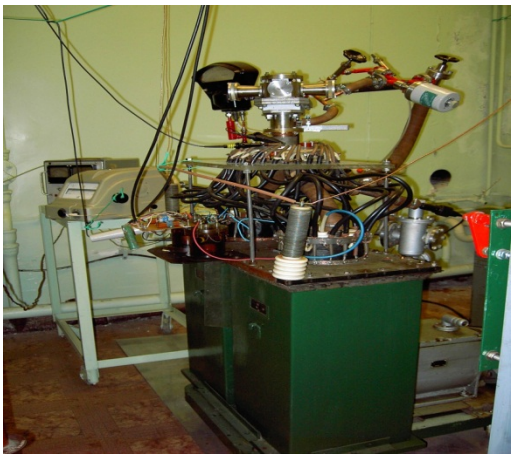

FIG. 1. Photo of PF-5M device.

2.2. New demountable stainless steel DPF chamber

DPF chamber of the open type we used up to the start time of this CRP was realized as no separable unit. A special technology of erection welding of metal with ceramic is realized in the process of chamber assembling. So it is impossible to work mechanically with the anode of DPF chamber as a complete product in order to set a test sample on its surface safely to the construction itself.

Besides, due to the fact that all used by us DPF chambers are realized from copper (both electrodes) the inescapable presence of Cu ions in plasma interacting with a test sample

located on the cathode chamber part sometimes turns out to be objectionable in respect to material science. It is significant that copper is the only material of the anode at every DPF devices known to us all over the world.

In the order to overcome named hardship we have designed new demountable DPF chamber based on the main usual geometric dimensions. Stainless steel was picked out as a material both for the cathode and for the anode. In the case when new DPF chamber tests will be found successful, it will be the opportunity to try other materials, such as tungsten or molybdenum etc. for the anode realizing. It will be the possibility to design and to realize operatively a target unit located at the anode surface as well.

The design drawing of new demountable stainless steel DPF chamber and photo of chamber details - **a);** and assembled new chamber - **b),** are shown on FIG. 2, FIG. 3.

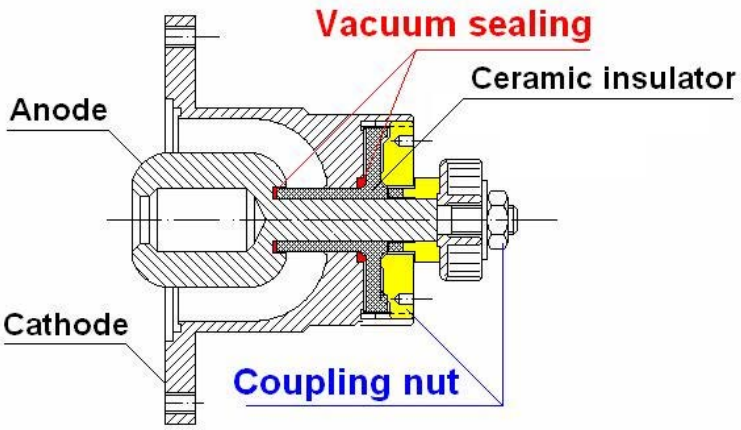

FIG. 2. The design drawing of new demountable stainless steel DPF chamber.

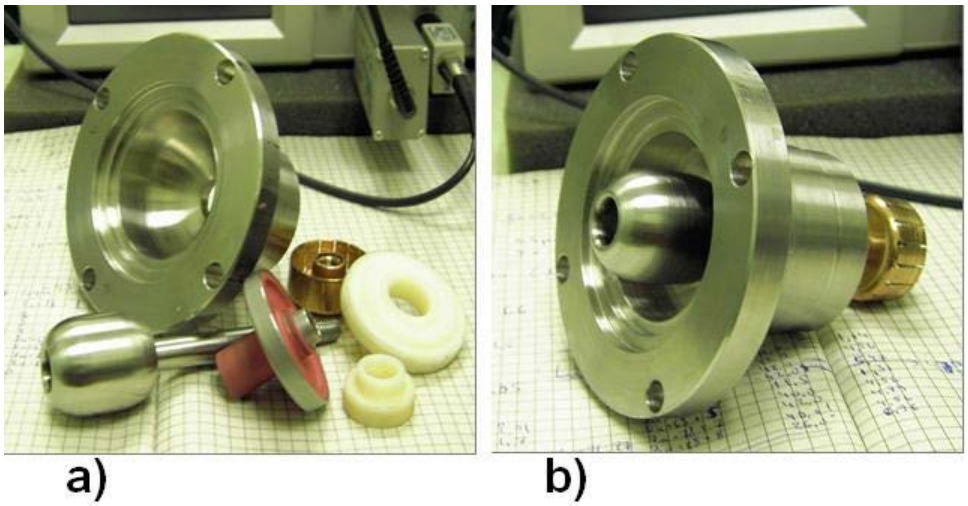

FIG. 3 Photo of new stain less steel chamber details - a); and the new chamber assembled - b).

The assemblage of the demountable stainless steel DPF chamber as well as its test was realized during reporting term. Test carried out shows good capacity for work of the chamber. Every described below experiment was carried out just using this stainless steel DPF chamber.

2.3. The moving target technique

The moving target unit discribed below was scheduled to elaborate in order to vary within broad range of the irradiation dose exposed by test sample by means of changing distance between a sample and the source of radiation (DPF anode). To accomplish the task the sampleholder has been set on the butt-end of steel rod coming into DPF chamber through the stuffing box seal of Wilson type (FIG. 4). A combination of teflon and ruber layings was used as a vacuum gasket. All metallic details of the unit were realised from non-magnetic stailess steel. Using of moving target unit discribed in combination with an extension pipe to DPF chamber as well as extention nozzle to the rod, makes it possible to vary the distance from DPF anode to a test sample in the range from 1,5 cm to 40 cm.

The moving target unit was tested in composition with copper DPF chamber of the open type. The demonstration experiment was carried out with using helium as a working gas on a device energy store level of 1 kJ. Robert Wood fusible alloy sample (melting temperature T_{melt} = 65.5°C) was used as test sample. Each test sample was exposed for 5 DPF shots. The samples irradiated on the distance of 10 – 15 cm from the anode have obvious evidence of meltback on the irradiated surface. Some meltback was recognizable just with the aid of optic microscope for the sample irradiated on the distance of 25 cm. No evidence of meltback was obtained on the surface of the sample irradiated on the distance of 30 cm, wile the analycis carried out by means of mass spectroscopic methode shows presents of implanted helium atoms in test sample.

The demonstration experiment shows that DPF device has the ability to change smoothly irradiative dose falling onto sample surface from zero to some maximum value.

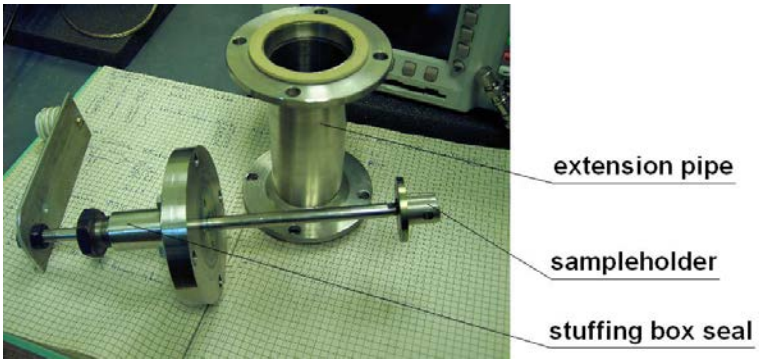

FIG. 4. Moving target unit.

2.4. The experimental study of the energy of plasma-surface interaction using thermocouple calorimeter method

The determination of power flux density on the target distant from the anode of DPF chamber experiment was planed to consist on the two stages. On the first stage incident on the target radiation energy has to be measured by means of calorimetric diagnostics. The thermocouple calorimeter method was applied at the first stage. The copper washer of precisely weghted mass (FIG. 5 b) was used as calorimetric detector. Digital termocouple termometer of K-type was used to measure the temperature differential directly after each tested DPF shot. A special probe detector head able to insert into vacuum region not disturbing vacuum conditions has bean disigned and realised (FIG. 6). The moving target technique discribed in the previous item is used in calorimetric experiment.

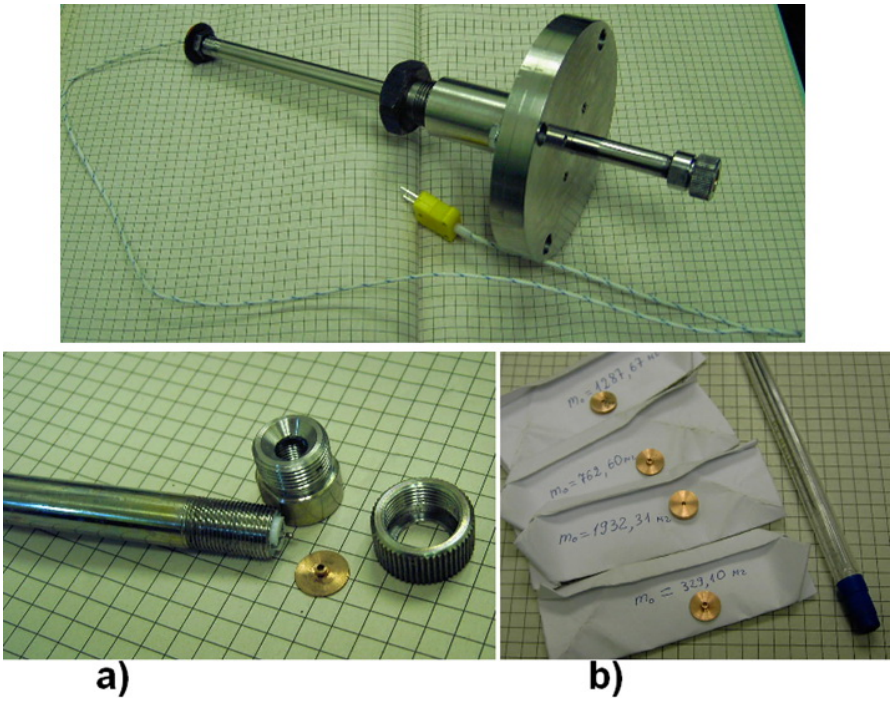

FIG. 5. Thermocouple calorimeter probe ready-mounted. The details of thermocouple probe unit - ***a)****;a collection of calorimetric washers of different mass –* ***b).***

The structure of thermocouple calorimeter probe presented in FIG. 6. The photo of experimental set and target heat differential density as function of source-target distance diagram presented in FIG. 7.

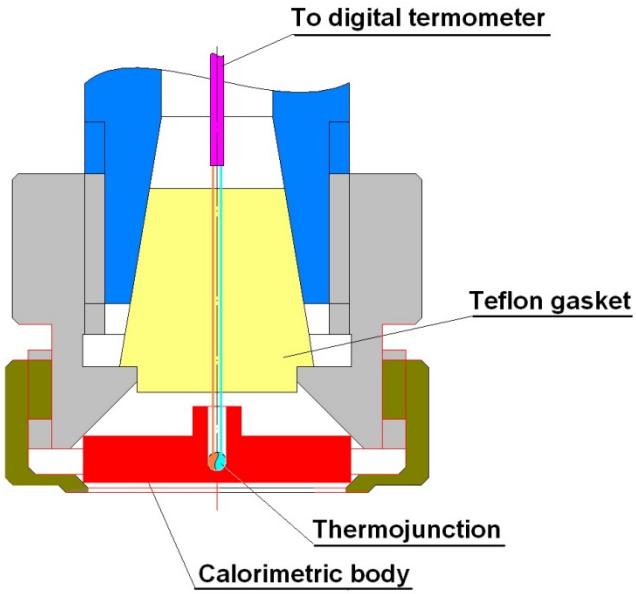

FIG. 6. The structure of thermocouple calorimeter probe.

The picture shows that place of calorimetric body contact with the rest construction is very small. Practically the digital thermometer reading rises and become stable 1.5 min after DPF device shot. Then the calorimetric body cools down during about half an hour.

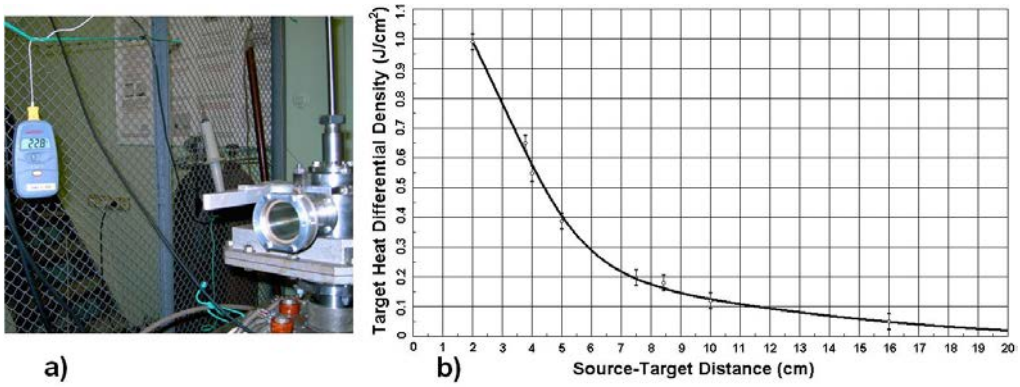

FIG. 7 Photo of the experimental set – a); target heat differential density as function of source-target distance – b).

2.5. The experimental set for fast measurements

For investigation of temporal characteristics of generated by DPF X ray radiation and light pulses (which are the shortest ones between all other used within the frame of the Project) we applied detectors of the type E.CCDI38 based on the photomultiplier tubes (PMT) of the type manufactured by NIIIT, (Moscow) on the base of photomultiplier of the type SNFT18 (time resolution τ < 1 ns, linear output current $I_{line} \leq 1$ A) equipped with plastic scintillators. Photo of the detector presented on FIG. 8, 9. Tektronix TDS 3054B oscilloscope is used as recording equipment.

FIG. 8. An appearance of the detector E.CCD138.

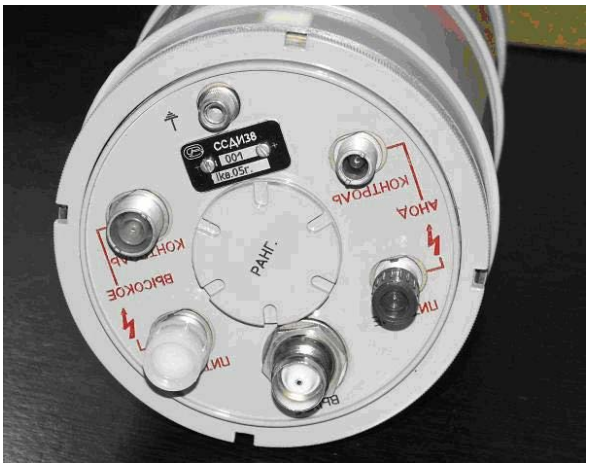

FIG. 9. An outward of the PMT connectors' panel.

The proper allowance is important to note about a description of any operation with high sensitive pulse technique in the conditions of DPF discharge. The problem in question is the appearance of *strong e/m noise* interfering with any recorded signal. It turned out, that first switching on of an apparatus describing here has demonstrated absolute impossibility of its using for DPF shot characterizations without an application of some specific means of noise suppression. In fact looking-for and followed then a realization of such a specific means formed the most part of our effort at the reporting period.

First, we have study the moment of generation of e/m noise by the operating DPF device and the character of the noise. It has not been a surprise that the time of noise origination is strictly corresponds to the moment of peculiarity moment on the *di/dt* oscilloscope trace. The noise signal typical form is relaxation oscillations of the frequency about 0,5 GHz.

On the way of e/m noise control our decision was to locate the complete recording equipment included: PMT, oscilloscope, PMT power source, an assistant laptop, and the all system uninterruptible power supply into the shielded enclosure. We utilized appropriate metallic control cabinet with the walls realized from perforated steel plate. We perfectly cover inside the cabinet by aluminum foil of thickness 20 micron. Above the foil, we affix opaque scotch tape to protect thin aluminum foil. A photo of ready for work shielding case including the recording equipment presented in FIG. 10.

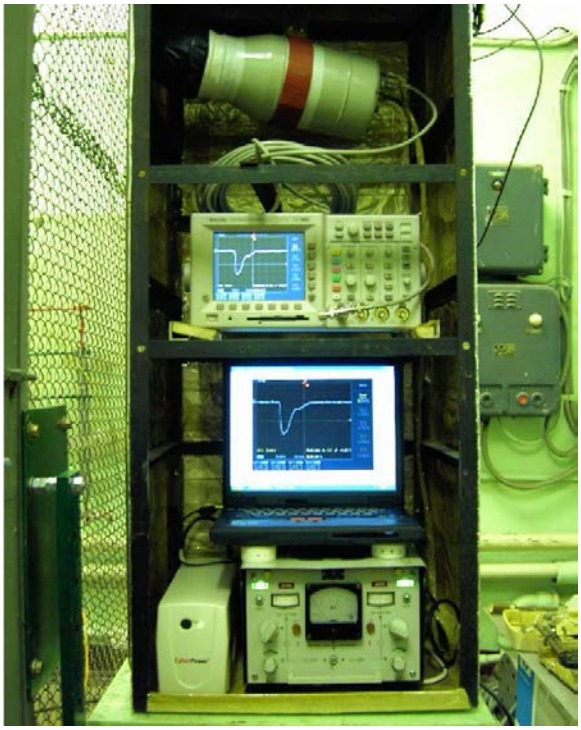

FIG. 10. Photo of the control cabinet enclosing reading apparatus (without a front door).

In order to demonstrate the capacity for work of the experimental set device described an oscilloscope trace of hard X ray signal from PF-5M device is presented on FIG. 11.

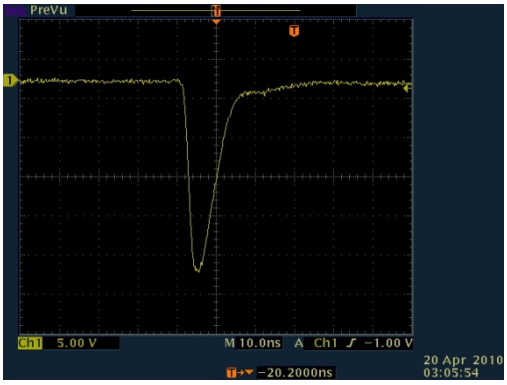

FIG. 11. Hard X ray pulse oscilloscope trace.

The fast photomultiplier technique is used to measure flash duration from the surface of target sample induced by plasma jet incidence by using of. A flexible lightguide conducts the light from the flash point to the photomultiplier tube. A combination of plasma-surface energy characteristic determined on the first stage with flash duration value determined on the second one makes it possible to calculate power flux density value. Moreover, the utilization of another flexible lightguide conducting the light from DPF point to the same PMT makes it possible to determine as DPF flash duration as well as time domain between those two flashes. A plasma jet velocity thus becomes easy to determined able. A diagram of the experiment is presented in FIG. 12.

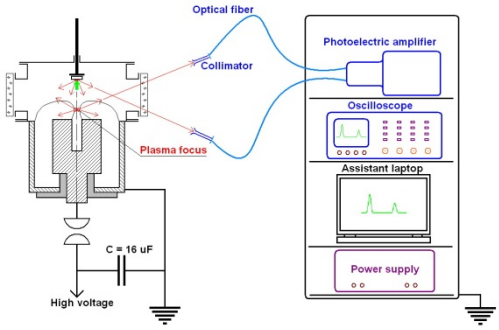

FIG. 12. A diagram of the experiment.

The FIG. 13 shows the details of the experimental set described above. This set now is completely ready for work. The pilot experiment has been successfully carried out. The full-scale carrying out of the experimental study is pre-arranged on the next CRP period.

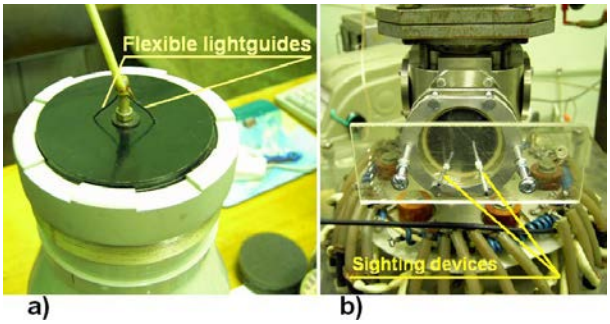

FIG. 13. Fixing of flexible lightguides on the PMT head – a);sighting devices for the other ends of lightguides at the DPF chamber window – b).

2.6. Mutual experiments with colleagues from other institutes-participants of the CRP

In general during reporting period our joined experimental study were carried out in close cooperation with the A.A. Baikov IMET researching group fulfilling CRP No 14540/R (Moscow) and IPPLM team, CRP No 14526/R (Warsaw). The task of MPS (CRP #14638/R) was in main the engineering decision of the irradiative experiment. The analytical procedure of formerly irradiated test samples is to a greater or lesser extent the task of other participants of the researches. The reporting period our common effort was focused on the analytical treatment of data collected as a result of the irradiations on PF-5M device as well as of the experiments carried out on PF-6.0 and PF-1000 installations in Warsaw. Sintered W with impurities (Fe, Ca, C, N, H, O up to 0.05% prepared at A.A. Baikov IMET, specimens of the composition W/CFC (CFC sample with shrunk-in W cylinder) prepared in KFA, Julich (Germany), and CFC material reinforced with SiC particles up to 8 and 40 vol% prepared in Royal Institute of Technology (Stockholm, Sweden) are the materials irradiated by flux of deuterium plasma in our previous researches. Listed solid matters are considered as promising engineering materials for fusion reactor. Ferritic and austenitic steel specimens were irradiated by deuterium plasma also. The materials damage analytical results of our team-work are reported and published.

3. CONCLUSIONS

As a result of the MPS activity under the Research Contract № 14638/R during reporting period 2007 – 2011 the *Programmes of Work Plan* had been fulfilled.

DYNAMICS OF DENSE MAGNETIZED PLASMA STREAMS AND THEIR INTERACTION WITH MATERIAL SURFACES: COMPARATIVE STUDIES WITH MAGNETOPLASMA COMPRESSOR (MPC) AND QUASI-STEADY-STATE PLASMA ACCELERATOR QSPA KH-50

I.E. GARKUSHA, V.A. MAKHLAJ, A.V. MEDVEDEV, S.V. MALYKHIN, A.T. PUGACHEV, V.V. CHEBOTAREV, M.S. LADYGINA, A.K. MARCHENKO, O.V. BYRKA, A.N. BANDURA, V.V. STALTSOV, N.V. KULIK, YU.V. PETROV, V.I. TERESHIN

Institute of Plasma Physics of the NSC KIPT, Kharkov, Ukraine

Abstract.

The quasi-steady-state plasma accelerator QSPA Kh-50 and short-pulsed magnetoplasma compressor (MPC) have been used for comparative studies of plasma-surface interaction and materials erosion issues, development of recommendations for fusion reactor materials and in numerical models for validation of predictive codes. The main advantage of QSPA in simulation experiments is possibility of generation of long magnetized pulse plasma streams with the pulse duration of 0.2-0.3 ms, the ion impact energy of 0.9 keV, the heat loads up to 20 MJ/m^2, and the plasma parameter betta up to 0.3, which combination is not achievable in other types of plasma sources. Using within the framework of one problem both short- (~1-3 μs) and long pulsed (300 μs) plasma devices permitted to investigate the plasma effects on materials surfaces in a wide range of plasma pulse duration with varied energy and particle loads to the exposed surfaces. Crack patterns (major- and micro-type) in tungsten targets and cracking thresholds (both threshold energy load for the cracking onset and threshold target temperature related to ductile-to-brittle transition) as well as residual stresses after repetitive plasma pulses have been studied for different tungsten grades and, in particular, for a deformed W material, which is considered as the ITER-reference grade. The thickness of major- and micro-cracks, the network distance as well as the penetration of cracks into the material depth are analyzed. Comparisons of the cracking failure of deformed tungsten with behaviour of sintered W samples are performed. Results of QSPA plasma exposures are compared with short pulse PSI experiments with pulsed plasma gun and dense plasma-focus facilities, aiming at features of surface damage and tungsten impurities behavior in near-surface plasma in front of the target.

1. INTRODUCTION

For evaluation of the materials performance under short transient events, such as Edge Localized Modes (ELMs) and plasma disruptions, the comprehensive experimental investigations of threshold values for the damaging processes (such as roughening, crack formation and melting of the PFCs surfaces) under ITER or DEMO relevant loading scenarios are required. Armor erosion caused by high-energy plasma impacts results in both surface damage and impurities production that also lead to radiative cooling of the plasma. All these aspects are critical issues for a good performance of the tokamak. In present-day tokamaks, experimental simulations of high energy fluxes of transients, as expected in fusion reactor, are quite problematic. For this reason the simulation experiments are carried out by the use of quasi-stationary plasma accelerators (QSPA), powerful pulsed plasma guns and e-beam facilities, which are capable to simulate, at least in part, the ITER loading conditions.

Quasi-steady-state plasma accelerators (QSPA), which are characterized by much longer duration of the plasma stream generation in comparison with pulsed plasma guns, are especially attractive for experimental study of plasma-target interaction under the high heat loads and for investigations of macroscopic erosion of tokamak armor materials, under the conditions expected at ITER off-normal events [1-10].

The experiments with short-pulse plasma devices (dense plasma focus, pulsed plasma gun, z-pinch) can simulate the magnitude of the tokamak off-normal heat loads but not the time duration of such events. In a tokamak the time duration of the off-normal heat loads

might be up to several orders of magnitudes larger and the guiding strong magnetic field is also should be taken into account. Nevertheless some very important features of plasma-surface interaction and materials erosion under the high plasma heat loads and, in particular, sputtering effects, brittle destruction, could be investigated.

E-beams provide the essentially longer duration of heat load, they especially attractive for simulation of VDE impacts and also disruptions. Repetitive ELM-like heat load to the surface can be reproduced too. Also runaway electrons effects can be studied. But some "plasma" features, such as contribution of ion bombardment to surface relief, plasma shield, picked pressure profile of impacting load and it influence on resulting erosion crater, transport in magnetized plasma of the impurities, which are produced due to the surface erosion and study of its redeposition require the involvement of plasma devices.

Therefore, analysis and comparison of experimental results on materials behavior under irradiation with electron and ion beams, and high-power plasma streams generated in different pulsed plasma devices (QSPA, dense plasma focus, pulsed plasma gun and other) with different heat load levels and different time duration of pulsed load gives the unique possibility to understand an important common features of surface damage in extreme conditions, to investigate it peculiarities and possible differences in erosion mechanisms in dependence on the plasma parameters and temporal profile of the impacting load [9-24] .

The present-day experimental investigations of plasma-surface interaction under conditions simulating ITER transient events are aimed at the determination of erosion mechanisms of plasma facing materials, dynamics of erosion products, the impurities transport in plasma, the vapor shield effects and its influence on plasma energy transfer to the material surface [9-18].

For the tungsten material an important issue is W cracking that requires further studies [11]. In particular, determination of a threshold load for the major- and micro- crack formation at various preheating temperatures and measurements of a residual stress for different W grades should be performed in wide ranges of energy loads. This report presents results of experimental investigations of dynamics of dense magnetized plasma streams and their interaction with material surfaces, which were performed with magnetoplasma compressor (MPC) and quasi-steady-state plasma accelerator QSPA Kh-50.

2. DYNAMICS OF PLASMA STREAMS IN MPC DEVICE

Magnetoplasma compressor (MPC) of compact geometry with conical-shaped electrodes having the stored energy in the discharge equal to 28 kJ was used in two operation modes of the plasma source: pulsed gas supply of Xe directly to the discharge area, which provides generation of pure Xe plasma stream, and pulsed injection of Xe to the plasma focus region during the MPC operation with He [3,12,19-21]. The operation modes are shown schematically in Fig.1.

Measurements of the plasma characteristics were carried out at the MPC output, where dense compression zone is formed. Spectroscopic measurements of plasma density and electron temperature in compression region of MPC have been performed on the basis of Stark broadening of spectral lines and intensities ratio in visible wave-range [23,24]. Radial distributions of the plasma density were estimated using Abel inversion procedure. Dynamics of the discharge and time behavior of plasma focus were analyzed for both Xe and He-Xe

plasma streams as well as for varied discharge voltage and time delays between the discharge and gas supply pulses. EUV radiation was detected by registration system consisting on absolutely calibrated AXUV diodes with integrated thin-films filter for different wavelength ranges and multi-layered MoSi mirrors.

Measurements with AXUV photodiodes with different filters showed that the total radiated energy and peak power strongly depends on time delay between the gas supply start and the discharge ignition. The results are shown in Figs.2 and 3. Maximum value of discharge current achieved 500 kA for U_c=20 kV and discharge half-period was ~10 μs (Fig.2).

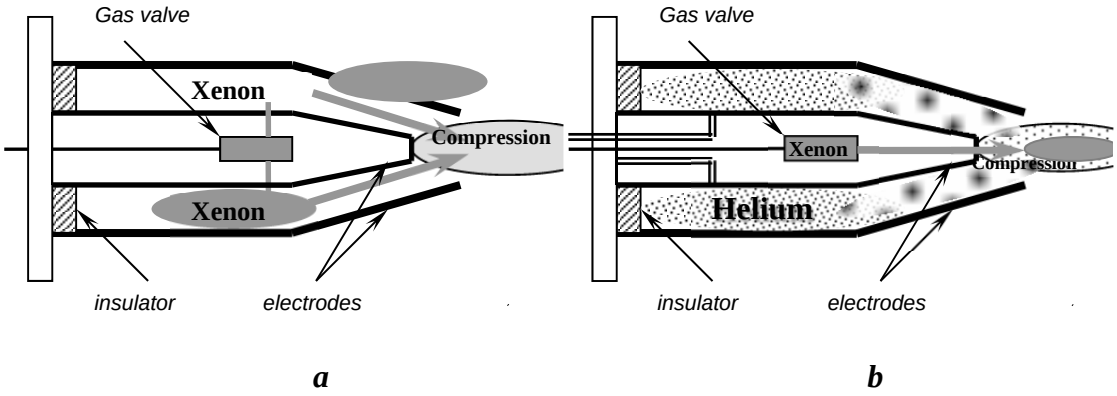

FIG. 1.Modes of MPC operation: a) – pulsed regime of MPC operation with pure Xe; b) – use of helium as working gas in the discharge gap and Xe injection directly to compression region with varied time delays.

It is shown that the maximum radiation intensity corresponds to the spectral range of 12.2-15.8 nm. First measurements of radiation spectrum with an EUV spectrometer were also carried out.

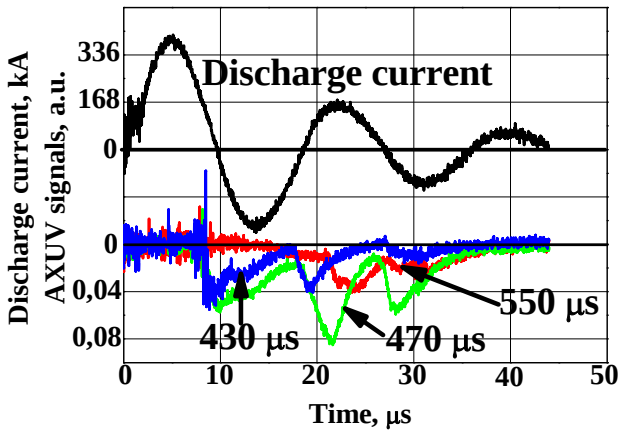

FIG. 2. Waveform of discharge current Id and AXUV 20 Mo/Si signals (wave range 12.2-15.8 nm) for Xe discharge and different time delays.

Temporal dependences of the plasma electron concentration (Fig.4) have been obtained using electron-optical converter, which was synchronized with discharge ignition. Xe II spectral lines are recorded with exposition ~0.5 μs and for different delays with respect to discharge ignition, providing valuable information about temporal changes of plasma parameters.

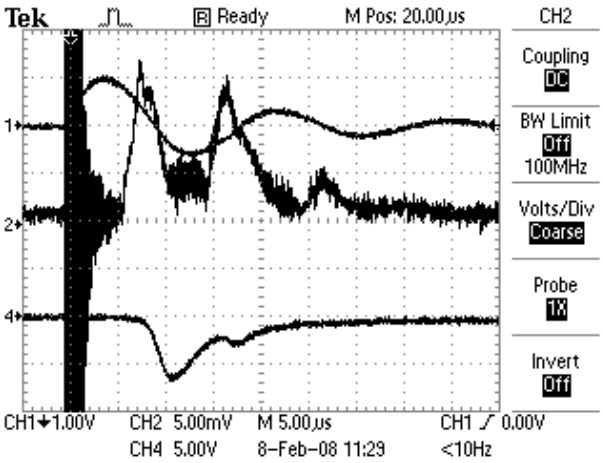

FIG. 3. Waveforms of Id (1), EUV 12.2-15.8 nm (2) and photodiode signal in visible range (4) for MPC discharge with helium and Xe injection into compression zone. PHe =5 Torr.

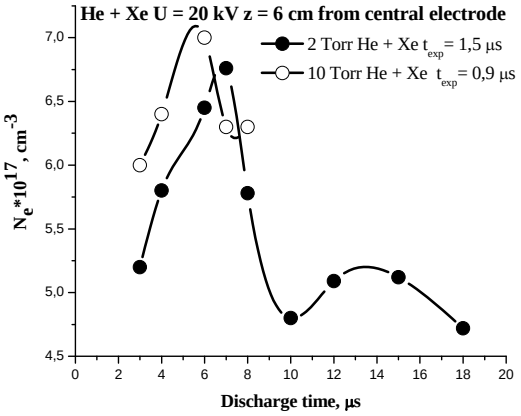

FIG. 4. Temporal evolution of N_e for different MPC operation regimes.

It is obtained that maximal value of electron density is found to be $7*10^{17}$-10^{18} cm^{-3} and it corresponds in time to the discharge current peculiarity, typical for plasma foci. The second peak on N_e temporal dependence is observed in 8 μs after the first one and it concurs with zero current [27-30].

Xe V spectral lines (535,2 and 539,4 nm) were identified in near-axis area for operation regime with 2 Torr He + 7 cm^3 Xe. Duration of these lines emission is quite short 1.5 - 2 μs. It should be noted that selected wave-range of 520 – 545 nm doesn't contain impurity spectral lines, but previous spectral analysis has shown that some C II, O II and Cu I, II (electrodes erosion) are appeared in later time moments. Taking into consideration rather good symmetry of the plasma column, radial distributions of electron density were obtained using Abel inversion of the chord measurements. Experimental results (Fig.5) reveal that plasma compression zone of 1-1.5 cm in diameter and 3-5 cm in length is formed at the MPC output. Plasma pinch evolution which typically characterized by fast implosion stage (fig.6b), shock wave occurrence (Fig.6c) and secondary plasma injection (Fig.6d) was monitored with high-speed imaging. The diffusion of copper ions from the electrodes (Fig.6e) to the focus region promotes the disintegration of the plasma focus column in later time moments. Some dynamical features in the compression zone are still observed even after 40 μs, when discharge in MPC gap has been finished (Fig.6f).

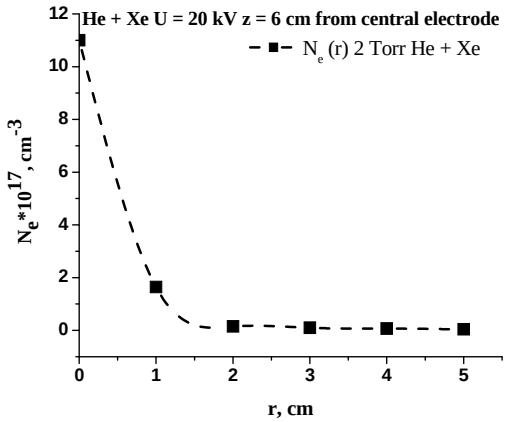

FIG. 5. Radial distribution of the N_e at 6 μs after discharge beginning.

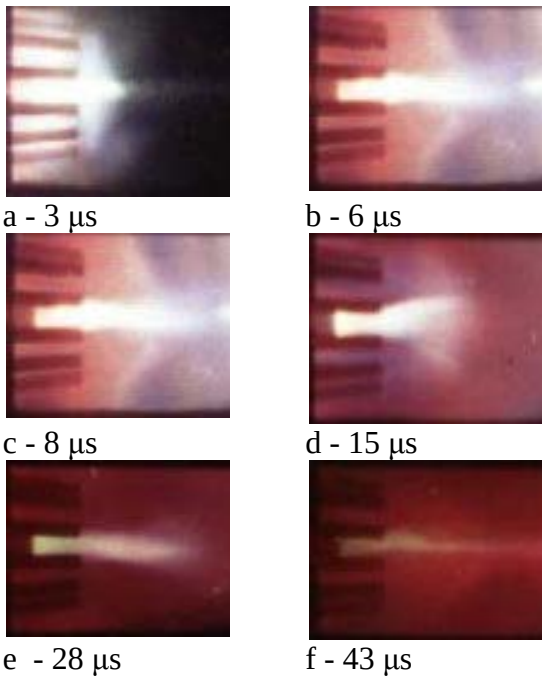

Fig. 6. High-speed imaging of plasma compression.

Measurements of EUV radiation from MPC compression zone revealed that maximum radiation energy corresponds to very narrow wavelength range of 12.2-15.8 nm. It is shown that radiation energy increases with increasing discharge current and it strongly depends on xenon mass flow rate and time delay between gas injection and discharge ignition. Xe injection applied directly into the compression zone and optimization of operation regimes allowed 50% increase of EUV energy in 12.2-15.8 nm wavelength range.

Spatial distributions measurements of magnetic field in the MPC plasma streams were carried out with local movable magnetic probes. Reconstruction of electrical current distributions has been performed from measurements of azimuthal magnetic field using Maxwell equations. Lines of equal electrical current value in the plasma stream for different modes of MPC operation are presented in Fig.7.

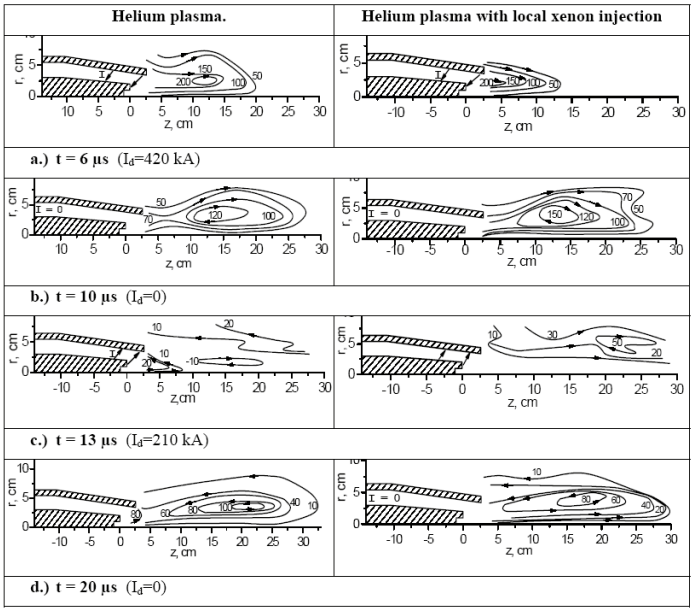

FIG. 7. Time evolution of outlet currents in helium and helium-xenon plasma stream. Values of outlet currents are in kA, direction is marked by arrow. Current magnitude in plasma layer is difference of corresponding values of current lines.

Performed measurements show that total value of electric current flowing outside accelerating channel is about 25-30% of discharge current I_d. Electrical current propagated to the distance up to 25-30 cm from MPC output during first half period of discharge current for both modes of operation with buffering gas and pulsed gas supply.

For MPC operation with local pulsed Xe injection into the compression zone the average velocity of current front propagation is decreased as compare to the operation mode with pure He discharge. It is found that there is clear correlation between configuration of output current and dynamics of compression plasma focus region. The current vortexes appearance is attributed to the inclined shock wave formation in compression zone that affects plasma dynamics outside the source. Shock wave is observed by high-speed imaging technique. Shock wave existence can also be recognized from electric current peculiarities as it is shown in (fig.4b). In some regimes the current displacement from the compression region was observed. In conditions when currents are pushed away and compression region became current free, the magnetic and gas dynamical pressure balance at the boundary of compression zone is achieved at the B-field energy of (10-15) J/cm^3. For measured by Stark broadening electron density in compression region N_e= (5-10)*10^{17} см$^{-3}$ the plasma temperature can be estimated as (Te +Ti) ≈ (50-100) eV.

Features of plasma compression zone formation in different modes of MPC operation have been comprehensibly investigated. Spectroscopic analysis of XeII – XeV lines identified in visible wavelength range was performed. Electron density was measured with high resolution (~0.5 μs) using Stark broadening of XeII and XeIII lines. Described above the measurements of temporal behavior of N_e were supplemented with spatial ones. Example of space-time distributions of electron density at distance 6 cm from central electrode is presented in Fig.8. for MPC operation at buffering gas pressure of 2 Torr and Xe local injection. Again, maximum plasma stream density achieves 10^{18} cm^{-3}, average electron temperature along the line of view ~ 5-7 eV and plasma stream velocity at the MPC output ~ 10^7 cm/s.

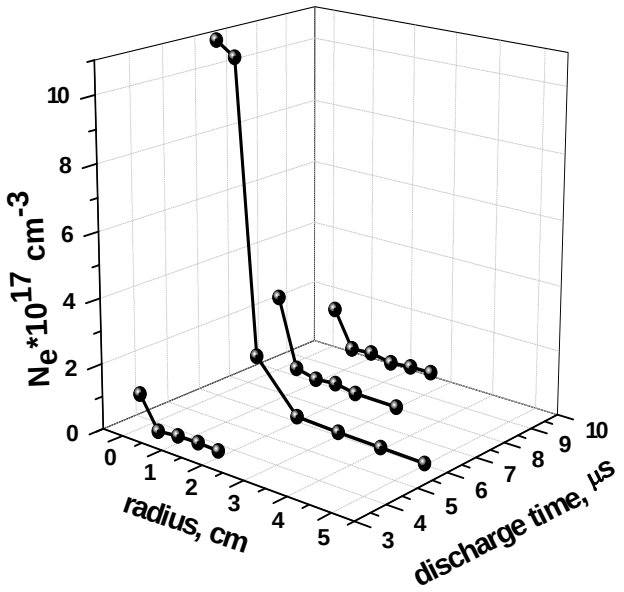

FIG. 8. Space-time electron density distribution at distance of 6 cm from central electrode obtained for MPC operation at buffering He pressure of 2 Torr and local Xe injection.

Plasma source efficiency was analyzed from electro-technical discharge characteristics [33,36]. It was concluded that dense plasma streams of heavy noble gases generated by MPC device are important for different technological applications: EUV lithography, plasma thrusters, surface processing etc.

3. INTERACTION OF MPC PLASMA STREAMS WITH MATERIAL SURFACES

Measurements of the heat load to the tungsten targets surface, irradiated by plasma streams of MPC were carried out in a series of plasma-surface interaction experiments. The target has been set perpendicularly to plasma stream. Maximal heat load to the target surface under exposures with helium plasma stream is achieved 0.39 MJ/m^2. The heat load to the tungsten surface under exposures with additional injection of xenon is decreased to 0.33 MJ/m^2. Microscopy observations have shown that applied heat load results in pronounced melting of the tungsten surfaces (Fig. 9). Network of major cracks is formed on the target surfaces. Typical size of major crack mesh is 0.7 mm for both helium and helium–xenon exposures. Major cracks width after 10 plasma pulses is within 5-15 μm for both cases. There are two characteristic networks of the micro-cracks' with size of a few microns inside the major crack mesh. Typical cells sizes of such micro-cracks are 20-40 μm and 15-25 μm respectively. Additionally, more fine cracks appear in the background of micro-crack meshes, with typical cell size of 2–7 μm.

The XRD measurements of exposed samples have shown that the tungsten lattice spacing in the stress-free plane section is initially grows, but then it decreases with increasing number of plasma pulses resulting in melting. Probably, this is caused by appearance of melt layer on the exposed surface. Increasing solubility rate in the molten layer promotes effective penetration of light impurities, first of all helium, into the surface layer structure.

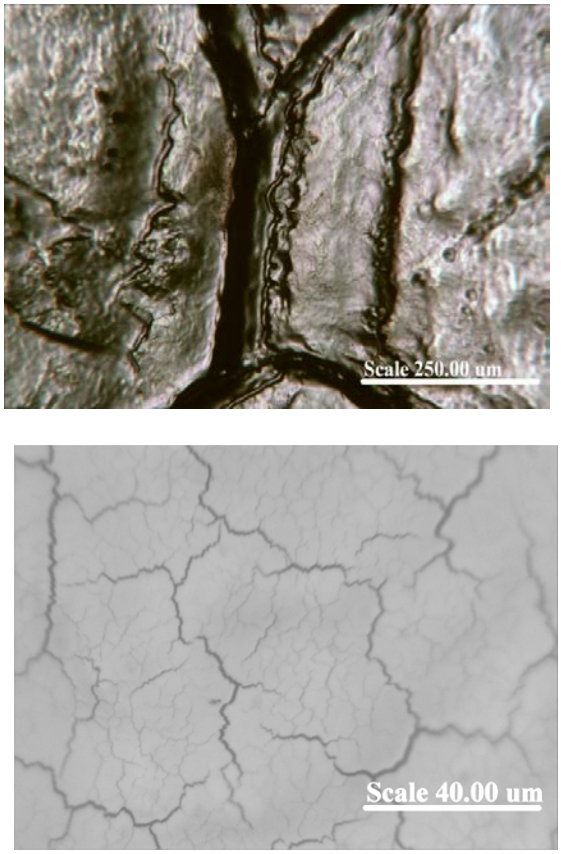

FIG. 9. Images of major cracks (a) and the network of fine cracks on the tungsten surface exposed by helium plasma streams.

4. PLASMA-SURFACE INTRACTION STUDIES WITH QSPA KH-50

The samples of sintered and rolled tungsten grades as well as CFC and graphite targets have been exposed to hydrogen plasma streams generated by the quasi-steady-state plasma accelerator QSPA Kh-50. Also, a deformed W material (Plansee AG) was used for the plasma load tests. The grain orientation was parallel to the heat transfer direction, which corresponds to ITER specifications. Cylindrical shaped specimens with a diameter of 12 mm and a height of 5 mm were prepared from a 1-m-long rod (Ø 12 mm, with the deformation axis along the rod).

An electric heater was installed at target's back-side to keep the target temperature in the range 200 - 600°C before the plasma pulse. For temperature monitoring both a calibrated thermocouple and an infrared pyrometer were used.

Calorimetry, interferometry, spectroscopy and different probes were applied for measurements of plasma stream parameters and surface heat loads in various operation regimes [25]. Observations of plasma interactions with the exposed surfaces and ejected particles monitoring were performed with high-speed CMOS PCO AG camera [26]**.**

In QSPA experiments the onset loads for tungsten melting and evaporation were measured precisely by calorimetry in combination with surface microscopy analysis. It was demonstrated that tungsten melting threshold under QSPA Kh-50 exposures is 0.56-0.6 MJ/m^2. The evaporation onset is estimated as 1.1 MJ/m^2 [9, 10].

The main parameters of QSPA plasma streams in ELM simulation experiments were as follows: ion impact energy about 0.4-0.9 keV, the maximum plasma pressure 3.2 bars, and the stream diameter about 18 cm. The surface energy loads measured with a calorimeter were 0.2 MJ/m^2, 0.3 MJ/m^2 and 0.45 MJ/m^2, i.e. below the melting threshold, or 0.75 MJ/m^2, which is between the melting- and evaporation thresholds. The plasma pulse shape was approximately triangular, and the pulse duration was 0.25 ms.

A surface analysis was carried out with an MMR-4 optical microscope equipped with a CCD camera and Scanning Electron Microscopy (SEM) of the JEOL JSM-6390 type. Measurements of weight losses and micro-hardness of the surface were also performed.

To study a micro-structural evolution of the exposed W targets, the X ray diffraction technique (XRD) has been used. The so-called 'θ-2θ scans' were performed using a monochromatic K_α line of the Cu anode radiation. Diffraction peaks intensity, their profiles, and their angular positions were analyzed in order to evaluate the texture, the size of a coherent scattering zone, the macrostrains and the lattice parameters.

After the QSPA plasma impacts with energy loads resulting in surface melting, a fine mesh of intergranular micro-cracks appeared. The width of fine intergranular cracks grows with the pulse number. Threshold changes in surface morphology in form of appeared corrugation structures and pits on the surface as well as important contribution of surface tension to resulted "micro-brush" structures are discovered [25]. Example of morphology changes is shown in Fig.10. Degradation of thermophysical properties of tungsten under multiple plasma exposures was also identified.

Due to relatively large diameter of the plasma stream in QSPA Kh-50 the influence of the plasma pressure gradient on the melt motion in described experiments was negligible, that was confirmed by direct measurement of plasma pressure distribution along the surface with movable piezo-detectors. Absence of melt motion provides a possibility for accurate analysis of surface crack dynamics by monitoring the selected surface regions after different number of exposures.

Surface analysis concerned the crack width evolution (both major- and micro-cracks) in different regimes of exposures for RT and preheated at 650 ^{o}C targets, average mesh size, correlation of cracks development with stresses relaxation, fine structure of surface etc.

Experiments show that major cracks are attributed to ductile-to-brittle transition, they arise for RT targets exposed with all 3 different loads. Mesh size, i.e. distance between major cracks is in the range of 0.5-1 mm. Major crack mesh is formed after the first plasma impacts. Cracking development correlates with microhardness changes of exposed surface (Fig. 11). The width of major cracks grows with number of pulses but remains to be below 10 microns after 270 exposures without melting (Fig. 11). In regimes with surface melting it is essentially increases due to the surface tension effects in the melt layer and achieves saturation level of 60-70 μm after 200 pulses.

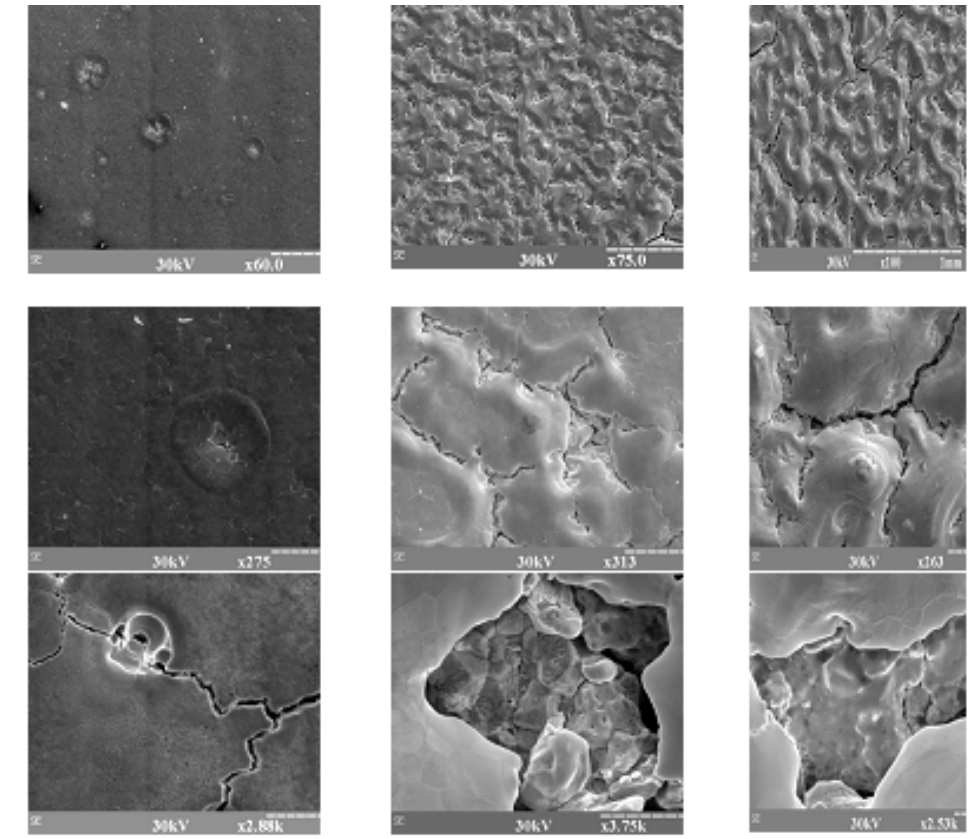

FIG. 10. SEM images of the tungsten target after 100 (a), 210 (b) and 350 (c) pulses with different magnification illustrating threshold character of morphological evolution of exposed surface.

Fig. 12 shows the cracking dynamics for preheated at 650 ^{o}C tungsten in the course of plasma exposures below the melting threshold. Due to preheating above DBTT, major cracks are avoided. No cracks at all (at least visible with microscopy) found during first hundred of pulses. Then some single micro-cracks are formed. They can be classified as fatigue cracks in results of numerous repetitive plasma impacts. Separate cracks initially arisen do not form the complete mesh on the surface. The complete mesh of the cracks became clearly seen after 150-200 pulses. Growing error bars in Fig. 12 are due to new cracks appearance with further pulses. Microscopy observations show that new very thin cracks are still arisen in addition to well developed thicker cracks from the previous pulses.

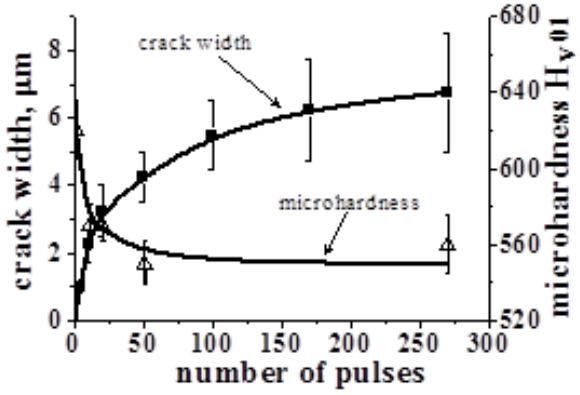

FIG. 11. Average width of major cracks and microhardness of the tungsten surface vs. impacting plasma pulses for RT target in the regime without melting (q=0.45 MJ/m2, =0.25 ms). Statistical analysis of microscopy measurements.

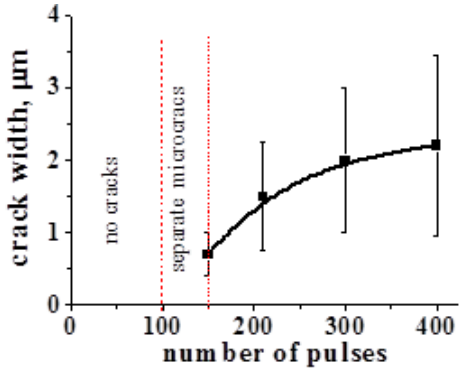

FIG. 12. Development of cracks on the tungsten surface in result of preheated target exposures (q=0.45 MJ/m^2, τ=0.25 ms).

Therefore in spite of increasing width of each chosen crack, average width of fatigue cracks in Fig. 12 grows slowly. Although their width is smallest in comparison with other crack types, fatigue cracks lead to essential damage of the surface. Mesh size of fatigue micro-cracks lays the scale of several grain sizes i.e. 30-60 μm and mesh cells are primary oriented along the machining traces from initial surface preparation. Further plasma exposures of tungsten surface pre-damaged by developed cracks lead to the surface modification with formation of submicron cellular structures and melting onset in modified surface areas due to degradation of tungsten thermal properties.

Typical feature of plasma exposures with pronounced melting is development of intergranular micro-cracks for both RT (together with major cracks) and preheated targets [31,32]. Evolution of micro-cracks due to repetitive plasma loads is summarized in Fig. 13. Steep increase of micro-crack width is observed after 200 pulses. It corresponds to qualitative evolution of surface morphology. From comparison with corresponding dependence of fatigue cracks width vs. number of pulses it is seen that both types of cracks may exist for multi-pulsed exposures of RT tungsten with melting. Fatigue cracks are identified for exposures with melting among appeared earlier micro-cracks.

Average size of the crack meshes in different regimes of exposures is shown in Fig.14. It should be noted that mesh size of micro-cracks is initially 20-40 microns being comparable with grain size. In the course of several hundreds exposures merging of mesh cells is detected (mesh size increases to 100 μm). Some micro-cracks disappear in result of remelting, but simultaneous step increase of remained cracks width is occurred.

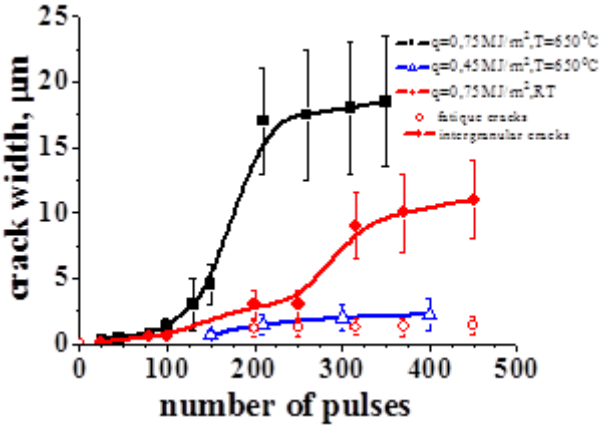

FIG. 13. Width of micro-cracks for different regimes and width of fatigue cracks vs. the number of pulses.

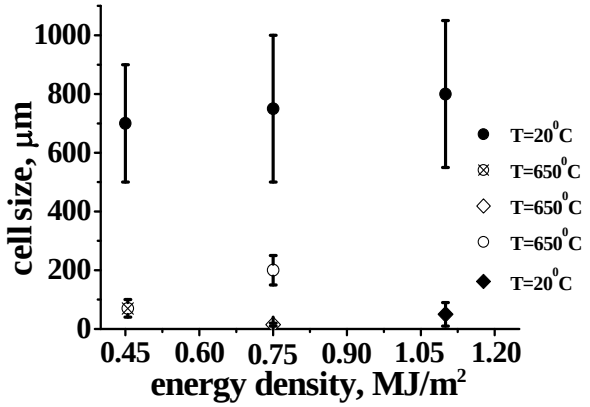

FIG. 14. Average size of the crack meshes in different regimes of exposures in QSPA Kh-50.

Cracks studies correlate with residual stresses measurements, which were performed using XRD $\sin^2\Psi$ method. Maximal stresses are observed in tungsten without preheating, i.e. RT targets after the irradiation with plasma loads below the melting threshold. In this case only major cracks are detected. Tungsten preheating above DBTT allows some decreasing of the stresses value. Almost complete relaxation of stresses was found in preheated target as result of increased up 300- 400 number of plasma exposures, that corresponds to development of fatigue crack mesh.

Influence of plasma pulse duration on crack dynamics was analyzed comparing results of tungsten exposures with QSPA Kh-50 (τ=0.25 ms) and short-pulse plasma gun (τ=0.02 ms) for similar load parameter $q/t^{1/2}$. It is seen that that the short pulse exposures are more dangerous from the viewpoint of major cracks that became more pronounced and faster form the complete mesh. As to micro-cracks, in both cases they are attributed to melting and the mesh size is similar. Nevertheless the micro-crack mesh is also stronger developed for short pulses due to smaller resolidification time.

4.1. Thresholds for tungsten cracking

Investigation of a tungsten response to the repetitive pulses with heat loads below the cracking threshold is important for the determination of an ITER divertor lifetime with controlled ELM loads. As showed in QSPA experiments, only few isolated cracks have appeared in some areas on the surface when the surface load was less than 0.3 MJ/m^2. The change of initial target temperature in the range 200-600 °C, and the plasma exposures with 1 and 5 pulses of heat load of 0.2 MJ/m^2 did not result in cracks (Fig. 1). Rather weak dependencies of residual stresses on the initial temperature and the irradiation dose were obtained. The values of residual stresses were ≈160…180 MPa.

The irradiation of tungsten samples with QSPA plasma heat loads above the cracking threshold and below the melting onset have shown that sometimes we do not observe crack appearance after an exposure to a single pulse (Fig.15). This delay can be explained assuming an appearance of some initial protecting film on the surface (oxides, impurities etc.), which decreases the actual load to the tungsten material, because some additional energy is needed for a removal of this film, as well as some micro-particles and weakly coupled fragments that can remain at the surface after the polishing. Thus, at the identical QSPA discharge

conditions, during impact of first 1-2 plasma pulses the energy absorbed by W target is smaller, what was directly confirmed by calorimetry measurements. This result is indicated by arrows in corresponding diagram after 1 pulse (in Fig.15).

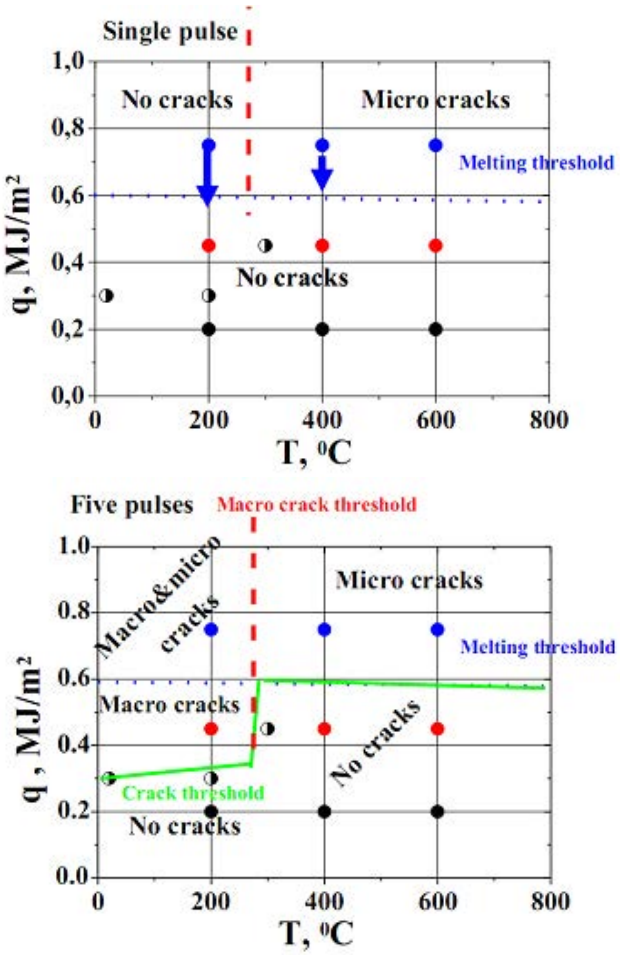

FIG. 15. Cracking thresholds diagrams for ITER reference W grade: after a single pulse (a) and after 5 (b) QSPA plasma pulses.

For the initial temperature $T_0 \geq 300$ °C and after 5 plasma pulses of 0.45 MJ/m^2 there are no cracks (either major- or micro-cracks). It can be understood if the DBTT point for this tungsten grade lies in the range of 200 °C < $T_{DBTT} \leq 300$ °C. For the initial temperature 200 °C and with increasing number of pulses up to 5, the formation of major cracks network (macro-meshes) is observed (see Fig. 16). In the central area of exposed surface the crack meshes have approximately rectangular shapes with average cell sizes 0.8-1.3 mm. At the sample edge the mesh cell sizes decrease down to 0.3-0.6 mm, and the cell shapes become approximately elliptical. Probably, due to the edge effects the gradients of temperature are higher for interface between exposed hot surface and unexposed surface area, which has the initial temperature. But in the central part of the sample the mesh is not completely formed yet due to a rather homogeneous heat load in this area. So the mesh size is approximately 2 times larger.

From a SEM surface investigation it is obtained that after 5 pulses the width of cracks is about 0.5-1.5 μm. From the initial mesh of cracks descendant cracks develop with a typical width of 0.2-0.3 μm. An increase of the impacting pulses up to 10 does not result in more or

less pronounced changes of crack meshes. Nevertheless, some new thin descendants of the primary macro-cracks were registered. The crack width grows up to 1-3 μm, and the descendant width is about 0.3-0.5 μm.

Thus it is discovered for low cyclic exposures (1-10 pulses) that the crack width grows for 2 times after a double increase of the pulse number. For the target at 400 °C initial temperature, a further increase of the exposition dose up to 5 pulses did not result in cracking. Absence of cracks indicates that we overcame the DBTT point. Exposures of tungsten targets preheated at 600 °C do not also practically change the surface profile in a comparison with the previously described impacts of 1 pulse and 5 pulses. Thus the cracks are absent completely on the surface. In contrast to the previous cases, after those plasma exposures some "etching pattern" is registered, caused probably by higher ion energies and initial surface temperatures.

After a single exposure of W targets with heat loads of 0.45 MJ/m^2 the residual stress decreases when T_0 increases. The maximum stress (about 314 MPa) appears on the surface preheated to 200 °C, and the stress drops down to 250 MPa when T_0 overcomes the DBTT point. An increase in the number of plasma pulses leads to some saturation of residual stress which does not depend on T_0.

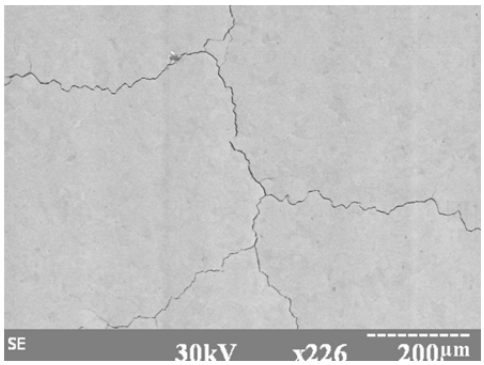

FIG. 16. Major cracks on W surface after 5 pulses of 0.45 MJ/m^2. T_0=200℃.

Tungsten exposures resulting in surface melting reveal that already after 5 exposures with the pronounced melting of surface layer (0.75 MJ/m^2) some networks of micro- and macro-cracks develop on W surface if T_0 < 300°C. Typical mesh sizes of major cracks in the central area of exposed surface are 0.8-1.3 mm. In the periphery of the exposed area they decrease till 0.3-0.6 mm, similarly as described above. The crack width is estimated to be 2-4 μm, and after 5 pulses the descendants of the major cracks appear having typically the width of (0.3 – 0.5) μm. A typical cell size of the inter-granular micro-cracks mesh is 10 – 80 μm. Mostly, the cell sizes are within a range of 10–40 μm, which corresponds to the grain size of this W grade.

The micro-cracks propagate along the grain boundaries completely surrounding and splitting off the grains. After following load pulses the whole crack network melts and each time new cracks with typical width of 0.2-0.4 μm appear again along the grain boundaries after the re-solidification. In some cases, more fine cracks arise in the background of micro-crack meshes, with a typical cell size of 2-6 μm and the width less than 0.1 μm. This finest mesh is either inside the initial grain, or it may result from a grain refinement due to some modification of the surface layer by the plasma pulses with repetitive melting and fast re-solidification.

The formation of submicron- and nanostructures on the surface of tungsten, as a sequence of the surface modification, was observed also [15, 25]. Further increase in the number of pulses up to 10 shots did not result in any essential changes of the surface morphology and major crack network. The width of the major cracks is growing up to 4–8 μm, crack descendant thickness is typically 1–2 μm. The cells of major crack network are intensively covered by the micro-cracks meshes.

A cross-section metallographic analysis provides the important information about crack propagation in the material bulk and morphology changes in a heat affected layer (Fig. 17).

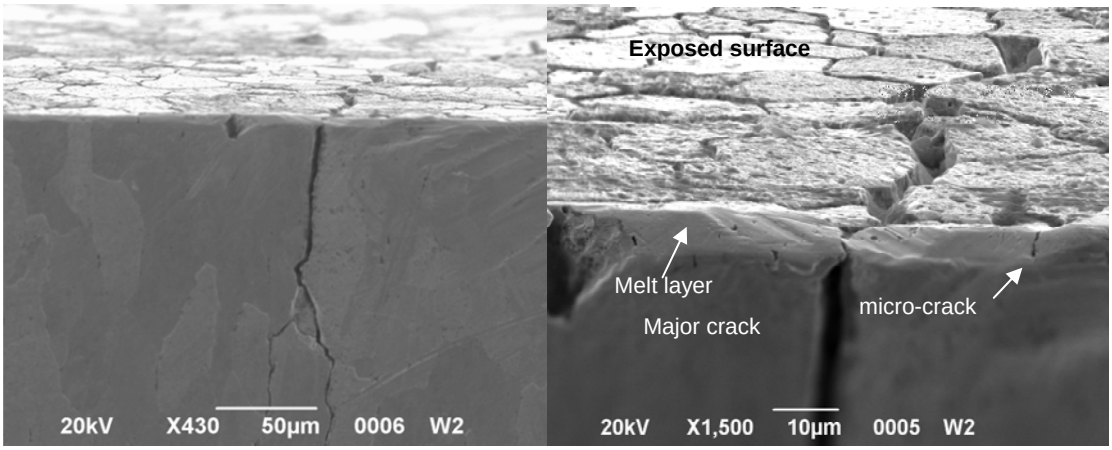

FIG. 17. Cross-section of the deformed W target preheated at 200 ^{0}C and exposed to 10 pulses of 0.75 MJ/m^2.

After 5-10 pulses a typical penetration depth of major cracks is 200-400 μm. Cracks propagate to the bulk material along the grain boundaries. Basing on this analysis it is possible to deduce that the cracks originate in the bulk (i.e. in some depth), where the DBT-transition can occur earlier than at the surface during the cooling front propagation. The maximal width of the major cracks is registered sometimes in the depth of 10-20 μm, which seems to confirm the hypothesis. A typical depth of the micro-cracks is 5-15 μm, which roughly corresponds to the scale of the melt layer thickness (about 5-10 μm), which was also measured directly in the experiments. In Fig.17 it is shown as an ultra-fine structure resistant to etching.

For heat loads above the melting threshold and an elevated surface temperature $T_0 > 400$ C the cracks appear after single pulse. This can also be an evidence of the above mentioned film removal by the preheating in vacuum at high temperatures, but it can also indicate an annealing effect. Some cracks surround the grain boundaries, which we clearly see, and higher initial temperature results in a more pronounced melting (even after a single pulse) and the micro-cracks formation. Separate insulated cracks are formed primary in the areas where the boundaries of 3 grains merge. However, they do not surround the neighbor grains (Fig. 18). After 5 plasma pulses the crack width remains to be 0.3-0.5 μm and the crack length does not exceed 20 μm. Also, shorter cracks (below 10 μm) are registered with the width of 0.1-0.2 μm. Generally, after each plasma-pulse the surface roughness changes very small. The visualization of grains is possible due to an elevation of the edges of some grains in respect to others and due to their different deformation, which may be caused by local intensification of the sputtering under increased ion impacts.

On the W samples preheated at 600 ^{o}C, after a single pulsed exposure there appears a network of micro-cracks (Fig. 18). An average cell size of the crack mesh is about 20 μm, which again corresponds to the grain size. The cracks can be subdivided into 2 groups. To the first group belong relatively thick cracks (0.4-0.6 μm) with a typical length of 10-40 μm, which arose at the turn of several grains boundaries, and second group - is formed by thin cracks of thickness 0.1-0.3 μm, which stretch alone single grains.

In the points where the boundaries of 3 grains merge - the material pieces with sizes of several microns surrounded by cracks split off. These pieces can constitute a serious concern for the W dust formation and contamination of plasma. Inside the grain areas some fine structure can be seen. An increase in the exposures up to 5 pulses resulted in a clear visualization of micro-cracks network (Fig. 18).

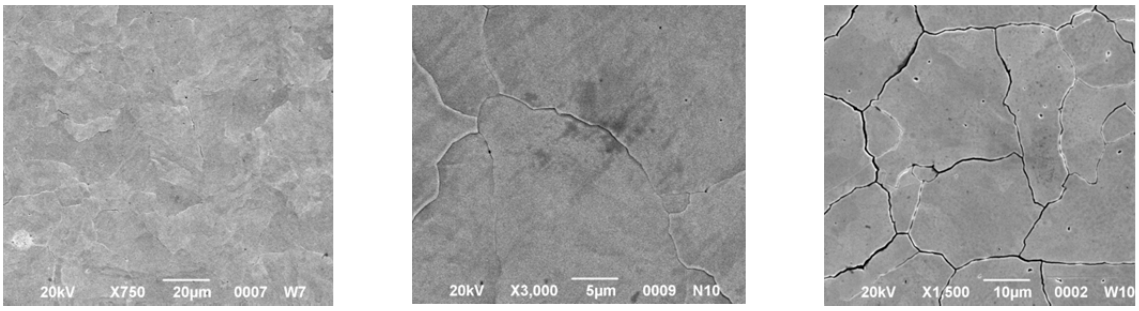

FIG. 18. W surface after 5 pulses of 0.75 MJ/m^2, at T_0=400 ℃; after a single pulse, and after 5 pulses of 0.75 MJ/m^2, at T_0=600 ℃.

The cells of crack network may have various sizes. Larger cells exceed 30 μm, and small ones are of 10 μm. The micro-cracks with typical width up to 1 μm can propagate along the boundary of several grains (grain blocks). Such cracks have length of 30-80 μm. The smaller cracks with thickness of 0.1–0.5 μm propagate along single grains, and they form a mesh with sizes of typical grains. Finally, inside the initial grains there are formed finest cracks with typical width below 0.1 μm.

The XRD diffraction analysis has confirmed that there is no material phases built of impurities. Only W lines on the surface and in deeper layers were observed. This was the important indication of plasma and target purity. The single pulse irradiation of a W surface preheated at 200 ^{0}C with the heat load above the melting threshold 0.75 MJ/m^2 led to the absolute maximal residual stress of 390 MPa for the deformed W grade (measured in the described experiments). Preheating of tungsten at the temperature larger than 400 ^{o}C causes the saturation of the residual stress in tungsten at the level of 300 MPa. In the course of 5 plasma pulses the residual stress linearly decreases from 362 MPa down to 200 MPa with rising of initial surface temperature from 200 ^{0}C up to 600 ^{0}C.

The results of QSPA plasma exposures [31,32,35] have also been compared with the previous e-beam experiments on thermal shock loads of the deformed W material [37]. Similar sizes of the crack meshes have been observed. However, in our experiments the micro-cracks network is always attributed to the surface melting. After e-beam exposures, fine cracks were detected for energy loads below melting threshold. To explain somewhat different results obtained in both cases, a probable reason for the observed difference can be a volumetric heat deposition of e-beam power with the maximal temperature in the bulk (several μm below the surface), while plasma load deposits at the very surface. This feature of

a plasma energy transfer do not contribute to the dynamics of the major cracks due to their large scale and significant penetration depth, but for fine inter-granular cracks having ten μm depths it provides a qualitative difference [38-41].

4.2. Comparison with short pulse exposures

Results of QSPA plasma exposures are compared also with short-pulse PSI experiments (τ~ 0.1-5 μs) with a pulsed plasma gun and dense plasma-focus facilities in Poland [13], aiming at studies of a surface damage and tungsten impurities behavior in near-surface plasma formed in front of the target. It is found that higher thermal stresses under short-pulse exposures influence on the cracks dynamics. In these experiments, optical spectroscopy studies of WI and WII lines emitted from eroded tungsten-plasma provide possibility for the monitoring of tungsten spectral lines and measurements of a W plasma density in front of the target (Fig. 19).

Information about dynamics of the W-ions production was also obtained. On the basis of the space and time-resolved spectroscopic measurements of the D_α line in the RPI-IBIS experiment, it was estimated that the highest density of a plasma layer in front of the target surface amounted to about 3.4 x 10^{16} cm^{-3}. For QSPA exposures, long pulse duration hampers the tungsten lines analysis due to additional background influence of impacting plasma and formation of dense plasma layers near the targets exposed to a plasma stream pressure [5- 6].

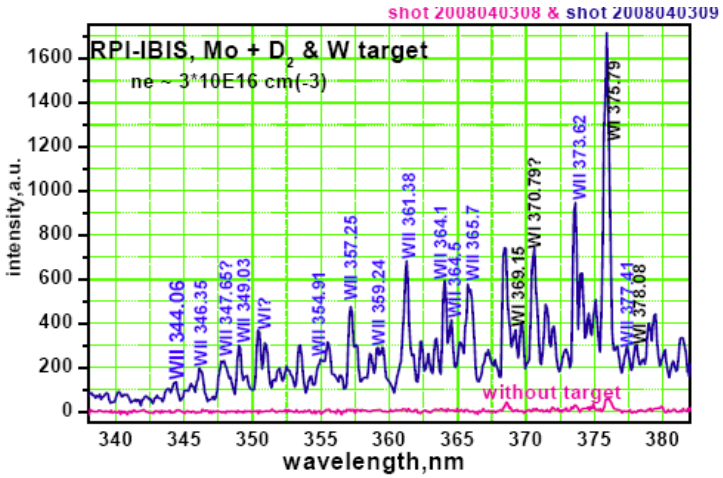

FIG. 19. Spectral lines recorded within the RPI-IBIS experiment (with and without W-target) in spectral range (340-380 nm).

4.3. Features of plasma energy transfer to the material surfaces in QSPA experiments

Fig.20. shows the heat load to the tungsten, graphite and combined W-C target surfaces, which was measured with calorimetry, in dependence on energy density of impacting plasma stream. For tungsten target exposure the onset of melting is observed on the surface at the surface heat load of 0.57 MJ/m^2. The measurements demonstrate that even for plasma exposures, which not result in the melting, the absorbed heat load is about 55-60 % of the impact plasma energy. The dynamical screening of the surface from impacting plasma stream appears in this case probably due to the shock wave formation and plasma stream thermalization under the interaction with the target surface. The stopped plasma layer, formed from the head of the plasma stream, ceases to be completely transparent for subsequently impacting plasma ions.

Tungsten vapor shield formation and its influence on plasma energy transfer to the surface becomes clearly seen as the surface heat load achieves 1.1 MJ/m^2. The fraction of plasma energy, which is absorbed by the target surface, is rapidly decreased with achieving the evaporation onset for exposed targets. At this, the value of heat load to the surface remains practically constant with further increase of the energy density of impacting plasma (plateau region in Fig. 20).

The evaporation leads to enhanced mass losses of tungsten: increase of the heat load from 0.75 to 1.1 MJ/m^2 raises mass losses for one order of magnitude and causes bubble structures at the surface. Due to achievement of evaporation threshold the erosion crater become visible even on the "background" of the surface roughness and swelling. The erosion rate, caused by evaporation, is ~ 0.05 μm/pulse. Microscopy observations of tungsten targets show boiling bubbles on the surface exposed with heat load of 1.1 MJ/m^2 (Fig. 21). For initial pulses the boiling is initiated on the surface by impurities. With further exposures it becomes predominantly volumetric and deep bubbles are arisen at the surface. The volumetric boiling occurs predominantly at the vicinity of crack edges.

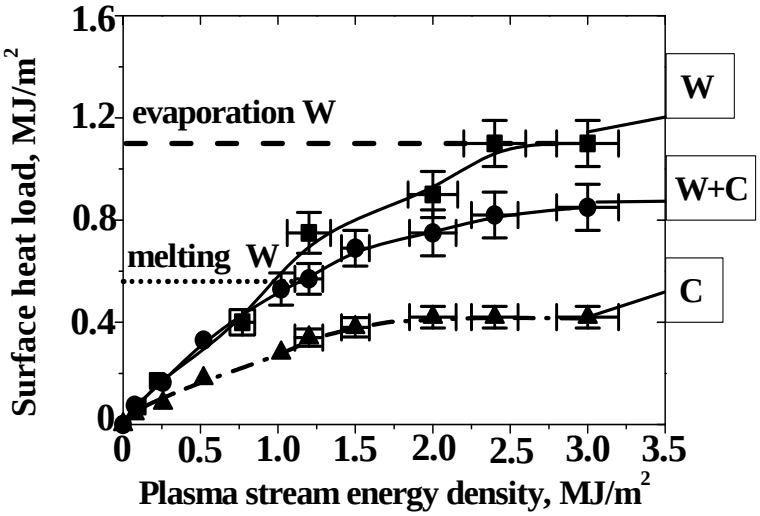

FIG. 20. Heat load to the target surfaces vs. the energy density of impacting plasma stream.

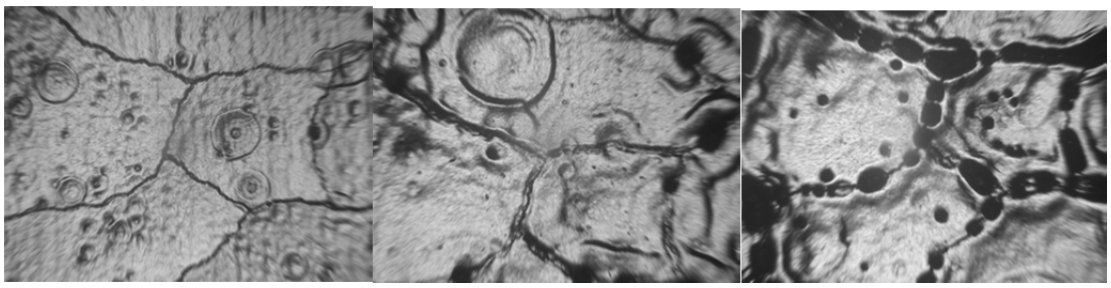

FIG. 21. Boiling bubbles on the tungsten surface, exposed with 5, 25 and 80 pulses of 1.1 MJ/m^2 (the same surface region).

It was shown that the repetitive heat loads (up to 450 cycles), typical for ELMs in ITER, lead to the formation of two types cracks at the tungsten surface: macro cracks (with mesh size of an order 1 mm) and the net of intergrannular micro cracks (with the mesh of 10-20 μm).

Evolution of macro cracks in the course of plasma exposures is shown in Fig. 22. Crack width is increased with pulse number with following saturation after about 200 pulses. Nevertheless the crack width achieves several tens microns in result of plasma exposures demonstrating significant damage of tungsten surface.

It should be stressed again that macro and micro cracks have principally different physical nature. Macro cracks are the result of transition from ductile to brittle state at the process of the surface layer cooling (i.e. ductile to brittle transition). At the same time the fine cracks are the attribute of intensive melting and their formation is dealing with non-equilibrium solidification of melt. This is confirmed by the fact that under the irradiation of preliminary heated target up to the temperature of 650 ^{0}C (above the temperature of ductile to brittle transition) the macro cracks are not observed while the micro cracks are developed on the surface, similarly to non heated targets.

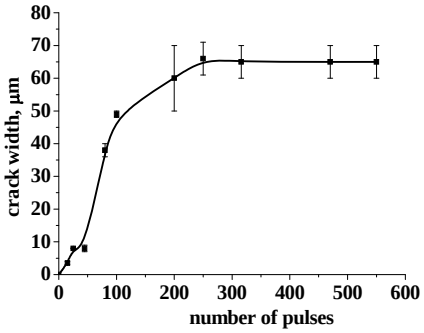

FIG. 22. Evolution of macro cracks on the tungsten surface, exposed with repetitive pulses of 0.75 MJ/m^2.

Measurements of the energy transfer to combined tungsten-graphite targets of different sizes demonstrate that the value of energy density delivered to such target surface is reduced in comparison with the irradiation of the pure tungsten target (Fig. 20). Carbon neighborhood resulted in the shielding which has been developed for lower heat loads. Experiments with MPG-7 graphite targets show that carbon evaporation starts at (0.4 - 0.45) MJ/m^2. Carbon vapor shield formation during exposures of combined W-C targets results in additional decrease of the heat loads to W surface (from 1.1 MJ/m^2 to (0.8 – 85) MJ/m^2) preventing tungsten evaporation. It should be noted that tungsten evaporation threshold in the case of adjoined graphite surface was not achieved even with increasing plasma stream energy density (Fig. 20).

Plasma impacts with the loads above the melting threshold cause the droplets splashing from the tungsten surface. As an example, Fig 23 shows images of the droplets traces for different time moments after the end of the plasma pulse. Exposition time for each image is 1.2 ms and the velocity of the droplets can be estimated from the lengths of their traces. Movement in perpendicular direction to the image plane is derived from consecutive frames. Consequences of the images form movie with possibility to analyze the dynamics of droplets splashing from the surface.

Particles continue to be ejected from the melt after plasma impact during > 10 ms. It is obtained that their velocities may achieve several tens m/s. Fast droplets were generated at earlier time moments. Smaller velocities are observed for late stage of observation (Fig. 23). During intermediate stage both groups with fast and lower velocities have been observed (Figs. 23 and 24a).

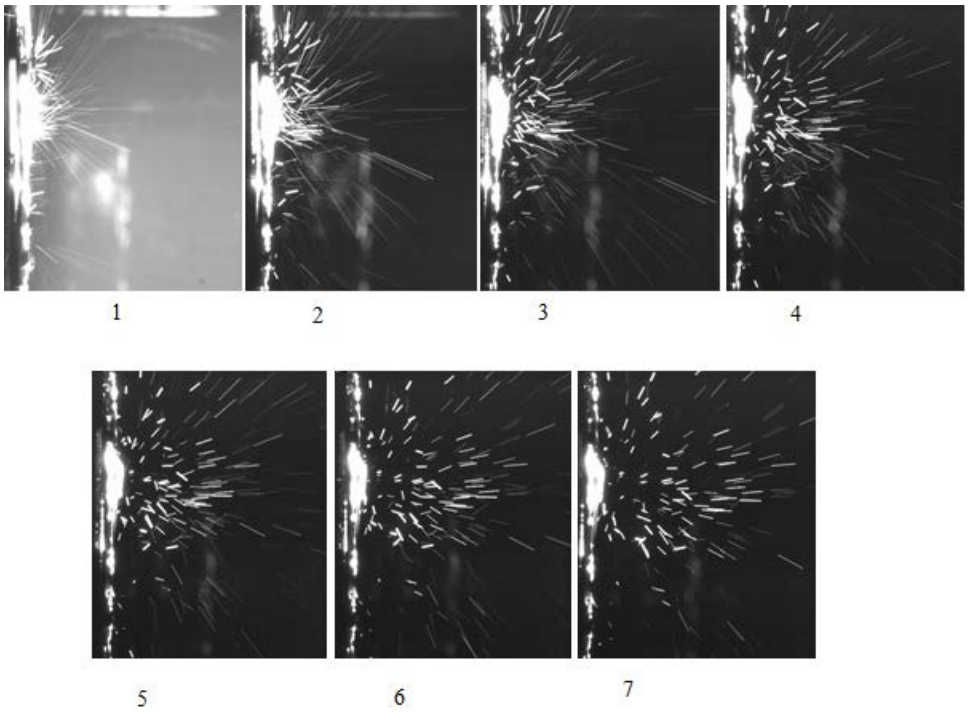

FIG. 23. Droplets splashing from tungsten melt. Images of droplet traces: t_1 = 1.8 ms, t_2 = 3.0 ms, t_3 = 4.2 ms, t_4 = 5.4 ms, t_5 = 6.6 ms, t_6 = 7.8 ms, t_7 = 9.0 ms after the end of plasma pulse, ($t_{exposure}$ = 1.2 ms).

Angular distribution of ejected droplets is presented in Fig. 24b. For perpendicular to the surface plasma impacts droplets and solid particles are ejected primarily with small angles to the normal. Nevertheless rather large angles up to 80^0 are measured also. Analysis of particles traces from consecutive images show the influence of gravitational force for droplets with higher mass and smaller velocities. Due to the gravitation the resulting angular distribution of the droplets became non-symmetric (Fig. 24b). With achieving evaporation threshold the tungsten boiling results in intensification of the droplets splashing. Their size is varied in the range of (5-100) μm.

Dynamics of tungsten and carbon vapor in front of the targets surfaces, which was studied with spectroscopy and high-speed photography during the plasma pulse, and it dependence on the magnitude of external magnetic field is described in [8]. Here it can be only mentioned that evaporated tungsten is concentrated in rather thin plasma layer of < 0.5 cm close to the surface and it does not propagate significantly in upstream direction during the QSPA pulse. In the case of graphite target exposure, high-speed photography shows continuous region of carbon vapor luminosity. Thickness of the shielding layer increases during the pulse and exceeds 5 cm. Spectroscopy measurements demonstrate that carbon lines are registered not only in front of the target surface, but also for larger distances (up to 20 cm) from the target.

Fig.25 shows the hot spots indicating overheated local areas on the graphite surface of combined W-C target (tungsten rod of 1 cm diameter surrounded by MPG-7 graphite of 8 cm in diameter). The target was subjected to inclined plasma impact, $\alpha = 45^0$. Surface heat load Q_{surf} = 0.5 MJ/m^2. The images correspond to t_{start} = 0.7 ms and t_{start} = 3.7 ms after plasma pulse respectively. Exposition time of each image is t_{exp} = 0.5 ms. It should be noted much more pronounced heating of upstream part of the inclined target edge, which is demonstrated by Fig.25. This is valid also for tungsten rod in target center (Fig.25.1).

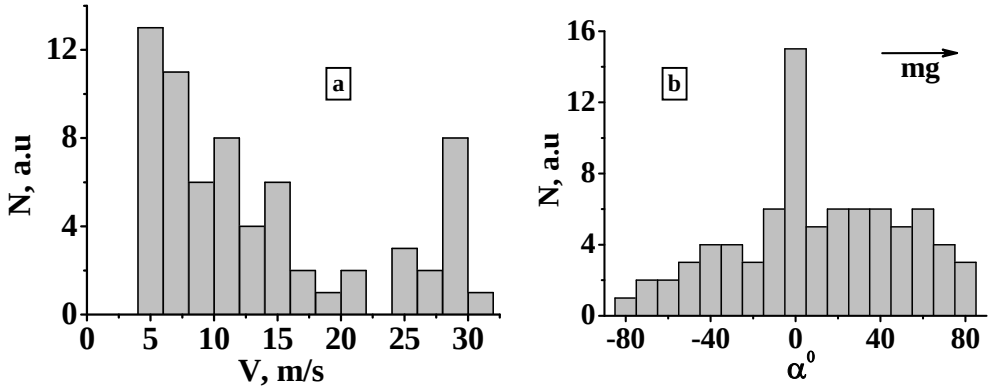

FIG. 24. Velocity (a) and angular (b) distributions of ejected droplets.

The hot spots are probably formed on graphite surface due to the surface relief developed. The heat load to the inclined target surface (0.5 MJ/m^2) is below the melting threshold of tungsten. Thus the observed bright spots are not caused by W droplets. Corresponding high-speed imaging had proved that this luminosity can not also be attributed to carbon dust, which could be redeposited back to the surface in the end on plasma pulse.

The hot spots indicate the areas of enhanced evaporation and their luminosity is observed during ~ 30 ms after plasma impact. Size distributions of the hot spots are also presented in Fig.26 for time moments of t_1 and t_3. It was impossible to perform analysis of micro-spots with larger magnification while the target is in vacuum chamber. Nevertheless, most of registered spots are of ~ (0.1 - 0.5) mm in diameter, which is much larger than maximal size of the grains in MPG-7 graphite ((10 - 25) μm). Qualitatively the size distribution of the spots remains similar for different time moments after the end of pulse. The only number of overheated areas is decreased and luminosity of some spots disappears with time.

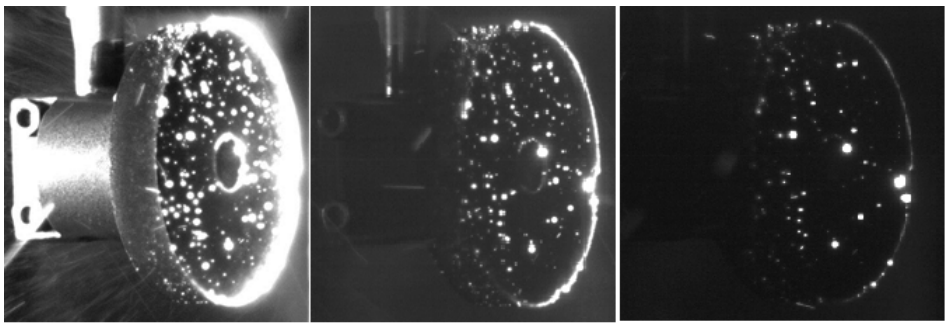

FIG. 25. Images of hot spots on graphite surface of combined W-C target (W rod of 1 cm in diameter surrounded by MPG-7 graphite of 8 cm in diameter) indicating overheated areas (1-3). Inclined impact $\alpha = 45^0$, t_{exp} = 0.5 ms, t_1= 0.7 ms, t_2 = 1.7 ms, t_3= 3.7 ms after pulse, Q_{surf} = 0. 5 MJ/m^2.

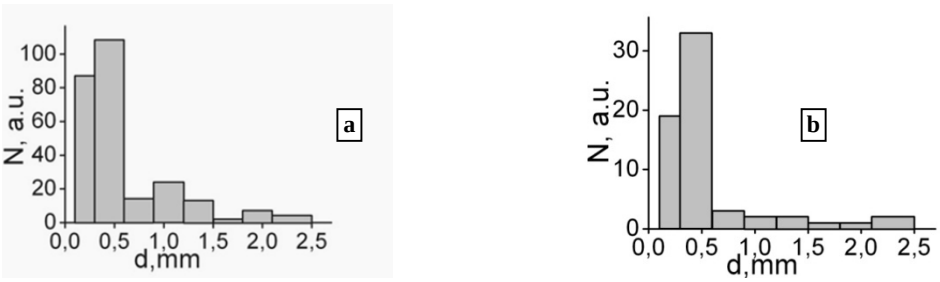

FIG. 26. Size distributions of hot spots at the moments of t_1 (a) and t_3 (b).

5. CONCLUSIONS

The performed experiments were concentrated on comparative studies of plasma surface interaction features under irradiation of different candidate materials of fusion reactor with high power plasma loads of variable parameters. The investigations were aimed to support mainstream fusion research in part of testing of radiation-resistant materials perspective for large thermonuclear devices of both types (with magnetic and inertial plasma confinement) and for plasma technologies. The performed activity included:

- Upgrade of existing experimental device on the base of magneto-plasma compressor (MPC) to create experimental stand for investigations on plasma-surface interaction.
- Optimization of plasma compression dynamics in MPC device. Measurements of plasma density and electron temperature in plasma focus region of MPC.
- Measurements of EUV and SXR radiation from the focus region.
- Comparative analysis of surface morphology after exposures of tungsten with QSPA Kh-50 and MPC. Analysis of the influence of pulse duration and irradiation dose (number of exposures) on the surface evolution of tungsten targets.
- Spectroscopic study of quasi-steady-state and pulsed plasma streams interaction with tungsten and carbon surfaces under high heat loads.
- Investigation of the melt layer properties and the surface structure after multiple plasma exposures, study of brittle mechanism of surface damage produced for tungsten targets.
- Analysis of compatibility of tungsten and carbon as divertor neighborhood components, namely carbon redeposition on tungsten surface and formation of tungsten carbides.
- Participation in joint experiments with dense plasma devices in Poland, taking part in workshops, schools (Kudowa Zdroj, Poland and Alushta, Ukraine), creation of joint database**.**

Magnetoplasma compressor (MPC) of compact geometry with conical-shaped electrodes having the stored energy in the discharge equal to 28 kJ was used in two operation modes of the plasma source: pulsed gas supply of Xe directly to the discharge area, which provides generation of pure Xe plasma stream, and pulsed injection of Xe to the plasma focus region during the MPC operation with He. Spectroscopic measurements of plasma density and electron temperature in compression region of MPC have been performed on the basis of Stark broadening of spectral lines and intensities ratio in visible wave-range.

Radial distributions of the plasma density were estimated using Abel inversion procedure. Dynamics of the discharge and time behavior of plasma focus were analyzed for both Xe and He-Xe plasma streams as well as for varied discharge voltage and time delays between the discharge and gas supply pulses. Measurements with AXUV photodiodes with different filters showed that the total radiated energy and peak power strongly depends on time delay between the gas supply start and the discharge ignition. It is shown that the maximum radiation intensity corresponds to the spectral range 12.2-15.8 nm. Plasma source efficiency was analyzed from electro-technical discharge characteristics. It shows that dense plasma streams of heavy noble gases generated by MPC device are important for different technological applications: EUV lithography, plasma thrusters, surface processing etc.

ELM-simulation experiments with QSPA Kh-50, largest and most powerful device of this kind, were focused on reproduction of necessary particle and energy loads, testing of

tungsten as fusion reactor material and comparisons of damage features for different regimes of exposures.

Cracking thresholds and crack patterns (of major- and micro-type) in tungsten targets as well as residual stress after repetitive plasma pulses have been studied for different W grades including deformed monolithic tungsten (Plansee AG), which is the ITER reference grade. The targets were preheated to different bulk temperatures T_o in a range of 200-600 °C, aiming at estimations of a ductile-to-brittle transition effect on the material cracking.

The cracking development is characterized by the measured threshold load and threshold target temperature, which determine the existing region of W performance without cracks. The energy threshold for the cracking development, for the QSPA Kh-50 pulse of the 0.25 ms duration and triangular shape, is found to be about 0.3 MJ/m^2. For lower heat loads there are no cracks, and the residual stress after the plasma pulse is below 300 MPa.

The DBT effects are experimentally estimated. The DBT-transition occurs in the temperature range of 200 ºC $\leq T_{DBTT} <$ 300 ºC for deformed W grade. For the initial temperature $T_0 > 300\ ^0$C no major cracks are formed on the exposed surface. Major cracks network forms only in cases of the initial target temperatures below DBTT. This network develops after the first plasma impacts and its further evolution is accompanied only by an increase in a crack width. Thus the deformed W material is found to be more resistive against cracking and grain losses as compared to other grades (sintered, rolled). However, once a major crack develops in the deformed W, it grows quickly and propagates transversely to the surface to the depth of about 400 μm along the grain boundary.

The micro-cracks network in our experiments was always attributed to the surface melting and following re-solidification. This is principal difference of plasma exposures in a comparison with the e-beam results reported recently. The probable reason is a volumetric heat deposition by e-beams with the maximal temperature appearing a few μm below the surface, while plasma load is transferred mostly to the surface. Typical cell sizes of the inter-granular micro-cracks network are within a range of 10–40 μm, which corresponds to the grain size of the W grade. The micro-cracks propagate along the grain boundaries surrounding the grains completely. A typical depth of the micro-cracks is 5-15 μm, and it is corresponds to the melt layer thickness.

The plasma irradiation results in a symmetrical tensile stress in a thin subsurface layer. The maximal residual stress in the plasma affected layer is reached after the first plasma pulses, and further pulses do not change the stress substantially. If the residual stress is below 300-350 MPa, the cracks do not develop. It is observed as a rule that an increase in the number of exposures decreases the residual stress. The residual stress does not depend practically on the initial target temperature and it grows significantly with increased thermal loads. It is found that under the similar loading conditions a magnitude of the residual stresses for the deformed tungsten material is smaller in a comparison with those observed for sintered samples and rolled W plates under similar conditions. It can be due to the combination of 2 factors: the initial compressive stresses existing in the deformed W grade, and its improved structure in a comparison with the sintered and rolled W grades.

Features of plasma-surface interaction and plasma energy transfer to the material surface are studied in ELM simulation experiments with QSPA Kh-50 in dependence on plasma heat loads. Plasma exposures of tungsten, graphite and different combined W-C

targets were performed with repetitive pulses of 0.25 ms in duration and the heat loads varied in the range of (0.2-2.5) MJ/m^2. Onset of vapor shield formation in front of the surface under ELM-like plasma loads was studied. Achievement of evaporation threshold for exposed targets resulted in almost saturation of the surface heat load with further increase of the plasma energy density. For tungsten targets the vapor shield and its influence on plasma energy transfer to the surface become clearly seen when the surface heat load achieved 1.1 MJ/m^2. The evaporation resulted in enhanced mass losses of tungsten, formation of erosion crater and bubbles on the surface.

Influence of carbon PFCs neighborhood on the plasma energy transfer to the tungsten surface was demonstrated. Carbon neighborhood resulted in protection of tungsten surface starting with lower heat loads. Carbon become to evaporate at (0.4 - 0.45) MJ/m^2 and its vapor shield formation resulted in additional decrease of heat loads to the tungsten surface (from 1.1 MJ/m^2 to (0.8 - 0.85) MJ/m^2) preventing tungsten evaporation.

High-speed imaging showed non-uniform surface heating and formation of overheated areas even for exposures of isotropic fine grain graphite MPG-7. Hot spots of ~ (0.1 - 0.5) mm were formed on graphite surface probably due to the surface relief developed. Hot spots indicated the areas of enhanced evaporation and their luminosity was observed during ~ 30 ms after plasma impact.

Plasma impacts caused the droplets splashing from the tungsten surface. Angular distribution of splashed droplets and dust particles was analyzed. Particles continued to be ejected from the surface after plasma impact during ~ 10 ms. Droplets velocities could achieve several tens m/s. Fast droplets were generated at earlier time moments. Smaller velocities corresponded to late stage of observation.

The obtained experimental results are used for validation of the PEGASUS 3D numerical code Results of QSPA plasma exposures are compared also with short pulse PSI experiments (τ~ 0.1-5 μs) performed with a pulsed plasma gun and dense plasma-focus facilities, aimed at studies of a surface damage and tungsten impurities behavior in near-surface plasma formed in front of the target.

REFERENCES

[1] TERESHIN, V.I., BANDURA, A.N., BYRKA, O.V., CHEBOTAREV, V.V., GARKUSHA, I.E., LANDMAN, I.S., MAKHLAY, V.A., NEKLYUDOV, I.M., SOLYAKOV, D.G., TSARENKO A.V., Application of powerful quasi-steady-state plasma accelerators for simulation of ITER transient heat loads on divertor surfaces. Plasma Phys. Control. Fusion, 49 (2007) A231-A239.

[2] MAKHLAY, V.A., BANDURA, A.N., BYRKA, O.V., GARKUSHA, I.E., CHEBOTAREV, V.V., TERESHIN, V.I., LANDMAN, I., Effect of preheating on the damage to tungsten targets after repetitive ITER ELM-like Heat Loads. Physica Scripta T.128 (2007) 239-241.

[3] CHEBOTAREV, V.V., GARKUSHA, I.E., LADYGINA, M.S., MARCHENKO, A.K., PETROV, YU.V., TRUBCHANINOV, S.A., Dynamics of nitrogen and xenon plasma streams generated by MPC divice. Problems of Atomic Science and Technology. Series: Plasma Physics, 1. (13) (2007) 104-106.

[4] GARKUSHA, I.E., BURDAKOV, A.V., CHEBOTAREV, V.V., IVANOV, I.A., KRUGLYAKOV, E.P., KUKLIN, K. N., LANDMAN, I., MAKHLAJ, V.A., POLOSATKIN, S.V., SHOSHIN, A.A., TERESHIN, V.I., Plasma-surface interaction during ITER transient events: simulation experiments with QSPA Kh-50 and GOL3 facilities. Problems of Atomic Science and Technology. Series: Plasma Physics. 6 (2008) 58-60.

[5] GARKUSHA, I.E., MAKHLAJ, V.A., CHEBOTAREV, V.V., LANDMAN, I., TERESHIN, V.I., AKSENOV, N.N., BANDURA, A.N., Experimental study of plasma energy transfer and material erosion under ELM-like heat loads. Journ. Nucl. Mater. 390-391 (2009) 814-817

[6] GARKUSHA, I.E., BANDURA, A.N., BYRKA, O.V., CHEBOTAREV, V.V., I. LANDMAN, V.A. MAKHLAJ, S. PESTCHANYI, V.I. TERESHIN. Damage to Preheated Tungsten Targets after Multiple Plasma Impacts Simulating ITER ELMs. Journ. Nucl. Mater. 386-388, (2009) 126-131.

[7] MAKHLAJ, V.A., GARKUSHA, I.E., LINKE, J. , PINTSUK, G., TERESHIN, V.I., BANDURA, A.N. , CHEBOTAREV, V.V. , STALTSOV, V.V., Exposures of EU W-CFC combined targets with QSPA Kh-50 plasma streams simulating ITER ELMS. Problems of Atomic Science and Technology. Series: Plasma Physics. 1, (2009) 58-60.

[8] MAKHLAI, V.A., GARKUSHA, I.E., BANDURA, A.N., BYRKA, O.V., CHEBORAREV, V.V., FEDORCHENKO, V.D., MEDVEDEV, A.V., TERESHIN, V.I.. Features of materials alloying under exposures to pulsed plasma streams. European Physical Journal D. 54, (2009) 185–188.

[9] GARKUSHA, I.E., ARKHIPOV, N.I., KLIMOV, N.S., MAKHLAI, V.A. , SAFRONOV, V.M., LANDMAN, I. , TERESHIN, V.I., Latest Results from ELM-simulation Experiments in Plasma Accelerators. Physica Scripta. T135 (2009) 014054

[10] MAKHLAI, V.A. , GARKUSHA, I.E., MALYKHIN, S.V. , PUGACHOV, A.T. , LANDMAN, I., LINKE, J. , PESTCHANYI, S. , CHEBOTAREV, V.V. , TERESHIN, V.I. , Residual Stresses in Tungsten under Exposures with ITER ELM-Like Plasma Loads. Physica Scripta. T135 (2009) 014060.

[11] PESTCHANYI, S., GARKUSHA, I., LANDMAN, I., Simulation of tungsten armour cracking due to small ELMs in ITER. Fusion Engg. and Design 85 (2010) 1697–1701.

[12] MARCHENKO, A.K., CHEBOTAREV, V.V., LADYGINA, M.S., GARKUSHA, I.E., PETROV, YU.V., SOLYAKOV, D.G., STALTSOV, V.V., TERESHIN, V.I., Compression zone formation in magnetoplasma compressor operating with heavy gases Problems of Atomic Science and Technology. Series: Plasma Physics 6 (2010) 94-96.

[13] MALINOWSKI, K., CZAUS, K., SADOWSKI, M.J., SKLADNIK-SADOWSKA, E., GARKUSHA, I.E., TERESHIN, V.I., Experimental studies of ion emission from RPI-IBIS facility and modeling of ion motions Problems of Atomic Science and Technology. Series: Plasma Physics 6 (2010) 208-210.

[14] GARKUSHA, I.E., LANDMAN, I., LINKE, J., MAKHLAI, V.A., MEDVEDEV, A.V., MALYKHIN, S.V., CHEBOTAREV, V.V., PESCHANYI, S., PUGACHEV, A.T., TERESHIN, V.I., Performance of Deformed Tungsten under ELM-like Plasma Exposures in QSPA Kh-50. Journal of Nuclear Materials 415 (2011) S65–S69.

[15] SHOSHIN, A.A., BURDAKOV, A.V., CHEBOTAREV, V.V., GARKUSHA, I.E., IVANOV, I.A., KUKLIN, K.N., MAKHLAJ, V.A., MARCHENKO, A.K., POLOSATKIN, S.V., TERESHIN, V.I., Plasma-Surface Interaction During ITER Type 1 ELMs: Comparison of Simulation with QSPA KH-50 and the GOL-3 Facilities. Fusion Science and Technology. 59, 1t (2011) 57-60.

[16] BANDURA, A.N., BYRKA O.V., CHEBOTAREV, V.V., GARKUSHA, I.E., MAKHLAY, V.A., TERESHIN, V.I., SKOBLO, T.S., PUGACH, S.G. Alloying and Modification of Structural Materials under Pulsed Plasma Treatment. International Journal of Plasma Environmental Science & Technology,.5, No 1, (2011) 2-6.
[17] PESTCHANYI, S., GARKUSHA, I., LANDMAN, I.. Simulation of residual thermostress in tungsten after repetitive ELM-like heat loads. Fusion Eng. Des. (2011), doi:10.1016/j.fusengdes.2011.01.034.
[18] MAKHLAJ, V.A., GARKUSHA, I.E. , BYRKA, O.V. , CHREBOTAREV, V.V. , LANDMAN I.S. , LEBEDEV, S.I. , MALYKHIN, S.V. , PUGACHEV, A.T., SHEVCHUK, P.B., TERESHIN, V.I., Influence of hydrogen and helium plasma streams exposures on modification of tungsten structure under powerful transient loads. Problems of Atomic Science and Technology. Series: Plasma Physics. 1 (2011) 71-73.
[19] BANDURA, A.N. , BYRKA, O.V. , GARKUSHA, I.E. , LADYGINA, M.S. , MARCHENKO, A.K. , PETROV, YU.V. , SOLYAKOV, D.G. , CHEBOTAREV, V.V. , CHUVILO A.A., Characteristics of plasma streams and optimization of operational regimes for magnetoplasma compressor. Problems of Atomic Science and Technology. Series: Plasma Physics № 1 (2011) 68-70.
[20] PETROV, YU.V. , GARKUSHA, I.E. , HASSANEIN, A., SOLYAKOV, D.G. , MARCHENKO, A.K. , CHEBOTAREV, V.V. , LADYGINA, M.S. , STALTSOV, V.V. , YELISYEYEV, D.V., Diagnostic system for EUV radiation measurements from dense xenon plasma generated by MPC. Problems of Atomic Science and Technology. Series: Plasma Physics № 1. (2011) 185-187.
[21] MARCHENKO, A.K., GARKUSHA, I.E., CHEBOTAREV, V.V., LADYGINA, M.S., PETROV, YU.V., SOLYAKOV, D.G., TERESHIN, V.I., AKSENOV, N.N., STALTSOV, V.V., HASSANEIN, A., SKLADNIK-SADOWSKA, E., Features of plasma focus formation in different operation modes of gas-discharge magnetoplasma compressor. Acta Technica, 56, (2011) T113-122.
[22] BYRKA, O.V., BANDURA, A.N., GARKUSHA, I.E., MAKHLAI, V.A., TARAN, V.S., TERESHIN, V.I., Application of pulsed plasma streams for surface modification of constructional materials. Acta Technica, 56 (2011) T362-T372.
[23] LADYGINA, M.S., GARKUSHA I.E., MARCHENKO, A.K., MAKHLAI, V.A., SADOWSKI, M.J., SKLADNIK-SADOWSKA, E., AKSENOV, N.N., TERESHIN, V.I.. Spectroscopy of Plasma Surface Interaction in Experiments Simulating ITER Transient Events. Fusion Science and Technology 60 /1t (2011) 27-33.
[24] SKLADNIK-SADOWSKA, E., MALINOWSKI, K., SADOWSKI, M.J., KUBKOWSKA, M., JAKUBOWSKA, K., PADUCH, M., SCHOLZ, M., GARKUSHA, I.E., LADYGINA, M., TERESHIN, V. I. Optical Spectroscopy of Free-Propagating Plasma and Its Interaction with Tungsten Targets in PF-1000 Facility. Contrib. Plasma Phys. 51, No. 2-3, (2011) 288-292.
[25] TERESHIN, V.I., CHEBOTAREV, V. V., GARKUSHA, I. E., LANDMAN, I. S., MAKHLAJ V. A., Application of Quasi-Steady-State Plasma Streams for Material Studies AIP Conference Proceedings PLASMA 2007: 4th German-Polish Conference on Plasma Diagnostics for Fusion and Applications; 6th French-Polish Seminar on Thermal Plasma in Space and Laboratory. V. 993. 2008 P. 371-378.
[26] GARKUSHA, I.E., MAKHLAJ., V.A., CHEBOTAREV, V.V., LANDMAN, I., TERESHIN, V.I.. Experimental study of plasma energy transfer to the material surfaces under ELM-like loads. Proc of PSI-18, Toledo, Spain May 2008, p.195.
[27] GARKUSHA, I.E., CHEBOTAREV, V.V., HASSANEIN, A., LADYGINA, M.S., MARCHENKO, A.K., PETROV, YU.V., SOLYAKOV, D.G., TERESHIN, V.I., TRUBCHANINOV, S.A.. EUV Radiation of Xenon Plasma Streams Generated by

Magnetoplasma Compressor. 35th EPS Conference on Plasma Phys. Hersonissos, 9 - 13 June 2008 ECA Vol.32 (2008) , P-2.170.
[28] MAKHLAY, V.A., GARKUSHA, I.E., BANDURA, A.N., BYRKA, O.V., CHEBORAREV, V.V.. FEDORCHENKO, V.D., MEDVEDEV, A.V., TERESHIN, V.I., Features of materials alloying under exposures to pulsed plasma streams. Proc. 18 SPPT, Prague, Czech. Rep.June 2008, p.158.
[29] GARKUSHA, I.E., PETROV, YU.V., SOLYAKOV, D.G., CHEBOTAREV, V.V., HASSANEIN, A., LADYGINA, M.S., MARCHENKO, A.K., TERESHIN, V.I., TRUBCHANINOV, S.A., Characterization of Dense Xe and He-Xe Plasma Streams Generated by Magnetoplasma Compressor. Proc. 18 SPPT, Prague, Czech. Rep.June 2008, p.44.
[30] GARKUSHA, I.E., CHEBOTAREV, V.V., HASSANEIN, A., LADYGINA, M.S., MARCHENKO, A.K., PETROV, YU.V., SOLYAKOV, D.G., TERESHIN, V.I., TRUBCHANINOV, S.A., BYRKA, O.V., Dynamics of Xenon Plasma Streams generated by Magnetoplasma Compressor. In book "PLASMA-2007" edited by H-J. Hartfuss, M. Dudeck, J. Musielok, M.J. Sadowski. AIP CP 993 (2008) p.341-344.
[31] GARKUSHA, I.E., ARKHIPOV, N.I., KLIMOV, N.S., MAKHLAI, V.A., SAFRONOV, V.M., LANDMAN, I., TERESHIN, V.I., Latest Results from ELM-simulation Experiments in Plasma Accelerators. 12th Int. Workshop on Plasma-facing Materials and Components PFMC-12, Juelich, Germany.11-14 May,2009, p.20. Invited talk.
[32] MAKHLAI, V.A., GARKUSHA, I.E., MALYKHIN, S.V., PUGACHOV, A.T., LANDMAN, I., LINKE, J., PESTCHANYI, S., CHEBOTAREV, V.V., TERESHIN, V.I., Residual Stresses in Tungsten under Exposures with ITER ELM-Like Plasma Loads. 12th Int. Workshop on Plasma-facing Materials and Components PFMC-12, Juelich, Germany.11-14 May,2009, p.91.
[33] PETROV, YU.V., GARKUSHA, I.E., CHEBOTAREV, V.V., HASSANEIN, A., LADYGINA, M.S., MARCHENKO, A.K., SOLYAKOV, D.G., Generation of dense magnetized plasma with compact magnetoplasma compressor. 18th TCM IAEA on using small fusion devices. Alushta, Ukraine, Sept.,2008. Rep. DPE-5, p. 19.
[34] TERESHIN, V.I., BANDURA, A.N., BYRKA, O.V., CHEBOTAREV, V.V., GARKUSHA, I.E., LANDMAN, I., MAKHLAJ, V.A., SOLYAKOV, D.G. Simulation of ITER Transient Heat Loads to the Divertor Surfaces with Using the High Power Quasi-Steady-State Plasma Accelerator. Proc. IAEA Fusion Energy Conference, Geneva, October 2008.
[35] PESTCHANYI, S., GARKUSHA, I., Landman, I. Simulation of Tungsten Armour Cracking Due to Small ELMs in ITER. 9th International Symposium on Fusion Nuclear Technology (ISFNT-9) Dalian, China, October 11-16, 2009, PO3-043.
[36] GARKUSHA, I.E., CHEBOTAREV, V.V., LADYGINA, M.S., MARCHENKO, A.K., PETROV, YU.V., SOLYAKOV, D.G., TERESHIN, V.I., YELISEEV, D.V., HASSANEIN, A.. Dynamics of Dense Xe Plasma Generated by MPC and Features of EUV Radiation from Compression Zone. Proc. Sixth International Conference on Plasma Physics and Plasma Technology (PPPT-6), Minsk, 2009, P4-8.
[37] LINKE, J., GARKUSHA, I., MAKHLAJ, V., PINTSUK, G., RITZ, G., RODIG, M., SCHMIDT, A., THOMSER, C., TERESHIN, V., Simulation of plasma-wall interaction processes in future thermo-nuclear fusion reactors with energetic particle beams. Ukrainian-German Symposium on Accelerators for Advances in Materials Science and Medical Radionuclide Production. Kharkov, Oct.27-29, 2009, p.24-25.
[38] GARKUSHA, I.E., AKSENOV, N.N., CHEBOTAREV, V.V., LANDMAN, I., LINKE, J., MAKHLAJ, V.A., TERESHIN, V.I., PUGACHOV, A.T., MALYKHIN, S.V.,

Studies of Plasma-Surface Interaction under QSPA Kh-50 Plasma Exposures Simulating ITER Transient Events. Proc. Sixth International Conference on Plasma Physics and Plasma Technology (PPPT-6), Minsk, Sept.2009, P38-42.

[39] GARKUSHA, I.E., LANDMAN, I., LINKE, J., MAKHLAI, V.A., MEDVEDEV, A.V., MALYKHIN, S.V., CHEBOTAREV, V.V., PESCHANYI, S., PUGACHEV, A.T., SADOWSKI, M., SKLADNIK-SADOWSKA, E., TERESHIN, V.I., Experimental Simulation of ITER ELMs Impacts to the Tungsten Surfaces with QSPA Kh-50. Synopsis of Twenty-Third IAEA Fusion Energy Conference, 10 - 16 October 2010, Daejon, Republic of Korea.

[40] BAZYLEV, B., LANDMAN, I., PESTCHANYI, S., IGITKHANOV, YU., LOARTE, A., PITTS, R., LEHNEN, M., SAFRONOV, V., PODKOVYROV, V., KLIMOV, N., GARKUSHA, I., MAKHLAY W. Simulations of Material Damage and high Energy Fluxes to ITER Divertor and First Wall during Transients and Runaway Electron Loads. Proc. of Twenty-Third IAEA Fusion Energy Conference, 10 - 16 October 2010, Daejon, Republic of Korea ITR/P1-08.

[41] MAKHLAJ, V.A., GARKUSHA, I.E., AKSENOV, N.N., CHUVILO, A.A., LADYGINA, M.S., LANDMAN, I., LINKE, J., MALYKHIN, S.V., PESTCHANY, S., PUGACHEV, A.T., SADOWSKI, M.J., SKLADNIK-SADOWSKA, E., Simulation of ITER ELM'S impacts to the divertor surfaces with plasma accelerators 13-th International Workshop on Plasma Facing Materials and Components for Fusion Applications. 1-st International Conference on Fusion Energy Materials Science, May 9–13, 2011, Rosenheim, Germany, accepted for Physica Scripta.

DEVELOPMENT OF THE PF-6 DEVICE FOR THE GOAL OF THE MAINSTREAM FUSION RESEARCH AND SPIN-OFF APPLICATIONS; MEDICINE, BIOLOGY, MATERIAL SCIENCES ETC.

S. JEDNORÓG[*], V.A. GRIBKOV[*,**,***], M. SCHOLZ[*,**], L. KARPINSKI[*,**], M. PADUCH[*], E. ZIELINSKA[*], V.N. PIMENOV[***], E.V. DEMINA[***], A.V. DUBROVSKY[***], S.V. MASLYAEV[***], E. SKLADNIK-SADOWSKA[+]

[*] Institute of Plasma Physics and Laser Microfusion, Warsaw, Poland
[**] International Centre for Dense Magnetized Plasmas, Warsaw, Poland
[***] A.A. Baikov Institute of Metallurgy and Material Science, Moscow , Russian Federation
[+] The Andrzej Soltan Institute for Nuclear Studies, Warsaw, Poland
Email: jednorog@ifpilm.waw.pl

Abstract

In the framework of the Project we have elaborated a new design of the electrical circuit (in co-operation with *ICTP*) to increase the repetition rate *f* of the operational regime of PF-6 device till the level: U = 23 kV, E = 7.4 kJ, f = 5 Hz. With this power supply we have elaborated and tested our new DPF chambers able to work with the deuterium-tritium mixture as a working gas. We have developed, implemented and tested new diagnostics of X ray and neutron pulses with temporal resolution 0.3 ns and 16-frame 1-ns laser interferometry. In cooperation with our partners on this IAEA CRP we provided radiation tests of materials candidate for the main-stream fusion reactors (tungsten, CFC, ceramics Al_2O_3 and NB, low-activation steels, etc.) using besides the PF-6 facility the Dense Plasma Focus devices PF-5M, ING-103 and PF-1000. In addition with the same partners we undertake initial experiments with an aim to improve characteristics of the surface layer of materials (mechanical and tribological behavior, radiation resistance, etc.) using the above devices. The idea is to use *hot* plasma streams and beams of *fast* ions generated in DPF in treatment of internal hard-to-reach compartments of the machine components. In cooperation with Pirelli we have provided first experiments in the field of X ray dynamic quality control with DPF aimed to disclosure imperfections in car tyres. Also we spread our previous X ray based experiments on pulsed radio-enzymology to the pulsed *neutron* irradiation of enzymes and other bio-test objects. We have provided experiments intended to detect large-volume objects containing illegal substances (explosives, drugs, etc.) and first experiments on irradiation by neutron pulses a fuel element containing fissile materials by means of time-of flight neutron technique. These experiments give an opportunity to use DPF in a single-shot technique of unveiling illegal materials hidden in a luggage or in containers.

1. INTRODUCTION

The PF-6 apparatus [1] belongs to a class of Z-pinch devices known as Dense Plasma Focus (DPF). It is manufactured on a base of modern technology and it is one of the most effective DPF of medium size operating with deuterium as a working gas and, consequently, producing fusion neutrons of 2.5 MeV energy with parameters: total yield per shot – 10^9, pulse duration – about 10 ns, maximal neutron flux attainable at the chamber wall ~ 10^{14} n/cm^2·s. Simultaneously this DPF generates soft ($E_{h\nu} \approx$ 0.1-3.0 keV), medium ($E_{h\nu} \approx$ 3.0-10.0 keV) and hard ($E_{h\nu} >$ 10 keV) X ray flashes. The pulse of the hard component with photon energy in the range 40-200 keV has the overall yield up to 10 J and pulse duration ~ 10 ns. Besides the PF-6 device produces powerful beams of fast ions and electrons (energy ~ 100 keV) and hot plasma streams (temperature $\leq$ 1 keV) ensuring a power flux density on the target placed either in cathode or in anode parts of the DPF chamber in the range up to 10^{10}-10^{12} W/cm^2. Such high values make this compact device a very attractive instrument for different applications. We implement it for testing of materials perspective for use in the mainstream fusion reactors of both types (with magnetic and inertial plasma confinement), for modification of materials surface layers to impart them better characteristics (hardness, corrosion and radiation resistance, etc.), for applying it in a single-shot dynamic quality control of machines and their parts during operation as well as in the detection of hidden object in the airport luggage, for various experiments in biology and medicine, etc. Before start of this IAEA CR Project this device was able to produce 1 shot per 20 s only (i.e. its repetition rate was about 0.05 cps).

In the contemporary main-stream fusion researches a deuterium-tritium (DT) mixture as a working gas is already used both for filling tokamak chambers (JET) (Magnetic Plasma Confinement – MPC) and for manufacturing capsule for laser fusion (Rochester Uni., LLNL) (Inertial Plasma Confinement – IPC). In spite of the successful development of the above-mentioned fusion programs the problems, which present a serious challenge and must still be resolved in future in both fusion reactor types, are as follows.

1) Plasma facing materials must withstand extremely high temperatures for years on end. These materiasls crack because of the heat loads and absorption of hydrogen isotopes.

2) Construction materials are turned brittle by the high-energy neutrons coming from fusion reactions.

3) Future Laser and Z-pinch (IPC) reactors will produce powerful intermittent blasts of plasma equal to about several hundred kg of TNT in tens of nanoseconds; chamber and blanket materials must withstand such spasmodic very powerful loads exceeding presently generated in such systems by about 6-7 orders of magnitude.

4) MPC-based systems must maintain plasma for weeks, not seconds as now; it exceeds presently achieved time intervals by circa 6 orders of magnitude.

5) Cost of each shot in reactors with IPC – amortization and target price – must not exceed a few US$. Meantime just a single target capsule used presently in Laser Fusion in a scheme of hohlraum with fast ignition costs about $1 million – again 6 orders.

6) Possibilities of production of initial quantity of tritium for a fusion reactor (100-1000 kg) and of its extended reproduction in a course of the reactor functioning are uncertain.

All these and some other considerations result now in a renovation of interest to hybrid and symbiotic energetic reactors combining fusion and fission reactions in various schemes, which were vividly discussed in the end of previous century. Certain preferences of this concept using fissile blanket for fusion-based neutron-producing core against pure fusion are lower demands to efficiency of fusion reactor and consequently lower power, size and price of the thermonuclear reactor. Its advantage versus fission concept is sub-criticality of the system (i.e. higher safety). This direction of research demands experimental data on interaction of 14-MeV neutrons with fissile materials.

Experiments provided in the full-energy devices to resolve the above-mentioned problems with large amount of tritium are very expensive and dangerous. Meanwhile some of them can be resolved with a small-scale fusion device operated with DT working mixture. DPF device is one of the most convenient facilities which can be used for this aim. In particular it is so for the new type of DPF chambers, which are sealed, have a built-in D-T generator and present “a radioactive source on demand” (a push-button device). Such a fusion device can be considered as a “closed or sealed radiation source”. Thus it is a question of vital importance if the idea “To make heavy science by light technology” appears to be real with DPF. However experience with DT-operational DPF is rather poor up to now. Data on interaction of 14 MeV neutrons with real fission fuel elements are also meagre. In this CRP we undertake efforts to make PF-6 a repetitive device, to equip it with modern diagnostics, and to clarify its opportunities opened in the above mentioned directions.

2. MODERNIZATION WORKS AT THE PF-6 DEVICE

2.1. Generator of the PF-6 device

The device’s modernization was devoted to a reconstruction of this multifunctional Dense Plasma Focus facility (Fig. 1) with the bank energy of 7 kJ to make it more fitted to different applications, to provide a capability to work with a repetition rate up

to 5 Hz and to ensure a possibility to operate with D-T mixture as a working gas for production of 14 MeV neutrons.

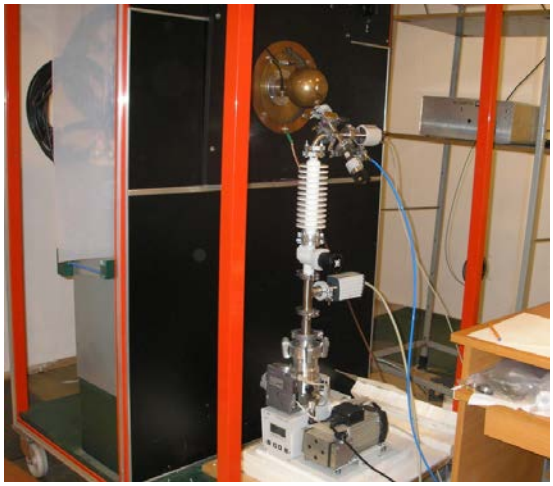

FIG. 1. PF-6 device – front view.

To increase a repetition rate up to frequency f = 5 cps we have elaborated a new electrical circuit. We increased a power of our charger (see Fig. 2) and we have substituted our separation resistors (Fig. 3*a*) by inductive coils (Fig. 3*b*). In this case from one side the inductances of these separating coils will prevent any hazardous consequences in a case of breakdown of some capacitor (i.e. preventing the discharge of the whole battery into a single problematic capacitor), thus providing the same function as it was meant for the previously used resistors. This functionality will be ensured by the reactive impedance of each of these coils $X_L = \omega L >> X_{DPF}$, where ω – characteristic frequency of the discharge, L – inductance of our new coils, and X_{DPF} is an impedance of the DPF chamber.

From the other hand having a very low active resistivity these coils will not restrict the charging current thus giving a possibility to increase repetition rate of our device up to 5 Hz with the same charger.

FIG. 2. A new powerful charger of the PF-6 device that is able to ensure a repetition rate of it equal to 5 Hz.

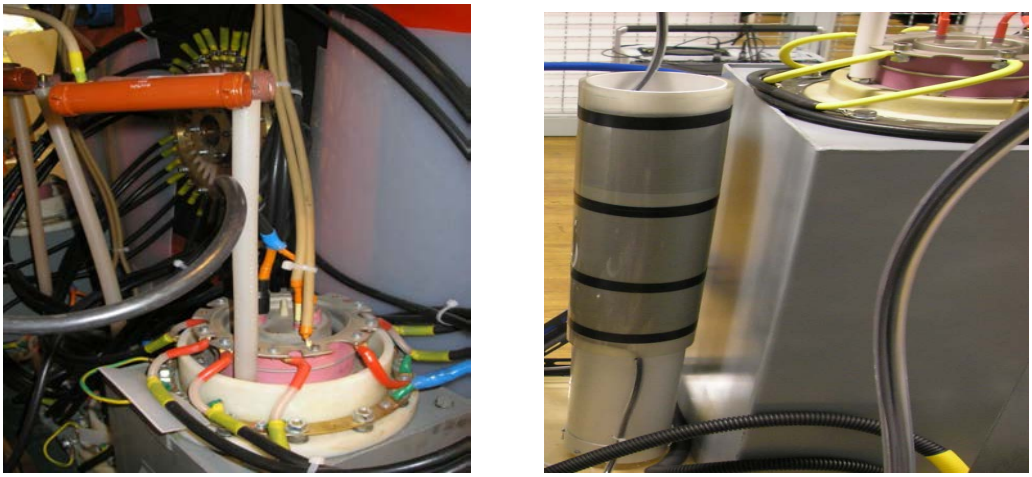

a) b)

b)

FIG. 3. Substitution of separating resistors (a) by inductive coils (b).

2.2. D-T chambers of PF-6

At the same time we have elaborated (in cooperation with the Moscow Physical Society – *MPS*) designs of 2 DPF chambers (for energy supply 3 and 7 kJ) filled with deuterium-tritium mixture by means of built-it hydrogen isotopes generators and won a contract with the N.L. Dukhov All-Russian Institute for Automation (*VNIIA*) to manufacture them. We received a license from the National Atomic Energy Commission of Poland giving us a permission to work with deuterium-tritium mixture as a working gas of DPF. We conclude an agreement for mutual work with the A. Soltan Institute for Nuclear Studies (*INS*), Poland, to exploit these tritium-containing chambers supplied to the PF-6 device and to work with fuel elements containing fissile materials. We have also prepared a special work-place in this Institute for the experiment with PF-6 with these DPF chambers and fuel elements.

2.3. Diagnostics

We have tested new diagnostics of X ray and neutron pulses (in cooperation with ACS Laboratories, Poland) having higher temporal resolution. The new CCD-based apparatus gave us the duration of the rise-time of hard X ray pulse equal to 0.3 ns (see Fig. 4). This value is an order of magnitude shorter than previously measured with conventional photomultiplier tubes plus plastic scintillator (PMT+S).

In the CCD-based detector our scintillator was of 1-cm thickness whereas in the PMT+S detector its length was 5 cm. So in our subsequent works we used the first technique for characterization of the source itself whereas the second one having much higher sensitivity – for collecting of wanted neutrons as many as possible.

3. RADIATION MATERIAL SCIENCE EXPERIMENTS

3.1. Introduction

It was shown in the experiments, the results of which were reported in [2-6], that the irradiation of solid-state targets by pulsed streams of fast ions (FI) and high-temperature plasma (HTP) in the devices of the plasma accelerator type makes it possible to perform a powerful impact on their surface layer (SL), to change its composition, structure and

properties. We provided our experiments described below by using PF-6 device and PF-1000 facility, the last one – in cooperation with our colleagues from ICDMP.

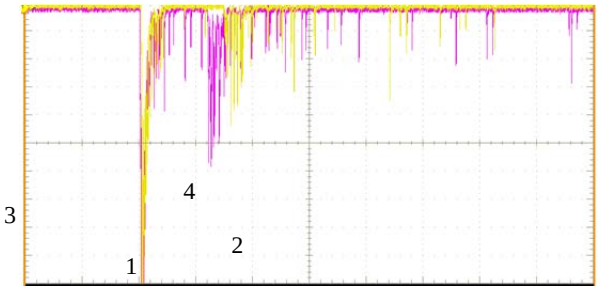

a). Time, 100 ns per division.

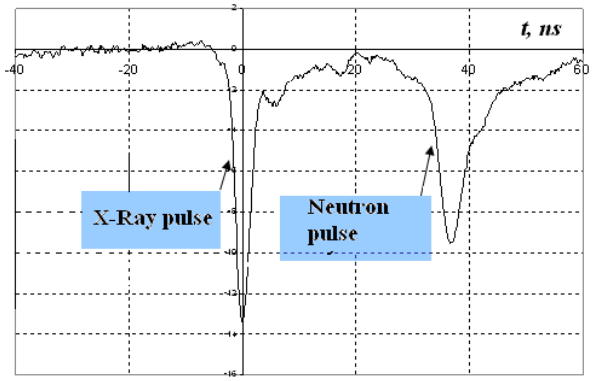

b). Time, 20 ns per division.

FIG. 4. Oscilloscope traces of pulses of X rays and neutrons generated by DPF and registered by a detector with a scintillator having time resolution equal to 0.275 ns (a): groups of individual flashes produced inside a scintillator by each hard X ray photon (i.e. by photoelectron) (1) and 14 MeV neutron (i.e. by recoil proton) (2) during the time intervals when the radiations have low intensities; their merged parts (3) and (4) correspondingly, which were registered during the period of their high intensities; red and yellow traces refer to two detectors placed at slightly different distances from the source (6 and 7 meters accordingly); the same traces (b) for the distance of about 2 m but for temporal resolution of PMT+S of 1.3 ns.

An accelerator device of the DPF type is able to generate directed streams of fast ions with the energy E_i ~ 100 keV and of plasma with the temperature T_{pl} ~ 0.3-1.0 keV of very high power (up to ~ P ~ 10^{12} W/cm^2). This makes possible to use the devices of the DPF type with the relatively low power supply (5-500 kJ) in comparison with the full-scale prototypes of reactors of the above types (with MPC and IPC) for modeling the conditions on the first wall of the latter [7, 8] exactly by the same radiation types and with the identical parameters.

Thus ensuring the maximum values of the streams of the radiation types specified above makes it possible to perform tests of materials, which can be used in control fusion reactors of both types – with magnetic and inertial plasma confinement (MPC and IPC, respectively). In these our experiments in the framework of the current IAEA CRP we have tested tungsten and CFC materials as well as two type of ceramics – BN and alumina – used in spherical tokamaks for insulation of antenna placed inside the discharge chambers.

At the same time, at the optimum choice of the irradiation mode it is possible to get a modified SL with improved mechanical and corrosion properties, as well as with higher radiation stability of the irradiated material. In our previous works during the fulfillment of the IAEA CRP “Integrated approach to Dense Magnetized Plasma applications in nuclear fusion technology” we have shown [6*a*] that by using a DPF device it is possible to modify

both the external SL of the processed product and its parts, which are not easily accessible. In particular, it was demonstrated by the example of the irradiation of hollow tubes, made of low activated austenitic steels that it is possible to create a strengthened modified SL both along the external and internal surfaces of a rather extended tube cavity. The relevant changes of the structural-phase state of the irradiated surface along with the possibility of the ion-plasma doping of the surface layers opens new prospects for the improvement of mechanical and physicochemical properties of the material.

However in those experiments we marked a narrow zone of anomalous damage of the internal surface of the tubes. Now we have investigated this phenomenon that was observed both with stainless steel and copper when the tubes were placed along the axis of the DPF chamber in front of the anode [6*b*]. At first we shall discuss physical processes occurring inside the DPF chamber above the pinch as well as at the pulsed action of the powerful streams of hot plasma and fast ions upon flat targets or on the internal and external SL of steel and copper tubes installed along the DPF chamber axis at the cathode part of it.

3.2. Dynamics of the discharge at the cathode part of a DPF

3.2.1. Dynamics of fast ion and hot plasma streams at the cathode part of a DPF

Physical processes taking place during hydrodynamic and kinetic stages of the Dense Plasma Focus dynamics at the PF-1000 facility were investigated in the work [9]. The schematic of the generation and the subsequent dynamics of the streams of fast ions and HTP, formed in the DPF device, are shown in Fig. 5.

First, a cumulative stream of the hot plasma (T_{pl} = 300-1000 eV) is formed at the axis of the chamber *Z* as a result of the non-cylindrical implosion of the current-plasma shell (CPS). It propagates along this axis from the anode at the velocity of > 10^7 cm/s and pushes a shock wave (SW) in gas in front of it [9*a*]. Then in 30-150 ns (depending on the size of the device) a plasma diode is formed on a pinch [9*b*]. At this moment fast electron beams are generated inside the diode, directed to the anode. Afterwards fast ion beams substitute the e-beams and propagate along the cumulative stream (the energy of the particles of both sorts is on the order of 100 keV). Inside this hot and dense plasma cloud both charge and current neutralization for the ion beam is occurred. It is so because of much higher plasma density compared with the density of fast ions and due to back current induced by the ion beam in plasma (which is a wake electron current in this case). The ion beam comes up with SW and at a certain moment passes through its front. Before this moment the fast ion beam has a double cone-shaped structure (the opening angle of cones enclosed in each other is of approximately 25-35 and 5-7°) with the main energy of the beam concentrated in the internal (narrow) cone.

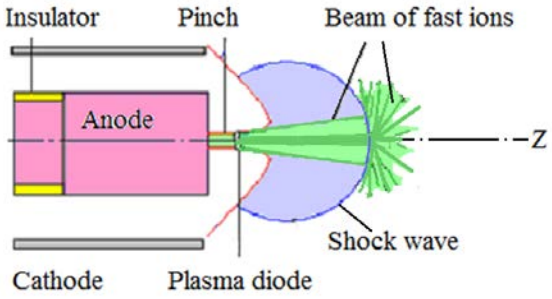

FIG. 5. Dynamics of hot plasma and fast ion streams at the cathode part of a DPF chamber.

The energy in the moving bunch of the hot plasma and in the stream of fast ions is determined by the efficiency of their generation in the DPF. The coefficient of efficiency of the formation of each of them is on the order of several percent from the total energy supply of the capacitor bank of the DPF. Taking into account the short duration of the HTP and fast ion pulses, it is easy to estimate the power flux density of these radiations on the target surface. When it is perpendicular to these streams (flat target perpendicular to the *Z* axis), the power flux densities vary within 10^6-10^{12} W/cm^2 depending on the distance of the target from the anode and the battery supply of the DPF device.

The magnitude of the current of our ion beam exceeds the Alfven-Lawson limit [10]. That is why after the penetration through the SW front (about 10–20 cm from the pinch and 20–30 cm from the anode outlet) into a low-density neutral gas, this beam cannot propagate as a narrow beam and it also acquires a hemispherical shape similar to the SW front (see Fig. 5). If the distance of the target (specimen) from the anode outlet is shorter than that mentioned above (not more than 30 cm in the described experiments), the interaction of the central part of the ion beam can be localized within the spot of about 1–2 cm in diameter. In this case, the secondary (ablation) plasma can have the same transversal size.

To check this specified pattern of the interaction and to confirm the above estimates of the flux densities, a preliminary experiment was performed with a flat target. In these experiments we placed thin (the thickness is of 1.5 mm) steel and thick (5 mm) tungsten targets having the shape of plates in front of the chamber anode and perpendicular to the Z axis. The distances from the anode's lid were 10-15 cm.

Sixteen-frame laser interferometry (the exposure time and time of the synchronization accuracy were 1 ns, time intervals between frames were 10…20 ns) has shown that secondary plasma is formed on the whole frontal plane of the target. Its transparency to the laser radiation and the propagation velocity (on the order of 10^7 cm/s) indicate that the temperature in it is on the order of several hundreds of electron volts.

Examination of the surface relief of the flat targets gave us an opportunity to find the beam's contour trace – the "autograph" as it is called in the technique of high-current beams. The diameter of the spot, recording the most powerful component of the fast ion beam on the tungsten plate, located at the distance of 10 cm from the anode, was about 12 mm (Fig. 6). This gives the angle of the beam divergence of about 7° that is close to the angle recorded in [9] from the self-luminescence of the ion beams in plasma.

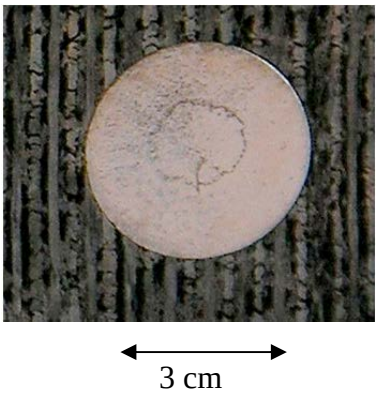

FIG. 6. An "autograph" of the beam of fast ions on the surface of a tungsten target.

However when we put our plate of stainless steel at a distance about 50 cm from the anode lid we found that the most powerful part of the beam of fast ions (FIB) is already disintegrated in a manner shown in Fig. 5. So the surface of the plate has a large spot as a consequence of irradiation by HTP and FIB without small “autograph” as shown in Fig. 7.

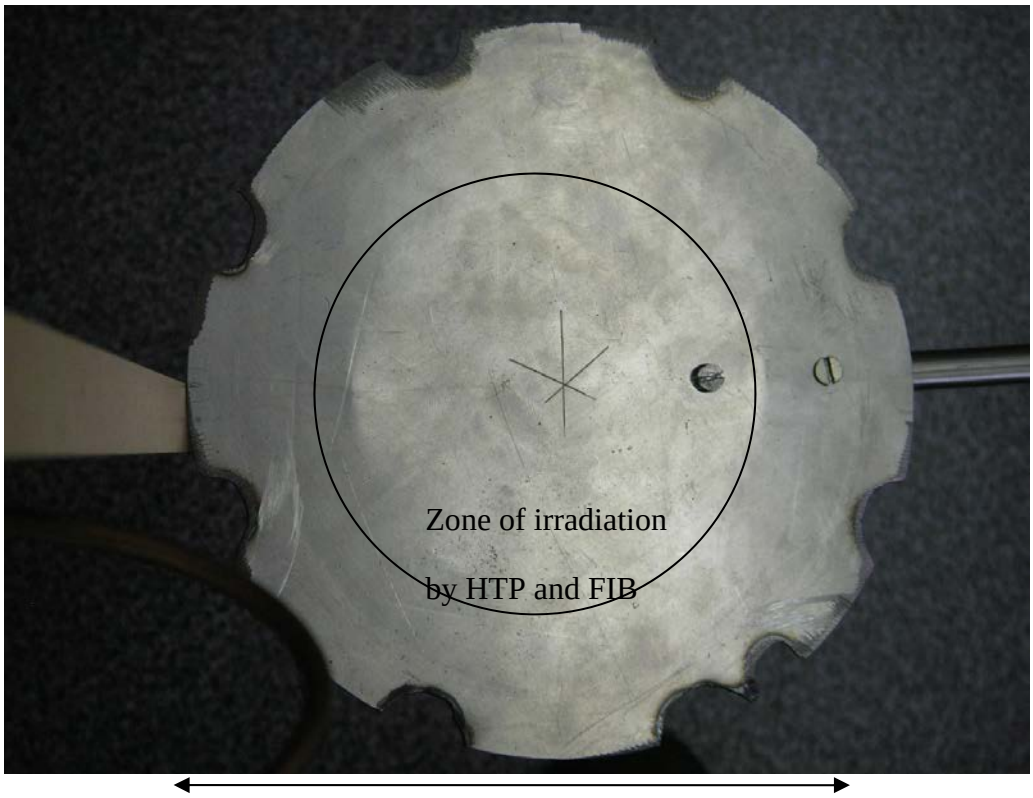

FIG. 7. Stainless steel disc placed at a distance of about 50 cm from the anode lid with the large spot produced by streams of high temperature plasma and fast ions.

3.2.2. Plasma dynamics during the late stages of the DPF discharge

Experimental studies of plasma dynamics were also performed during later stages of the PF-6 and PF-1000 operation (up to 30 and 100 μs after the pinch formation, i.e. during the whole damping oscillating discharge of the both banks having half-periods of about 3 and 16 μs correspondingly). Measurements carried out by laser interferometry (with a temporal resolution of 1 ns), by the magnetic probe technique (four probes) and by optical spectrometry (with a resolution of 0.5–1 μs) [5, 6] showed that after the ‘powerful stage’ described above, the plasma between the anode and the irradiated specimen is disconnected from the bank and exists as a toroidal structure until the end of the whole discharge as it shown in Fig. 8.

Spectroscopic measurements were carried out perpendicular to the *z*-axis, at different distances from the central electrode, by means of a Mechelle R 900 spectrograph operated within a wavelength range from 300 nm to about 1100 nm and equipped with a CCD camera.

The linear Stark broadening of deuterium Balmer lines, and particularly that of the $D_ß$ (486 nm) line, was used to estimate the plasma electron concentration after the PF pinch phase. These measurements were verified by laser interferometry. To determine the plasma

temperature evolution in time, the Inglis–Teller method was used. In Fig. 9, one can see temporal changes of these parameters, as measured for the secondary plasma produced on the surface of the irradiated specimens.

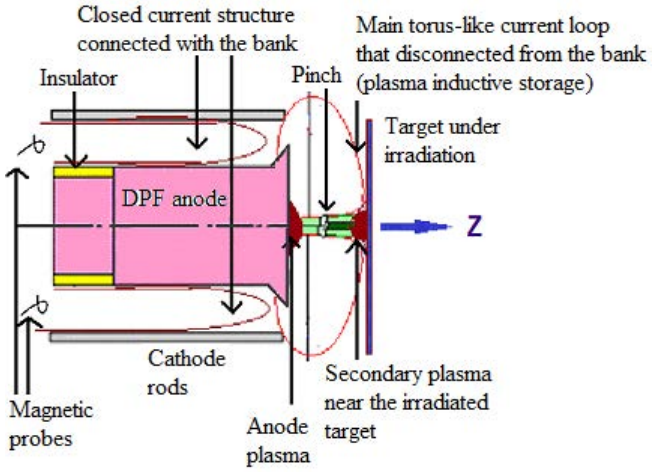

FIG. 8. A schematic showing current configurations inside the DPF after secondary breakdown between ends of cathode rods and anode's edge.

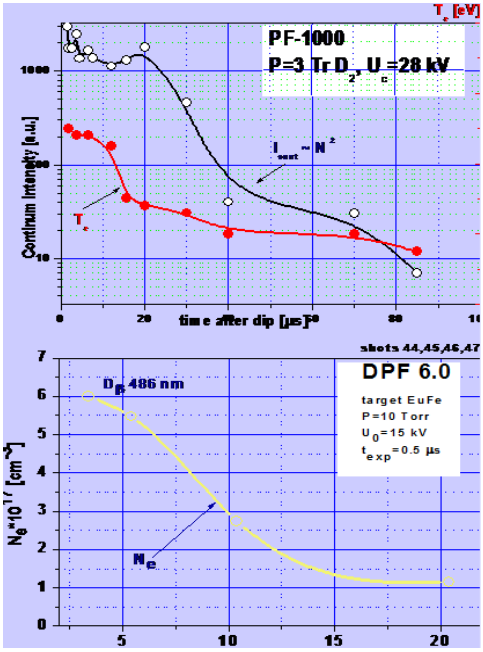

FIG. 9. Temporal changes of temperature and density of the secondary plasma produced at the surfaces of specimens irradiated by streams of hot plasma and beams of fast ions at PF-1000 and PF-6 devices

Verification of temperature measurements was done by means of estimation of laser light absorption within the secondary plasma. It can be easily seen that the ablation plasma cloud near the target surface is characterized by temperature, which is decreasing during about 30 μs for the PF-6 device and 100 μs for PF-1000 facility, i.e. during the time periods comparable with the existence of edge-localized modes (ELMs) at the plasma-facing components in tokamaks.

So it was found that after the 'powerful phase' lasting ~ 0.1 or 1 μs for each of the devices accordingly the temperature decreases during the above-mentioned long time periods

down to the value of about 2 eV (about 20 000 K). Thus thermal loads producing by HTP and FIB in DPF are decreased during up to 0.1 ms to these values of temperature of secondary plasmas, which is still well above the decomposition temperature of the investigated materials.

Therefore these experiments proved a basis for adequate experimental tests of different types of materials (including ceramics) intended for use in fusion devices by means of plasma/fast ion radiation action within a DPF device [2-5]. As one can see from the above-described results, this facility produces plasma and fast ion streams having mainly those main parameters (or higher) as existed near the first wall of the mainstream fusion facilities. Now we shall describe our experimental tests made with two types of ceramics.

3.3. Materials used in TAE Antenna coil on MAST

TAEA coil installed on MAST (EURATOM/CCFE Fusion Association, Culham Science Centre, Abingdon OX14 3DB, UK) inside vacuum vessel has dimensions 600×270×8 mm^3 without the BN shell. Each coil is made of 0.8×0.8 cm^2 aluminum bar (Al-alloy 6082 T6) (Fig. 10). Boron Nitride used usually as plasma-facing material in the region ~ 10 cm apart from plasma edge. The customer was interested whether coils can be used without BN shielding. Coils are covered with C2C ceramic Al_2O_3 coating of ~ 20 microns thickness, which provides insulation up to 3 kV. The advantages of this ceramic are high hardness, 700-2400 HV depending on alloy, and high wear resistance (coated components are harder wearing than stainless steel). It has high temperature resistance and can withstand short exposure to temperatures of up to 2000°C without undergoing changes of any kind. The C2C coating has excellent resistance to thermal shock. This ceramic coating is an electrical insulator and forms a very good insulating layer around metallic components. The coating is highly flexible. It combines with the surface of the substrate, and grows onto the interface layer, giving an incredibly high adhesion, which is virtually impossible to remove. Due to the nature of the deposition process the coating can be applied down small holes providing very uniform coating.

FIG. 10. Physical configuration of toroidal Alfvén eigenmode (TAE) coils with a ceramic cover in a chamber vessel of a spheromak MAST.

3.4. Conditions of the irradiation of the Boron Nitride and C2C ceramic (Al_2O_3) performed on Plasma-Focus PF-1000 device in Warsaw and results received

The irradiation procedure was similar to the one we have performed in June 2006 within the frame of Round-Robin tests leaded by Dr. J. Linke (Julich). Samples of the materials to be tested were placed on the axis of the 1 MJ Plasma-Focus PF-1000 device and exposed to an intense stream of plasma (velocity $>10^7$ cm/s and density of the order of $10^{17\text{-}18}$ cm^{-3}) as well as to the beam of fast ions (see Fig. 11).

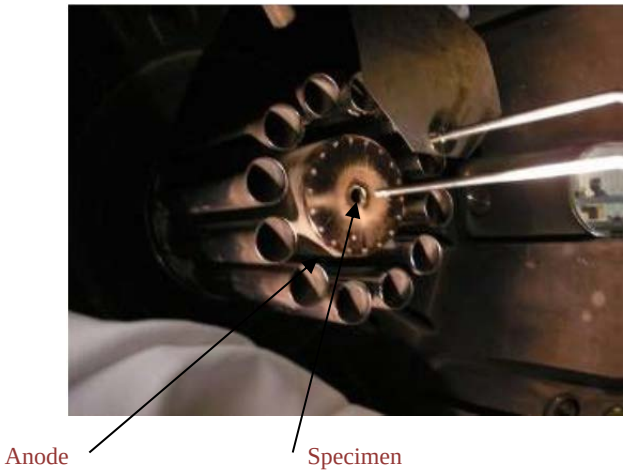

FIG. 11. The anode of the PF-1000 facility (in the centre) and a sample (on the right).

The samples were placed at distances of 15 or 30 cm from the PF-1000 electrode outlet and were exposed to 1–8 shots. During each irradiation experiment the above samples were fixed side by side. However, the conditions of the irradiation were somewhat different. A part of the Al_2O_3 specimen was irradiated in a certain zone near the *Z*-axis by a pulsed stream of hot deuterium plasma and by a powerful part of the beam of fast ions with a power flux density of an order of magnitude higher than the main plasma/fast ion stream.

This zone is visible, in photographs taken of these samples after irradiating them, as a round spot of about 2 cm in diameter (Fig. 12). The other parts of the C2C sample as well as the BN specimen were irradiated by plasma and fast ion streams with power flux densities lower by an order of magnitude.

FIG. 12. Equipment used for positioning of BN specimens and Al_2O_3 ones. A semicircular dark spot visible on the Al_2O_3 sample was a result of its irradiation by the axial powerful beam of fast ions.

The interaction period of a so-called ‘powerful phase’ of the shot was about 0.2–2μs for plasma streams and 0.2–0.6μs for the fast ion beams. The total energy deposited on a sample surface depended on the distance from the stream source (plasma pinch column) and the positioning of the samples in relation to the *Z*-axis of the PF-1000 device. In principle, it could be easily regulated. Taking into consideration that the described investigations had a preliminary character, the positions of the samples were chosen to achieve three types of the heat load conditions:

1. Below the material's degradation point.
2. Corresponding to the degradation point.
3. High above the degradation point.

Positioning brackets with samples made of BN and Al_2O_3 are shown in figure 12. No special measures were taken to prevent the evaporation of the brackets material, but it should be noted that such evaporation was not observed in the majority of cases.

3.5. Experimental results

3.5.1. Results of optical microscopy

Figure 13 shows images, which were obtained by means of optical microscopy of the Al_2O_3 coating irradiated under the toughest conditions (the third case described above). It appeared that after eight pulses of fast ion beams (with a power flux equal to about $10^{11\text{-}12}$ Wcm^{-2}) and of plasma streams (with the power flux equal to $10^{9\text{-}10}$ Wcm^{-2}), the irradiated ceramic layer was almost completely evaporated, and pure melted aluminum (white spots in the photographs) as well as cracks on it became visible.

The most interesting case was found in the experiment where just a single plasma-ion pulse was applied to the both specimens placed at a distance of 30 cm from the anode outlet. In that case, the power flux density was not very high; it amounted to about 10^8 Wcm^{-2} for the plasma stream and 10^9 Wcm^{-2} for the beam of fast ions. The results obtained for that case are shown in Fig. 14.

Since the appearances of both the samples in the optical microscope images was very similar (although the BN looked a little smoother), it was important to compare the results of weighting the investigated specimens. The corresponding results are given in Table 1.

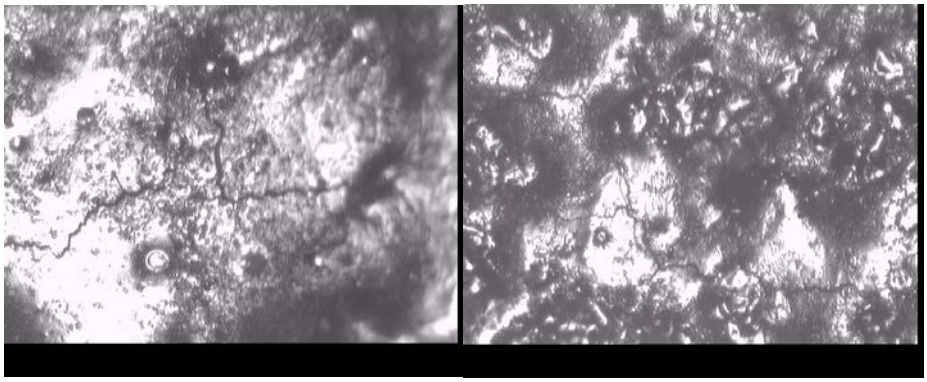

Sample No. 1 (center) *Sample No. 1 (margin)*

FIG. 13. Images obtained with optical microscopy of the Al_2O_3 sample, which was placed at a distance of 15 cm from the PF-1000 anode end (5 cm from the top of the pinch) and irradiated by eight plasma-ion pulses.

3.5.2. X ray structure (phase) analysis

All the samples (samples 1–3) were investigated in two regions: in a central part and in a region close to the sample edge. For comparison, the virgin samples were also analyzed.

(a) Al_2O_3 on Al substrate; specimen 1 (irradiated at 15 cm by eight pulses)

In the X ray diffraction patterns (DPs) of the virgin sample, two dominant lines of Al (111 and 200) were observed. At that background all other lines of the X ray spectrum, as

observed for the Al_2O_3 phase and for compositions of Al with precipitated Cu and Fe, were below 1%. Qualitative and quantitative analyses were difficult because some peaks of the Al_2O_3 phases and combinations of Al with Cu and Fe were placed on slopes of the main reflections from Al—near the base of the lines (at 18°–20°). In this region the Al lines of the spectrum were broadened, and the extraction of Al_2O_3 lines was practically impossible. That effect introduced an additional uncertainty into the described analysis.

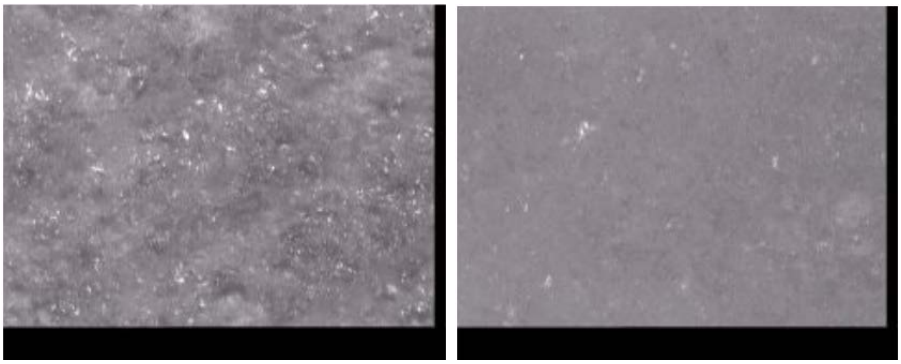

Specimen Al_2O_3 (#3, ×125). *Specimen BN (#2, ×125).*

FIG. 14. Parts of specimens of Al_2O_3 (left) and BN (right) after a single-pulse irradiation (central part of the samples).

TABLE 1. RESULTS OF THE SAMPLES' WEIGHING

Number of the sample	Specific weight, [g cm^{-3}]	Mass before irradiation, [g]	Mass after irradiation, [g]	Mass loss, [mg]	Distance from the anode, [cm]	Number of pulses	Thickness of evaporated layer, [μm]
a) Al_2O_3							
1	3.97	9.1339	9.0520	81.9	15	8	206?
2	3.97	8.9270	8.9161	10.9	30	4	~27.4
	2.7				30		~40
	3.97 (20 μm) +2.7 (Al)						20 (Al_2O_3) +12.6 μm (Al)
3	3.97	5.3029	5.301	1.6	30	1	4
b) BN							
1	2.34	2.6503	2.6456	4.7	30	4	20
2	2.34	2.6434	2.6419	1.5	30	1	6.4

It should be noted that no lines of the Al_2O_3 phase were found in the central part of the sample, whereas in regions close to the sample edge such lines have been recorded. For the irradiated sample, a very strong increase in the intensity of the (200) line in comparison with the virgin sample was observed; in particular, it was so for the central part. Considering the width of X ray peaks, one can deduce that the smallest grains were in the central part of the specimen. It means that the surface layer (SL) of the sample was melted more strongly in its center, and after the recrystallization a low-grain structure was created along the temperature gradient.

The broadening of the lines in the DP was connected with the decrease in grain sizes, appeared due to the production of the thermo-tension and a change in the lattice parameter induced by implantation of deuterium and mixing of Cu and Fe with liquid Al (compositions of Al with Cu and Fe were found). Table 2 shows that the central part of the sample became dirtier after the irradiation.

TABLE 2. APPROXIMATE CONTENT OF DIFFERENT PHASES

Phase	Volumetric percentage in the central part	Volumetric percentage at the sample's edge
Al	91.74	92.59
Al_2O_3	-	0.93
Composition of Al with Cu and Fe	8.26	6.48

(b) Al_2O_3; specimen 2 (irradiated at 30 cm by four pulses)

In this case we did not observe any strong melting of the Al_2O_3 sample. The character of the DP lines was similar to that observed for the virgin sample, but there were some differences in intensities, as shown in Table 3.

TABLE 3. APPROXIMATE CONTENT OF DIFFERENT PHASES

Phase	Volumetric percentage in the central part	Volumetric percentage at the sample's edge
Al	93.46	93.46
Al_2O_3	2.79	0.93
Composition of Al with Cu and Fe	3.75	5.61

One can easily see that the concentration of Al_2O_3 in the central part of the sample was much higher than that at its periphery where the beam of fast ions produced strong damages to a sample (namely in the case of this particular specimen).

(c) Al_2O_3; specimen 3 (irradiated at 30 cm by one pulse)

In this case no melting was observed, and from the sample characteristics given in Table 4, one can see that the Al_2O_3 concentration in the central part was higher than in the previous cases.

TABLE 4. APPROXIMATE CONTENT OF DIFFERENT PHASES

Phase	Volumetric percentage in the central part	Volumetric percentage at the sample's edge
Al	94.02	94.02
Al_2O_3	3.16	3.76
Composition of Al with Cu and Fe	2.82	2.82

(d) BN samples

DPs of the BN samples investigated before and after irradiation [4] have shown that the virgin BN sample contained some silicium (Si) (about 2% volumetric). The irradiation of this sample by a deuterium plasma produced no changes in DPs except the (200) line intensity, which appeared to be lower in the irradiated samples. It resulted from the fact that in the SL the Fe nitrides of the Fe_2N and Fe_4N types were appeared, as well as the iron boride FeB and Fe_4Cu_3 compounds.

Their total content in the BN specimen after its irradiation by four pulses of a deuterium plasma amounted to about 1–2% volumetric. It was connected with the deposition of iron and copper on the sample surface after the evaporation of an about 20 μm-thick layer (see Table 1). It should be noted that Fe and Cu were materials contained in different parts of the PF-1000 facility, and in particular in the constructional elements and samples holders.

In general, the main positive feature of the investigated BN material was its high structural stability in the applied pulsed regime of its irradiation by hot and dense deuterium plasma streams and beams of fast ions. Its negative feature was its high evaporability.

3.6. Irradiation of hard-to-reach compartments

The possibility of processing of parts of the details not easily accessible (in our case, the internal surface of a tube) [6*a*]is related to the circumstance that in a DPF device, unlike other plasma devices applicable in materials science, plasma is generated with the very high temperature (on the order of 10^6 °C).This hot plasma expands very fast in all directions during its propagation (with velocities on the order of the translational velocities of a plasma bunch, i.e., > 10^7 cm/s), filling the specified cavities, which are not easy to reach. In the case of the axial location of the tube, the irradiation power and, consequently, the extent of the radiation effect on both (internal and external) surfaces should obviously be decreased gradually with the distance from the anode of the device chamber. In general it is follow to that law.

However it was noted in the experiments that there is a ring zone approximately 6 cm wide with the anomalously high impact on the internal surface of the irradiated steel tube of the 10CR12MN20W composition. This zone is located at the distance of 22 cm from the "hot" cut of the tube.

In present series of tests [6*b*] it was found that a similar effect took place in our experiments with a steel tube of the 25CR12MN20W composition (Fig. 15*a*) and a copper tube (Fig. 15*b*). The geometry of the experiments on the irradiation of tubes, performed on a PF-1000 device, was the same in all specified cases.

As it is seen in Fig. 15 in both cases of the irradiation of steel and copper tubes the modification degree of the internal surface decreases gradually along the tube from the left to the right from the chamber anode. No traces of the impact are visually observed already in the middle of the tube at the distance of approximately 15 cm from the "hot" cut. Obviously, this is related to the decrease in the density of the stream of both radiation types (HTP and fast ions). However, in a certain zone on the surface of the steel tube, closer to its "cool" end, the value of the damage of the internal surface increases unexpectedly sharply and it takes the zone approximately 6 cm long. This phenomenon is absent on the outer face of the tube. The same effect is observed in the very end at the “cold” side of the copper tube.

We suppose that this phenomenon of the "anomalously high damage rate" of a definite part of the internal cavity of a tube in comparison with its damage rate at a closer distance from the radiation source is related to the specifics of the interaction of the pulsed streams of fast ions inside an extended hollow conductive target, located along the chamber axis. In this respect, it deserves a special consideration.

We performed the main part of our studies using PF-1000 facility (in the frame of cooperation with the ICDMP). The targets being tubes were placed inside a DPF chamber in front of the anode along the *Z* axis. Thus, the streams of HTP and fast ions were tangent to the surfaces of these tubes. The distance from the anode surface to the front cut of the tube was 14 cm at the pinch length along the *Z* axis of 8 cm. Length of both tubes was 30 cm.

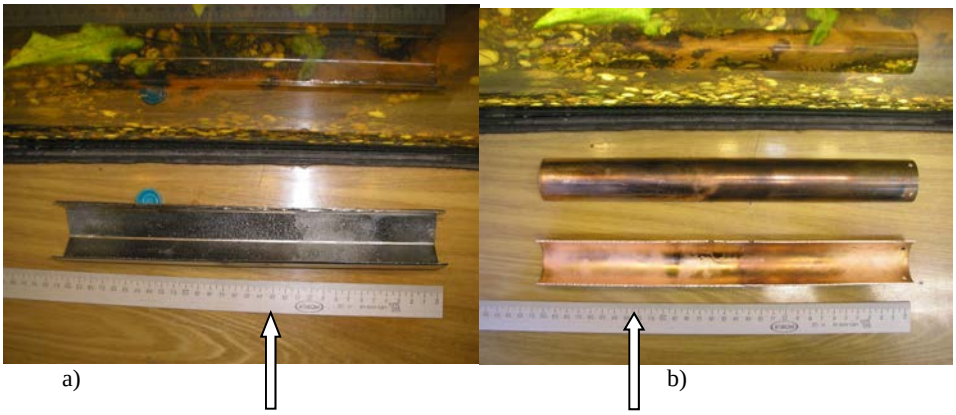

FIG. 15. Internal surfaces of the stainless steel (a) and copper (b) tubes. "Hot" edges of them are on the left-hand side of the pictures. "Anomalous" damage of the tubes are shown by arrows.

The internal cavities of the steel tubes, which were irradiated by the streams of ions and dense deuterium plasma, were analyzed. It was found that the specific ring zone in the steel tube is observed at the distance $L \sim 22$ cm from the tube cut, which is nearest ("hot") to the DPF anode. In the case of the copper tube this zone was observed in the very end of the tube, i.e. at the distance equal to 30 cm from its "cold" part.

This zone is about 6 cm wide and is characterized by the SL damage rate, which is anomalously high in comparison with the rest parts of the tube (see below). This effect of the anomalously high damageability may result from the following reasons.

A cloud of dense plasma (density is of the order of $10^{17}…10^{18}$ cm^{-3}) propagating from the pinch as a cumulative plasma stream and as a SW produced by this stream has temperature of the order of several hundred eV that is much higher compared with the ionization potential of hydrogen. Besides plasma of this cloud is quasi-neutral one; so propagation inside and outside a tube of the plasma stream is ruled by an ideal gas law. It means that the cloud spreads at its movement as a hemisphere. So at the external surface of a tube its power flux density decreases according to a quadratic law. Yet inside the tube we have channeled plasma stream where its density decreases much slower.

For the experiments in the PF-1000 mean speed of fast ions is $u_i \approx 3 \times 10^8$ cm/s whereas velocities of the rise-up portion and of the trailing edge of the plasma cloud are $u_{pl,1} \approx (3…5) \times 10^7$ cm/s and $u_{pl,2} \approx 10^7$ cm/s correspondingly. All fast ions are mainly concentrated inside the above-mentioned cone. Moreover at the moment of acceleration of fast ions almost the whole current of the pinch may be carried namely by these ions thus making concentration of them inside the ion bunch up to 10^{16} cm^{-3}. If there is no hot dense plasma in the chamber this fast ion beam having high (i.e. higher compared with the Alfven-Lawson limit [10]) value of current during its propagation in vacuum or in low-density neutral gas along Z axis must generate high azimuth magnetic field. This field in our case should have a magnitude:

$$B_\varphi = 0.2\, I/r^2 = 1.6 \text{ MGs} \quad (1)$$

where the beam current is $I \sim 2$ MA and its radius is $r \sim 0.5$ cm. It means that the Larmor radius for the 100-keV deuterons would be:

$$r_{Bd} \geq 204\, (W_\perp)^{1/2}/B_\varphi \quad (2)$$

where $W_\perp$ is in eV, B_φ in Gs and r_{Bd} in cm. It gives estimation for the value of the Larmor radius of these fast ions in their own magnetic field: $r_{Bd} \approx 0.04$ cm.

But this magnitude is much less compared with the ion beam radius (0.5 cm). It means that this ion current in the beam exceeds the Alfven-Lawson limit [10], which is in our case:

$$I_{A\text{-}L} = M_D\, c^2\, \beta\gamma / e = 6\times10^5 \text{ [A]} \qquad (3)$$

where M_D – deuteron mass, c – light velocity, β and γ are relativistic factors, and e – deutron's charge. However this is much lower compared with the beam current equal to 2.0 MA. This implyies that all ions must be magnetized thus preventing propagation of the beam into vacuum and into residual gas. As a result the ion beam should be disintegrated.

However in the presence of hot and dense (more than 2 orders of magnitude higher compared with beam's density) plasma of the shock wave ("background" for the beam of fast ions) the character of the beam's propagation is changed. Notably, a back-current is induced in this plasma cloud: in this our case it is a wake (following) current of electrons. This current is concentrated at the external border of the ion beam and it has a collisional character in contrast to the collisionless beam of fast ions. Due to high plasma density n_{pl} and presence of the back-current in this configuration both charge and current compensation take place in spite of the exceeding of the Alfven-Lawson limit: in fact fast ions of the beam do not magnetized and there is no charge repulsion of the beam.

Such a beam can propagate towards long distances that are determined by dissipation processes of the back-current. Inside the plasma cloud of the DPF pinch itself and SW above it this transportation is realized satisfactorily until the SW front. However when this ion beam starts to pass through the front it is injected into neutral residual gas filling the chamber at the initial density of the order of 1 Torr, which is about the same as mean density of fast ions in the beam. Mean free path of the 100-keV ions inside the gas is about 1 m. It means that this beam of positively charged fast ions is not able to ionize the residual gas in the DPF chamber and it has to propagate inside the neutral environment; in this media there is no either charge or current neutralization.

But at the presence of a tube made of conducting material with its "hot" edge immersed into the dense hot plasma the situation is changed again (see Fig. 16). At the external part of the tube the ion beam is disintegrated after penetration through the SW front and ions go to the cathode. However inside the tube the beam of fast ions can be compensated by the back-current induced inside the tube's wall enveloping the beam. The length where this compensation can exist is determined by dissipation of the back-current, i.e. in our case by conductivity of the tube's material.

Our experiments have shown that such compensation inside the stainless steel tube takes place until the distances of the order of 35 cm from the anode, i.e. at about 20 cm along the tube. So this length where dissipation is sizable occupies about 2/3 of the length of our stainless tube.

However because conductivity of copper is 50 times higher compared with the steel's conductivity one would expect the transportation length of the beam in this tube extended up to 10 meters. On the other hand as the length of our copper tube was only 30 cm the beam of fast ions cannot be transported further and it falls out to the end zone of the tube. Thus in both types of tubes we had a strong action of fast ions upon a certain region of them where the above-described current compensation was ceased because of low conductivity (steel) or due to a finite size (copper) of the tube.

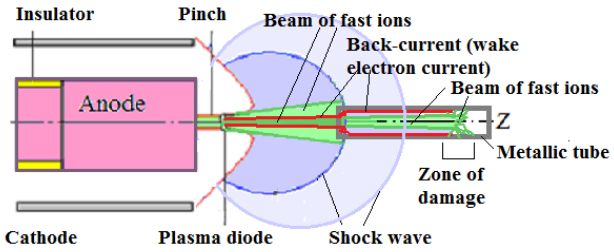

FIG. 16. Schematic of formation and subsequent dynamics (propagation) of plasma stream, fast ion beam and back-current ensured by wake electron current, that are generated in the DPF device, hot dense plasma and conducting tube.

This effect results in a very high damageability of this zone of a tube due to two reasons:

First because energy of fast ions (~ 100 keV) is two orders of magnitude higher compared with plasma particles energy (~ 1 keV).

Second this process of falling out of fast ions onto the internal surface of the tubes takes place perpendicular to the surface and occupies a limited region of the tube; it produces much stronger action upon material compared with oblique and dispersed interaction of plasma with the wall. Taking into consideration the length of the zone of anomalous damageability (about 6 cm) the process of the falling out of the beam is spread in space and time occupying the interval of about several tens ns. It may find an explanation on the base of wide spectrum of fast ions of the beam. Let's examine the characteristic features of the damage produced inside the tubes. In Fig. 17 one may see electron microscopic pictures of three zones of the internal surface of the stainless steel and optical microscopic pictures of three zones of the copper tube. One may clearly see the strong difference observed in these dissimilar cases.

4. DYNAMIC QUALITY CONTROL (DEFECTOSCOPY)

In these set of experiments we have tried to understand whether a DPF device can be better compared with a conventional X ray tube for the quality control of car tyres. Main aim which has been formulated for us by "Pirelli Tyres Company" was: will it be possible to see an internal structure of tyres, in particular a very thin Kevlar threads and low-diameter artificial voids inside the background material, at the illumination of tyres by X rays from DPF. This task is inaccessible for the conventional X ray tubes. The answer received during our experiment was positive. Fig. 18 and 19 presents our results.

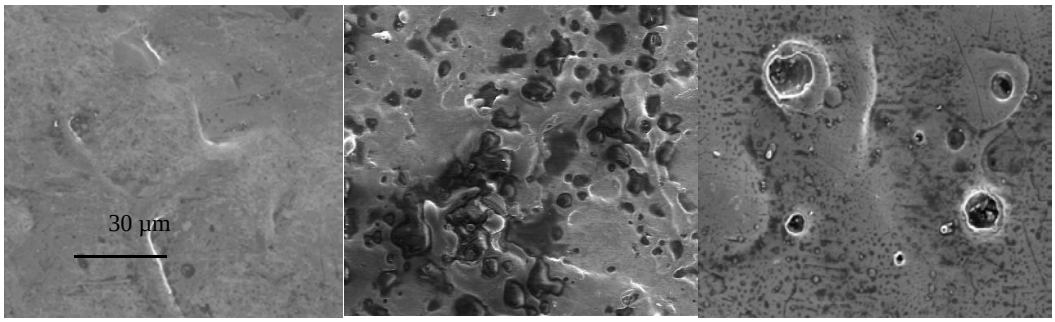

Hot zone *Zone of anomalous damage* *Cold zone*

a)

Hot zone *Middle zone* *Zone of anomalous damage*

b)

FIG. 17. Structural (morphological) changes of damageability of the tube 25Cr12Mn20W after the 4-pulses action onto its internal surface by FI and DHP; scanning in secondary electrons (a). Microphotography of internal surface of a tube made of copper produced for different parts of the tube irradiated by 4 pulses of FI and HDP: 2 cm from the "hot" edge; 15 cm (in the central part of the tube); 28 cm (zone of the abnormal damageability of the tube – at the end of the tube near its "cold" edge) – optical microscopy (b).

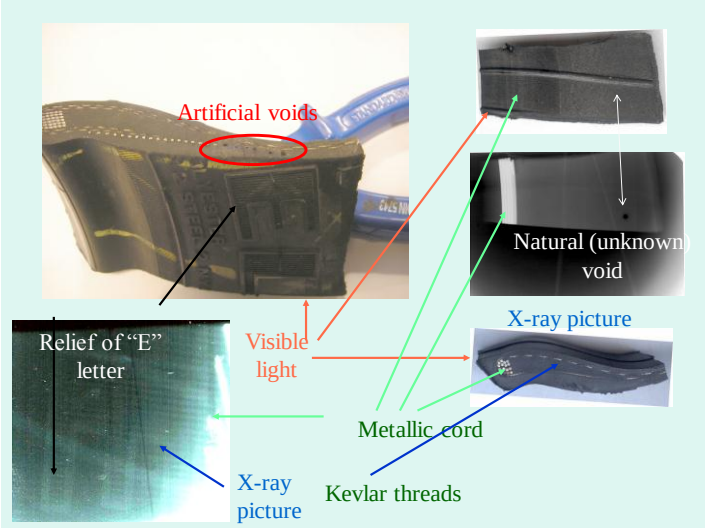

FIG. 18. Visible and X ray images of a fragment of the Pirelly tyre with Kevlar threads and artificial voids.

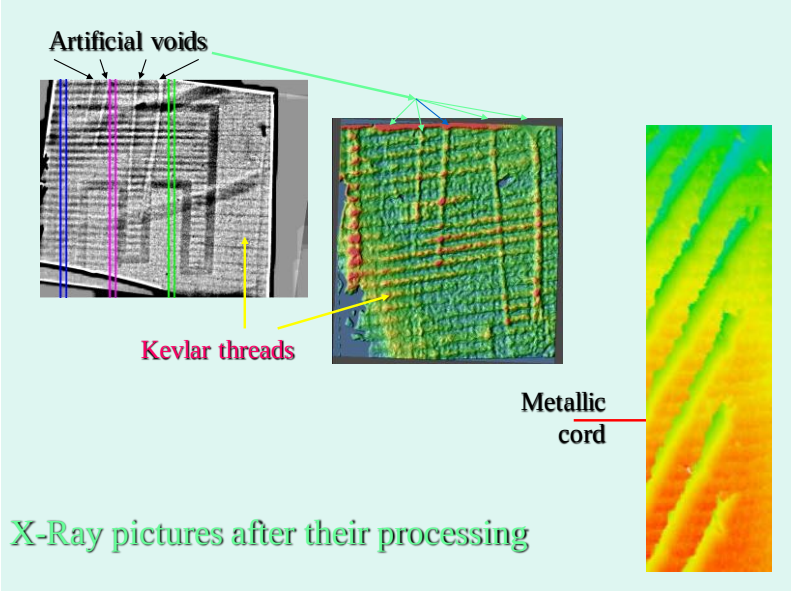

FIG. 19. X ray images of the Fig. 18 after their processing.

From these pictures one may clearly see that very small details having a very low contrast – such as thin Kevlar threads, small voids etc. – can be disclosure by the technique which use DPF device.

Spatial resolution of an image of a part of machine or mechanism during the operation of the latter is determined by the following parameters of the DPF-based source of X rays [11]:

- Duration of the pulse of hard X ray radiation generated by a source (in ns).
- Size of a component under investigation and a distance till the source (< 100 μm and 10-100 cm correspondingly).
- Diffraction (wavelength, distance).
- Image contrast (X ray spectrum of the source).

Theoretically this value for the source based on DPF device can be ~ 1 μm for the distance between the source and the object ~ 10 cm.

5. RADIOENZYMOLOGY

5.1. Introduction

We have provided experiments with the PF-6 facility, as well as with ING-104 (the N.L. Dukhov All-Russia Research Institute of Automatics – VNIIA), PF-5M (the A.A. Baikov Institute of Metallurgy and Material Sciences, RAS, – IMET), and PF-10 (A.I. Alikhanov Institute of Theoretical and Experimental Physics, Rosatom, – ITEP) devices, plus we used isotopes (M.V. Lomonosov Moscow State University – MSU) and fission reactors working in pulsed and continuous modes of operation (the Medical Radiological Research Center, RAMS, – MRRS RAMS, the A.I. Leipunsky Institute for Physics and Power Engineering – IPPE, and the Physics-Energy Institute – FEI, Obninsk, Russia) for assessment of specificity of our case, in the field of radiation enzymology. We undertake these researches together with our colleagues from the above institutions. Main aim of these experiments was to compare effects of pulsed powerful irradiation of enzymes by X rays, by fast neutrons, by gamma-rays and by their combinations.

5.2. Objects under investigation

As the model objects for investigation of the pulsed mode of action for neutron and X ray radiations of various doses, dose powers and spectrum and for comparison of this mode with continuous exposure the enzymes of two types were used [12]: 1) the angiotensin converting enzyme (ACE) – somatic and testicular (mono-domain – C-domain) and 2) various vegetative peroxidases – the native horseradish peroxidase (nHRP), the native tobacco peroxidase (nTOP), the recombinant (anionic) tobacco peroxidase (WT TOP), the tobacco peroxidase expressed (activated) in the cells of transgenic tomato (TTOP), the peroxidase from the African palm leaves (OAPP), the anionic peanut peroxidase (APP), the cationic peanut peroxidase (CPP), and the soy peroxidase (SBP). Additional objects used for irradiation in these our experiments were the blood serum containing ~ (2-3)×10E-9 M ACE and the seminal fluid, where the ACE concentration was within the limits (6-8)×10E-8 M.

5.2.1. Angiotensin converting enzyme

5.2.1.1. Somatic enzyme

The angiotensin converting enzyme (ACE) is a central regulation part of the rennin-angiotensin system (RAS) – one of the most important control systems of organism. ACE is a Zn-dependent peptidase – catalyst of hydrolytic detaching of dipeptides (mainly) from the

carboxyl end of the set of physiologically active oligopeptide substrates. ACE consists of a single oligopeptide chain including two high homological domains, which contains an active centre with an atom of Zn. Being a component of RAS the ACE executes its interaction with kallikrein-kinin system [by Orekhovich V.N., Lokshina P.A., Eliseeva Yu.E., Pavlikhina L.V., Bulletin of Ac. Med. Sci., 1984, No 8, pp. 3-11, *in Russian*]. Promoting the creation of a powerful vasoconstrictor angiotensin II and inactivation of vasodilator bradykinin the ACE takes an important part in regulation of cardiac tone. It plays also a role in various cardiovascular pathologies. ACE presents in a majority of tissues and liquid media of organism [by Erdos E.G.//Lab. Invest., 1987, V. 56, pp. 345-348]. Maximum of it is contained in the membrane-bound state on the luminal surface of plasmatic membranes of endothelial and epithelial cells.

5.2.1.2. Extraction and purification of somatic angiotensin-converting enzyme from bovine lungs

Fresh bovine lungs were exempted from large blood vessels. Then they were cut by small pieces and preserved until use in a frozen state at -40°. All operations on the enzyme's extraction were at 4°.

1. Extraction and fractionating by ammonium sulfate

1 kg of the lung tissue was homogenized in phosphate buffer, pH 7.4, containing 150 mM of NaCl, 1 μM $ZnCl_2$ (buffer A), twice during 45 s at 8,000 cps at homogenizer RT-1. Then triton X-100 was added in this homogenate until 0.05%, the substance was mixed mechanically by a stirring rod during 12 hours and centrifuged in the «Beckman J-6» (USA) during 40 min. at 2,500 cps. Sediments were thrown away whereas a supernatant was used for the subsequent work.

At the intensive mixing a fine grinded dry ammonium sulfate was added by small portions up to a 35%-saturation. The number of grams necessary to add to 1 liter of the solution with the saturation S_1 (%) to receive the solution with a saturation S_2 (%) was calculated by a formula [Doson R, Eliot U., Johnes K., Handbook of biochemist, 1991, Mir, Moscow, pp. 461-466, *in Russian*]:

$$\text{amount of } (NH_4)_2SO_4 = 533 \cdot (S_1 - S_2)/(100 - 0.3 \cdot S_2) \qquad (4)$$

After adding of the last portion the solution was mixed again during 30 min., centrifuged in «Beckman J-21» (USA) at 30,000 spc during 30 min. Sediments were thrown away whereas a supernatant was secondly precipitated by ammonium sulphate bringing its concentration up to 65%. Then one more centrifuging was done during 30 min. at 30,000 spc. Supernatant was thrown away whereas sediment was preserved at 4°.

2. Affine chromatography

Enzyme was purified up to homogeneous state by the affine chromatography [by Bull H.G., Thornberry N.A., Cordes E.H.// J. Biol. Chem., 1985, V. 260, pp. 2963-2972] at the carrier synthesized by us (described below). A portion of the sediment (50 g) was diluted in 400 ml of buffer A and centrifuged at 30,000 cps during 30 min. The sediment was thrown away whereas a supernatant was placed onto a column (1.6 × 40 cm) with affine sorbent based on the specific inhibitor lysinepropyl equalized by the same buffer with the speed 14 ml/h. Then it was rinsed by the initial buffer until the end of the washout of ballast proteins (300 ml) at the speed 30 ml/h, then the enzyme was eluted at the same speed of elution 100 ml 0.05 M of borate buffer, pH 9.5. In the collected fractions by 2 ml the activity of the enzyme

was measured. Fractions that contained active enzyme were combined into one, poured out to plastic test-tubes and preserved at -18°.

3. Synthesis of affine sorbet [by Sundberg L., Porath J.// J. Chromatogr., 1974, V. 90, P. 87-98]

100 ml of 1.4-butanedioldiglycide ether (70% solution) and 100 ml of solution contained 2 mg/ml $NaBH_4$ in 0.6 M NaOH were added to 100 ml of agarose, mixed by help of a swinger during 8 hours at room temperature. The epoxyactivated agarose received was placed on the Buchner funnel with a glass filter G-3 and washed with 3 ml of distilled water.

6-[N-(p-aminobenzoyl)amino] caproic acid (200 ml 90 mM of solution in 0.1 M NaOH) was added to 100 ml of the washed epoxyactivated agarose, and the blend was mixed during 16 hours at 25°. Then 100 ml 1 M of glycin (pH 10) was added with a subsequent additional mixing during 6 hours at 25°. The gel was placed on the Buchner funnel with a glass filter and washed 4 times with 500 ml of the solutions as follows: 0.1 M $Na(CH_3COO)$ (pH 3.8), 0.5 M NaCl, 0.1 M $Na_2B_4O_7$ (pH 8.7), 0.5 M NaCl. The modified agarose was washed on the glass filter by 500 ml of dioxane and reslurried in 300 ml (3 volumes) of dioxane, added N-hydroxysuccinimide by small aliquots under mixing up to the final concentration 0.1 M. Then it was mixed during 70 min. at 25° and washed on the glass filter successively by 8 volumes of dioxane, 3 volumes of methanol, and 3 volumes of distilled water. Reslurring of the gel was done in 250 ml of 2.2 mM of solution of lysinpropyl in 0.3 M K_2CO_3 (pH 11), then it was shaken during 12 hours at 4° and washed in 1.5 l of distilled water and 1.5 l of 0,5 M NaCl. Affine sorbent received was preserved in 0.05 M borate buffer, pH 9.5, which contained 0.1% NaN_3.

5.2.1.3. Examination of concentration and purity of the extracted enzyme preparation

1. Purity of the received ACE preparation was measured by the results of Ds-Na-electrophoresis. The electrophoresis was done in the 7.5% polyacrylamide gel in a presence of 0.1% Ds-Na and 0.1% of β-mercaptoethanol by the method of Laemmli [Laemmli, U.K. //Nature, 1985, V. 227, pp. 668-672]. For coloration of proteins Cumassi brilliant blue G-250 was used.

2. Protein concentration C was determined by the method of Lowry [Lowry U.K., Rosenbrough N.J., Farr A.L., Bandall K.L.// J.Biol.Chem., 1951, V. 193, pp. 265-271] or by spectrophotometric method by measuring of optical density on the wavelengths 240 and 280 nm. In the latter case the protein concentration was calculated by a formula [Doson R, Eliot U., Johnes K., Handbook of biochemist, 1991, Mir, Moscow, *in Russian*]:

$$C_{protein}\ (mg/ml) = 1.55 \cdot A_{280} - 0.76 \cdot A_{260} \qquad (5)$$

3. Measurements of the ACE activity during the extraction process was done by initial speed of hydrolysis N^{α}-3-(2-furyl)-acryloyl-L-phenylalanil-glycyl-glycine (FA-Phe-Gly-Gly) with the help of spectrophotometer Shimadzu UV-265FW having a thermostatic (at 25°) test-tubes compartment [Holmquist B., Bunning P., Riordan J.F.// Anal. Biochem., 1979, V. 95, P. 540-548]. In a typical experiment 980 μl 100 μM of the substrate solution in 50 mM Hepes-buffer (or Tris-HCl buffer), pH 7.5, containing 150 mM NaCl and 1 μM $ZnCl_2$, was placed into the spectrometric cuvette, then 20 μl of the enzyme's solution was added. The reaction blend was mixed whereupon the speed of the optical density decrease at 328 nm was measured.

4. Concentration of the active centers of ACE was determined by the method of the stoichiometric titration [by Bieth J.-G. // Methods Enzymol., 1995, V. 248, pp. 59-84] with a

help of specific competitive inhibitor lysinopryl. Reaction was done in 50 mM Hetes-buffer, pH 7.5, containing 150 mM NaCl, 1 μM $ZnCl_2$ at 25°. For this aim the enzyme solution (about 50 nM) and inhibitor (0 - 120 nM) in 980 μl of buffer was incubated 30 min. to reach a steady-state equilibrium, then 20 μl of 3 mM of the solution of the substrate FA-Phe-Gly-Gly in the same buffer was added and the rest activity of ACE was measured as it is described above. In a separate experiment it was shown that the 30-min. time interval is enough to establish equilibrium for the concentrations of inhibitor and enzyme used.

Calculation of the number of active centers was done by using a linearization of data in coordinates v_i/v_0 and I, where v_i – the reaction speed in the presence of inhibitor, v_0 – the reaction speed in the absence of it, I – the inhibitor concentration. Length of the segment cut by the linearized part of the curve on the axis of abscises, corresponds to the concentration of the active molecules of the enzyme.

5.2.1.4. ACE activity after irradiation

ACE activity after irradiation was measured by initial speeds of hydrolysis of the substrate N-carbobenzoxy-L-phenyl-L-histidil-L-leucine (Cbz-Phe-His-Leu) by determining of the reaction product (His-Leu) with the help of orto-phtalic aldehyde using fluorometric method [by Conroy J.M., Lai C.I. // Anal. Biochem., 1978, V. 87, pp. 556-561]. For this aim a sample of ACE (10^{-7} and 10^{-8} M) was diluted till the concentration 10^{-9} M. In centrifugal test-tubes 0.4 ml 0.05 M of the phosphate buffer, pH 7.5, containing 0.15 M NaCl and 1 μM of $ZnCl_2$, was placed. Then 50 μl of the 1 mM solution of the substrate in methanol was added. The blend was thermostabilized at 37°, and then 50 μl of the enzyme solution was added. The reaction blend was mixed and incubated for 20 min. at 37°.

Reaction time was selected in a way to make the hydrolysis depth not exceeding 5%. The reaction was stopped by adding of 0.25 ml 1 n NaOH. Then 50 μl of 0.2% solution of orto-phthalic aldehyde in methanol was added, the blend was incubated 10 min., and the 0.063 ml of 6 n HCl was added. Fluorescence of the created adduct was measured by a spectrofluorimeter Hitachi MPF-4 (Japan) at the wavelength of excitation 370 nm and the wavelength of emission 500 nm.

Measurements of ACE samples with initial concentration 10^{-9} M were done analogously, however in this case the starting enzyme solution was diluted preliminary to the concentration of 10^{-10} M, whereas a fermentative reaction was accomplished during 200 min. At the measurements of the ACE activity within the human blood the latter was diluted by 10 times and the reaction was accomplished during 60 min. Background fluorescence was measured in the same conditions but enzyme was introduced after adding to it of 0.25 мл 1 n NaOH. Standard fluorescence was measured in the same way as the background one, but instead of the substrate the solution of the His-Leu of the predetermined concentration was used. Each point was measured three times.

As a result of extraction the preparation of ACE with a very high purity to the starting extract (> 1,500 times) containing 90-95% of active molecules from the total quantity of protein by results of titration by means of lysinopryl inhibitor (Fig. 20) was obtained. According to the results of the electrophoresis ACE migrated by one band as a protein with the molecular mass 180 kDa what is in conformity with the expected molecular weight.

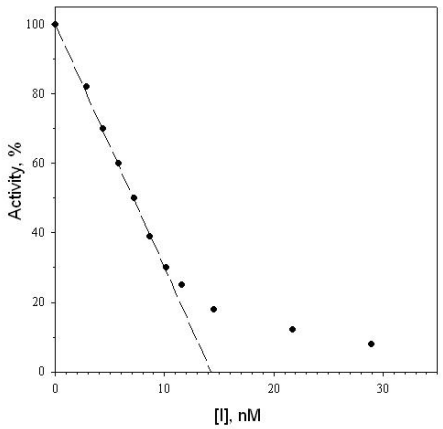

FIG. 20. Titration of somatic ACE by a specific inhibitor lysinopryl. Conditions: 50 mM Hepes-buffer, pH 7.5, containing 150 mM NaCl, 1 μM $ZnCl_2$, 25°. Concentration FA-Phe-Gly-Gly - 50 μM, enzyme concentration (by protein) - 16 nM.

5.3. Sources of radiation (facilities)

We used in our experiments a number of X ray and neutron sources with pulsed and continuous operation.

1. Dense Plasma Focus PF-6. It is described in the beginning of this work.
2. Dense Plasma Focus PF-5M. The pulsed source of X ray radiation of the DPF type, having the bank energy 1.8 kJ. It operates without production of neutron emission. Working gases – hydrogen, nitrogen or helium. Charging voltage – 10-15 kV. Initial gas pressure – 1.6-2.8 Torr. Duration of X ray pulse ~20 ns. Its discharge chamber has an anode made by copper. Two regimes of irradiation were used:

a) Regime with the radiation extraction window of the chamber covered by relatively thick aluminum foil (thickness is 1 mm); in this case X ray radiation has hard spectrum with X ray photons having energy above 40 keV; we shall name this regime here below as "with filter";

b) Regime with the radiation extraction window of the chamber covered by thin copper foil (100 μm); in this case X ray radiation contains a medium-energy X ray component with the K_α-line of copper ($h\nu$ = 8.98 keV); we shall name this regime here below as "without filter".

The dose range obtained here was 10^{-5} – 10^{-1} Gy. The dose power was changed in the limits 10^5 – 10^9 Gy/min.

2. Isotope source γ-400 (Cs-137). Its spectrum consists of the principal line $h\nu$ = 662 keV and two additional lines in the soft zone – 32 keV (double line Ba K_α) and another line with photon energy below 10 keV. Irradiation by this source was executed in a continuous mode. Its dose rate is equal to ~ 5×10^{-4} Gy/min. Obtainable doses were in the range 0.5-100 Gy.

3. Dense Plasma Focus ING-104. This source of the DPF type produces both X rays and neutrons that can be used for irradiation either separately or in combination. Its bank energy is equal to 6 kJ. Working gas is an equal-component mixture of deuterium and tritium. Its neutron yield was changed within the limits 0.5-2.0×10^{11} neutrons per pulse. Neutron energy is 14 MeV. Duration of the pulses of neutrons and hard X rays changed within the limits 10-20 ns. Maximal dose and dose power in neutrons reached in with this device were

0.1 Gy and ~10^9 Gy/min correspondingly. X ray component with energy of photons above 70 keV had dose and dose power within the limits 10^{-5} – 1.0 Gy and 10^5 – 10^{10} Gy/min correspondingly.

4. Pulsed fission reactor BARS-6 (FEI). This reactor may work both in continuous and pulsed modes of operation. It forms the neutron/gamma-ray fields with different ratio of these components depending on the particular position of a sample under irradiation. Average neutron energy is about 1.5 MeV. Pulse duration is 70 μs with the maximal dose rate up to 10^9 Gy/min. The gamma-ray component is may reach up to 35%.

5.4. Experimental results

Investigation of somatic and testicular forms of ACE as well as of complex compositions having dissimilar concentrations of ACE – namely serum and seminal fluid – produced at variations of conditions of enzyme existence and parameters of sources has shown as follows [12*b*]:

1. Important factor for appearance of deviations in catalytic activity (in particular for the case of its activation) during nanosecond pulsed X ray irradiation is the presence of the copper line K_α = 8.98 keV in the X ray spectrum of a source. The dose range near ~ 10E-5 Gy appeared to be the specific one, what has been demonstrated in all experiments both for enzymes and for seminal fluid. Besides the dose range (0.2-0.5)10E-5 Gy must be marked as the range, within which deviations for 10E-9M enzyme solutions were observed even at the presence of only hard component of X ray radiation. Meanwhile in serum certain activation was observed at a dose 1.9×10E-5 Gy.
2. Testicular form of enzymes is sensitive enough to X ray irradiation. However the experiments produced has shown as weak activation so inactivation effects. Thus for reliable conclusion here we must provide additional investigations namely with doses about 10E-5 Gy.
3. Presence of such effects at so infinitesimal doses of X rays in the conditions of very high intensity of them (nanosecond pulse durations) demonstrates punctured (peculiar) points in a dose curve. They may be dangerous for the biological objects' functioning.
4. Neutron irradiation in the combined X ray/neutron and gamma-ray/neutron fields did not produce noticeable effect on catalytic activity of ACE. However in certain experiments this influence was registered.

Investigation of different plant peroxidases has shown the following peculiarities:

1. Presence of the special points in a dose curve, in particular near dose's values equal to 0.5×10E-5 and 1×10E-5 Gy, which produced both activation and inactivation of the enzyme.
2. Appearance of an opportunity to trace dissimilarities in the structure of the substrate-connecting centers by means of pulsed irradiation.
3. An opportunity of a certain increase of activation processes in the peculiar points of dose curve at the presence of neutron radiation additional to the X ray radiation.

Aggregate result on activation/inactivation of various enzymes obtained with pure X ray sources of different types are presented in Fig. 21.

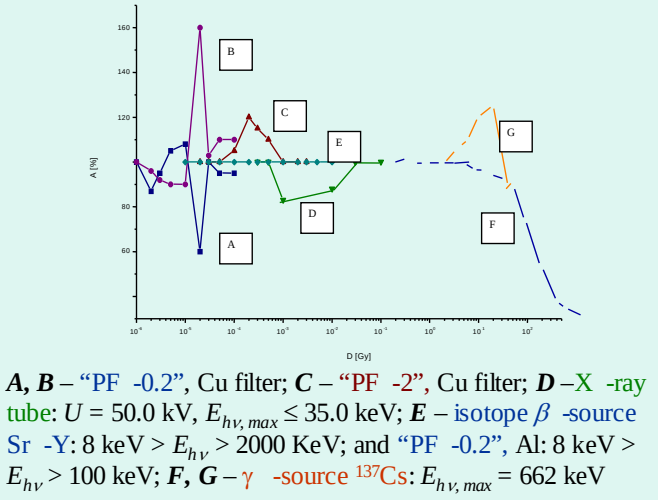

A, B – "PF -0.2", Cu filter; ***C*** – "PF -2", Cu filter; ***D*** – X -ray tube: U = 50.0 kV, $E_{h\nu,\,max} \leq$ 35.0 keV; ***E*** – isotope β -source Sr -Y: 8 keV > $E_{h\nu}$ > 2000 KeV; and "PF -0.2", Al: 8 keV > $E_{h\nu}$ > 100 keV; ***F, G*** – γ -source ^{137}Cs: $E_{h\nu,\,max}$ = 662 keV

FIG. 21. Data on activation and inactivation of different enzymes obtained with dissimilar X ray sources.

One may clearly see that rather strong activation and inactivation are observed in different dose ranges for high power (DPF – left side of the graph) and low dose rate (isotopes – its right-hand side) sources. Attempt to re-graph this data in the coordinates "activation – A" versus "product of dose and dose power (rate) – $D{\times}P$" gave a result shown in Fig. 22.

It is seen that almost all data are now collected in a very narrow "corridor" of $D{\times}P$. However this quantity is similar to those very well known in radiation material science as a so-called "damage factor" F:

$$D{\times}P = D^2/\tau = (F)^2 = (D{\times}\tau^{-1/2})^2 \qquad (6)$$

where D – dose, P – dose power (dose rate for continuous sources), and τ – duration of the radiation pulse.

It means that these phenomena – anomalous interaction of nanosecond high power pulses of radiation with matter (with solid states and with bio-test objects) – observed in so different branches of science as radiation material science and radio-enzymology have probably similar character and produced during physical/physical-chemical stages of the interaction.

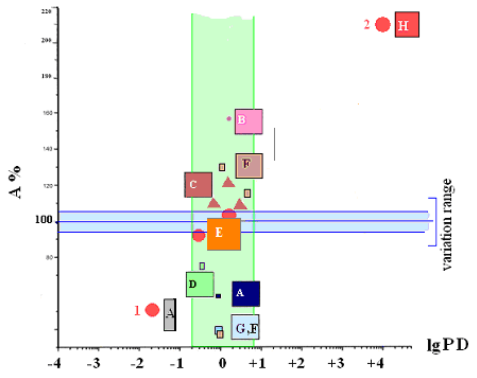

A, B – PF-0,2 ; Cu filter; ***C*** – PF-2 ; Cu filter;
D – X-Ray tube : U = 50.0 kV, $E_{h\nu,\,max} \leq$ 35.0 keV;
E – isotope β-source Sr -Y and Al filter : 40 keV < $E_{h\nu}$ < 150 keV
F, G - γ -source ^{137}Cs for different enzymes : $E_{h\nu\,max}$ = 662 keV
H - PF-6, d =3 cm; Cu filter; ***D*** = 10^{2}Gy; ***P*** = 10^{10}Gy/s

FIG. 22. Dependence of activation of enzymes on the product of dose and dose power.

However, one may note that two regions of the graph of Fig. 2 – “A” and “H”, i.e. the lowest and the highest values of quantity *DP* lie outside of the above range (by the way the magnitude $DP \sim 10^4$ Gy^2/s was obtained in such biological experiments at the first time). Both these events need further investigations.

At the same time at the neutron dose power changes within 9 orders of magnitude the range of changes of the coefficient of biological effectiveness as a rule does not go out from the limits of physiological oscillations. I.e. it is the same for pulsed and continuous sources of neutrons. It opens an opportunity to use in these works a DPF in this dose range instead of cumbersome, expansive and dangerous neutron sources based on fission reactors [10].

6. A SINGLE-SHOT METHOD OF DETECTION OF HIDDEN OBJECTS

Previously [13] we have proposed and successfully tested a single-shot Nanosecond Impulse Neutron Investigation System (NINIS) in the detection of various objects having in its contents elements with light nuclei. It is important in the procedure of unveiling of illegal materials (explosives, drugs, etc.) hidden e.g. in the airport luggage. In those experiments we used elastic scattering of neutrons on nuclei of these elements, because in this case energy changes are quite high and can easily be detected by a time-of-flight technique with relatively short flight bases (about several meters).

Now we have decided to check a possibility to disclosure of hidden fissile materials [14]. In this case the difference in energy of neutrons coming directly from the source (DPF) and elastically scattered by heavy nuclei of uranium will be negligible. So we have to try to find another way of separation of these neutrons.

We have provided MCNP calculations for this hypothetical experiment that has shown the following two way of unveiling these items by detection of fission neutrons produced in the fissile materials by almost mono-energetic neutrons generated by DPF:

1) To detect fissile neutrons produced by neutrons from DPF and passed ahead of the direct 2.5 MeV neutrons generated by PF-6 operating with pure deuterium as working gas.
2) To detect fissile neutrons delayed in relation to the 14 MeV neutrons generated by PF-6 operating with the deuterium-tritium mixture as working gas.

Numerical modeling has shown that in the latter case (where we shall have 2 orders of magnitude higher neutron yield of the PF-6 device) has higher chance for success. So we have provided our tests namely in this scheme using as a sample of the fissile materials a fuel element EK-10.

Premises where we have done our first experiments were given by the Andrzej Soltan Institute for Nuclear Studies, 05-400 Otwock-Swierk n. Warsaw, Poland (see Fig. 23 and 24).

Our set of diagnostics used in these experiments comprised a Rogowski coil and a magnetic probe, a photomultiplier tube with fast scintillator (time resolution 1.3 ns) and a Chevron-type MCP with fast scintillator (time resolution 0.275 ns) (see Fig. 25), and the neutron activation technique for absolute neutron yield measurements using copper foil.

FIG. 23. Premises of INS, Otwock-Swierk with screens blocking direct beam of 14-MeV neutrons.

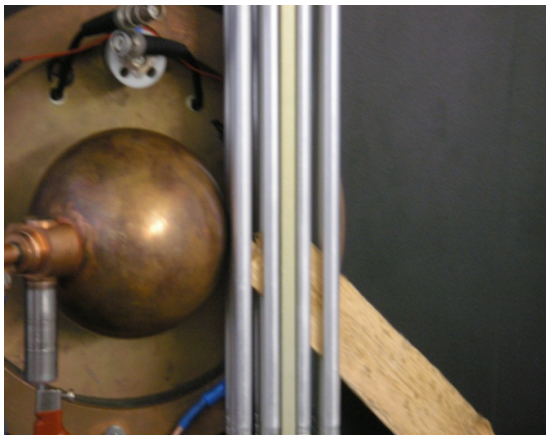

FIG. 24. D-T filled DPF chamber of PF-6 device (on the left) with a fuel element EK-10 (tubes on the right hand side) prepared for irradiation.

FIG. 25. Movable stand with PMT+S and CCD detectors for registration of inelastically scattered neutrons.

Our preliminary experiments gave us results presented in Fig. 26 (neutrons generated by PF-6 device without fuel element) and in Fig. 27 (the same with fuel element). One may see some additional peaks related to the chemical content of the fuel assembly. In future we intend to decrypt these peaks determining their attribution, and to decrease parasitic scattering and to increase the signal-to noise ratio.

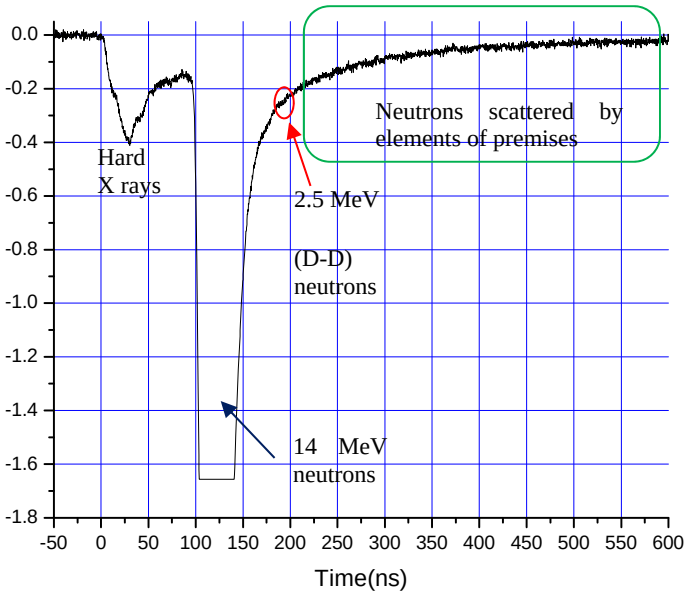

FIG. 26. Oscilloscope trace taken without fuel element.

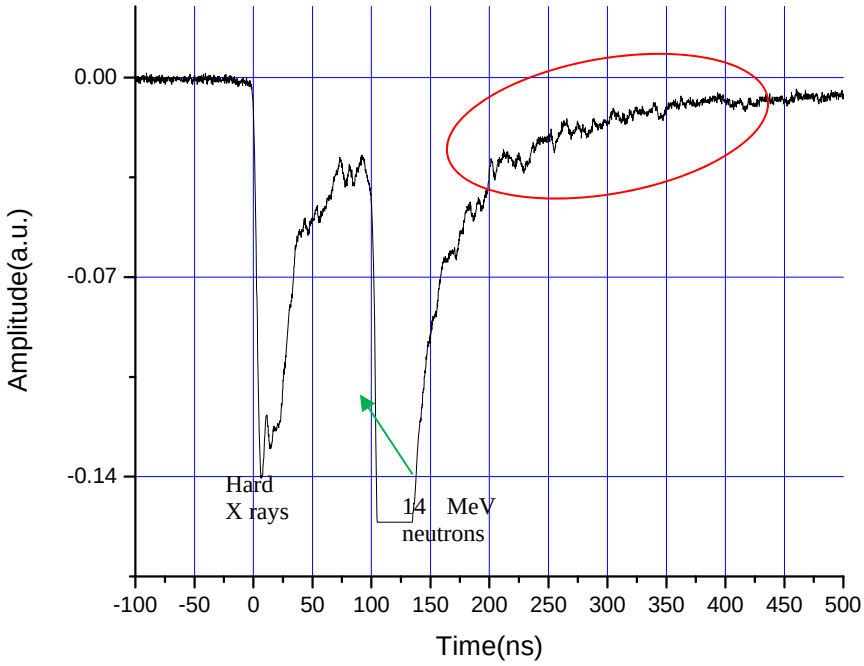

FIG. 27. The same experiment with the fuel element EK-10 placed near the DPF chamber. The oval envelopes additional peaks related to the materials contained in the fuel element assembly.

7. CONCLUSION

In the framework of the IAEA CRP we have modernized our PF-6 device making it able to operate with D-T chamber (producing 14 MeV neutrons) with a repetition rate up to 5 cps. We have equipped it with new neutron/X ray detectors having resolution time down to 0.3 ns.

We have provided a cycle of experiments in radiation material science where we have investigated physics of hot plasma/fast ion streams dynamics in a cathode part of DPF. We found regimes of its operation where duration of heat loads upon tested specimens may be increased by 2 orders of magnitude. We elaborated a method of plasma/ion treatment of hard-to-reach compartments of samples, and we discovered and explained a phenomenon of anomalous damage of the internal parts of them at these types of irradiation.

Our experiments in dynamic defectoscopy have shown advantages of the use of DPF here compared with conventional X ray tubes realized in higher spatial resolution and contrast of X ray images.

Results on our works in radio-enzymology gave us an opportunity to find regimes (ranges of doses and dose powers) where nanosecond powerful flashes of X rays can produce effects that were reached before at doses several orders of magnitude higher. At the same time it was shown that the same doses of pulsed neutron emission from DPF produce the same action upon bio-test objects as classical neutron sources (isotopes, accelerators, fission reactors). It opens opportunity to use DPF in bio-medical applications instead of cumbersome, expensive and dangerous classical neutron generators.

Numerical modeling and first experiments with the single-shot method of detection of fissile materials have shown a prospect of this method.

REFERENCES

[1] GRIBKOV, V.A., KARPINSKI, L., STRZYZEWSKI, P., SCHOLZ, M., DUBROVSKY, A.S., "New efficient low-energy dense plasma focus in IPPLM", Czechoslovak Journal of Physics 54 (2004) Suppl. C, C191–C197.

[2] GRIBKOV, V.A., "Dense Plasma Focus as a Tool for Material Science and Technology", J. Moscow Phys. Soc. 3(3) (1993) 231–240.

[3] GRIBKOV, V.A., PIMENOV, V.N., IVANOV, L.I., DYOMINA, E.V., *et al.,* "Interaction of High Temperature Deuterium Plasma Streams and Fast Ion Beams with Condensed Materials in Dense Plasma Focus Device", Journal of Physics D: Applied Physics 36 (2003) 1817–1825.

[4] PIMENOV, V.N., DEMINA, E.V., MASLYAEV, S.A., *et al.*, "Damage and modification of materials produced by pulsed ion and plasma streams in Dense Plasma Focus device", Nukleonika 53(3) (2008) 111–121.

[5] GRIBKOV, V.A., TUNIZ, C., DEMINA, E.V., *et al.*, "Experimental studies of radiation resistance of boron nitride, C2C ceramics Al_2O_3 and carbon–fiber composites using a PF-1000 plasma-focus device", Phys. Scr. 83 (2011) 045606; doi: 10.1088/0031–8949/83/04/045606.

[6] a) DEMINA, E.V., IVANOV, L.I., MASLYAEV, S.A., PIMENOV, V.N., SASINOVSKAYA, I.P., GRIBKOV, V.A., DUBROVSKY, A.V., "Modification of the surface layers of stainless steel tubes by pulsed streams of ions and high temperature plasma", Perspective materials #5 (2008) 42–48, *in Russian.*

b) GRIBKOV, V.A., DEMIN, A.S., DEMINA, E.V., *et al*., "Physical processes taking place at the interaction of pulsed ion and plasma streams with target surface having shapes of plate and tube inside the working chamber of the Dense Plasma Focus device", Applied Physics #3 (2011) 43–51, *in Russian.*

[7] JACJUINOT, J., "Fifty years in fusion and the way forward", Nuclear Fusion 50 (2010) 014001.

[8] HAYNMAN, C.A., WEGNER, P.J., AUERBACH, J., *et al.*, "Ignition Facility laser performance status", Appl. Opt. 46 (2007) 3276–3286.

[9] a) GRIBKOV, V.A., BIENKOWSKA, B., BOROWIESKI, M., *et al.*, "Plasma dynamics in PF-1000 device under full-scale energy storage: I. Pinch dynamics, shock-wave diffraction, and inertial electrode", *J. Phys. D: Appl. Phys.* 40 (2007) 1977–1989.
b) GRIBKOV, V.A., BANASZAK, A., BIENKOWSKA, B., *et al.*, "Plasma dynamics in PF-1000 device under the full-scale energy storage: II. Fast electrons and ions characteristics versus neutron emission parameters, and the gun optimization properties", J. Phys. D: Appl. Phys. 40 (2007) 3592–3607.

[10] HUBA, J.D., NRL Plasma Formulary, The Office of Naval Research (2004).

[11] GRIBKOV, V.A., "Current and Perspective Applications of Dense Plasma Focus Devices", in PLASMA AND FUSION SIENCE (Proc. 17th IAEA Technical Meeting on Research Using Small Fusion Devices, October 22 - 24, 2007, Lisbon, Portugal), Ed. C. Varandas, C. Silva, AIP Conference Proceedings, Melville, NY, 996 (2008) 51–64.

[12] a) ORLOVA, M.A., KOST, O.A., GRIBKOV, V.A., *et al.*, "Enzyme activation and inactivation induced by low doses of irradiation", Applied Biochemistry and Biotechnology 88 (2000) 243–255.
b) GRIBKOV, V.A., SVIRIDOV, A.S., BOGOLUBOV, E.P., *et al.*, "The development of methods and apparatus for cancerous growth diagnostics and therapy on the base of neutron and X ray radiation pulse generator", Issues of Atomic Science & Technology, Nuclear Instrument-Building (BARMAKOV, Yu.N., Ed.) The All-Russia Research Institute of Automatics, Issue #1 (27), Moscow (2010) 178 pp.

[13] GRIBKOV, V.A., MIKLASZEWSKI, R., "On a possibility of the single-shot detection of hidden objects by using nanosecond impulse neutron inspection system", Acta Phys. Chim. Debr., XXXVIII-XXXIX (2005) 185–193.

[14] GRIBKOV, V.A., LATYSHEV, S.A., MIKLASZEWSKI, R.A., *et al.*, "Monte Carlo Simulations of Powerful Neutron Interaction with Matter for the Goals of Disclosure of Hidden Explosives and Fissile Materials and for Treatment of Cancer Diseases versus their Experimental Verifications", Applications of Monte Carlo Methods in Biology, Medicine and Other Fields of Science (MODE, C.J., Ed.) ISBN: 978-953-307-427-6, InTech (2011) 217–242. Available at: http://www.intechopen.com/articles/show/title/monte-carlo-simulations-of-powerful-neutron-interaction-with-matter-for-the-goals-of-disclosure-of-h

RESEARCH OF D-D FUSION REACTIONS AT THE CTU IN PRAGUE

P. KUBES

Czech Technical University in Prague
Faculty of Electrical Engineering
Czech Republic
e-mail kubes@fel.cvut.cz

Abstract

This report deals with the study of the fusion plasma on the z-pinch and plasma focus devices filled with deuterium gas. Investigation was done on the PFZ -200 in Prague, PF- 1000 in Warsaw, S-300 in Moscow and GIT 12 in Tomsk in Russian Federation with comprehensive X ray, neutron and interferometry diagnostics. During investigations the energy spectra of neutrons and deuterons were calculated using Monte Carlo simulation and adapted time-of-flight analysis. The interferometry instalated on the PF-1000 enabled to describe the plasmoidal, toroidal and helical structures in the plasma column and their evolution. Neutrons are produced in correlation with formation and disintegration of plasmoids and constrictions. On the z-pinches S-300 and GIT-12 the gas-puff injection of deuterium was tested. The characteristics of neutrons from both PF and z-pinches were compared at currents of 1-2 MA and their similarity and differences were described. On the PF-1000 the modified electrode system with cathode disk was used and the results showed moderation of plasma transformation and the lower neutron yield at the higher energy density in the column. Experimental of thermonuclear neutrons was published. The results obtained can be used as enter parameters for simulations of the neutron production on the devices above 2 MA done in SNL in USA.

1. INTRODUCTION

Study of DD fusion reaction on the z-pinch and plasma focus devices in deuterium filling is done in laboratories due to high efficiency of neutron production and detection of neutrons is possible to obtain in small devices as well. These devices are the simple sources of fusion plasma and were historically the first, where fusion was investigated. Research of magnetized plasmas at CTU was provided during a few decades. The small devices PFZ-200 at CTU is studied namely for testing of diagnostic and device component to use them on high-current devices, where only a few shots per day it is possible to done. As well, the education of students in the field of fusion it is simple to realize in the university laboratory in table-top configuration. The PF-1000 in IPPLM in Warsaw working at 2 MA is the huge discharge source of fusion neutrons in EU and our common collaboration continues more than 10 years. Similarly, S-300 and this year GIT-12 are the generators where the neutron production at the gas-puff input of deuterium are the most efficient out of USA. The Z-machine in SNL in Albuquerque in USA (17 MA) tested the deuterium gas-puff in 2005 and 2006 in 10 shots and the promissible neutron yield $6x10^{13}$ neutrons per shot was achieved, two orders more than in shots with deuterium in the target in solid state. The possibility of detail investigations of plasma parameters in this device is limited; therefore the devices working at the current level of 1-2 MA are the convenient sources for detail X ray and neutron diagnostics necessary for simulation of plasma at higher currents. Moreover, the parameters of the fusion plasma, density and time of confinement, are more convenient for diagnostics with temporal spatial and energy resolution then the plasma produced in tokamaks or by lasers. Especially, the heating of the plasma with deuteron beams and evolution of plasma structures have close analogy, because the collision frequency depends linearly on the plasma density and 6 orders difference in both values give according to formulas the same results in energies.

2. EXPERIMENTS AND RESULTS

2.1. PFZ-200 device

Construction of the plasma focus device at CTU in Prague was finished in April 2008. This device has cylindrical electrode configuration with possibility of modification using

cathode disk 1 cm in front of the anode. The maximum of the current of 200 kA was reached within 2 μs. The initial pressure of deuterium in the discharge chamber was 200-300 Pa. The neutron yield reached 10^5-10^7 per one shot. In 2011 the reconstruction of the spark gaps enabled increase of the current maximum to 250 kA. The possibility of the device to repeat the shots after a few minutes enabled to provide a few tens of shots per day and to test some device and diagnostic components for using at bigger facilities.

In 2008 we obtained permission of the Government Institute for Nuclear Security for D-D fusion experiments and education of students. For detection of soft X rays we used the filtered silicon PIN detector with an Al 1.5 μm foil, and a microchannel-plate detector split into 4 quadrants in the photon energy range above 10 eV with 2 ns exposure time and the delay between exposures 5 ns. The fast plastic scintillation detectors of 5 cm thickness equipped with fast photomultipliers enabled a detailed time-resolved registration of neutrons and hard X ray radiation with energy of photons above 100 keV (such X rays penetrated steel and lead shielding). The total neutron yield (supposing angular isotropy) was estimated from calibrated scintillation and bubble detectors.

We provided experiments in different electrode configuration without and with cathode disc to study their influence on the neutron production. The reason for using disc was both: diminish the volume for deuteron acceleration and neutron production and study of the structure of the plasma column in configuration of plasma focus electrodes close to classical z-pinch configuration. The experience was utilized in the experiments provided at PF-1000 during experiments 2010 and 2011.

The triggering of the spar gap of the discharges was done on the gas-puff principle. We use our practice with gas-puff components for realization of this input of deuterium into the cathode on the S-300 on this. The opportunities were utilized also later in measurement on the GIT-12 in 2011.

For schlieren and interferometry visualization the laser with 4 ns pulse duration was used. It enabled to realize two schlieren pictures with the time delay of 5-10 ns during one shot. The synchronization of the diagnostic laser pulse with multi channel plate (MCP) soft X ray frames on the base of the electric-optic conversion depressed the fluctuation of the time of triggering of the both signals with fluctuation below 10 ns. These adaptations made possible using of comprehensive diagnostics from one shot and study the correlation of plasma density with temperature at the time of hard X ray and neutron emission in more detailed. Experience with this conception was used in PF-1000 and PALS facilities.

The deep of the current derivative correlated with the first peak of the soft X rays and hard X rays. The X ray full width of half maximum (FWHM) is about 10-50 ns. After the first peak the next one or two can be observed. The presence of anti-anode decreased the total neutron yield. In short pulses the onset of the neutron pulses was the same as at the onset of hard X rays.

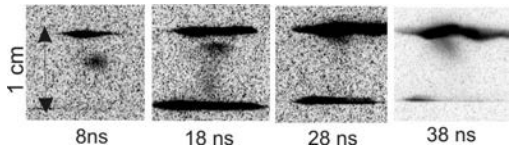

FIG. 1. Shot 08060213. MCP frames registered in the shot with a higher neutron yield at the plane anode and anti-anode with the gap of 10 mm.

The shots with high neutron yield were characterized with high amplitude of the current derivative dip. At the time of hard X rays and neutron emission the XUV frames recorded emission only from near-electrode localities. The results achieved at the disk configuration – confirmation of existence of the structure similar that observed in plasma focuses as a source of neutrons is imaged in Fig. 1. The distance of neutron detectors below 3 m did not allow determination of the neutron energy spectra. Results were published in [1,2].

2.2. S-300

This device was equipped with the z-pinch electrode configuration and worked at the voltage of 800 kV at the current of 2 MA which reached its maximum during 100 ns. The fusion experiments were done from 2000 year and from 2008 with gas-puff injection of deuterium. The plasma of fusion parameters was investigated with X ray and neutron time resolved diagnostics. The neutron detectors were localized into 3 perpendicular directions to measure the spatial anisotropy of neutrons. The maximal neutron yield of $6x10^{10}$ was achieved in 2009. In 2010 this device was closed for experiments due to reconstruction of security protection.

In 2008 the study of the implosion of the deuterium gas-puff z-pinch was started on the S-300 generator. The neutron energy distribution function was determined from 12 neutron time-of-flight signals by the Monte Carlo simulations. The peak of neutron yield above 10^{10} was achieved. The fusion neutrons were generated at about 150 ns after the current onset and the emission lasted on average 25 ns. The side-on energy spectra peaked at 2.42 ± 0.04 MeV with about 450 keV full width of halve maximum. In the downstream direction, the peak neutron energy and the width of neutron spectrum were 2.6 ± 0.1 MeV and 400 keV, respectively. The average kinetic energy of fast deuterons producing neutrons was about 100 keV. The emission of neutrons had axial symmetry and energy distribution of neutrons was close to 2.45 in comparison with shots with deuterium in solid state measured at the same generator or plasma focuses with deuterium gas filling at the same current [3].

In 2009 the neutron production and dynamics of deuterium gas-puffs were studied on the S–300 generator also. The axially homogenous gas-puff taken shape with the zipper lasting below 10 ns. The study of neutron emission was focused mainly on the estimation of neutron energies and neutron emission time, the anisotropy of neutron emission, and the energy distribution of deuterons which produced fusion neutrons. In the case of the linear mass density of 20 μg/cm, the gas puff imploded on to the axis before the current peak at about 100 ns. The fusion neutrons were generated after the gas puff implosion during the global expansion of a plasma column. The neutron emission lasted on average 35±5 ns. In the downstream direction (on the z–pinch axis behind the cathode), the mean neutron energy was 2.6±0.1MeV. The side-on neutron energy spectra peaked at 2.40 ± 0.05 MeV with about 600 ± 150 keV FWHMs. The broad width of the side–on neutron spectra implied a high radial component of deuteron velocity. The average kinetic energy of fast deuterons, which produced fusion neutrons, was about 150 keV. Most of the fusion neutrons were produced by deuterons with the kinetic energy below 300 keV. At the current level of 1.5 MA, the peak neutron yield reached the value of 6×10^{10}. It is by one order higher value in comparison with previous experiments with deuterated fibers, x–pinches, deuterated foams, and imploding wire–arrays on the same current generator. On the basis of the above mentioned experimental data and observed plasma parameters, we concluded (i) most of the neutrons were not of the thermonuclear origin and (ii) the total energy of deuterons accelerated to fusion energy was

above 1.5 kJ. It is more than 15 % of the energy input into a plasma and therefore gas puff z–pinches seem to be not only powerful sources of x–ray radiation but also efficient sources of ≈ 100 keV deuterons. Such a result is consistent with a high neutron yield observed on the Angara Z–pinch and plasma foci with similar currents [7].

2.3. PF-1000

On the device PF-1000 in IPPLM Warsaw the neutron production from DD fusion reaction is studied during last ten years. This facility is equipped with Mather-type coaxial electrodes, and it operates at the charging voltage of 24-27 kV, stored energy about 400-500 kJ, and the current during the pinch phase 1.2 -1.8 MA . The initial pressure of the deuterium filling was 150÷300 Pa and neutron yield reached value 10^{10}-10^{11} per shot.

The voltage, current and current derivative signals were measured at the current collector near the main insulator. The soft X ray pulses in the range of 0.6-15 keV were recorded with a silicon PIN detector shielded by means of a Be-foil of 10 μm in thickness. The time-resolved measurement of hard X rays and neutrons was made with a set-up of scintillation detectors coupled with fast photomultipliers. The energy of registered HXR passing through the chamber wall was above 100 keV. The detectors were situated side-on and upstream in order to estimate the neutron energy spectra in more detail using the time-of-flight analysis. The interferometric measurements were performed with a Nd:YLF laser working at the second harmonics (527 nm). One laser pulse (lasting below 1 ns) was split by a set-up of mirrors into 16 separated beams, penetrating through a Mach-Zehnder interferometer during 220 ns. The total neutron yield was calculated from the data recorded with silver-activation counters.

The neutron energy distribution in the direction downstream (along the movement of the current sheath) was calculated from the recorded 9 signals. The distance of 84 m of the detector placed upstream from the neutron source, gave us a good possibility to determine the energy distribution of neutrons with very good accuracy. Knowing the energy distribution of the fast neutrons we can evaluate the energy distribution of the fast deuterons [3,4] as well. It is possible to summarize the results as follows:

The intense high-energy electrons and ions were produced in correlation with the formation and disintegration of the dense spherical structures and constrictions. The dense spherical structures, plasmoids were the dominant sources of fusion reactions as well. It was estimated that each intense neutron pulse was produced by about 10^{17} fast deuterons with the total energy of 3-5 kJ. The reported results were obtained at the current amounting to maximum of 1.7-2.2 MA and 1.0-1.4 MA in the pinch phase. Comparing shots with high and low neutron yields, a considerable difference was observed in the neutron energy distribution, as well as in neutron isotropy and temporal evolution. In the shots with a low neutron yield, the fast deuterons were emitted during the period lasting 100-200 ns, energy of neutrons was in the range of 2.2-2.7 MeV (close to 2.45 MeV) and the neutron emission showed only a small spatial anisotropy. In the shots with high neutron yields, a similar character of the neutron production was overlaid by a considerably higher portion of neutrons emitted during the last phase of stagnation and during development of instabilities. The range of energy of neutrons was relatively wide (1.9-3.1 MeV) and the spatial anisotropy with the dominant energy component of deuterons producing fusion neutrons in the downstream direction was higher. Also the side-on energy component of these neutrons (up to 2.7-2.8 MeV) was

significant, what was interpreted by high component of radial velocity of deuterons producing neutrons. These results were published in [4-6,9].

During 2009 and 2010 the modified electrode configuration was used without anode hole and with cathode disc. The reason for these modifications was obtain a configuration close to z-pinch and increase the energy density in the pinch. As the results we observe increase of the current and energy density delivered to the pinch phase and decrease of the voltage, current derivative, total neutron yield and decrease of the energy of neutrons close to 2.45 MeV. Increase of the current at the time of pinch phase is a consequence of the lower inductance. The current in the pinch phase at the disc configuration was increased by about 20%. The depth of the current and the peak of voltage were depressed to 50-90%, but the energy density in the pinch increases more than 40 %. The neutron yield was decreased to 30 % and the mean energy of deuterons produced neutrons was depressed usually below 100 keV. The upper energy boundary for confinement of fast deuterons and isotropic neutron energy distribution in the pinch was evaluated as 20-30 keV. The increase of the energy density in the plasma column surprisingly increases its stability. In interferograms, at the final phase of the constriction implosion we observe the transport of a part of the plasma (and probably of the current) to the external layers of the pinch. At the lower current going through the constriction, its development proceeds more slowly.

A slower destruction of the constriction correlates with generation of fast deuterons with lower energy usually below 100 keV. In configuration without disc and with open anode hole, this energy overcame 200 keV. Also the compact plasmoids are formed for the longer time at the higher plasma density and then we can observe their evolution in more details. During some phases of plasmoid evolution we can observe fuzzy fringe pattern evocated probably with turbulent structures. The decrease of neutron production is a consequence of lower cross-section of fusion DD reaction evocated with the lower velocity of fast deuterons. But the fast deuterons with lower energies should be better confined in magnetic field and they can more effectively heat the plasma through Coulomb ion-ion collisions. The decrease of the neutron yield at the higher current at the electrode configuration with the cathode disc could be related with saturation of neutron yield. This saturation effect is well known from the all plasma foci working with the current about 2 MA is being observed during last 30 years. Then, there arises the question, if the lower neutron yield is not accompanied with higher ion temperature and a higher number of neutrons with thermonuclear origin. Therefore, the experiments at the currents above 2 MA should be studied. The results for publication are in review process. The first results obtained at configuration with disc, experimental evidence of thermonuclear neutrons in the first pulse on the PF-1000 was published in[8, 10]. This conclusion was enabled on the base of the knowledge of the implosion velocity of the current sheath, ion temperature and signals of neutron in upstream direction, where the neutrons with thermonuclear origin have the highest energy. The technique of neutron registration was described in [11].

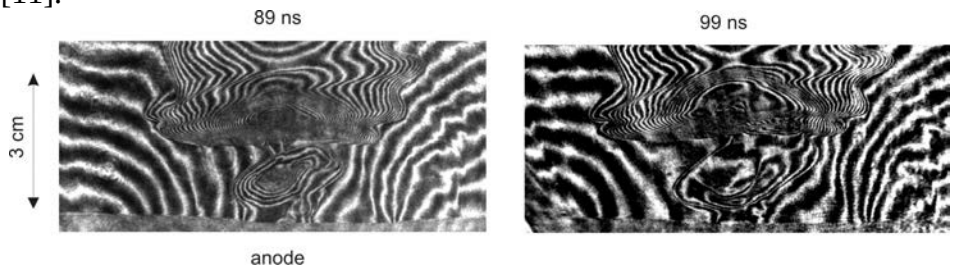

FIG. 3. Plasma column near the anode before (left) and after (right) HXR and neutron pulse, shot 8963.

2.4. GIT 12

The impossibility of experiments on the S-300 implied finding of another huge z-pinch device. It succeeds to realize the first experiments on the device GIT 12 located in the Institute of High Current Electronics in Tomsk in Russia this year 2011. This current generator with the intermediate storage of an inductive energy and a microsecond plasma opening switch (POS) reached the currents two times higher than S-300 or PF-1000. There was possible to realize shots with and without POS to compare two regimes with different rise time of 0.21 and 1.5 μs using the multilayer gas-puff input of deuterium.

The results obtained during our first 6 weeks campaign on the GIT 12 brought new knowledge about neutron production at the current of 2-3 MA increasing during 250 ns (using plasma opening switch POS) and 800 ns (without POS). The regime with POS is similar to the fast z-pinch ZR in Sandia National Laboratories in USA and the second without POS to the plasma focus devices. The neutron yield in both regimes was similar, but characteristics of neutron production were different. Example of the results obtained in the shots without POS (#1408) and shot with POS (#1414) are seen in Figs. 4, 5.

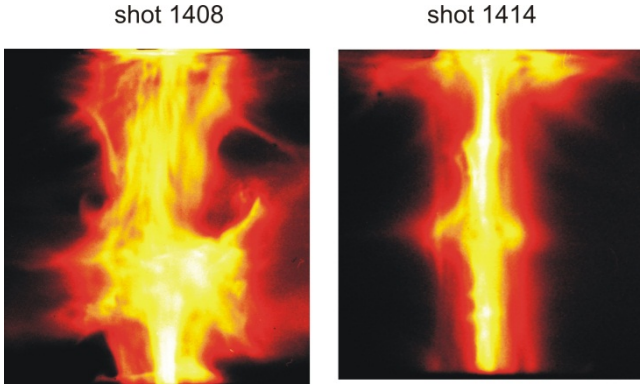

FIG. 4. Pinhole picture filtered with Be 25. Shot #1408 without POS, neutron yield $2x10^{11}$: Shot #1414 with POS, neutron yield $1.5x10^{11}$.

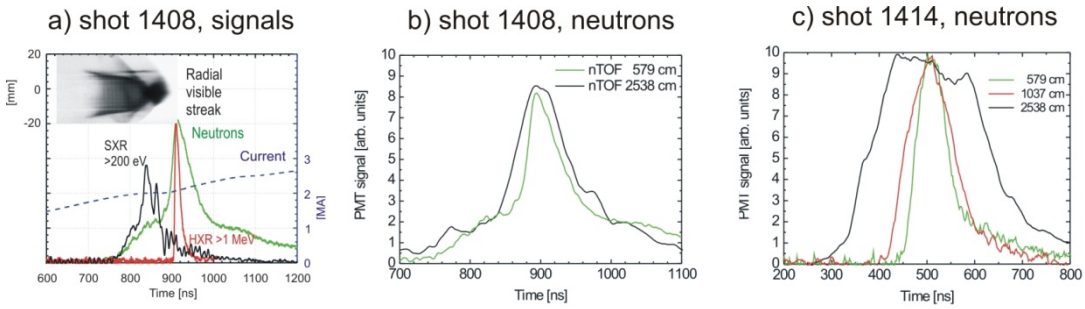

FIG. 5. Signals X ray and neutrons (a), narrow radial energy spectrum of neutrons without POS (b) and wide with POS (c)

Plasma in both parts of Fig. 4 had the same initial conditions: pressure in gas-puff and current. At the longer implosion (#1408) the higher diameter can be interpreted by more intense axial magnetic field self-generation. On the both images you can see the plasmoidal and filamentary structures. The onset of the waveforms of the neutron production correlates

with soft X rays a significant fraction of neutrons can be explained by thermonuclear mechanism. The dominant neutron peak occurred at 40 ns after the soft X ray peak. In the shots without POS the side-on energy spectrum of neutrons was close to 2.45, whiles this spectrum with POS has the FWHM of 1000 keV. Fast deuterons in this shots had considerably higher energy.

In Fig.5 a) the two X ray and neutron waveforms are imaged, the first neutron pulse is connected with soft X rays and the second with hard X rays. The side-on neutron energy spectrum at the longer implosion has the FWHM of 250 keV (b), similarly to plasma focus, whiles at the fast increase of the current the neutron radial energy spectrum has the FWHM of 800 keV (c). In the case (c) the wide energy spectrum could be caused by a stronger confinement of the faster deuterons in the higher magnetic field of the narrower pinch diameter. Continuation of experiments on the base of these results we plane in the next year.

3. DATA PROCESSING

The developed methods for data processing and smoothing of the noise were realized in the works of students. Influence of scattered, moderated and delayed neutrons was estimated as 50% . These estimations are important for the answer to question about the instant of acceleration of fast electrons and deuterons in z-pinch discharges. It seems more probable, that acceleration occurs at the same time with uncertainty of 5%.

The using of deconvolution of neutron signals made possible to estimate the amount about 40 % of scattered neutrons in diploma work and presentations of J. Hitschfel.

Ratio of HXR and neutron signals was used for comparison of energy of fast electrons and deuterons in diploma work of M. Filingerova. The ratio of number of fast electrons and deuterons decreases with the time emission after its start of the pinch phase.

E. Litseva and O. Sila used the program of the MCNP code for estimation of the influence of scattered and moderated neutrons for different chamber configurations. J. Kortanek processed the interferograms with temporal ns resolution using the interpolation and extrapolation in the Matlab software. The reduction of the electromagnetic noise with adaptive filtration was studied by J. Cikhardt.

The problem of optimal number of detectors, their optimal distances from the neutron source and the advantage of placement of detectors in opposite directions solved K. Rezac in Ph.D. thesis [FEE CTU Prague. 2011]. He developed methods of the reconstruction of neutron and deuteron energy spectra in z-pinch experiments.

4. DISCUSSION ABOUT THE ROLE OF INTERNAL MAGNETIC FIELD IN THE PINCH DYNAMIC

The internal magnetic field and especially its poloidal component plays a dominant role at the dynamic of the Z-pinch discharge. It is self-generated with the dynamo effect during implosion of the current sheath. Using the interferometric diagnostics at PF-1000 we were able to correlate the hard X ray and neutron emission with transformation of the plasma density in the column. Hard X rays and fusion neutrons are produced in four different phases of plasma column transformations - at the time of the dense plasmoid formation, at the time of escape of the plasma and current density from the region between dense structure and anode,

at the development of the constriction and at the integration of the lobule into the column. These transformations can be explored with common spontaneous evolution of toroidal and poloidal magnetic field leading to the formation of the force-free structures with minimal energy. The high energy electrons and deuterons are produced with annihilation of opposite components of magnetic field during reconnection of magnetic lines. A quantified base for calculations could give the experimental measurement of magnetic field inside of the pinch. The methods using magnetic probes were developed in Trinity (Troitsk). Members of this team used the probes on the PF-1000 in 2010 and 2011. The probes located radially in 4 cm from anode axis proved existence of axial magnetic field in the 1 cm layer in front of the imploded current sheath. The probe located at the anode axis proved presence of the axial component of magnetic field inside the plasmoid and inside the helical structures at the surface of the plasma column. The results are prepared for publication.

5. CONCLUSIONS

We provided experimental research of the plasma produced on the z-pinch and plasma focus devices filled with deuterium gas. Investigation was done on the PFZ -200 in Prague, PF- 1000 in Warsaw, S-300 in Moscow and GIT 12 in Tomsk in Russian Federation with comprehensive X ray, neutron and interferometry diagnostics. During investigations the energy spectra of neutrons and deuterons were calculated using Monte Carlo simulation and adapted time-of-flight analysis. The interferometry installed on the PF-1000 enabled to describe the plasmoidal, toroidal and helical structures in the plasma column and their evolution. Neutrons were produced in correlation with formation and disintegration of plasmoids and constrictions. On the z-pinches S-300 and GIT-12 the gas-puff injection of deuterium was tested. The characteristics of neutrons produced in both PF and z-pinches were compared at the currents of 1-2 MA and their similarity and differences were described. On the PF-1000 the modified electrode system with cathode disk was used and the results showed moderation of plasma transformation and the lower neutron yield at the higher energy density in the column. Experimental evidence of thermonuclear neutrons was published. The results obtained can be used as enter parameters for simulations of the neutron production on the devices above 2 MA.

ACKNOWLEDGEMENT

This research has been supported by the research program No. LA08024 “Research in Frame of the International Center for Dense Magnetized Plasmas”, No. ME09087 “Research of Plasma of Fast Z-Pinches”, “Research Center of Laser Plasma” LC528 of the Ministry of Education, Youth and Sport of the Czech Republic and the GACR grants No. 202-08-H057 “Modern Trends in Plasma Physics”, grant CR IAEA 14817 “Research of D-D fusion reactions at the CTU in Prague”, grant CTU SGS 10-2660-OHK3-3T-13.

REFERENCES

[1] KUBES, P., KLIR, D., KRAVARIK, J., LITSEVA, E., REZAC, K., Research of D-D Fusion Reactions at the CTU in Prague, Plasma Phys. Reports, 35 (2009) 824.

[2] KUBES, P., KLIR, D., KRAVARIK, J., REZAC, K., Neutron Production at the Small Plasma Focus Device with Antianode, IEEE Transactions on Plasma Science, 37 (2009) 1786.

[3] KLIR, D., KUBES, P., KRAVARIK, J., REZAC, K., ANAN'EV, S.S., BAKSHAEV, Y., BLINOV, P.I., CHERNENKO, A.S., KAZAKOV, E.D., KOROLEV, V.D., USTROEV, G.I., Neutron energy distribution function reconstructed from time-of-flight signals in deuterium gas puff Z-pinch, IEEE Transactions of Plasma Science, 37 (2009) 425.

[4] KUBES, P., KLIR, D., KRAVARIK, J., REZAC, K., BOHATA, M., SCHOLZ, M., PADUCH, M., IVANOVA-STANIK, I., KARPINSKI, L., TOMASZEWSKI, K., Determination of Deuteron Energy Distribution from Neutron Diagnostics in a Plasma Focus Device, IEEE Transactions on Plasma Science, 37,(2009) 83.

[5] KUBES, P., PADUCH, M., PISARCZYK, T., SCHOLZ, M., CHODUKOWSKI, T., KLIR, D., KRAVARIK, J., REZAC, K., IVANOVA-STANIK, I., KARPINSKI, L., TOMASZEWSKI, K., ZIELINSKA, E., Interferometric Study of Pinch Phase in Plasma Focus Discharge at the Time of Neutron Production, IEEE Transactions on Plasma Science, 37 (2009) 2191.

[6] KUBES, P., PADUCH, M., PISARCZYK, T., SCHOLZ, M., CHODUKOWSKI, T., KLIR, D., KRAVARIK, J., REZAC, K., IVANOVA-STANIK, I., KARPINSKI, L., TOMASZEWSKI, K., ZIELINSKA, E., Transformation of the Pinched Column at the Time of Neutron Production, IEEE Transactions on Plasma Science, 38 (2010) 672.

[7] KLIR, D., KRAVARIK, J., KUBES, P., REZAC, K., CIKHARDT, J., LITSEVA, E., HYHLIK, T., ANAN'EV, S.S., BAKSHAEV, BRYZGUNOV, V. A., CHERNENKO, A.S., KALININ, YU.G., KAZAKOV, E.D., KOROLEV, V.D., USTROEV, G.I., ZELENIN, A. A., JUHA, L., KRASA, J., VELYHAN, A., VYSIN, L., SONSKY, J., VOLOBUEV, I.V., Efficient production of 100 keV deuterons in deuterium gas puff Z – pinches at 2 MA current, Plasma Physics and Controlled Fusion 52 (2010) 065013.

[9] KUBES, P., PADUCH, M., PISARCZYK, T., SCHOLZ, M., CHODUKOWSKI, T., KLIR, D., KRAVARIK, J., REZAC, K., IVANOVA-STANIK, I., KARPINSKI, L., TOMASZEWSKI, K., ZIELINSKA, E., SADOWSKI, M. J., Spontaneous Transformation of Magnetic Fields as a Mechanism which Regulate Dynamics in Plasma Focus, IEEE Transactions on Plasma Science 39 (2011) 562.

[10] KLIR, D., KUBES, P., PADUCH, M., PISARCZYK, T., CHODUKOWSKI, T., SCHOLZ, M., KALINOWSKA, Z., ZIELINSKA, E., BIENKOWSKA, B., HITSCHFEL, J., KARPINSKI, L., KORTANEK, J., KRAVARIK, J., REZAC, K., IVANOVA-STANIK, I.., TOMASZEWSKI, K., Experimental Evidence of Thermonuclear Neutrons in Modified PF-1000 Plasma Focus, Applied Physics Letters, 98 (2011) 071501.

[11] KLIR, D., KRAVARIK, J., KUBES, P., REZAC, K., LITSEVA, E., TOMASZEWSKI, K., KARPINSKI, L., PADUCH, M., SCHOLZ, M., Fusion Neutron Detektor for Time-of-Flight Measurements in Z-Pinch and Plasma Focus Experiments, Rev. Scient. Instruments 82 (2011) 033505.

STOCHASTIC PROCESSES AT DENSE PLASMA BEAMS INTERACTION WITH CONSTRUCTION MATERIALS

T. LAAS, A. AINSAAR, K. LAAS, R. MANKIN, J. PRIIMETS, A. REKKER, V. SHIROKOVA, Ü. UGASTE

Institute of Mathematics and Natural Sciences
Tallinn University
Estonia

Abstract

In this work processes at dense plasma beams, electrons and high energy ions interaction with construction materials of fusion devices are investigated. Experimental research of stochastic phenomena at plasma - materials interaction are carried out using dense magnetized plasma devices PF-12 and PF-1000 as plasma sources generating 1 keV plasma and 100 keV ions.

1. INTRODUCTION

A number of different types of large fusion facilities are in progress. Many of the basic problems facing the specialists are common for both (magnetic and inertial confinement types) main types of fusion energy facilities as well as for different alternative ones. One of the main problems still deficiently investigated is connected with material sciences, namely, how longstanding irradiation and heat loads generated in fusion devices affect the construction materials (first-wall and invertor materials) of the fusion devices, which are in direct exposure of plasma, X-radiation and neutron flows, as well as how it affects other materials used in construction and diagnostics (low-activation metal alloys, ceramics, optical materials). Therefore it is of utmost importance to carry out investigations into the structural defects appearing in materials due to irradiation, using different types devices including dense magnetized plasma (DMP) devices, which can generate high power heat loads and irradiation.

For prediction of defects generated in the the structure of materials it is important to find out the characteristics of stochastic processes in plasma and/or heat and materials interaction. Analysis of the density and characteristics of surface and inner defects, the conditions (density of plasma flow, density of energy flow etc) of generation and development of defects under irradiation utilizing DMP devices provides data to predict material damage by high temperature plasma and ion beams whose characteristics are close to those realized at plasma disruption in ITER.

The overall objective of this project is to carry out investigations using generation of powerful radiation and heat loads with DMP devices to test their effect on different materials which are of interest for both types of fusion facilities, analysis of the generated structural defects, and elaboration of a phenomenological theory which allows to predict the characteristics of defects of construction materials, generated by plasma beams, irradiation and heat load.

The specific objectives were as follows:

— by means of our own as well as the partners' (Warsaw Institute of Laser Microfusion and Plasma Physics) DMP devices, to carry out experiments with high energy plasma, ions and electron beams investigate their influence on low-activation steels, tungsten and its alloys,

to analyze the outputs and compare them with the results of experiments carried out by other types of devices;

— to develop the DMP technology and diagnostics of soft and hard X ray as well as neutron pulses for fusion application;

— to investigate the basic processes in construction materials and on contact surfaces of materials used in large fusion facilities due to direct and indirect irradiation and heat loads.

— to elaborate a theory of stochastic interaction of high power plasma flow and materials.

2. DEVELOPMENT OF PLASMA FOCUS DEVICE PF-12

The DMP device PF-12 was constructed during 2006-2007. As preliminary tests with the initial configuration of the electrode set (anode, cathodes and insulator) with nitrogen, argon and hydrogen indicated the need for a change in the electrode configuration, the instalment of a new electrode set and preliminary testing of the device with a new setup was carried out at Tallinn during several joint experimental sessions with our CRP partners from Warsaw Plasma Physics and Laser Microfusion Institute (Poland) during 2008 (see Fig. 1). Experiments with deuterium as working gas indicated the presence of 2.45 MeV neutrons and soft X rays due to microfusion processes in the experimental chamber at a 1.1-1.5 Torr pressure of gas. In 2011 a new chamber was installed allowing to carry out plasma-materials tests as well as various photometric or spectrometric analyses of phenomena taking place at the moment of pinch or plasma-materials interaction.

Measurements of the current *I*, current derivative *dI/dt* and a simultaneous measurement of X rays and neutrons (the Warsaw Plasma Physics and Laser Microfusion Institute's detector was used) in the case of deuterium as work gas show that neutrons are generated even in case the drop of the current *I* due to pinch is quite small (Figs. 2, 3). A preliminary estimate of neutrons per shot was about 10^6 - 10^7.

a *b*

FIG. 1. a) Chamber of the dense plasma focus device PF-12. Most of the device is behind the front panels. b) New chamber, suitable for simultaneous spectroscopic and photometric measurements in the process of sample irradiation.

With the new configuration of electrodes the current rise time was $T_{1/4} = 1.8\mu s$. PF-12 allows operation with the voltage range *U=16..25 kV*, while I_{max} *= 160..260 kA.*

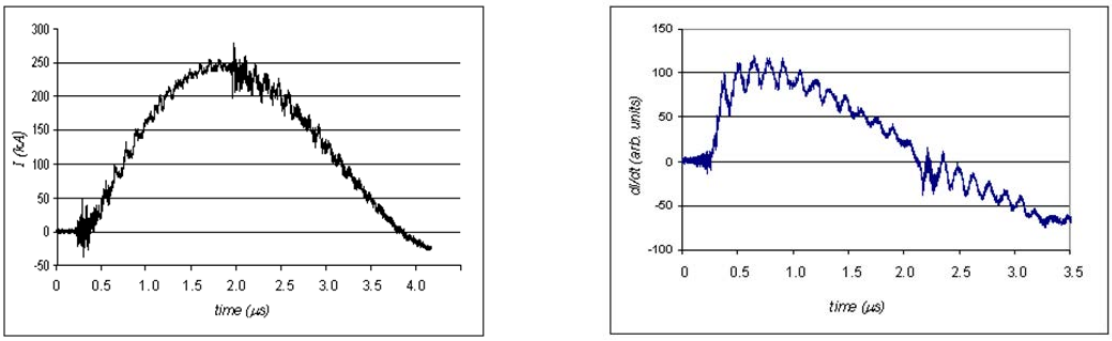

a *b*

FIG. 2. a) Dependence of current (I) on time (t) with a 25 kV voltage load on the capacitors. The maximum current is about 250 kA. b) Dependence of dI/dt on time t. The pinch is located at about 1.8 μs fromthe start of shot.

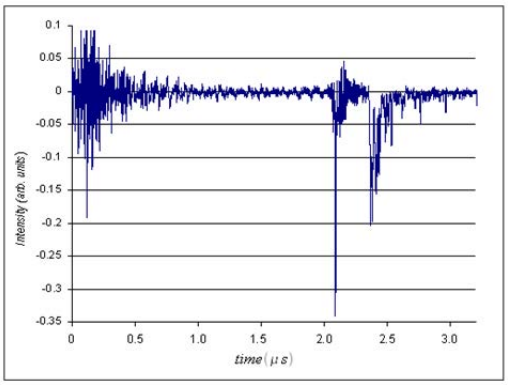

FIG. 3. Dependence of registered neutron and X ray radiation on time. Negative values indicate the intensity of the radiation. The first peak at about 1.9 μs is due to soft X rays, the second peak at about 2.15 μs after start is due to neutrons.

3. IRRADIATION OF SAMPLES WITH FAST IONS, PLASMA BEAMS AND NEUTRONS

Experiments with plasma focus devices are of a special interest for investigation of interaction of powerful plasma streams and fast ions streams with materials [1, 2, 3]. In these experiments material samples in the form of plates are placed in front of the anode on the axis of the chamber (see Fig. 4). Fast ions, plasma streams, radiation and neutrons affect the target. The power flux density may be up to ~ 10^{12} W/cm^2 (depending on the PF device parameters) and the duration of the plasma pulse is in the interval of 10^{-8}-10^{-6} s. The joint experiments were planned and carried out in PF-12 (Tallinn University) with power flux densities of $5\times10^6..5\times10^8$ W/cm^2 and in PF-1000 (Warsaw Institute of Plasma Physics and Laser Microfusion) with a power flux density of about 10^{12} W/cm^2, in cooperation with the teams of Moscow Physical Society and A.A. Baikov Institute of Metallurgy and Material Science's.

The experimental setup for PF-12 is shown in Fig. 4. In a case of a DPF device three different regimes can be used [2]: (i) implantation mode of irradiation; where the power flux density of the streams is $q \approx 10^5 - 10^7 W/cm^2$; (ii) detachment mode; screening of the surface by a secondary plasma cloud - $q \approx 10^7 - 10^8 W/cm^2$; (iii) explosive destruction mode; strong damage with absence of implantation - $q \approx 10^8 - 10^{10} W/cm^2$. The regime and power flux density were changed by changing the distance between anode and sample from 10.5 to 3.5 cm. At PF-1000 only the destructive mode with $q \approx 10^{12} W/cm^2$ was used.

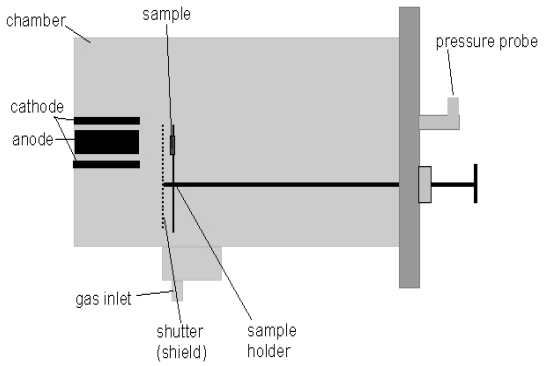

FIG. 4. Experiment setup at PF-12. The sample for plasma-ions irradiation is located on the holder at about 3-10 cm from the anode.

3.1. Investigations considering low activation stainless steels

Considering that in different thermonuclear devices (e.g. inertial confinement devices) not only W, Be and CFC (which are the main functional materials for ITER), but also low activation stainless steels are used, we also investigate the influence of high-density plasma on stainless steels in current research. The effect of plasma on Eurofer 97, besides other steels, was analysed in the previous research [1, 2]. In the current period our workgroup has been concentrating on two martensitic-ferritic stainless steels: B.S. 92B and B.S. 183A [3, 4]. The chemical composition of these steels in comparison with Eurofer 97 is given in Table 1.

TABLE 1. CHEMICAL COMPOSITION OF STAINLESS STEELS (%)

Elements	BS 183 A	BS 92 B
C	0.172	0.15
Si	0.37	0.42
Mn	0.35	0.42
Cr	12.14	15.92
Mo	0.12	0.17
Ni	1.85	2.12
Co	0.036	0.04
Cu	0.93	0.13
Nb	0.006	0.006
Sn	0.003	0.006
V	0.09	0.07
W	0.006	0.02
In minute amounts: S, Al, Ca, N, O, P		

The metal alloy samples (two types of stainless steel and tungsten for comparison) samples were in the form of $1\times1\times0.2$ cm^3 plates. Analysis of the irradiated sample's surface has been carried out using scanning electron-microscope images and by microroughness measured by MAHR Perthometer Concept (MFW 250). It can be concluded that in the case of stainless steel (B.S. 183A) a layer with a thickness of about 12 μm has been eroded. In the case of tungsten the thickness of the eroded layer is about 1-2 μm. As for defects, comparison with a tungsten sample irradiated in the same conditions shows that in stainless steel the defects are about four times as high as in tungsten.

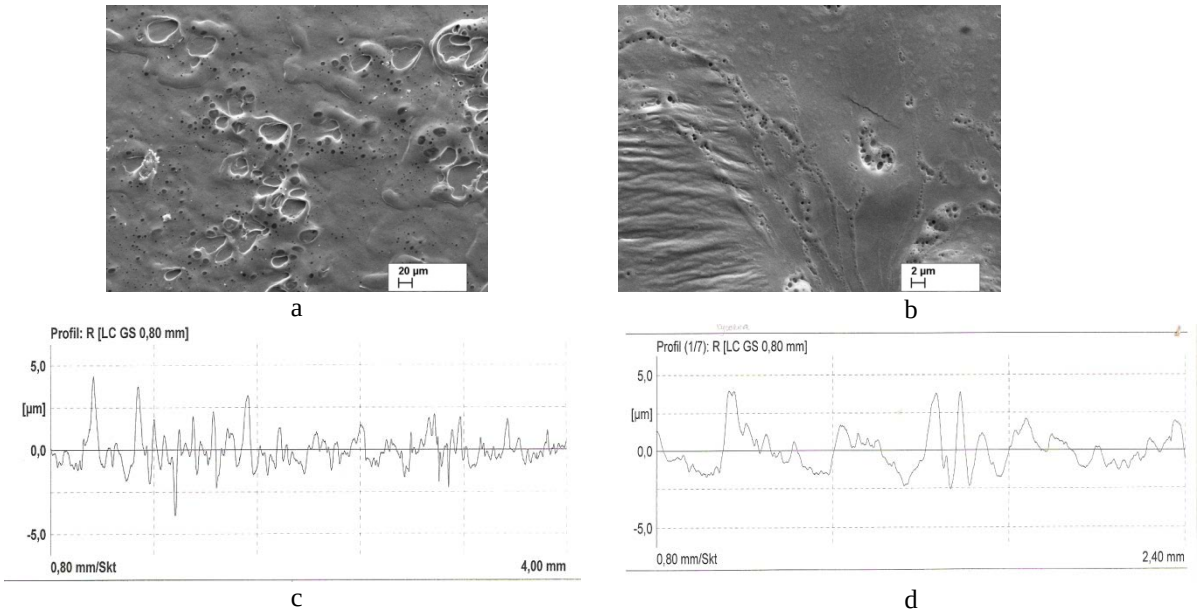

FIG. 5. Stainless steel samples irradiated in PF-12 by 8 shots, distance between anode and sample d= 3.5 cm, power flux density $q=5\times10^8$ W/cm^2. a) SEM image of steel B.S. 183A; b) microroughness profile of B.S. 183A, R_a = 0.87 µm; c) SEM image of steel B.S. 92B; d) microroughness profile of B.S. 92B, R_a = 1.01µm.

In Figures 5-7 SEM images of sample surfaces are given. In the case of stainless steel B.S. 92B formation of bubbles under the surface can be seen. Comparison with other samples enables the prediction that after the following shots of plasma flows these lines of bubbles will be a site of extensive damages after following shots (following plasma flows). Microcracks will appear and a reformation of macrocrystals begins. Also, a wavelike structure with a wavelength of about 80-100 µm can be seen. In Figures 6-7 it can be seen, that the surface of the sample is covered by a remelted layer of steel. Generally, the same defects can be seen in the steel B.S. 183A, irradiated in the same conditions.

For comparison, tungsten was irradiated in the same conditions as stainless steel. Due to the higher brittleness of tungsten a mesh of cracks appeared. In microscales lots of defects were detected (bubbles, craters, cracks, holes), but differently from stainless steels this remelted layer was thinner. Therefore, it can be concluded that if surface density of defects in tungsten is higher than in the case of steel, which it is due to the fact that vaporizing, (re)melting and (re)crystallization of steel has covered and erased the defects.

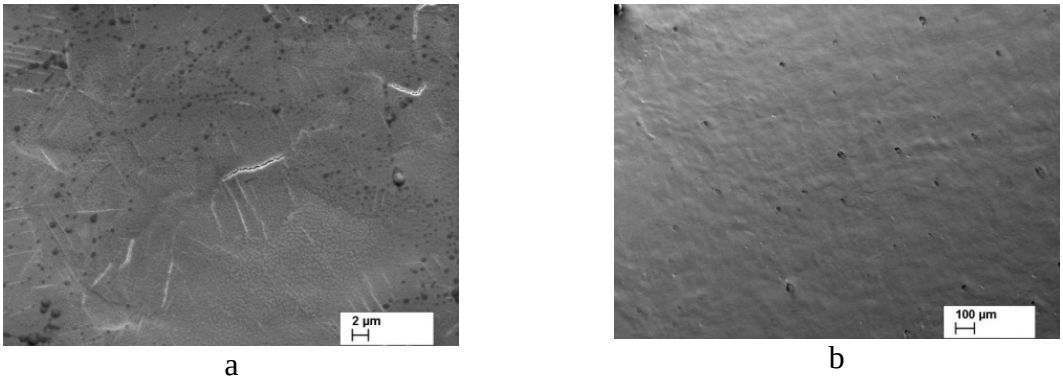

FIG. 6. Surface of stainless steel B.S. 92B after 8 shots. The power density is about (0.5-1)10^7 W/cm^2. The sample's distance from the anode is 6.5cm.

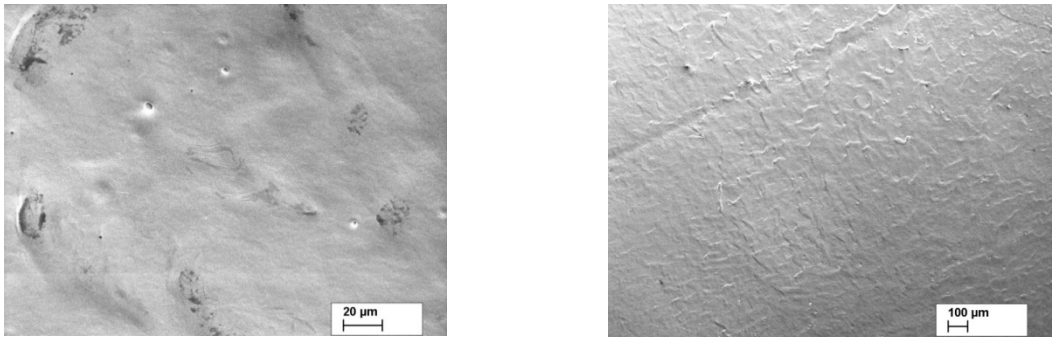

a b

FIG. 7. Surface of stainless steel B.S. 183B after 8 shots.The power density is about (0.5-1)10^7 W/cm^2. The sample's distance from the anode is 6.5cm.

3.2. Investigations considering tungsten and tungsten alloys

As samples tungsten (W) and tungsten doped with 1% lanthanum-oxide La_2O_3 (WL10) manufactured in PLANSEE from tungsten powder (by isostatic pressing, sintering and rolling the plates) were used. The W plates were 2 mm thick and the WL10 plates were 4 mm thick.

The power density may be up to about 10^{12} W/cm^2 (depending on the PF device parameters) and the duration of the plasma pulse is in the interval of 10^{-8}-10^{-6} s. However, the duration of secondary plasma with energies of some eV may last for hundreds of microseconds. The experiments were performed in PF-1000 (Warsaw Plasma Physics and Laser Microfusion Institute), in which case the power density of deuterium plasma and fast ions was about 10^{12} W/cm^2; and in PF-12 (Tallinn University), in which case the power density was varied from $5\cdot10^6$ - 10^9 W/cm^2. The surfaces and cross-sections of the irradiated samples were analysed by SEM, the microroughness of the samples surfaces was measured using MAHR Perthometer Concept (MFW 250). It has been found that microroughness can be used as a quite good estimate of macroscopic defects [10]. Also, the microhardness of the samples' cross-sections was measured.

Samples of irradiated tungsten (W) and tungsten alloys – tungsten dispersed with 1%La_2O_3 (WL10) - analyses were made together with our colleagues from A. A. Baikov Institute of Metallurgy and Material Sciences RAS.

The W and WL10 samples were irradiated by deuterium, the pressure of the working gas was 1.2 Torr and the reference voltage of the capacitors was 20 kV, i.e. all conditions were the same as in the case of stainless steels.

Analysis of microroughness showed that in the case of W the microroughness of the irradiated samples varied from 1.9-2.6 μm and in the case of W-1%La_2O_3 it varied from 3.3-3.9 μm, which is in the same magnitude as the initial roughness of non-irradiated material (for examples of surface profiles see Figures 8 and 9). This is different from stainless steels. On the other hand, the high-frequency component of roughness increases in the process of irradiation, showing emergence of small-size defects and their evolution.

Analysis of the SEM images (see Figures 10-13) of irradiated tungsten and tungsten alloy samples first indicates the appearance of cracks and a mesh of cracks in the case of W irradiated in a tough regime (a small distance of 3.5 cm between the sample and anode). This is similar to the effects of plasma irradiation found by other researchers. The case is different

with WL10 – there are fewer cracks, but the surface seems to be melted. However, it is still unclear whether the lack of melted surface in W is due to the tungsten vapor generated by low temperature plasma (E~0.1-1 keV) being blown off by high power ions (E~100 keV) later, or is there too little time for plasma-material interaction.

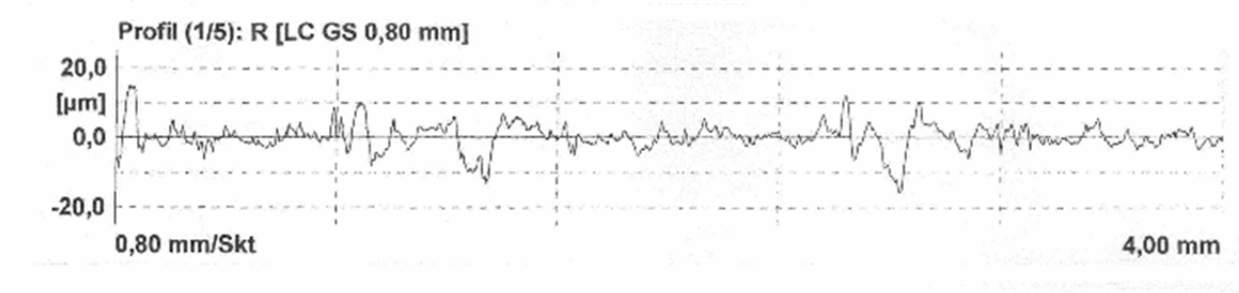

FIG. 8. Profile of W, roughness R_a =2.62 µm, number of shots 8, distance from anode 3.5 cm, power flux density q about 10^6-10^7 W/cm^2.

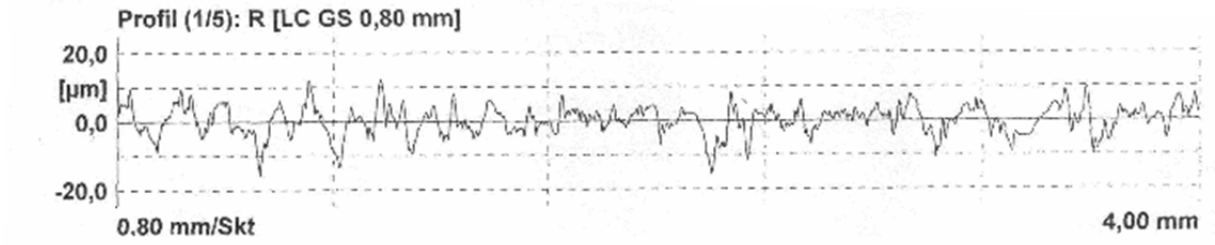

FIG. 9. Profile of W-1%La_2O_3, roughness R_a =3.28 µm, number of shots 8, distance from anode 3.5 cm, power flux density q about 10^6-10^7 W/cm^2.

Again, if the distance between sample and anode is 10.5 cm, the material is first influenced by fast ions and thereafter by low energy plasma. In this case the effect of deuterium plasma and vaporized and ionized tungsten plasma on the samples surface is longer, which leads to melting of the sample. Comparison of the irradiated samples - pure tungsten and tungsten dispersed with lanthanum oxide – shows that while in tungsten cracks and a mesh of cracks will appear, which is different from lanthanum oxide dispersed tungsten, then the surface of the last one seems to be more melted.

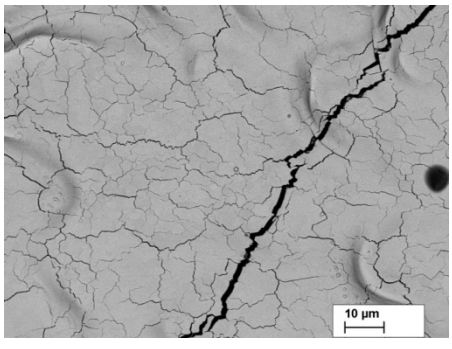

FIG. 10. W, distance between sample and anode 3.5 cm, 8 shots.

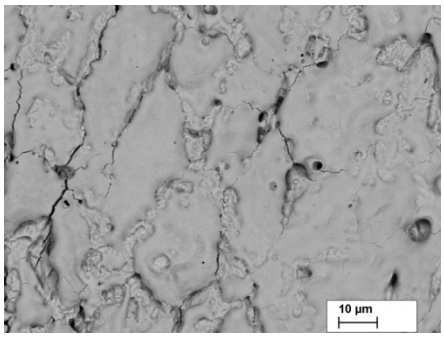

FIG. 11. WL10, distance between sample and anode 3.5 cm, 8 shots.

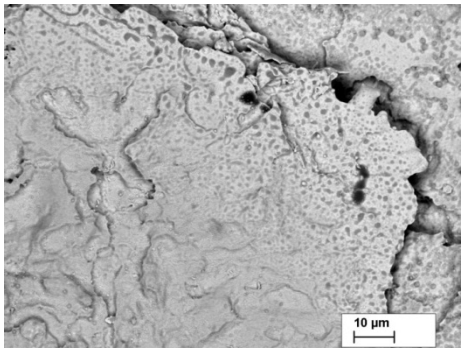

FIG. 12. W, distance between sample and anode 10.5 cm, 8 shots. The edge line has appeared due to the initial treatment (sintering and rolling) of the material.

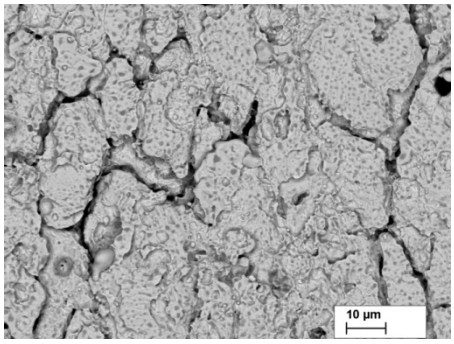

FIG. 13. WL10, distance between sample and anode 10.5 cm, 8 shots.

Tungsten (Fig. 14 b,d) and the samples irradiated at the PF-1000 device have the same melting traces. On the surface layer big cracks and meshes of small cracks have appeared. Strong melting traces are also revealed on both samples – W as well as WL10. On the surface layer of the tungsten and lanthanum-oxide alloy cracks have appeared, but tungsten, besides these damages, has other kinds of structures: bursted bubbles, just appeared bubbles (bubbles will develop from the white specks). The development of cracks and cracking, as well as the bursting of bubbles may be conditioned by the greater brittleness of pure tungsten in comparison with WL10.

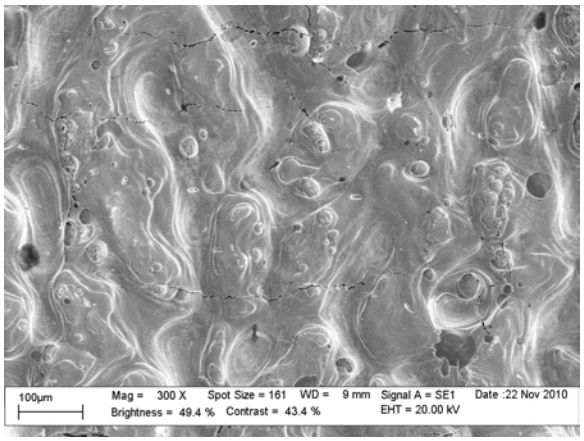

a

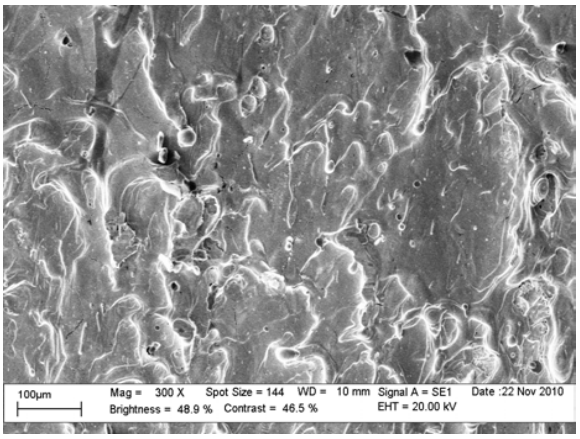

b

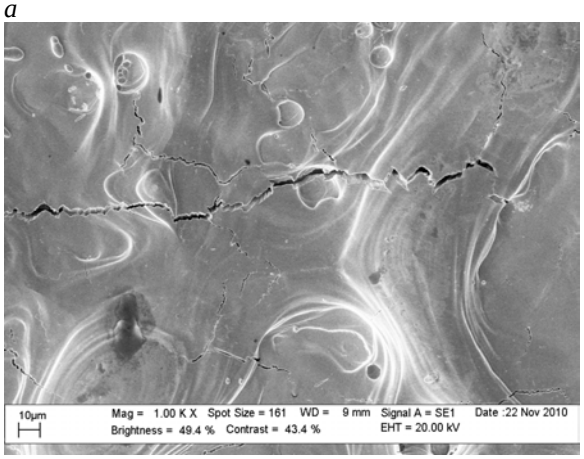

c

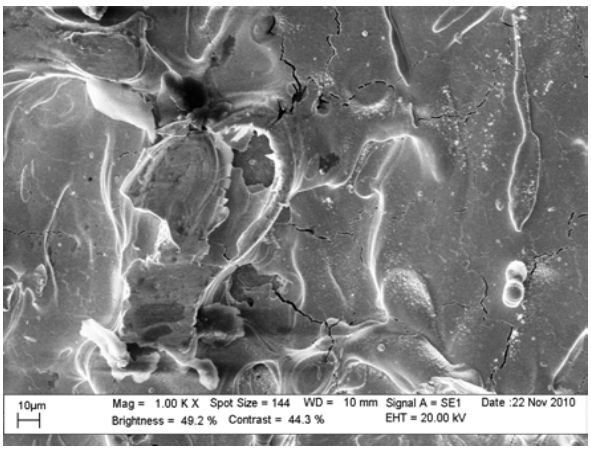

d

FIG. 14. Scanning electron microscopy images of the surfaces (irradiated in PF-1000) of tungsten and WL10: a,c – W, 2 shots, distance from the anode 7-7.5cm; b,d – WL10, 2 shots, distance from the anode 7-7.5 cm.

While at quite low power flux densities in WL10 the dominant defects were droplets, bubbles and holes, then in the case of a higher power flux density strong melting traces can be seen in WL10, with wavelike structures also found by other researchers. On the other hand, in pure tungsten, the density of microcracks is bigger, and also, cracked bubbles have appeared which at an increasing number of shots may lead to a bigger erosion of the material. Therefore it can be concluded that in WL10 the same characteristic defects appear at all power flux densities, while in tungsten more powerful plasma shots lead to more damaged surfaces and a change of dominating defects as the surface is covered with a mesh of microcracks. In WL10 microcracks will also appear, but their density is lower and their advancement with raising the number of shots is slower than in tungsten.

Cross-sections of samples were measured for hardness. The measurement results are given in Figures 15 and 16. It can be seen that hardness in the border layer changes abruptly, but deeper on the hardness oscillates near the mean value. In three cases it can be seen that there is a layer of lower hardness just below the first 30-60 μm layer. While tungsten samples have a decreased hardness zone insensitive to power flow density, then tungsten dispersed with 1% La_2O_3 has an about 250 μm thick layer with decreased hardness, though it should be noted that a sample irradiated with a power flux with a density of 10^{12} W/cm^2 first obtains a bigger hardness followed by a decreased hardness zone. The latter may be connected with melting and recrystallization of the surface layer. With increasing depth a hardness gradient appears in some samples. Hardness increases at depths bigger than the thermal influence zone. The reason may be in the shockwave effect of plasma on the material or in the preprocessing of the materials.

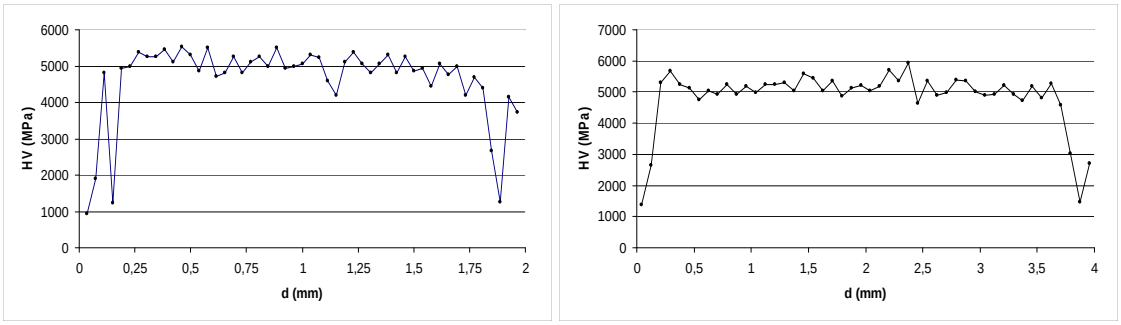

a b

FIG. 15. Hardness of cross-sections: a - tungsten, 2 shots, distance from the anode 3.5 cm; b - WL10, 2 shots, distance from the anode 3.5cm. d – distance from the irradiated surface; HV – microhardness.

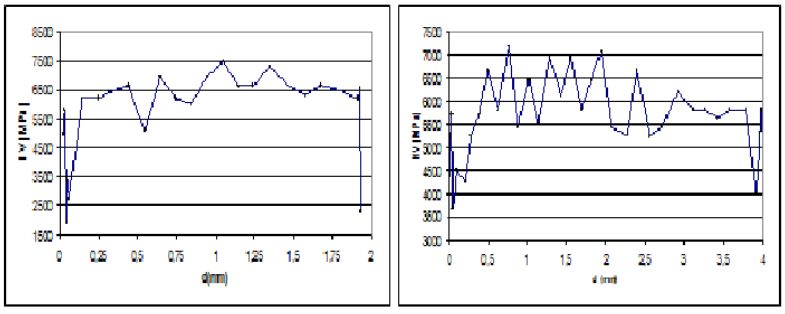

a b

FIG. 16. Hardness of cross-sections: a - tungsten, 2 shots, distance from the anode 7.0 cm (sample no. 11); b - WL10, 2 shots, distance from the anode 7.0 cm (sample no. 12); d – distance from the irradiated surface; HV – microhardness.

We can conclude that at small power flux densities, comparison of the surface defects in W and WL10 shows that microroughness, which characterizes macroscopic damages (with a characteristic length of 10-100μm and a height less than 1 μm), is about 1.5 times bigger in WL10. But an increase of the number of shots does not very much increase microroughness. Also, the characteristic damages in different materials are different: in WL10 bubbles, holes and wavelike structures dominate, while in pure tungsten a mesh of microcracks will appear. In the case of powerful shots the surface of pure tungsten is damaged more, but notably, while the dominating damage types will be the same for WL10 at all power flux densities, in tungsten craters will also appear, and the wavelike structure is more stochastic. The occurrence of craters and a mesh of microcracks in tungsten may be connected with the brittleness of tungsten and the smaller ductility of pure tungsten. Therefore, it may be concluded that a doping in tungsten may lead to a decrease in defects with sharp edges (craters, cracks) which in turn may lead to a detachment of bigger drops of material from the surface.

A preliminary investigation of the microhardness of the samples cross-sections shows that due to irradiation the hardness of the first layer will increase, while there follows quite a thick layer with a lower hardness. The thickness of the not so hard layer is the same in both sides of the samples. But powerful shots lead to a fluctuating microhardness in WL10, which may be caused by mechanical shocks of a shot-noise type on the material surface.

4. RESEARCH OF DIFFUSION IN MULTI-COMPONENT MATERIALS

Results and the papers published during the project are connected with theoretical as well as with experimental research of plasma - materials direct interaction, interaction of construction materials induced by plasma generated heat flow and diffusion of materials due to heat flow.

Stochastic processes generated on the contact surfaces of different construction materials due to heat and plasma flow on the materials, are tightly connected with diffusion phenomena. Investigation and explanation of the dependence of diffusion paths on system parameters and their a priori explanation is one of the most actual problems in experimental research of interdiffusion in multicomponent systems. In the current project the influence of diffusive mobility of component alloys and thermodynamic factors on effective diffusion coefficients and diffusion paths has also been investigated. As an outcome of the project, it has been shown that the deviation of a diffusion path from the ideal path (line in a ternary system) is mainly caused by the system's thermodynamic properties. This has been analysed more thoroughly in experiments with Co-Fe-Ni and Cu-Fe-Ni ternary systems, where it has been shown that effective interdiffusion coefficients are connected with changes of the thermodynamic properties in alloys and of diffusion path formed in the diffusion pair. [5-7]

For different diffusion pairs (e.g. 65Ni30Cu5Fe – 29.5Ni16.5Cu54Fe, 49.5Ni50.5Fe – 51Ni 49Cu, 84Cu16Ni – 50Ni50Fe, heated by 1000^{o}C 196h) the slope function of the diffusion path was calculated using the relation between thermodynamical factors and diffusion paths. The analytical results were compared with the numerical values of slope functions gained from experimental data. It turned out that the experimental and calculated values of the slope function of the diffusion path coincided despite the significant diffenerce between isotopic diffusion coefficients of components. This allowed us to conclude that the deviation of the diffusion path from linearity depends mainly on the system's thermodynamical properties. [5, 7] In our research it was shown that if the interdiffusion

coefficients of the components do not differ signicifantly from each other, the slope function of the reduced concentrations dY_{Co}/dY_{Ni} ($Y_i=(c_i-c_i')/(c_i''-c_i')$, where c_i' and c_i'' are the initial concentrations of the *i*-th component in the two alloys respectively) can be found using just the initial concentrations. This allows us to find diffusion path for different diffusion pairs knowing only the diffusion path for one pair, in the area investigated [7]. It was the first time that experimental evidence for the Kirkendall effect in was found a ternary system. The Kirkendall effect in ternary systems is based on the same physics as in two component diffusion pairs.

5. INVESTIGATION OF A STOCHASTIC OSCILLATOR MODEL AND ITS CONCLUSIONS FOR PLASMA-MATERIALS INTERACTION

In our theoretical investigations systems consisting of ensembles of oscillators under the influence of a Gaussian white noise and coloured noise are analysed [8-12], which is mathematically modeled with the equation

$$\ddot{X}+\gamma\dot{X}+(\omega^2+Z(t))X=A_0\sin(\Omega t)+\xi(t), \tag{1}$$

where X is the oscillator's displacement, $\dot{X}\equiv dX/dt$, $\xi(t)$ is the Gaussian white noise describing the heat bath by temperature, and *Z(t)* is a colored noise which at certain parameters can be taken as shot noise, which in case of certain parameters can be interpreted also as shot noise and/or plasma flux. Such system mimics the behavior of atoms (as oscillators) in crystals. The model systems investigated show that at certain noise parameters the second moments of oscillator displacements may increase without limit while the mean value of the displacements remains finite, which means generation of defects in the crystal structure. This may be connected with energetic instability of the system [8-12]. It should be noted that such system behavior can be observed only in the presence of both noises. This can give an explanation to the emergence of cracks in tungsten or other materials below the first layers, which are directly affected by high temperature plasma, ions and heat load [10]. It can be concluded that in plasma – materials interaction, layers deeper than those, directly affected by the plasma-ions flux, should also be carefully investigated, because, as has been shown, the presence of at least two different noises may essentially increase the mobility of atoms and new defects and vacancies in materials may be generated. [9]

Next models for oscillatory systems described by a generalized Langevin equation were analysed [13-16]. Model for one selected direction for a particle's (with mass m=1) in the fluctuating harmonic potential

$$V(X,t)=(\omega^2+Z(t))\frac{X^2}{2} \tag{2}$$

subjected to a linear friction with a memory kernel $\eta(t)$, an additive periodic force and an internal random force $\xi(t)$ of zero mean:

$$\ddot{X}+\int_0^t\eta(t-t')\dot{X}(t')dt'+\frac{\partial}{\partial X}V(X,t)=A_0\sin(\Omega t)+\xi(t), \tag{3}$$

where $\dot{X}(t)\equiv dX/dt$, $X(t)$ is the particle's displacement and A_0 and Ω are the amplitude and the frequency, respectively. The random force $\xi(t)$ is Gaussian and describes the heat bath temperature. If *Z(t)* does not vanish, an anomalously diffusive particle is subjected to the so-called memory effect. The memory kernel $\eta(t)\sim\gamma\tau^{-\alpha}E(t,\tau)$ depends on the friction

coefficient γ, the memory correlation time τ and a function $E(t,\tau)$. Exponent α can be taken as $0 < \alpha \leq 1$. It has been shown that in certain forms of the function E equation (3) can describe the diffusion of particles (and the diffusion flow) in viscoelastic media such as, for example, glasses, colloidal suspensions, polymer solutions, strongly coupled dusty plasmas and materials near of melting temperature.

We have studied, in the long-time regime, the response function and the complex susceptibility of a stochastic fractional oscillator with a power-law memory kernel for the friction term. The influence of the fluctuating medium is modeled by a multiplicative dichotomous noise *Z(t)*. The Shapiro-Loginov formula allowed us to find a closed system of equations for the first-order moments and an exact expression for the complex susceptibility. A major virtue of the investigated model is that an interplay of the colored dichotomous noise, the external periodic forcing, and memory effects in a noisy, fractional oscillator can generate a rich variety of nonequilibrium cooperation phenomena such as (i) multiresonance of the imaginary part of the susceptibility versus frequency of the driving force up to three peaks; (ii) existence of a critical memory exponent below which the resonance vs driving force frequency of the amplitude of the mean oscillator displacement <X> occurs for all values of the other system parameters; (iii) friction-induced multiresonance, i.e., two resonance peaks of the response function can be evoked by varying the friction coefficient; (iv) a nonmonotonic dependence of the response function on the amplitude *a* and the switching rate of the multiplicative noise i.e., stochastic resonance; (v) existence of a band gap for values of the friction coefficient between two regions of phase diagrams where SR vs *a* is possible at sufficiently small values of the memory exponent α, and the associated friction-induced reentrant transitions between different dynamical regimes of the oscillators. [14, 15]

One of our main results is that the energetic stability of a noisy fractional oscillator can be significantly enhanced at intermediate values of the memory exponent. We have shown that this interesting effect can be interpreted in terms of nonmonotonic dependence of dissipation on the memory of the viscoelastic friction kernel. As another main result we have found a multiresonance of the output signal-to-noise versus both the memory exponent and the friction coefficient. We show that these phenomena are significantly associated with the critical characteristics of stochastic parametric resonance. Furthermore, the memory of the friction kernel can induce repeated reentrant transitions between different dynamical regimes of the oscillator. Namely, in some cases an increase of the memory exponent induces transitions from a regime where the system is energetically unstable to a stable regime, but instability appears again through a reentrant transition at higher values of the memory exponent. It is remarkable that in the case of an additive external noise, related phenomena involving memory-induced energetic stability and, associated with that, a resonance-like behavior of signal-to-noise-ratio versus the memory exponent occurs for the unbound system, i.e., the harmonic potential is absent. The last mentioned phenomena are a manifestation of the cage effect which is present due to the viscoelastic friction kernel. [13, 16]

ACKNOWLEDGEMENTS

This work was supported by the International Atomic Energy Agency Grants No. 14797, and by the Ministry of Education and Research of Estonia under Grant No. SF0132723s06, and by the European Union through the European Regional Development Fund (Centre of Excellence Mesosystems: Theory and Applications, TK114).

REFERENCES

[1] GRIBKOV, V.N., DYOMINA, E.V., DUBROVSKY, A.V., IVANOV, L.I., KOVTUN, A.V., LAAS, T. I., MASLJAEV, S.A., PIMENOV, V.N., TARTARI, A., UGASTE, Yu.E., SCHOLZ, M., KOLMAN, B., Influence of pulsed deuterium and hydrogen plasma beams on ferritic and austenitic steel at Dense Plasma Focus device, J.of Adv. Mater. **1** (2008) 16.

[2] PIMENOV, V.N., DEMINA, E.V., MASLYAEV, S.A., IVANOV, L.I., GRIBKOV, V.A., DUBROVSKY, A.V., UGASTE, Ü., LAAS, T., SCHOLZ, M., MIKLASZEWSKI, R., KOLMAN, B., TARTARI, A., Damage and modification of materials produced by pulsed ion and plasma streams in Dense Plasma Focus device, Nukleonika **53** 3 (2008) 111.

[3] PELÕHH, V., AINSAAR, A., LAAS, T., The change and transformation of mechanical characteristics of alloys under the plasma influence, Materials, Methods & Technologies **4** 2 (2010) 352.

[4] BARASHKOVA, T., LAAS, T., PELÕHH, V., „Methods for Estimating the Damage Factor of Materials under the Influence of Plasma“. In: Proc. of the 7th Inter. Conf. of DAAAM Baltic Industrial Engineering: 7th International Conference of DAAAM Baltic Industrial Engineering, Tallinn, Estonia, 22-24.april 2010 (KÜTTNER, R., Ed.) Tallinn: Tallinn University of Technology Press (2010) 462.

[5] UGASTE, Ü., PRIIMETS, J., LAAS, T., Dependence of diffusion paths on thermodynamic factors in ternary systems. Defect and Diffusion Forum, **277** (2008) 119.

[6] PRIIMETS, J., UGASTE, Ü., Diffusion paths in the ternary system Fe-Co-Ni: an empirical approach. Defect and Diffusion Forum, **312-315** (2011) 411.

[7] UGASTE, Ü., KODENTSOV, A., PRIIMETS, J., Investigation of the Interdiffusion and Kirkendall Effect in the Co-Ni-Fe System. III. Dependence of Diffusion Parameters on the Initial Conditions. The Physics of Metals and Metallography, **110** 5 (2011) 485.

[8] MANKIN, R., LAAS, K., LAAS, T., REITER, E., Stochastic multiresonance and correlation-time-controlled stability for a harmonic oscillator with fluctuating frequency. Physical Review E, **78** 3 (2008) 031120.

[9] MANKIN, R., LAAS, T., SOIKA, E., SAUGA, A., REKKER, A, AINSAAR, A., UGASTE, Ü. Coloured-noise-induced transitions in nonlinear structures, Nukleonika **53** (3) (2008) 127.

[10] MANKIN, R., LAAS, K., SAUGA, A., Generalized Langevin equation with multiplicative noise: Temporal behavior of the autocorrelation functions. Physical Review E, **83** 6 (2011) 061131.

[11] LAAS, K., MANKIN, R., REITER, E., Influence of memory time on the resonant behavior of an oscillatory system described by a generalized Langevin equation. International Journal of Mathematical Models and Methods in Applied Sciences, **5** 2 (2011) 280 - 289.

[12] LAAS, K., MANKIN, R., REKKER. A., The influence of noise kurtosis on the dynamics of a harmonic oscillator with fluctuating frequency. International Journal of Mathematical Models and Methods in Applied Sciences, 3 1 (2009) 27.

[13] MANKIN, R., REKKER, A., Memory-enhanced energetic stability for a fractional oscillator with fluctuating frequency. Physical Review E, 81 4 (2010) 041122.

[14] SOIKA, E., MANKIN, R., AINSAAR, A., Resonant behavior of a fractional oscillator with fluctuating frequency. Physical Review E, 81 1 (2010) 011141.

[15] LAAS, K., MANKIN, R., „Friction-induced Resonance in a Noisy Fractional Oscillator“. In: Application of Mathematics in Technical and Natural Sciences: Proc. of the 2nd International Conference: 2nd International Conference - AMiTaNS-10, Sozopol, Bulgaria, 21-26 June 2010. (TODOROV, M.D., CHRISTOV, C. I., Eds.) Christov. Melville, New York, USA: Springer-Verlag, (Book Series: AIP Conference Proceedings; 1301) (2010) 205.
[16] SAUGA, A., MANKIN, R., AINSAAR, A., Noisy fractional oscillator: Temporal behavior of the autocorrelation function. WSEAS Transactions on Systems, **9** 10, (2010) 1019.

MODERNIZATION OF PF-1000 FACILITY FOR THE GOALS OF THE MAIN-STREAM FUSION RESEARCHES

M. SCHOLZ[*,**], V.A. GRIBKOV[*,**,***], L. KARPINSKI[*,**], S. JEDNORÓG[**], A. SZYDŁOWSKI[+], M. PADUCH[**], B. BIEŃKOWSKA[*,**], R. PROKOPOWICZ[*,*], E. ZIELINSKA[**]

[*] International Centre for Dense Magnetized Plasmas, Warsaw, Poland
[**] Institute of Plasma Physics and Laser Microfusion, Warsaw, Poland
[***] A.A.Baikov Institute of Metallurgy and Material Science, Moscow, Russian Federation
[+] The Andrzej Soltan Institute for Nuclear Studies, Warsaw, Poland

Abstract

Investigations provided with the PF-1000 facility is intended for use it in two programs related to the main-stream fusion researches – testing of various materials counted to be the candidate ones for the first-wall elements of fusion reactors and neutron activation measurements as a benchmark against numerical calculations. Besides these fields the efforts with this apparatus were directed along two main lines of investigation of physics of the DPF devices themselves: the understanding of the long-time scale dynamics, linked to the necessity of developing realistic scaling laws for the design of large energy PF devices, with evaluating their range of applicability, and the understanding of the short-time scale dynamics, including the intense anomalous effects accompanying the neutron production, and more recently, the very late phase of the implosion. For both the above groups of researches it was important to make operation of this largest DPF set-up with deuterium as a working gas more reliable as it was assembled on the base of high-voltage elements of 60's and it was exploited during more than 20 years to the moment. Thus a formidable work was done during this CRP on modernization of its most sensitive elements that were provided side by side with experiments in the field of radiation material science and in the sphere of activation experiments. Results of the upgrading of the device and its diagnostics as well as some data on materials' testing and neutron activation measurements are presented in this document.

1. INTRODUCTION

PF-1000 facility belongs to a class of Z-pinch devices known as Dense Plasma Focus (DPF). It has been for a long time the biggest device of this type operating with deuterium as a working gas and consequently producing fusion neutrons of 2.5 MeV energy with parameters: total yield per shot – up to $6 \cdot 10^{11}$, pulse duration – about 100 ns, maximal neutron flux attainable ~ 10^{17} n/cm^2·s. Such high neutron fluxes can be used for activation of various materials ensuring a benchmark for main-stream fusion facilities (like JET and NIF) and for MCNP characterization of them.

This device is also able to generate powerful streams of hot plasma (~ 1 keV) and fast deuterons (~ 100 keV) ensuring power flux densities of them on the target's surface up to $10^8...10^{10}$ MW/m^2. These streams can be used for radiation-thermal testing of materials intended for application in fusion reactors of both types – with magnetic and inertial plasma confinement (MPC and IPC correspondingly). Eminently the above streams reproduce real conditions existing near the first wall of the reactors (temperature, energy and nature of plasma/particle streams) with one exception: in the reactors with MPC the above pulse duration even during short emergency events like ELMs, VDs and disruptions are much longer compared with the corresponding time intervals in the DP foci. However power flux density in those real cases in the contemporary main-stream fusion facilities is 5-8 orders of magnitude lower (10...1000 MW/m^2) compared with those obtained in DPF. This fact gives an opportunity to use a so-called "damage factor" F in the radiation material science experiments with DPF [1]:

$$F = q \times \tau^{0.5} \quad (1)$$

where q is power flux density and τ is a duration of the pulse.

It means that too short duration of the radiation pulses (produced by DPF) at testing can be compensated by an increase of power flux density of the irradiating streams to simulate radiation damage effects realized in tokamaks. With DPF in general, and in respect to the PF-1000 facility in particular, this provision can easily be fulfilled with a big reserve.

For both the above groups of researches it was important to make operation of this largest DPF set-up with deuterium as a working gas more reliable because it was assembled on the base of high-voltage elements of 60's and it was exploited during more than 20 years to the moment. Thus a formidable work was done during this CRP on modernization of its most sensitive elements.

Measurements and monitoring of the parameters of the radiation streams generated in DPF are important parts of the work under the current CRP. In this framework it is also important to understand more deeply physical processes ruled the generation of the above-mentioned radiation types and scaling laws of them for variation of DPF bank energies and discharge currents.

These studies were provided at the PF-1000 facility side by side with experiments in the field of radiation material science and in the sphere of activation experiments.

2. MODERNIZATION WORKS AT THE PF-1000 FACILITY

2.1. Generator of the PF-1000

In principle the capacitor bank of the facility positioned at the 1st and 3rd levels of the building has the following parameters:

- Charging voltage: U_0 = 16…40 kV,
- Bank capacitance (12 section by 24 capacitors, i.e. total288 capacitors):C_0 = 1.332 μF,
- Bank energy: E_0 = 266…1,064 kJ,
- Nominal inductance: L_0 = 15 nH,
- Quarter discharge time: $T_{1/4}$ = 6 μs,
- Short-circuit current: I_{SC} = 12 MA,
- Characteristic resistance: R_0 = 2.6 mΩ.

This bank was reconstructed. Namely old cables were substituted by new ones and the new construction of the field distortion spark gaps was introduced. Their jitter was measured in the range 2…5 ns. It is short compared with the jitter of the previous sparks where this parameter was about 50 ns. A part of the reconstructed bank is presented in Fig. 1.

The cable collector was also reconstructed (Fig. 2), and the discharge chamber was supplied with a new automatic door (Fig. 3 *a*). The new outside appearance of the PF-1000 discharge chamber is presented in Fig. 3 *b*.

As a first step after reconstruction of the battery the following regime of operation has been chosen for the device:

- 25 kV charging voltage,
- 400 kJ stored energy.

With these parameters the output characteristics of the discharge were measured as follows (see Fig. 5):

- 2 MA peak current
- 6 μs quarter period.

With these parameters we used the following geometry of the main chamber electrodes:
- Anode: 22,6 cm diameter and 46 cm length,
- Cathode: 40 cm diameter; cathode consists of 12 rods (diam. 8 cm),
- Alumina insulator: 8,5 cm length.

We used pure deuterium as a working gas (i.e. neutron energy is about 2.5 MeV) at initial pressure 2…4 hPa.

Neutron yield of the PF-1000 facility had been measured on the level: $Y_n \sim 10^{11}…10^{12}$ DD neutrons per shot.

FIG. 1. A part of the modernized capacitor bank of the PF-1000 facility.

a) *b)*

FIG. 2. Reconstruction of the cable collector (a) and mounting of the new main insulator (b).

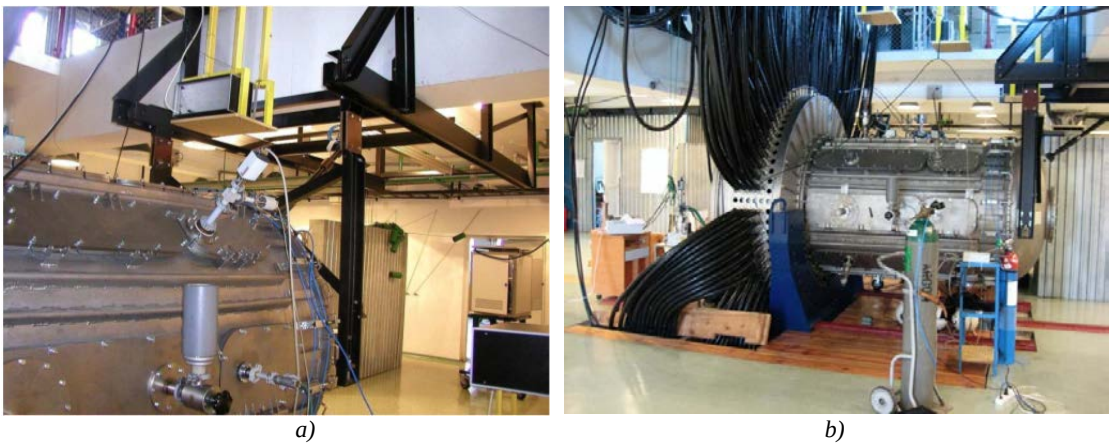

a) *b)*

FIG. 3. Automatic mechanism of a manipulation by the back chamber's door (a) and an outside appearance of the PF-1000 discharge chamber with current collector and cables (b).

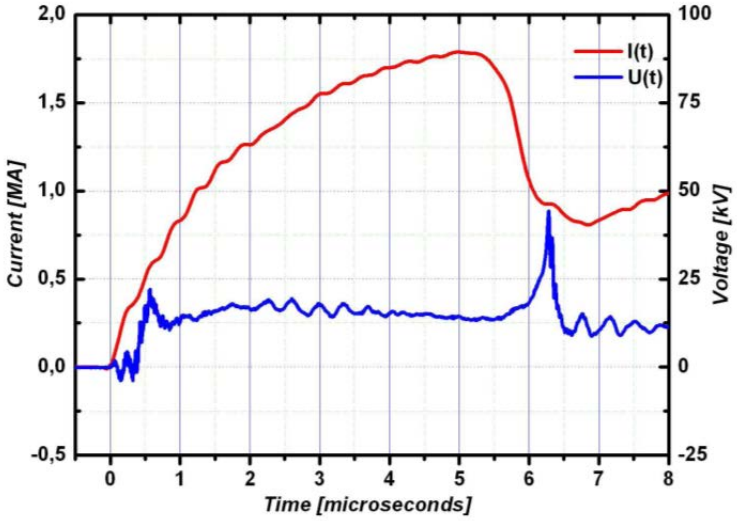

FIG. 4. Oscilloscope traces of the discharge current and voltage taken at the charging voltage U_0 = 25 kV.

2.2. Diagnostics

Side by side with our previous diagnostic complex (see e.g. [2]) we have elaborated a number of new sophisticated tools giving us valuable information on dynamics of hot plasma, electron and ion acceleration processes, etc. Among these methods we introduced into this set of measuring devices the following techniques.

2.2.1. Absolute calibrated magnetic probe inside the anode (ACMP).

The experimental set-up of this technique is shown in Fig. 5 *a* and *b*. It is intended for measurements of the current value inside hot pinched plasma.

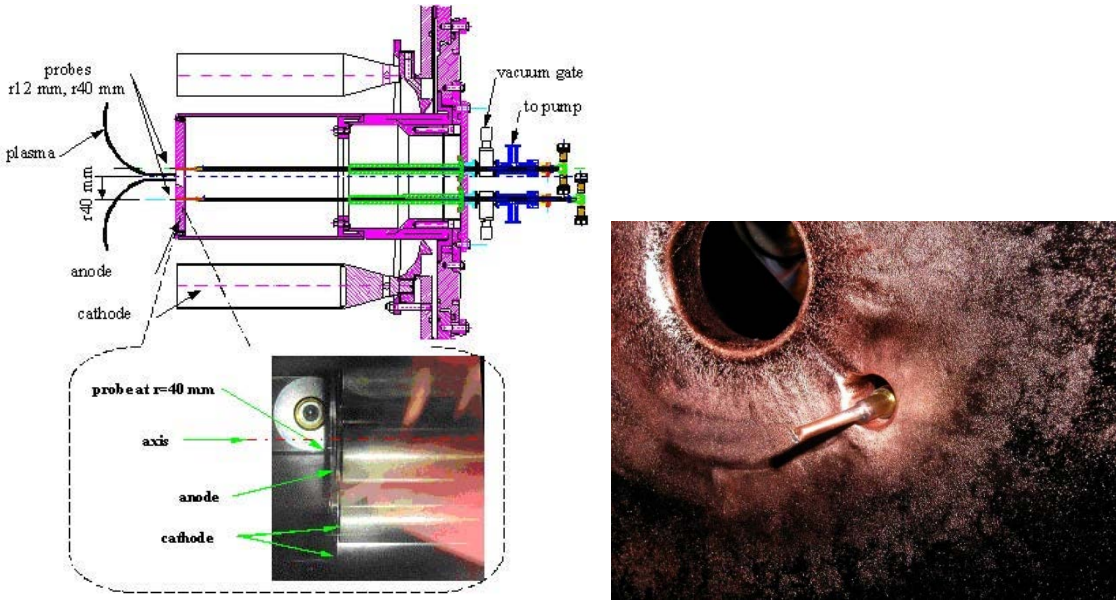

a) *b)*

FIG. 5. Scheme of positioning of ACMP inside the PF-1000 anode (a) and its photo.

2.2.2. 1-ns 16-frames laser interferometry

Despite the considerable progress noted in this area of research the understanding of basic processes taking place in the PF devices is still incomplete [3]. Therefore, construction of a new experimental setup based on an interferometer capable of recording up to 16 images in a single DPF "shot" with 1-ns temporal resolution will allow for further study of phenomena during one discharge. Intervals 10 ns alternating with 20 ns between frames allow the detailed study of time-resolved phenomena [4-8]. The experimental data collected with this apparatus is a unique source of information that makes possible not only to continue the progress in understanding the discharge phenomena but, also let optimize and control these processes.

The setup with an interferometer, described in detail below, made possible acquisition of sixteen interferometric images during one discharge in the PF-1000 device. A schematic diagram of this system is given in Fig. 6. The main element of the diagnostic setup is the Mach-Zehnder interferometer shown in Fig. 7. In the studies of the PF phenomena this apparatus used in the experiment has advantages over other types of interferometers for the following reasons:

- Sufficiently large field of vision of the interferometer
- Possibility to follow in time the fast changeable plasma fields due to a single passage of a laser light beam through the plasma for obtaining the interferometric image.

The most important element of the interferometric setup is the light source. In our case it is the Nd:YLF laser. This laser emits light of the basic wavelength of 1.06 μm with second, third and fourth harmonic frequencies. For interferometric purposes we are using the second harmonic with the wavelength of 527 nm, i.e. the visible green light.

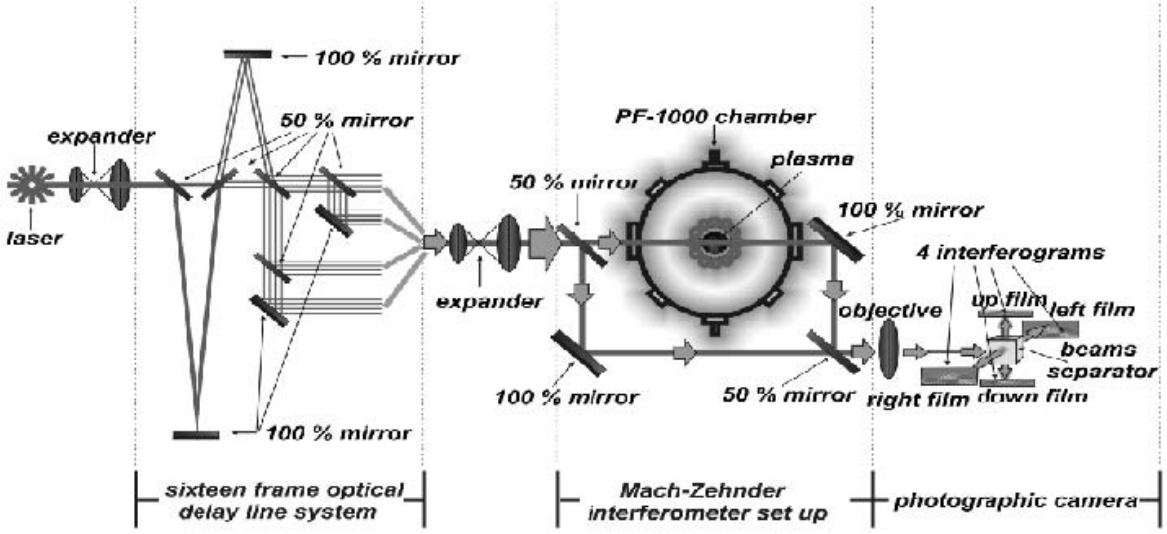

FIG. 6. A schematic diagram of the sixteen-frame' interferometer system.

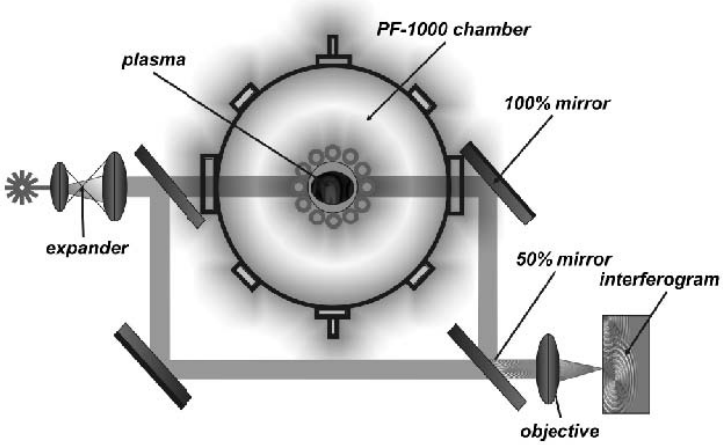

Fig. 7. Mach-Zehnder interferometer setup for plasma density measurements.

The energy carried by this wavelength in a single laser pulse is approximately 500 mJ, with energy stability of 7 %, time duration less than 1 ns, the diameter of the light beam 12 mm, and the time jitter of the generated laser pulses +/-1 ns. These parameters play a critical role in the studies especially to precise establish time correlation of all phenomena taking place during a plasma discharge.

An optical telescope increasing the beam diameter up to 60 mm was installed in front of the laser. Introduction of the telescope in such a location forms a parallel light beam and cancels the natural divergence of the laser beam which is very undesirable beam parameter in the multi-frame interferometry especially when operating with optical path dozens of meters in length.

An optical delay line shown in Fig. 8 allows for spatial selection between frames delays in the range from 0 ns to 220 ns and ensures the same linear sizes of interferograms in each frame. Two types of optical elements were used in this setup: 100 % mirrors and 50/50 beam splitters. They direct light beams corresponding to each frame at a small angle to the optical axis of the setup. In such a way we obtain sixteen light beams in form of 4×4 matrix around the center of optical axis of the first Mach-Zhender mirror. Such configuration allows obtaining fully separated frames in space with the same linear sizes and quality at their registration (Fig. 9).

The laser beams passing through the optical delay line enters into expander which increases beam diameter to the size of 150 mm. Collimated beams are directed to the mirrors of the Mach-Zehnder interferometer. The active diameter of the mirrors in the interferometer is 200 mm so it capable of complete observation of the phases of the possible PF phenomena.

A recording system has been built for the specific needs of this experiment. It allows for registration of interferometric images on photographic plates, and provides spatial separation of frames into four planes of registration. A special setup of prisms, specifically constructed for the needs of this experiment (Fig. 10), distributes 16 delayed in time beams onto four photographic plates of four images each. Beam outgoing of each of the sixteen prisms is passing through the system of optical interferometric filters preventing huge plasma irradiance in visible spectrum. The camera is equipped with optical filters in front, and four 130×180 mm photographic cassettes mounted at the exits, opened during exposure. For registration of images a special type of film was selected for optimal contrast and resolution of the registered images.

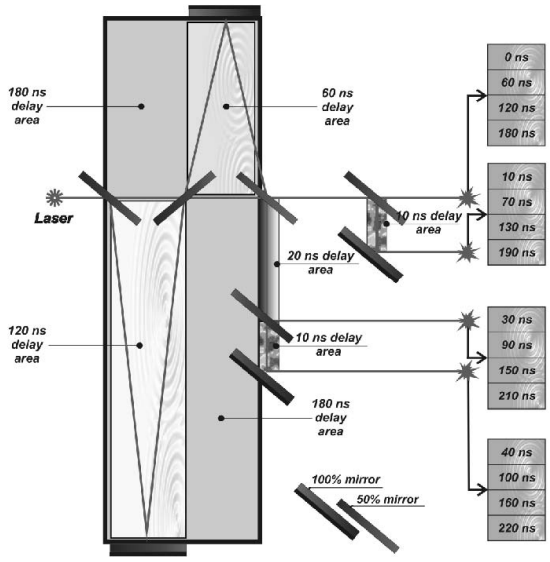

FIG. 8. Sixteen frame optical delay line diagram.

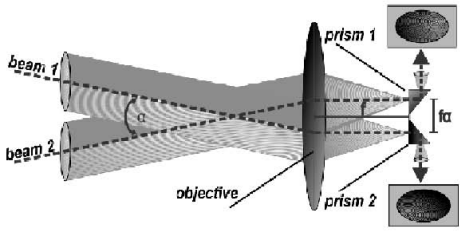

FIG. 9. Idea of beams separation.

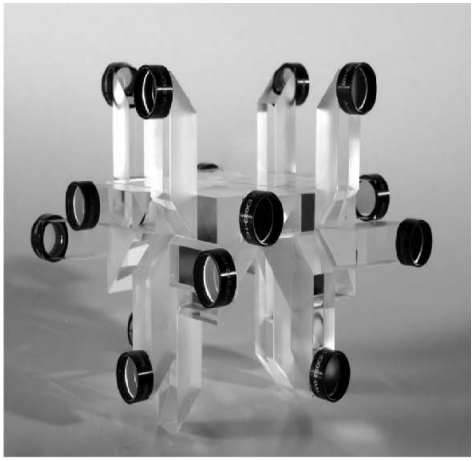

FIG. 10. Beam separator.

With this laser system we are able to investigate not only the dynamics of DPF pinch plasma itself, but a process of irradiation of an external target by fast ion beam and hot plasma streams and to study the "secondary" plasma created by these streams at the surface of a specimen under irradiation.

2.2.3. Spectroscopy

Spectroscopic technique is one of the main tools in plasma diagnostics [9]. Its ability to give data on the main plasma parameters as temperatures (electron, ion and ionization) and density (electron and ion) may help to trace the plasma state and in particular the plasma dynamics if it will be used with good temporal and spatial resolutions.

For spectroscopic study in visible range of spectrum we used the recording equipment containing a collimator and quartz light-pipe coupled to the MECHELLE®900 spectrometer. We may register both types of radiation emitted by pinch and by the above-mentioned secondary plasma produced near the target's surface.

That system had the spatial resolution of about 10 mm. Therefore, the obtained spectra have been averaged partially along the observed chord through the target (including periphery of a plasma stream) and also over the region extending up to 1 cm from the target surface.

To make possible observations of the temporal evolution of the investigated spectra, a triggering system of the spectrometer was synchronized with plasma discharges, and the beginning of the exposition was varied within the range of 0-100 μs, whereas the exposition time was 0.5 μs (as a rule).

Hence, it is necessary to keep in mind, that all magnitudes obtained from the spectra have been averaged to the above extents in space and time in such a way. Taking into considerations that the corresponding values of temperature and density have very sharp changes in this region, the peak values may considerably differ from the averaged ones measured in the experiment.

It should be noted that for plasma density measurements in the near target region we had no possibility to use the Stark broadening of *D*-lines, because of large values of plasma electron density N_e and significant re-absorption of corresponding lines. We could, however, use the well-known Inglis-Teller formula for a shift of boundary serial, which gives evaluations of the minimum values for N_e [9]:

$$\lg N = 23.26 - 7.5 \times \lg n_{max} \qquad (2)$$

where n_{max} is the general quantum number for the last Balmer line, which is observed as an isolated one (if D_β – n = 4, if D_α – n = 3, etc.).

3. RESULTS OF THE DPF PHYSICS STUDY

3.1. Magnetic probe measurements

Magnetic probe signals are presented in Fig. 11 *a*, whereas scaling for neutron yield of the device with respect to the value of current flowing through pinch measured by *ACMP* may be seen in Fig. 11 *b*.

3.2. Interferometry

Below we present 16 interferograms (Fig. 12). These experimental results were obtained for one discharge in PF-1000 device. Vacuum chamber initially was under pressure of 2×10^{-5} hPa, filled with deuterium gas under pressure of 2.6 hPa. Total neutron yield in this shot was 1.3×10^{11}.

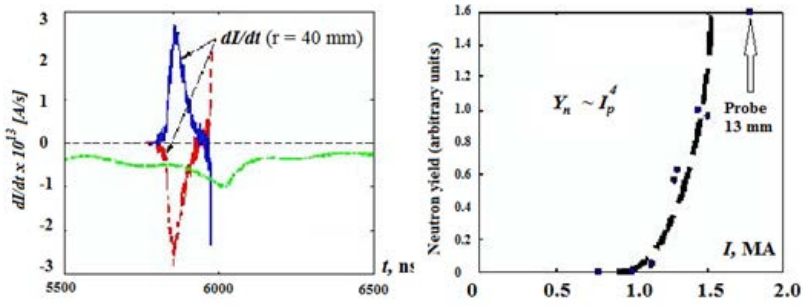

a) *b)*

FIG. 11. Magnetic probe signals (a) and neutron scaling law in dependence on pinch current magnitude (b).

We have also provided the interferometric measurements for the case when targets of different materials were irradiated by powerful streams of hot plasma (shock waves) having velocity of about (3-5)×10^7 cm/s and temperature of several hundred eV together with the beam of fast deuterons each having an average energy of about 100 keV. Power flux density in these experiments was in the limits from 10^8 till 10^{10} MW/m^2. One may easily see secondary plasma produced by these streams near the target's surface which are spreading in the direction opposite to the direction of the above streams (see Fig. 13).

Laser interferometry is an extremely valuable research method. The ability to quantitatively determine plasma density distribution from time developed interferograms is giving the information about:

- Space-time evolution of the electrons density distribution in the inspected configurations
- Efficiency of the gas gathering by the plasma sheath
- Degree of compression of plasma
- The total plasma volume in the pinch area and its dynamics (e.g. MHD plasma instabilities)
- Plasma leakage from pinch area thus forming powerful plasma streams that may be used for target's irradiation
- Evolution of secondary plasma and its main parameters (density and velocity).
  Laser interferometry has been used for many years and this technique is still in progress. Several solutions had been developed [4, 5, 6, and 7]:
- Use of several lasers and/or several wavelengths
- Use different beam splitter and mirror combinations
- Application of beam splitter, mirror and half-wave plate combinations.

All interferometric configurations are complicated in their alignment especially when we try to obtain multiple frames in one discharge. The main problem in a multiple-frame technique was that when was used an image-plan configuration to obtain high quality interferograms the minimum separation angle became too large. We resolved this problem by inventing the new beams separator which is making possible to record 16 interferograms during one discharge.

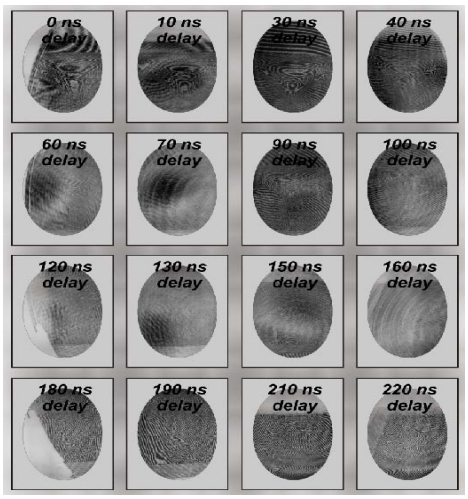

FIG. 12. Sixteen interferograms from one shot from PF-1000.

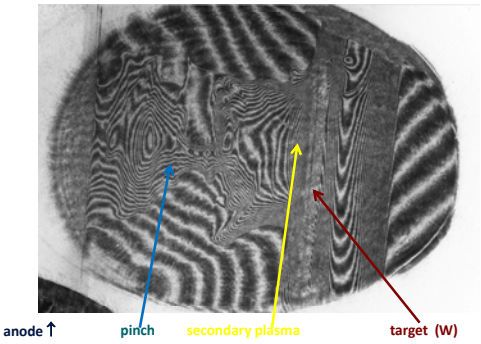

FIG. 13. Interferometric frame picture of interaction process (1-ns time exposure).

The sixteen-frame interferometry provides high resolution information ordered in time. It allows studying all phenomena in hot plasma of the PF-1000 facility [8] and gives information needed to verify the models describing plasma propagation and the structure of plasma coat.

Using our setup it is possible to:

- reconstruct evolution of pinch geometry;
- determine linear density of particles;
- determine distribution of plasma density in the pinch and in the secondary plasmas;
- correlate in time all this phenomena with evolution of X ray and neutron production;
- characterize the MHD instabilities in the processes of plasma development;
- analyze connections between processes of rising and decay of the plasma density with neutrons production efficiency;
- correlate precisely PF phenomena development with other diagnostics data which gives information about dependence between speed of thermonuclear synthesis reaction and the parameters of the PF setup generator.

3.3. Spectroscopy

Our spectroscopic measurements have shown the data as follows (see Fig. 14).

In our case, obviously, even D_α is merged with D_β line, so we must take n_{max} as 3 or 2. Hence, for the plasma density we have following evaluations: $N_e \sim 4.5\times10^{19}$ cm^{-3} – 10^{21} cm^{-3}, at the first 20 μs after the start of the plasma-target interaction. So enormous values are beyond any doubt, because we have $N_e > 10^{19}$ cm^{-3} for the near focus region (without any target), as measured with different techniques. Since the density increases during the next moments, we can determine N_e from the quadratic Stark broadening of carbon and copper spectral lines (CuII and CIII, IV, V). Corresponding data about the Stark widths for the CII lines are available in [10], and for CIII-IV lines in [11]. It is necessary to point out that at so large densities the quadratic Stark effect may be transformed into a linear one [11]. As a result, the obtained N_e values will be lower than the true ones. An example of the identified spectra is shown in Fig. 14.

Qualitative information about the temporal behavior of the plasma density may be obtained from the continuum intensity, taking into account that corresponding intensity is proportional to N^2 (more precisely – to $Z^2 N_e N_i$, but we may neglect the contribution of multi-charged ions and it may be assumed that $N_e = N_i$). Fig. 15 presents the time dependence of the continuum intensity (in arbitrary units) at the region $\lambda \sim 700$ nm taking into account the exposition time. The region $\lambda \sim 400$ nm shows a similar temporal dependence.

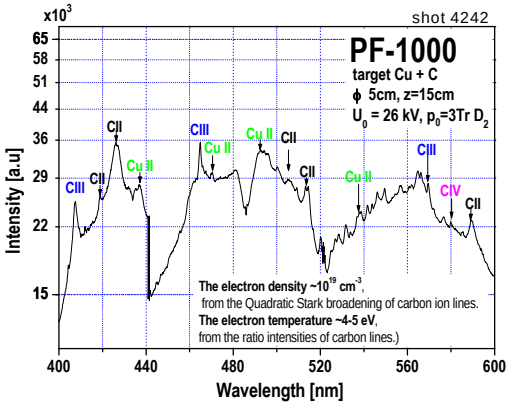

FIG. 14. Spectrum obtained for secondary plasma for Cu+C target at the moment 20μs after the start of plasma-target interaction. Exposure time is 0.5 μs.

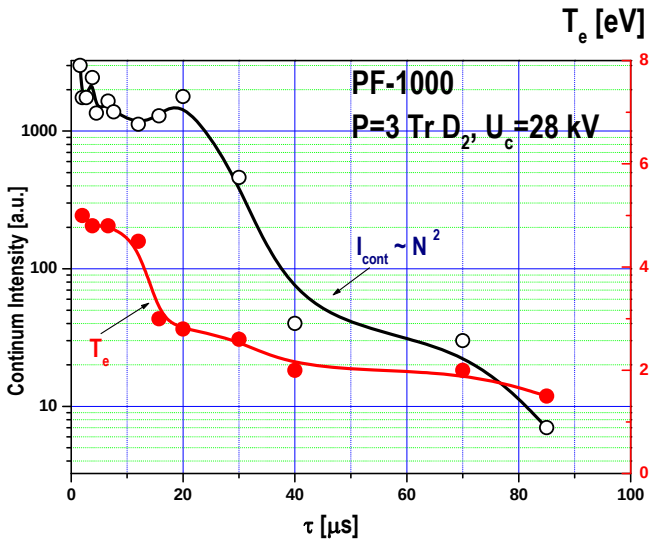

FIG. 15. Time dependence of the continuum intensity (in arbitrary units) at the region λ ~ 700 nm and dynamics of plasma temperature.

The electron temperature data on the secondary plasma were also collected and analyzed. T_e measurements were performed using the ratio of intensities of the CIV spectral lines (doublet 580.1 nm, 581.1 nm) and CIII line (multiplet 465.1 nm), assuming LTE conditions (high N_e). The ratio of intensities of the CIII and CII spectral lines gives somewhat lower T_e values. As for the probably existing CV lines, corresponding line shapes have so significant widths that makes them imperceptible at a level of the continuum, even if their total intensity is large.

Using all these data and Saha formula, we could reconstruct "the ionization distribution" for carbon ions (see Fig. 16).

The main results of the spectroscopic measurements of secondary plasma provided for the stages taking place after the “powerful phase of irradiation” can be summarized as follows:

- For the spectra recorded within the PF-1000 experiment with Fe, Ti, Ni-targets (stainless) and some other samples, the FeII and FeI spectral lines appeared to be dominant. There were recorded no lines of elements of the samples (e.g. Ga). For the Cu+C target there were observed intensive spectra of these elements
- The time duration of the high power plasma load upon the target appeared at ~ 20-30 μs, but the living time of secondary plasma the near target (including its recombination phase) was considerably larger: >100 μs.
- The peak values of N, T_e and T_i during the first 20-μs period were $>10^{20}$ cm^{-3} and ~ (5-10) eV, respectively.
- As regards the carbon ionization distribution, there were found the populations as follows: CII ~50%; CIII ~40% and CIV ~10%. The copper ion distribution was similar. Those data were obtained from the experiment performed with a composite target Cu+C.
- The plasma (gas-dynamic) pressure near the target during the high-power plasma load was ~ 1000 bar (or $\sim 10^{21}$ eV/cm^3 using “natural units”).

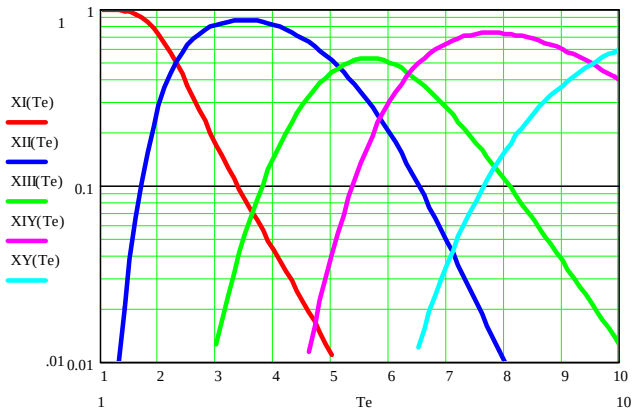

FIG. 16. Ionization distribution for carbon ions.

All these data let us an opportunity to determine a law of scaling for PF setups and radiations generated by them, as well as to provide valuable reference data for various work regimes of these devices including radiation material experiments.

4. RADIATION MATERIAL SCIENCE EXPERIMENTS

The PF-1000 facility was intensively used during the current CRP in radiation material science experiments by researchers (including participants of the current CRP) from Estonia, RF, Czech Republic, Bulgaria, Italy, Germany and other countries. These experiments were mainly devoted to testing of samples of the materials counted as perspective ones for use in the main-stream fusion devices with magnetic and inertial plasma confinement, such as JET, ITER, NIF, Z-machine etc. Among these materials both construction and plasma-facing (first-wall) elements have been irradiated in three dissimilar regimes: with strong melting of their surface, without melting and in the intermediate regimes (see e.g. [12]). Specimens were placed at the cathode part of the device.

Power flux densities used in these experiments were ranged from 10^2 MW/m^2 through 10^{10} MW/m^2. It means that the maximal magnitudes of heat loads realized in contemporary chambers of fusion reactors with magnetic plasma confinement during emergency events (disruptions, VDEs, ELMs, etc.) were exceeded even taking into account the damage factor (1). At the same time they were almost equal to those (by power flux densities, plasma temperature, nature of particles – hot plasma and fast ions – and pulse durations) as it is expected at the first wall of the chambers of reactors with inertial plasma confinement. Fig. 17 presents a geometry of irradiation (*a*) and an electron microscopic image (*b*) of the boundary between tungsten and CFC samples after irradiation of them with maximal power flux densities of hot plasma (T_e ~ 1 keV) and fast deuterium ions beam (E_D ~ 100 keV). In this geometry several construction and first-wall materials (tungsten, CFC, SiC, low-activated austenitic and ferritic stainless steels – including Eurofer-3, aluminum and others) were tested in different conditions.

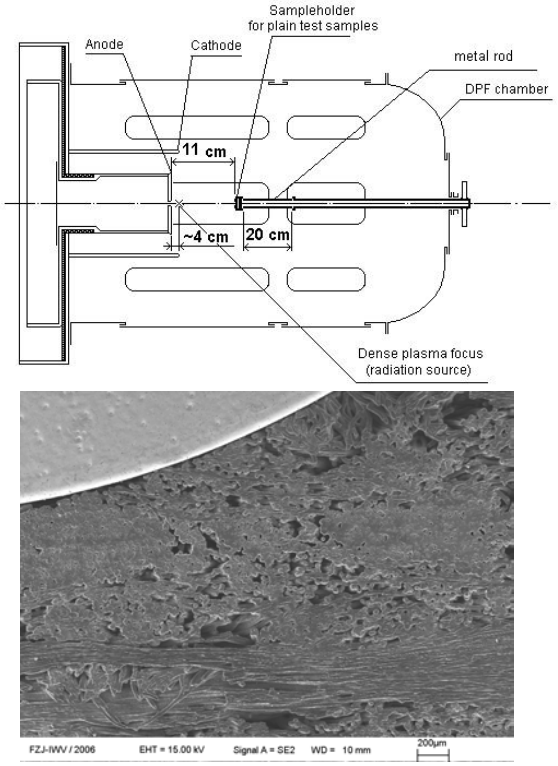

a) b)

FIG. 17.The geometry of irradiation (a) and an electron microscopic image (b) of the boundary between tungsten (top) and CFC samples (bottom) after irradiation of them with maximal power flux densities of hot plasma (T_e ~ 1 keV) and fast deuterium ions beam (E_D ~ 100 keV).

An important data concerning comparative radiation resistivity for two types of ceramics (boron nitride and alumina) used for insulation of coils in a spheromac were obtained with the PF-1000 facility [13]. It appears that in spite of the better surface smoothness the BN samples compared with the Al_2O_3 cover of aluminum coils (see Fig. 18) the mass loss is noticeably higher for the boron nitride sample.

In a set of experiments provided with the PF-1000 facility and a target having a shape of a tube (made of stainless steel or copper) a very specific picture of transportation of the fast ions stream and an anomalous damage in the internal surface of a tube were found [14]. Geometry of transportation and a macroscopic picture of the damage are presented in Fig. 19.

These and other experiments in the field of radiation material sciences provided by our colleagues – the other CRP participants – at the PF-1000 facility are described in more details in their reports.

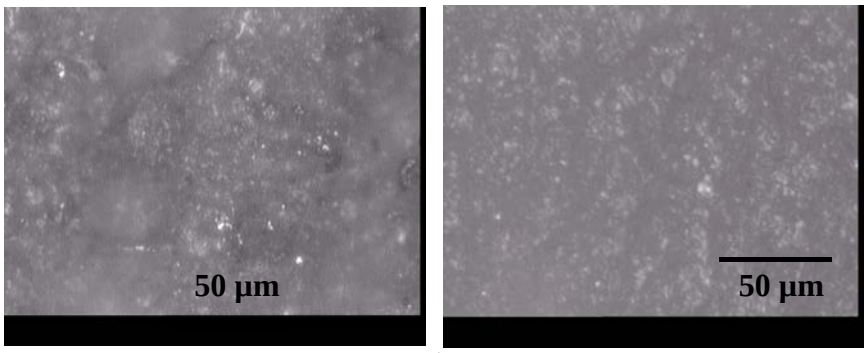

a)

Virgine sample of Al_2O_3 (x 250) *Virgine sample of BN (x 250)*

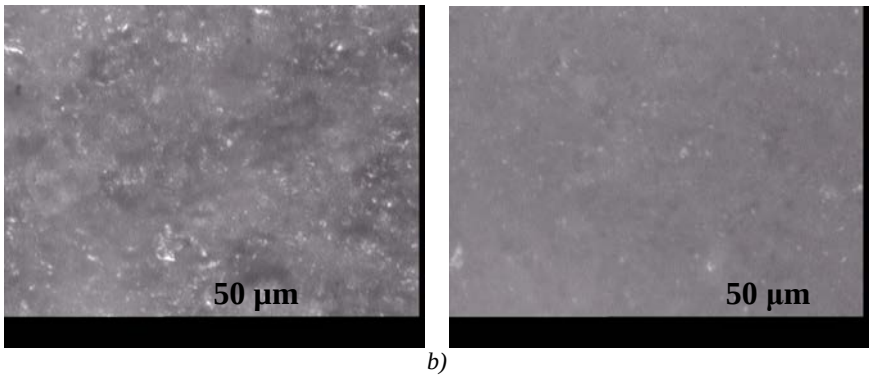

b)

Al_2O_3 specimen after a single-shot irradiation in the PF-1000 facility (No. 3, x250) *BN specimen after a single-shot irradiation in the PF-1000 facility (No. 2, x 250)*

FIG. 18. Alumina and boron nitride specimens before and after a single-shot irradiation in PF-1000 (SEM).

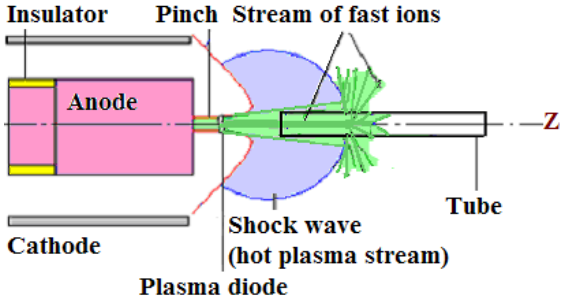

a)

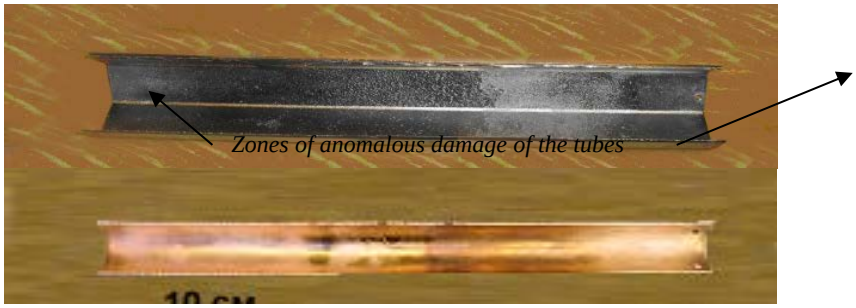

b) c)

FIG. 19. Scheme of the plasma and fast ions streams dynamics inside the tube (a). Macroscopic photo of stainless steel tube (b) and copper tube (c) with zones of anomalous damage; DPF anode was at the left-hand side of the tubes.

5. EXPERIMENTS ON RADIATION ACTIVATION OF MATERIALS

5.1. Neutron activations measurements

Neutron activation measurements are a benchmark against numerical calculations: Measured activity of reactions induced by neutrons from well known calibration source inside tokamak allow to obtain nuclear reaction rate:

$$\alpha_m = \frac{A}{N_a \cdot \left(1 - e^{-\lambda \cdot t_r}\right)} \tag{3}$$

Calculation of the same reaction rate by means of neutron transport code (MCNP) by implementation of the calibration source inside tested model:

$$\alpha_c = \int_0^{\infty} \sigma(E)\ \ \varphi(E)\ \ dE \tag{4}$$

If both results correspond to each other then we trust the numerical model.

REACTIONS RECOMMENDED FOR CF-252 NEUTRONS MEASUREMENT

Reaction	$T_{1/2}$	Expected activity [Bq]	E_g [keV(%)]
In-115 (n,g) In-116	54 m	3E+3	1097 (*59*), 1294 (*85*)
U-238 (n,g) U-239	23.5 m	9E+2	75 (*49*)
Au-197 (n,g) Au-198	2.7 d	2E+2	412 (*96*)
Mn-55 (n,g) Mn-56	2.6 h	6E+1	847 (*99*), 1810 (*27*)
W-186 (n,g) W-187	24 h	4E+1	480 (*27*), 686 (*33*)
In-115 (n,n') In-115m	4.5 h	2E+1	336 (*46*)
In-113 (n,n') In-113m	99 m	2E+0	392 (*65*)
Al-27 (n,p) Mg-27	9.5 m	2E+0	844 (*72*), 1014 (*28*)
Fe-56 (n,p) Mn-56	2.6 h	5E-1	847 (*99*), 1810 (*27*)
Ta-181 (n,g) Ta-182	114 d	2E-1	100 (*14*), 1121 (*35*)
Sc-45 (n,g) Sc-46	84 d	6E-2	889 (*100*), 1121 (*100*)
Ni-58 (n,p) Co-58	71 d	7E-2	811 (*99*)
Al-27 (n,a) Na-24	15 h	6E-2	1369(*100*), 2754(*100*)

(Handbook on Nuclear Activation Data, IAEA Technical Report Series No. 273).

In this part of our program we provided a set of experiments on activation of different materials including those specimens which are counted as the candidate ones for using in the mainstream fusion reactors [15]. Main idea of these experiments is to see consequences of

irradiation of materials by neutron flux from DPF comparable with the flux expected on the back-side of the first wall of the chambers of the large fusion installations. This flux may be supplied by PF-1000 facility as well as by small DPF devices on the walls of their chambers because the energy density of the neutron flux in all DPF devices is the same as the size of the DPF chamber is increased proportionally to the DPF bank energy.

During these sets of experiments performed on our DPF machines activations of several samples have been measured. They were measured at different angular and azimuth distributions for two groups of neutrons in respect to the main Z axis of the DPF chamber having a cylindrical shape.

We have prepared for activation the samples (ø18mm x 2mm) of the following materials: In, Au, W, Ta, Fe, Ni, Al, Mn (1 mm) and Sc (1.25 mm).

In Fig. 20 one may see simulation of the neutron spectrum in 3U irradiation end placed inside the vacuum vessel of the JET from the Cf-252 source located 30 cm below versus simulation of the neutron spectrum from the PF-1000 device behind the polyethylene moderator. The same graphs plus reaction cross-sections for different elements under irradiation are presented in Fig. 21. Irradiation was provided for the following samples: Sc, Ta, Mn, W, Au in on PF-1000 facility. The series of 7 shots within 2 hours was done with JET from the Cf-252 source located 30 cm below versus simulation of the neutron spectrum from the PF-1000 device behind the polyethylene moderator. Total neutron yield 1.33E+11 (according to calibrated Ag-activated counters.)

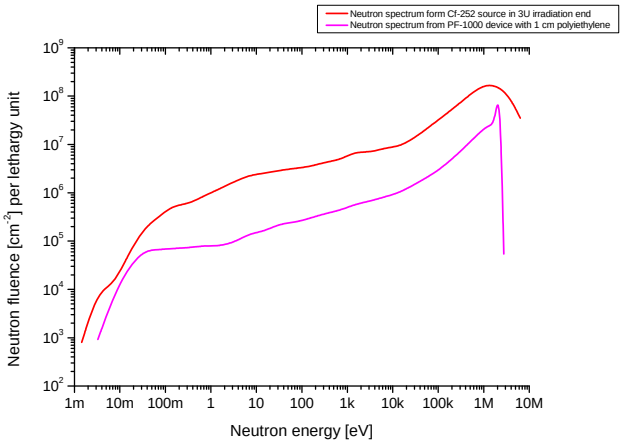

FIG. 20. Simulation of the neutron spectrum in 3U irradiation end placed inside the vacuum vessel of the JET from the Cf-252 source located 30 cm below versus simulation of the neutron spectrum from the PF-1000 device behind the polyethylene moderator.

In our experiments we used Gamma spectrometer consisting of the following elements (the hardware of it may be seen in Fig. 22):

- Precalibrated HPGe Coaxial Detector System
- Genie-2000 Gamma Analysis Software
- InSpector 2000 multichannel analyzer
- Labsocs Laboratory Efficiency Calibration Software
- Labsocs Characteristic of the HPGe detector
- Shielding system.

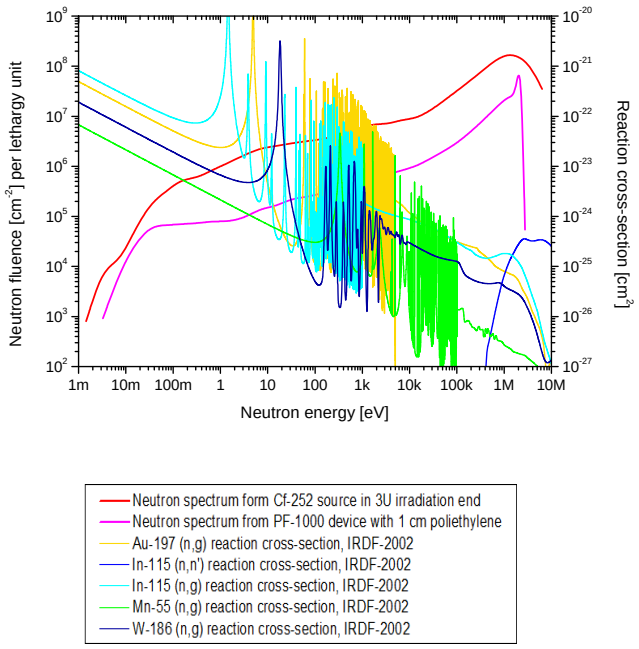

FIG. 21. The same as above plus reaction cross-sections for different elements under irradiation.

FIG. 22. The hardware of Gamma spectrometer.

Recorded reactions were: Au-197 (n,γ), In-113 (n,n'), In-115 (n,n'), In-115 (n,γ), Mn-55 (n,γ), W-186 (n,γ), Ta-181 (n,γ).

Mean value of reaction rate is:

$$\overline{\alpha} = A_0 \Big/ \left(\lambda \cdot n_a \cdot \sum_{i=1}^{n} w_i \cdot e^{-\lambda \cdot t_i} \right) \tag{5}$$

where A_0 – initial activity, λ – decay constant, n_a – number of target nuclei, w_i – weight of i-th shot, t_i – time from i-th shot.

The activation samples have had a special optimized geometry (shape – cylinder, diameter – 64 mm, and mass – 100 g). The optimization of sample allowed providing measurements even at a minimal activity excited by the minimal neutron flux.

ACTIVITY AND REACTION RATE

Reaction	$T_{1/2}$	Activity [Bq]	Reaction rate [s^{-1}]
In-115 (n,g) In-116	54 m	62.15 ± 2.21	(10.53 ± 0.38)E-18
In-115 (n,n') In-115m	4.5 h	17.12 ± 1.02	(8.36 ± 0.50)E-18
Au-197 (n,g) Au-198	2.7 d	2.50 ± 0.12	(8.10 ± 0.40)E-18
W-186 (n,g) W-187	24 h	1.06 ± 0.07	(5.21 ± 0.34)E-18
Mn-55 (n,g) Mn-56	2.6 h	6.07 ± 0.51	(1.66 ± 0.14)E-18
In-113 (n,n') In-113m	99 m	0.38 ± 0.76	(1.96 ± 3.90)E-18
Ta-181 (n,g) Ta-182	114 d	<0.1	-
Sc-45 (n,g) Sc-46	84 d	<0.01	-
Fe-56 (n,p) Mn-56	2.6 h	N/A	N/A
Ni-58 (n,p) Co-58	71 d	N/A	N/A
Al-27 (n,p) Mg-27	9.5 m	N/A	N/A
Al-27 (n,a) Na-24	15 h	N/A	N/A

5.2. Measurements of angular distributions of neutrons emitted from PF-1000 facility by indium samples.

Many high-temperature plasma experimental devices, and among them Plasma-Focus (PF) facilities, have reach a level of operation at which intense fluxes of fast neutrons are emitted.

1-MJ Plasma-Focus (PF-1000) fusion experiments involving deuterium plasma with ion temperature exceeding 1 keV, deuterium densities equal to a few 10^{19} cm^{-3}, plasma volume of a few cm^3 and plasma lifetime of a 200 - 300 ns generates a few 10^{11} or more neutrons per shot. With this level of emission it becomes feasible to extract information by making use of various techniques measuring neutron yield and energy distribution of fusion products.

Mechanisms of the neutron emission from pinched plasma discharges still remain not absolutely clear. In spite of many efforts, both theoretical and experimental, the problem of the prevailing mechanism of the interaction between two deuteron reagents leading to fusion reactions has not been solved. At the aforementioned neutron emission levels it is possible to obtain information about distributions of the plasma D^+-ions (nuclear reaction reagents) using suitable neutron diagnostic techniques. Such techniques can provide important information on nuclear reaction mechanisms as well. Neutron activation is one of the methods that is widely used to determine the neutron fluence at chosen locations and is well suited for precise measurements of the neutron yield. Two advantages of this method are: its immunity to electro-magnetic interferences and the large dynamic range of the measurements.

Information about neutrons is obtained by registering the products of nuclear reactions induced in samples of especially selected materials. The materials are selected so that they

have relatively high reaction cross-sections with neutrons, well defined nuclear reaction thresholds and the products of these reactions decay with half-lives that are of the order of dozen seconds or longer. Usually, the products decay with gamma-ray emission and can thus be detected using the gamma spectrometry. The measured gamma activity of samples (i.e. reaction rate) converted to the neutron fluence at selected locations around the pinch plasma is determined using neutron transport calculations (MCNP).

The anisotropy of neutron fluxes from D-D reactions occurring in Plasma Focus discharges was reported in many papers which were published during 1970s, 1980s, and also 1990s. It was generally assigned to the axial beam-target mechanism, whereby the beams were generated by strong electric fields associated with plasma diode zone [16]. The flux anisotropy comes from both the CM motion of the reagents and the angle dependence of the differential D-D reaction cross section in the target model. Measurements of the angle dependence neutron fluxes were generally made by the use of silver activation counters. However to measure such short neutron pulses thoroughly the detectors used must preserve the fluence information for analysis after pulse, the decay of the neutron induced reaction products must be distinct from the background and directly related to the incident neutron intensity. It seems that the silver activation detectors do not meet all these requirements, in spite of the fact that they have been used for many years to measure neutron fluence from many pulsed sources. These instruments consist of a silver foil wrapped around a Geiger-Muller (G-M) tube. Recorded neutrons are first slowed down in a hydrogenous moderator and after that captured in the silver foil to induce two reactions: $^{107}Ag(n,\gamma)^{108}Ag$ and $^{109}Ag(n,\gamma)^{110}Ag$. Subsequent beta decay of the activation products is counted with the G-M tube. The main drawback of this instrument is that it is excessively sensitive to scattered neutrons.

The scattered and slowed down neutron field constitutes a serious problem for neutron measurements in many high-temperature plasma experiments. The results of some neutron measurements are effectively influenced by the background of slowed down neutrons. In this work other method based on the threshold nuclear reaction with indium is demonstrated. The results of measurements of angular distribution of neutrons emitted from dozens of PF-1000 facility discharges, which were performed with the newly introduced indium monitor, are presented here.

The PF-1000 device is a Mather-type facility. It was equipped with two coaxial electrodes of the same length (460 mm). The inner electrode (anode) is made of copper (diameter - 230 mm). The outer electrode (cathode, diameter – 400 mm) consists of 12 stainless steel tubes (diameter – 80 mm). The anode is surrounded tightly by cylindrical, ceramic insulator (length - 85 mm). The experiment has been performed in vacuum chamber pumped out to the basic pressure of 2×10^{-5} hPa. The deuterium filling has been varied, for different discharges, in the range of 2 - 4 [hPa]. In most discharges the capacitor bank, capable to accumulate 1064 kJ energy at 40 kV, was charged to 24 – 25 kV.

The measurements were carried out in two different sample configurations. In the first configuration 10 light samples were used. All the samples were located *inside* the PF-1000 vacuum vessel. They were attached to a semicircular support at a distance 35 cm from the inner electrode face and each of them was inserted at a different angle to the electrode axis Z (Fig. 23).

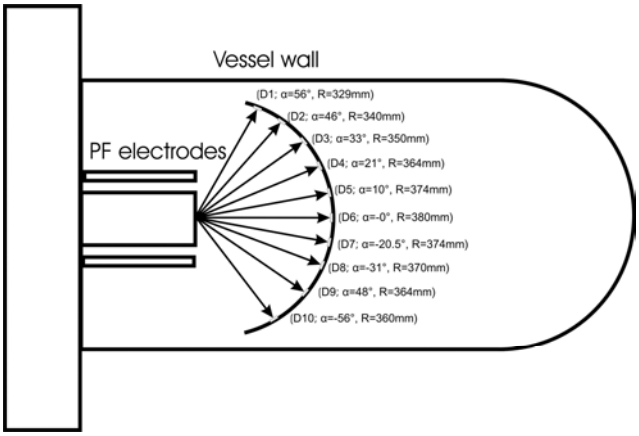

FIG. 23. Layout of indium samples inside of PF-1000 facility vacuum vessel. The activation samples allows to measure angular distribution of neutrons.

The samples were exposed to neutrons emitted from several PF-1000 discharges. After that they were removed from the vessel, and gamma-rays emitted by each sample were measured using a cross-calibrated NaJ(Tl) scintillation probe.

In the second configuration a set of heavy indium samples was used. These samples were located on the vacuum vessel's outer walls, in the plane parallel to the axis of the inner electrodes with each sample positioned at a different angle with respect to the electrode axis (Fig. 24).

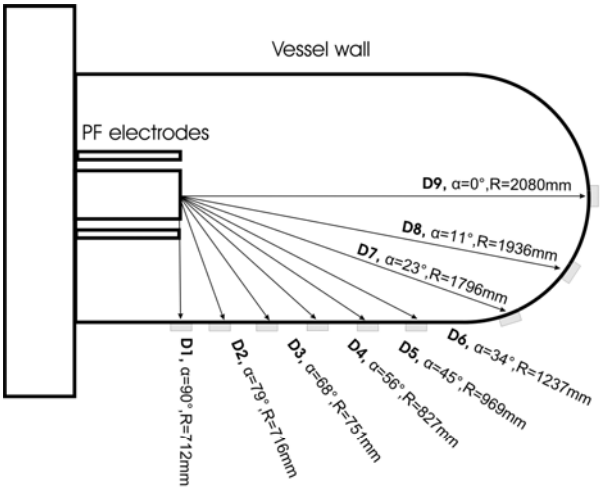

FIG. 24. Layout of heavy indium samples on the outer surface of the vacuum chamber walls. The configuration of nine large indium samples allows identification of horizontal distribution of neutrons by measurement of nuclear reactions caused by neutrons.

Such a configuration enabled quick removal of the irradiated samples and faster transportation them to the HPGe gamma spectrometer. Beside of that it was not necessary to open the vacuum vessel. Experiment was performed in two variants: with the sample D9 (Fig. 24) placed directly on the vessel's wall and the sample placed inside the sleeve approaching him to the main electrode.

5.3. Monitoring of neutrons based on nuclear reaction with indium.

The following nuclear reactions: $In^{115}(n,\gamma)In^{116}$, $In^{113}(n,\gamma)In^{114}$, $In^{115}(n,n')In^{115m}$, $In^{113}(n,n')In^{113m}$, play an important role in the neutrons interactions with indium nuclei. They are reactions of neutron capture and neutron scattering by the indium nuclei as well. The inelastic scattering reactions are threshold reactions, i.e. they occur only for the neutron exceeding a certain energy threshold. The nuclear reaction with In^{115} are the most important among other reactions because its occurring is most likely due to dominant abundance of this isotope (95.71%) inside the mixture of stable indium isotopes. In the case of In^{115m} the detection of photons with energy of 336 keV reveals the presence of neutrons with energies above ~ 400 keV. In spite of this threshold these reactions for neutrons with energy above 1 MeV are most common because the reaction cross section for neutrons of those energy is three orders of magnitude higher than for neutrons with energy slightly exceeding the threshold energy. Thus reactions induced by neutrons with energies above threshold energy are translated into gamma rays of specific energies.

The semiconductor detection system for gamma ray registration (Fig. 22 above) consists on an InSpector 2000 Multichannel Analyzer (MCA), a High Purity Germanium (HPGe) coaxial detector system, Genie-2000 Gamma Analysis Software, the numerical characteristic of the HPGe detector, Laboratory Sourceless Object Calibration Software (LabSOCS) and the shielding system. The shielding system consists of the specially designed electromagnetic shield (EMS) and the typical shield for radiation background reduction. The HPGe detector with radiation shield, MCA, and steering computer were placed inside the EMS and supplied with power from the uninterruptible power supply. This equipment protects the whole system against electromagnetic interference even propagated throughout the power network. The HPGe detector has been supplied by the manufacturer with its numerical characteristic which allows the determination of the sample activity without performing the efficiency calibration *in situ*.

The reliable detection and identification of the maximum number of nuclear reactions require finding the best sample geometry as well as measurement geometry (i.e. optimization) which ensures both high sample activation and effective registration of photons by means of the HPGe detector. During the activation process, the mass of the sample plays an important role because the number of activated nuclei in the target sample is strictly dependent on the sample mass. Also the shape of sample and its position in relation to the detector are important. The Integrated Mass Absolute Full Energy Peak Efficiency is a definite Riemann integral of mass and efficiency product and takes into account both the reactivity of the sample and the efficiency of its measurement by the HPGe detector. Optimization of it is a process of finding the best sample shape among plenty others, and the biggest sample mass. Fulfilling the above mentioned criteria the heavy cylindrical sample with diameter 6.37 mm and 4.3 mm in thicknesses was proposed as the activation sample.

The system consists of optimized in size and shape indium sample and particular HPGe detector. It is characterized by high resolution and the highest efficiency for gamma registration and allows measurement of samples activity in the range of even tenth part of Becquerel. Thus prepared the system was applied for measurement of samples activated outside vacuum vessel wall and both the horizontal and azimuthal distribution of neutron fluxes were determined by them.

The NaJ probe with Tucan MCA was applied mainly for the measurement of light samples (with 20 mm in diameter and 10 mm in thicknesses) activated inside the vacuum vessel. However the mentioned method was involved also with large (described previously) samples activated on the outer wall of PF-1000 facilities. Common spectrometric procedures were adapted to energy calibration and net area calculation. The efficiency calibration of the system was performed by cross calibration method. One sample representing both of types was taken from the set of samples and after that it was activated with Am-Be neutron source. Then the sample was measured with NaJ – probe and HPGe detector respectively. The activity of In^{115m} and In^{116} were both precisely estimated with HPGe spectrometry system. Finally these results were used to calculate the particular sample's efficiency for NaJ probe. The sample geometry and measurement geometry during cross calibration and experimental procedures were preserved.

5.4. The MCNP geometrical model

The most effort-consuming part of the neutron analysis for calculating the fluence of neutrons on the samples lies in providing an accurate description of the geometrical and material components of the device in the code. A geometrical model of the PF-1000 facility has been prepared for neutron transport Monte Carlo calculations by MCNP code. Structure of the steel chamber, steel and copper electrode set and indium samples have been modeled quite accurately. Cut view of the geometry from MCNP input is shown in Fig. 25. The MCNP5 code with MCNP5DATA cross section library has been used for calculations of neutron distributions outside the chamber of PF-1000 facility. Monte Carlo simulations have been performed for 2.5 MeV neutrons. It has been assumed that the neutrons are emitted from a point source placed at different positions of the pinch plasma. The number of simulated histories for each neutron source has been $2 \cdot 10^8$. The estimated relative errors achieved for the calculated results are usually below 1%.

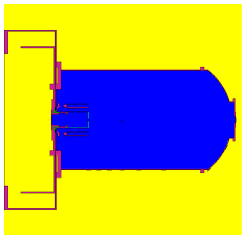

FIG. 25. Cut view of geometry from MCNP input.

5.5. Results

The results obtained with the set of small indium samples which were exposed inside the PF-1000 chamber to neutrons emitted from a series of 10 discharges are shown in Fig. 26.

The line that connects the measurement points is symmetrical and can be well fitted by a Gaussian distribution. Using this configuration we were able to measure integrated angular distributions of neutrons emitted from a number of discharges.

Using the $^{115}In(n,n')^{115m}In$ nuclear reaction and the semiconductor detection system the horizontal distributions of neutrons were measured for several single PF discharges. The samples were activated on the outer walls or sleeve and after that they were precisely measured with the gamma spectrometer and their initial activities were then calculated. The measurements were performed for discharges with different neutron emissions.

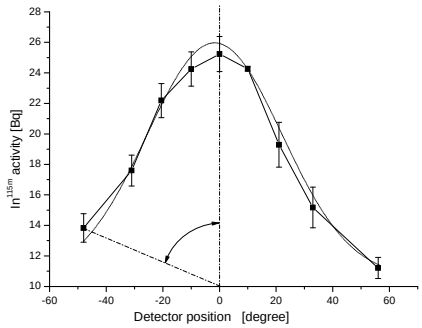

FIG. 26. Horizontal distribution of activity induced by neutrons emitted from PF-1000 facilities during 10 pulses. Measurements were committed with NaJ probe. Note: the distance from the anode plate to indium samples is taken into account in evaluation of the activity. Dot lines in the picture represent Gaussian fit of experimental data.

The activities of In^{115m} radionuclide were changed from tenths of Becquerel up to a few of Becquerel meanwhile the activities of In^{116} reaction products were ten times higher. Both values increased linearly with the neutron emission rate. All the horizontal distribution curves had very similar shape (Fig. 27) and could be fitted by a Gaussian distribution.

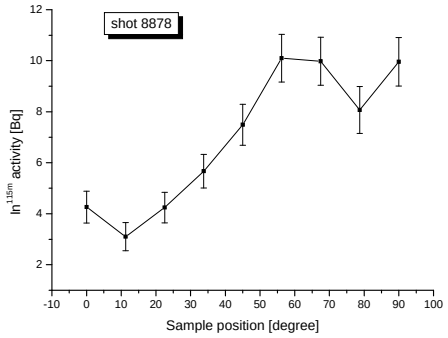

FIG. 27. Measured activities of indium samples located at different angles relative to the electrode axis. Note: the distance from the neutron source (plasma pinch) is different for each sample. Shot 8878 neutron yield measured by silver activation counter $Y_n=3\cdot10^{11}$.

MCNP calculations with a point source of D-D neutrons (2.5 MeV) placed at the different positions from the PF-1000 anode plate have been performed. Measured and calculated reaction rates for $^{115}In(n,n')^{115m}In$ reaction have been used to find the fluence rate of neutron in each sample from the following formula:

$$\varphi_{exp} = \varphi_{cal} \times (\alpha_{exp} / \alpha_{cal}) \qquad (6)$$

where: α_{exp} – measured reaction rate, α_{cal} – reaction rate calculated from MCNP, φ_{cal} – fluence rate of neutrons calculated from MCNP. Neutron fluence rate anisotropy at angle of θ_i in relation to electrode axis has been calculated from:

$$A(\theta_i) = \frac{\varphi^i_{exp}}{\varphi^0_{exp}} \cdot \frac{1}{c_i}$$

where: $c_i = \frac{\varphi^i_{cal}}{\varphi^0_{cal}}$ geometrical coefficient calculated from MCNP, determining the influence of surroundings on neutrons emitted at *i*-th angle in relation to neutrons emitted at angle of 0˚.

Using the results presented in Fig. 27 neutron fluence rate anisotropy can be evaluated. The $A(\theta_i)$ is shown in Fig. 28.

Using neutron fluence rate anisotropy evaluated from the experimental data the character of neutron emission from pinch plasma can be shown. Related to the data presented in Fig. 28 it can be noted that neutron emission from pinch plasma is provoked by axially streaming deuterons in pinch. Using this data and comparing them with neutron fluence anisotropy presented in [17] the evaluation of the deuteron beam energy may be done.

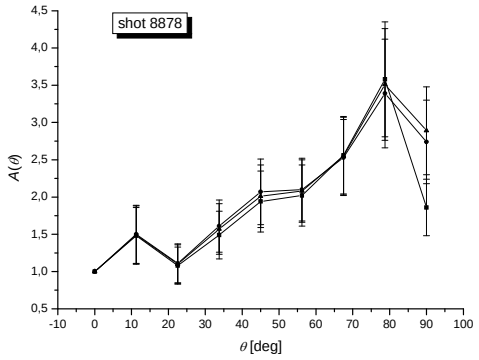

FIG. 28. Neutron fluence rate anisotropy evaluated from measurements of samples activity and calculations of $In^{115}(n,n')In^{115m}$ reaction rate in every sample. Calculations were performed for 3 distances of the point source from the inner electrode end: ■ – 0 cm, ▲ – 5 cm and ● – 10 cm.

6. CONCLUSIONS

The results of the studies described in this document can be summarized as follows:

1. Modernization of the 1-MJ Dense Plasma Focus facility serving for many groups from different countries for physics researches and radiation material sciences applications in the area of the mains-stream nuclear fusion program has been provided successfully. The renovated device has innovative sparks with shorter jitter, new cables and other elements and the automation systems of control and maintenance of the device operation for applications.

2. Diagnostic complex of the device became stronger due to introduction of the 16-frames 1-ns laser interferometric system, the visual spectrometery with temporal resolution and the absolute calibrated magnetic probe placed inside the anode.

3. Two different ways of measurements of neutron emission anisotropy using activation technique were used in the PF experiment. One with the samples near the pinch plasma (inside the PF vacuum chamber) and the second with the samples located far away (on the PF vacuum chamber). The results obtained for the second way is less sensitive to plasma neutron geometry. So, this way was used the more precise neutron anisotropy measurements.

4. Horizontal distributions of 2.5 MeV fusion neutrons emitted from PF-1000 discharges were measured using the activation technique. These researches were oriented to look for the new method needs as well as for better understanding the mechanism of neutron generation in PF-1000 facility.

5. The researches performed in this work confirmed the usefulness of the threshold nuclear reaction (e.g. $In^{115}(n,n')In^{115m}$) to measure anisotropy of neutron emission from pinch plasma. It should be emphasized that the MCNP calculation ought to be used with the measurements in order to proper elaboration of the neutron emission anisotropy.

6. A number of successful experiments in the field of radiation material sciences intended to test materials perspective for use in the main-stream fusion device (including round-robin tests of the same samples) were provided with the modernized PF-1000 facility. In these experiments participants of the CRP “Integrated approach to Dense Magnetized Plasma applications in nuclear fusion technology” from 7 countries took part.

7. The results on the activation of different elements by neutrons produced in DPF devices show that isotopes with a suitable cross-section of the activation reaction can be tested by a well defined deuterium plasma neutron source like a dense plasma focus device. The experiments were intended to see consequences of irradiation of materials by neutron flux from DPF comparable with the flux expected on the back-side of the first wall of the chambers of the large fusion installations. It was found that the total neutron yield values determined from the activities induced in different materials are comparable to those measured by means of a calibrated silver activation counters. However we have found that the results from measurements of indium's activity are burdened with very high uncertainty due to discrepancy between the library's cross-sections data for both reactions.

8. At present time the modernized PF-1000 machine being one of the largest Plasma-Focus devices operating with deuterium as a working gas is ready to serve as one of the principle facilities for the goals of the new IAEA CRP “Investigations of Materials under High Repetition and Intense Fusion-relevant Pulses”.

REFERENCES

[1] GRIBKOV, V.A., PIMENOV, V.N., IVANOV, L.I., DYOMINA, E.V., *et al.*, “Interaction of High Temperature Deuterium Plasma Streams and Fast Ion Beams with Condensed Materials in Dense Plasma Focus Device”, Journal of Physics D: Applied Physics **36** (2003) 1817–1825.

[2] SCHMIDT, H., KUBES, P., SADOWSKI, M.J., SCHOLZ, M., “Neutron Emission Characteristics of Pinched Dense Magnetized Plasma”, IEEE Trans. Plasma Science **34** (2006) 2363–2367.

[3] KRAUZ, V.I., “Progress in Plasma Focus Research and Applications”, Plasma Physics and Controlled Fusion **48** (2006) B221–B229.

[4] a) FILIPPOV, N.V., GRIBKOV, V.A., *et al.*, “Experimental and Theoretical Investigation of the Pinch Discharge of the Plasma Focus Type”, Proc. of the Int. Conf. on Plasma Phys. and Contr. Nuclear Fus. Research, IAEA-CN 28/D-6, Madison, USA: Vienna (1971) 573–600.
b) GRIBKOV, V.A., KROKHIN, O.N., *et al.*, “Methods of the Double Wavelength Interferometry of the Axisymmetric Dense Plasma Configurations”, Soviet Journal of Quantum Electronics, No. 6 (1971) 238–244.
c) GRIBKOV, V.A., FILIPPOV, N.V., *et al.*, “Observation of the Second Compression in a Final Stage of the Plasma Focus Discharge”, ZETP Lett. **15**(6) (1972) 132–135.
d) DENUS, S., A. KASPERCZUK, A., PADUCH, M., *et al.*, “Multi-frame interferometric setup for studying quick-change processes”, Journal of Technical Physics **18** (1977) 395-405.

[5] KASPERCZUK, A., MAKOWSKI, J., PADUCH, M., *et al.*, “Application of Fast Three-Frame Interferometry to Investigation of Laser Plasma”, Proc. SPIE 22 (1994) 449.

[6] SOTO, L., CHUAQUI, H., SKOWRONEK, M., “Eight Frame Holographic Interferometry System for Transient Plasma Diagnostics”, Applied Optics **34** (1995) 7831.

[7] OSTROVSKAYA, G.V., “Holographic Diagnostics of the Plasma: A Review”, Technical Physics **53** (2008) 1103–1128.

[8] KUBES, P., M. PADUCH, M., PISARCZYK, T., *et al.*, “Interferometric Study of Pinch Phase in Plasma Focus Discharge at the Time of Neutron Production”, IEEE Transactions on Plasma Science **37** (2009) 2191–2196

[9] GRIEM, H.R., Plasma spectroscopy, McGraw-Hill, New York (1964).

[10] Plasma diagnostics, edited by W. Lochte-Holtgreven, NorthHolland, Amsterdam (1968).
[11] DIMITRUEVIC, M.S., KONJEVIC, N., "Stark widths of doubly- and triply-ionized atom lines", J. Quant. Spectrosc. Radiat. Transfer. **24** (1980) 125–138.
[12] PIMENOV, V.N., DEMINA, E.V., MASLYAEV, S.A., *et al.*, "Damage and modification of materials produced by pulsed ion and plasma streams in Dense Plasma Focus device", Nukleonika **53**(3) (2008) 111–121.
[13] GRIBKOV, V.A., TUNIZ, C., DEMINA, E.V., *et al.*, "Experimental studies of radiation resistance of boron nitride, C2C ceramics Al_2O_3 and carbon–fiber composites using a PF-1000 plasma-focus device", Phys. Scr. **83** (2011) 045606; doi: 10.1088/0031-8949/83/04/045606.
[14] GRIBKOV, V.A., DEMIN, A.S., DEMINA, E.V., *et al.*, "Physical processes taking place at the interaction of pulsed ion and plasma streams with target surface having shapes of plate and tube inside the working chamber of the Dense Plasma Focus device", Applied Physics (2011) №3, pp. 43–51, *in Russian.*
[15] PROKOPOWICZ, R., BIENKOWSKA, B., DROZDOWICZ, K., *et al.*, "Measurements of Neutrons at JET by Means of the Activation Methods", EFDA–JET–PR(09)45 (2009) 15 pp.
[16] GRIBKOV, V.A., BANASZAK, A., BIENKOWSKA, B., *et al.*, "Plasma dynamics in PF-1000 device under the full-scale energy storage: II. Fast electrons and ions characteristics versus neutron emission parameters, and the gun optimization properties", J. Phys. D: Appl. Phys. **40** (2007) 3592–3607.
[17] STEINMETZ, K., "Neutron production and ion beam generation in Plasma Focus device", PhD thesis 1980, University of Heidelberg.

CODED APERTURE TESTS FOR FUSION SOURCE IMAGING

S.V. SPRINGHAM, A. TALEBITAHER, P.M.E. SHUTLER, R.S. RAWAT, P. LEE

National Institute of Education, Nanyang Technological University, Singapore

Abstract

For Coded Aperture Imaging (CAI) of moderately extended sources, it is shown that mask patterns based on Singer sets offer superior Signal to Noise Ratio (SNR) by comparison with those based on, more commonly used, Hadamard sets. This is because Singer sets inherently have a wide range of available open fractions, allowing the design of the CAI mask to be tailored to the spatial extent of the source being imaged. The basis of CAI is reviewed and relevant SNR formulae are derived. The performance of a Singer set mask pattern with 400 pixels and 57 open square holes (representing $\rho=1/7=14.3\%$ open fraction) is studied by both numerical simulation and experiment. Monte Carlo simulation studies confirm the validity of our decoding algorithm and the derived SNR formulae. The experimental setup comprised: a ^{226}Ra source of alpha particles, a laser-machined CAI mask, and CR-39 nuclear track detectors, arranged inside a vacuum enclosure. After chemical etching of the detectors, the area, circularity, mean optical density and positions of all candidate tracks were measured by an automated scanning system. Appropriate criteria were used to select alpha particle tracks, and a correlation algorithm applied to the (x,y) data produced the de-coded image of the source. The results demonstrate that the Singer set CAI masks can achieve the resolution and SNR requirements for our intended application: imaging of the DD fusion source in pulsed plasma focus devices.

1. INTRODUCTION

The motivation for this work is the development of the CAI technique for imaging the source of fusion in small plasma focus devices [1] using the ~ 3-MeV protons from the DD reaction. The objective is to image the fusion source for individual plasma focus shots with typically proton yields of ~ 10^8. Our theoretical studies indicate that, for such a source, the best SNR should be obtained using masks based on Singer sets, which have lower open fractions than the more frequently used Hadamard sets. In this work we have employed Monte Carlo numerical simulations to confirm the validity of our decoding algorithm and SNR formulae. Experimentally, we have used a ^{226}Ra α-particle source (as a more controllable source than the plasma focus) to test our SNR predictions and CR-39 detector scanning algorithms.

The Coded Aperture Imaging technique was first introduced by Mertz and Young [2], and was improved by Dicke [3], Ables [4] and many other researchers [5–7]. Since its invention, the most salient applications of the CAI technique have been in X ray and gamma-ray astronomy [8, 9]. However in recent years the CAI technique has also been investigated for a broader range of applications. For example, in medical imaging it may be a means of obtaining high resolution images while decreasing the radiation dose for patients [10]–[13]. And its uses for particle-source imaging include Coded Aperture Fast Neutron Analysis (CNFNA) [14, 15] and Inertial Confinement Fusion (ICF) neutron and proton imaging [16–18]. The two most essential components of a CAI camera are a position-sensitive detector and a patterned mask of alternately transparent and opaque areas (or pixels). The detector and mask planes are arranged to be parallel, and the pixels are usually square or hexagonal. In essence all CAI schemes are a form of multiplexed pinhole imaging.

The pinhole is of course the simplest and earliest known method of imaging, and its limitations, in terms of resolution vs. signal, are well known. However it is still important for types of radiation for which coherent imaging is not practicable (e.g. vacuum-ultraviolet, X rays (>30 keV), gamma-rays, etc.). The basic concept of the CAI technique is to open multiple small pinholes, thereby maintaining good angular resolution, while achieving the high signal throughput of a large aperture. But for a detector of reasonable size, and a mask of

useful open fraction, there will be considerable overlap of the multiple (inverted) pinhole images. Therefore a de-convolution step is necessary to extract the final image, known as the decoded image. The unprocessed image from the detector is referred to as the coded image.

The first CAI schemes simply used arrays of randomly positioned pinholes, but it was soon realized that patterns based on Cyclic Difference Sets (CDS) gave superior signal to noise performance through having flat side-lobes in their auto-correlation function. A considerable number of CDS-based mask patterns have since been designed and employed, with the aim of optimizing image quality, mostly for astronomical γ-ray sources. Some common classes of mask patterns are: Random Pinhole, Uniformly Redundant Array (URA), Modified-URA (MURA), Product Arrays, and No-Two-Hole-Touching (NTHT) arrays limits.

2. THEORY

Coded Aperture Imaging is a linear technique. If *O(x,y)* is the two-dimensional object distribution, *A(x,y)* is the aperture transmission function and *N(x,y)* is the signal independent noise, then the spatial distribution of the detected fluence (or coded image) is given by:

$$R(x,y) = A(x,y) * O(x,y) + N(x,y) \tag{1}$$

where * is the correlation operator. Then using the correlation method of de-coding, $\hat{O}(x,y)$, the estimate of the object or reconstructed image is defined by:

$$\begin{aligned}\hat{O}(x,y) &= G(x,y) * R(x,y) \\ &= G(x,y) * A(x,y) * O(x,y) + G(x,y) * N(x,y)\end{aligned} \tag{2}$$

where *G(x,y)* is the decoding function. From this equation it can be seen that the Point Spread Function, $PSF = G * A$, should ideally be a delta function for the best image reconstruction. Naturally, the choice of aperture pattern *A* and decoding function *G* have a large influence on the quality of the final image [19, 20].

A Cyclic Difference Set is a set of h positive numbers $\{a_1=0, a_2, a_3,..., a_s\} < p$, with the property that all differences $(a_i - a_j)$ modulo p for $i \neq j$, occur the same number of times $(= \lambda)$, corresponding to the flat auto-correlation side-lobe. The $i = j$ condition clearly occurs h times, corresponding to the auto-correlation peak. The numbers p and h are referred to as the modulus and size of the CDS, respectively. So the important parameters for any CDS can be abbreviated to (p, h, λ). Among the Cyclic Difference Sets there are two subclasses which are particularly suitable for generating masks for multiplex imaging:

1) Singer sets [21], [22] for which $p = \frac{t^{m+1}-1}{t-1}$, $h = \frac{t^m-1}{t-1}$ and $\lambda = \frac{t^{m-1}-1}{t-1}$ with t being a prime number, or a prime power,

2) Hadamard sets [23], [24] for which $p = 4t - 1$, $h = 2t - 1$ and $\lambda = t - 1$ with t being an integer.

To form a two dimensional mask the CDS is wrapped onto a rectangular array, where the sides of the rectangle are factors of p. Hence, p represents the total number of pixels in the mask, and h is the number of open pixels (holes). Considering these two sets, it can be seen that Hadamard masks have an open fraction of $\rho_H = h/p = (2t-1)/(4t-1)$, i.e. very close to 50%, whereas those based on Singer sets have a variable open fraction $\rho_S = (t^m - 1)/(t^{m+1} - 1) \approx 1/t$. Since t is a prime number, or prime power, the obtainable open fractions with Singer sets are: $\rho_S \cong \frac{1}{2}, \frac{1}{3}, \frac{1}{4}, \frac{1}{5}, \frac{1}{7}, \frac{1}{8}, \frac{1}{9}, \frac{1}{11}$... (open fractions of $\frac{1}{6}$ and $\frac{1}{10}$ etc. are not obtainable). It is known in the literature [6, 25] that for maximum SNR, the optimum

mask open fraction decreases as the spatial extent of the source increases. However, attempts to reduce the effective open fraction of Hadamard set masks have not been successful [10]. Hence for imaging extended sources, the wide range of open fractions attainable with Singer sets is an important advantage, enabling the mask to be designed to achieve near optimum SNR.

Fenimore [6] and Accorsi *et al*. [10] have compared the SNR for different Hadamard families and pinholes for a series of simulated sources using the standard "balanced" method of decoding. However, their definition of SNR corresponds to the variation in brightness of a given fixed pixel between hypothetically many exposures for a source with assumed constant intensity, which simplifies the statistical analysis at the cost of a loss of intuition. Also, balanced decoding, while relatively simple in the Hadamard case (the matrix G consists of +1 where A has a hole and −1 where it does not) becomes more complicated in the Singer case. In this paper we consider it more meaningful to define SNR in terms of the variation in brightness across different pixels within a single exposure, more precisely as follows:

$$SNR = \frac{signal\ from\ given\ pixel}{\sqrt{variance\ of\ signal\ across\ image}} \tag{3}$$

As well as being closer to our intuition, this within-exposure definition of SNR has the added advantage of being more readily compared with the results of experiment. And in cases of non-repeatability, where a single-exposure is the only thing available, it may be the only possibility. We shall also find it more convenient to use direct decoding, where the decoding matrix $G = A$ the aperture itself, which, although differing from balanced decoding by overall constants and scaling, separates the terms involved in a way which makes the statistical analysis more straightforward.

Direct decoding, where we take $G = A$, the aperture itself, uses the defining property of a CDS based coded aperture, namely that if two copies of the aperture are cyclically displaced relative to each other then the resulting open fraction, that is, where the holes of the two copies happen to coincide, is ρ^2 independent of the displacement, except of course when the two copies themselves coincide, in which case the open fraction is just ρ again. In other words, as the aperture A passes across the encoded image R we will pick up the signal from the object pixel matching that position but attenuated by a factor ρ, together with the signal from all other object pixels but attenuated by a factor ρ^2. More specifically, let N be the total number of particles incident on the mask, and $N' = \rho N$ the number which pass through the mask, and let n be the number of particles incident on the mask which arrive from a direction associated with a particular object pixel, and $n' = \rho n$ those passing through the mask, and let the object comprise m bright (illuminated) pixels. Then, when the decoding matrix is aligned with that particular pixel, the decoded signal will be $n' + \rho(N' - n') = \rho n + \rho^2(N - n)$, while if the decoding matrix is aligned with any other pixel in the field of view not corresponding to a pixel on the object the decoded signal will be $\rho N' = \rho^2 N$. So direct decoding produces a sharp image of the object but superimposed on an approximately uniformly bright background, where the average background brightness is $\rho N'$. Subtracting this average background brightness we recover a signal $\rho n + \rho^2(N - n) - \rho^2 N = \rho n - \rho^2 n = \rho(1 - \rho)n$ against an approximately uniformly zero background. It is then not difficult to show that, up to an overall scaling factor of $1/(1 - \rho)$ the resulting decoded image is identical with that obtained from balanced decoding.

Including this overall $1/(1-\rho)$ scaling, in which case the reconstructed signal is just ρn, has the advantage that the total particle count in the reconstructed image is identical with the number of particles actually detected. Since the SNR is invariant under overall scaling of the data, however, direct decoding allows us to neglect it for the purposes of the statistical analysis. An additional advantage of direct decoding, at least in the case where SNR is defined within-exposure, is that the overall constant $\rho N'$ subtracted also does not affect the computation of the variance and can be neglected, whereas in the case where SNR is defined exposure-to-exposure it does vary. To compute the SNR within-exposure it only remains therefore to compute the variance of the signal $n' + \rho(N' - n') = \rho n + \rho^2(N - n)$. It is a property of CDS based coded apertures that the second term represents a pseudo-random sampling of the detected particles with probability ρ and so follows binomial statistics. If we make the simplifying assumption that the *m* object pixels are uniformly bright, then the first term also follows binomial statistics with probability ρ. Neglecting the covariance between the two terms, and using the standard result that a $B(N,p)$ random variable of *N* trials with probability success p and failure $q = 1 - p$ has expectation *Np* and variance *Npq*, the variance of the directly decoded signal as the decoder moves across the coded image is $\rho(1-\rho)n + \rho(1-\rho)(N' - n') = \rho(1-\rho)n + \rho(1-\rho)\rho(N-n)$. Substituting this into our earlier formula defining the within-exposure SNR we obtain:

$$SNR = \frac{\rho(1-\rho)n}{\sqrt{\rho(1-\rho)n + \rho^2(1-\rho)(N-n)}} = \frac{\sqrt{\rho(1-\rho)}\,n}{\sqrt{n + \rho(N-n)}} \tag{4}$$

This expression happens to coincide with the formula derived by Fenimore [6] although under quite different assumptions i.e. exposure-to-exposure variance, and later shown by Accorsi [10] to be in error in that case. A more careful analysis, which takes account of some but not all of the covariance between the two terms in the signal, results in a modified version of the formula derived by Accorsi, although again under different assumptions, and the details of this derivation will be presented in a later paper. All of these formulae are, however, just approximations, and a complete SNR analysis of the within-exposure case has not to our knowledge been reported. A useful simplification is to consider the *m* bright pixels to be equally bright. Then differentiating the SNR function with respect to ρ gives the optimum open fraction in terms of the number of bright pixels:

$$\rho_{\text{opt}} = \frac{1}{1+\sqrt{m}} \quad \text{and} \quad SNR_{\max} = \rho_{\text{opt}}\sqrt{\frac{N'}{m}} = \rho_{\text{opt}}\sqrt{n'} = \sqrt{\rho_{\text{opt}}\, n} \tag{5}$$

Hence, for a mask of constant size (and therefore constant N'), both ρ_{opt} and $SNR_{\max}$ decrease as the source becomes more extended and illuminates more pixels; or alternatively, as the pixel-size shrinks and the number of pixels increases. Figure 1 shows a plot of SNR versus ρ for different numbers of bright pixels *m*.

This calculation is for a mask of the dimensions used for our experimental study (8×8 mm^2) and an isotropic source of 10^8 particles located at a distance of 45 mm from the centre of the mask. The solid angle subtended by the mask is 0.0314 sr, and the number of particles hitting the mask is $N' = 2.5 \times 10^5$. The vertical lines on the plot represent the values of $(\rho_S \cong 1/t)$ attainable with Singer set masks, while the circle symbols represent values of ρ_{opt} for each curve. Hadamard masks, being restricted to $\rho_H \cong 0.5$, are best suited to situations with very few bright pixels.

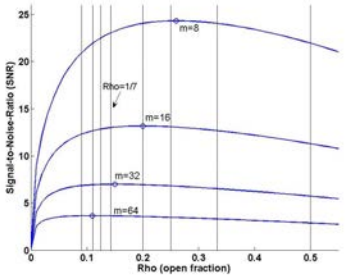

FIG. 1. SNR vs. open fraction (ρ) for objects (of the same total brightness) which illuminate different numbers (m) of pixels: m = 8, 16, 32, and 64. The mask has a total of 400 pixels. Open circles represent values of ρ_{opt} for each curve. Vertical lines represent open fractions: $\frac{1}{2},\frac{1}{3},\frac{1}{4},\frac{1}{5},\frac{1}{7},\frac{1}{8},\frac{1}{9},\frac{1}{11}$.

Also for pinhole imaging, the SNR is simply:

$$SNR_{\mathrm{ph}} = \frac{n}{\sqrt{n}} = \sqrt{n} \tag{6}$$

It should be remembered that the value of n for a CAI is h times greater than that for a pinhole of the same angular resolution. Hence the optimum enhancement of a CAI mask over a pinhole (i.e. always with a mask of optimum open fraction ρ_{opt}) is given by

$$\left(SNR_{\max}/SNR_{\mathrm{ph}}\right)_{\mathrm{opt}} = \sqrt{h\rho_{\mathrm{opt}}} = \rho_{\mathrm{opt}}\sqrt{p} = \frac{\sqrt{p}}{1+\sqrt{m}} \tag{7}$$

It is clear from this formula that the SNR advantage of CAI over pinhole imaging decreases as the source becomes more extended, until the limit at which the source fills the entire field of view ($m \approx p$) when CAI offers essentially no SNR advantage over pinhole imaging. As a rule of thumb, CAI can be considered advantageous, and worth the additional complexity, in cases where the source occupies no more than 10% of the field of view.

Experimentally it is usually the case (and certainly so for the plasma focus) that the precise number of bright pixels is not known prior to the exposure. It is probably best therefore to use a mask with ρ somewhat larger than ρ_{opt} for the anticipated value of *m*. As can be seen from Fig. 1, the SNR penalty for using a moderately larger value of ρ is slight. Also, for experiments using CR-39 detectors, the signal independent noise *N(x,y)* in equations (1) and (2) is primarily due to flaws, scratches, alpha tracks from background radon, which are always present to some extent on the etched CR-39 surface. With proper handling of the material this background is relatively low and uniform across the detector surface, resulting in a slightly degraded SNR in the decoded image.

3. EXPERIMENTAL SETUP AND PROCEDURE

For these tests we used a coded aperture mask based on the Singer set $(p, h, \lambda) = (400, 57, 8)$ giving a ρ = 1/7 = 14.3% open fraction mask with 20×20 pixels. For this CDS, $t = 7$ and $m = 3$. This mask pattern is shown in Fig. 2(a). To fabricate the physical mask, 57 square holes (400 μm side) were laser-machined in 50μm thick Havar alloy. The mask has overall dimensions of 8×8 mm^2 and is shown in Fig. 2 (b). A ^{226}Ra (half-life 1602 y) source of 5 μCi activity and 9 mm diameter (Fig. 3) was used as the α-particle source to be imaged. The decay chain of ^{226}Ra involves the emission of 5 α particles with energies lying in the range 4.6 MeV to 7.7 MeV.

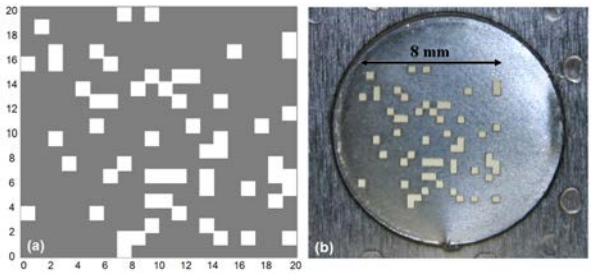

FIG. 2. (a) the CAI mask pattern, and (b) a photograph of the fabricated mask.

A straightforward arrangement of vacuum pipes, rotary pump and a linear translator, was used to perform imaging experiments for several simple source geometries. The ^{226}Ra disc-source and CR-39 detectors were located at opposite ends of a vacuum pipe, with the coded aperture positioned between them. The source-to-mask and mask-to-detector distances were $d_1 = 127$ and $d_2 = 11$ cm respectively (see Fig. 4). The de-magnified image of the ^{226}Ra disc-source has a diameter of approximately 2 pixels in the image plane, and this small feature will be referred to as a "spot". The rotary pump maintained the pressure below 1 mbar during exposures, ensuring that the α particles have ranges $\gg (d_1 + d_2)$ within the enclosure.

A 1-spot image was obtained for an exposure of 6.5 h duration. Using the linear translator we also synthesized a 2-spot image and an extended "ridge" image. For the 2-spot image, two 6.5 h exposures were performed, with ^{226}Ra source translated through 2.4 cm between exposures. The ridge-image comprised 13 individual exposures of 0.5 h duration, with 12 translations of 0.2 cm between exposures. Hence the brightest part of the ridge source is of length 2.4 cm, while its full length is 3.3 cm and its width is 0.9 cm. For the sake of comparison, 1-spot, 2-spot and ridge exposures were also performed with the coded aperture mask replaced by a conventional pinhole of the same size as one pixel of the mask (400 μm side). The duration of each pinhole exposures was the same as the corresponding mask exposure.

The linear dimensions of mask and detector determine the CAI Field of View (FOV) which is the maximum object size that can be fully coded on the detector:

$$FOV = \frac{d_1 L_D - (d_1 + d_2) L_M}{d_2} \tag{8}$$

where L_D and L_M are the lengths of the detector and mask sides respectively. The CR-39 detectors used were 2.5×3.5 cm^2, while L_M for the mask was 0.8 cm, giving a FOV in the source plane of 18.8×30.4 cm^2. So our simulated sources (full length ~3.3 cm) were easily within the fully coded FOV. Also the FOV for the pinhole was still wider than that of the CAI camera. The resolution of a CAI or pinhole camera is effectively the magnified pixel size in the source plane. For the present geometry; $Resolution = P_M \times \frac{d_1+d_2}{d_2} = 5.0$ mm, where P_M is the mask pixel size of 400 μm.

FIG 3. Radium-226 alpha-particle source.

CR-39 (PM-355, Page Mouldings Ltd., UK) polymer nuclear track detectors registered the arrival positions of the ~5 to 8 MeV α particles passing through the mask. The detection efficiency of C-39 for α particles incident at near normal incidence is effectively 100%. Suitable exposure times were calculated in the basis of obtaining a sufficiently high track count with minimal track overlap. Alpha particles are emitted isotropically from the ^{226}Ra source at a rate of $5 \times 5 \times 3.7 \times 10^4$ s^{-1} $= 9.25 \times 10^5$ s^{-1}. With the mask having an open area of 9.12 mm^2 and positioned 1270 mm from the source, the rate of α particle transmittance by the mask was $0.42\ s^{-1}$. So for an exposure of 6.5 h duration, the expected number of α particle tracks on the CR-39 is 9,740. Then for typical track densities of ~900 mm^{-2}, the fraction of overlapped tracks was found to be below 3%. A small correction factor was applied in the analysis to take account of overlapped and unrecognized α particle tracks. For the case of the pinhole the expected number of tracks (with the same exposure time) is simply $1/57$ of that for the mask; therefore about 140 tracks. Track overlap for the pinhole case was negligible.

It is worth emphasizing that linearity of detector response and high spatial resolution (ideally sub-pixel) are key factors for the successful application of the CAI technique. In both these respects CR-39 is an excellent detector: track-counting ensures very good linearity and the spatial resolution is of the order of microns.

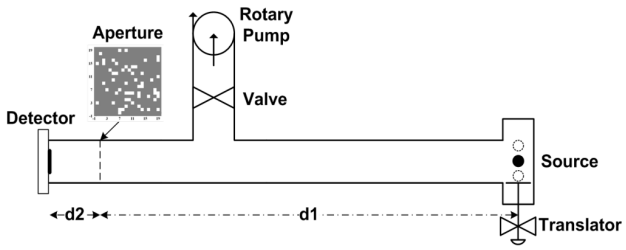

FIG 4. Experimental arrangement of CR-39 detector, CAI mask and ^{226}Ra source within vacuum enclosure.

4. TRACK ANALYSIS AND IMAGE DECODING

After exposure, the CR-39 detectors were etched in an aqueous solution of 6.25 n NaOH, at 70°C for 5 hours. The bulk etch rate under these conditions is 1.6 μm/h [26, 27]. A magnified image of etched tracks on the detector surface is shown in Fig. 5. Making use of a program for calculating the parameters of etched tracks [28–30], the track diameter and depth [31] for ~5 to 8 MeV α particles were predicted to be ~8 μm and ~7 μm respectively. The diameter value was found to be in good agreement with the experimentally measured average track diameter. An optical microscope (Olympus BX51) was used to acquire the images of CR-39 surface. Using an MPlan×20 objective lens, the 1.4 Mpx CCD field of view was a 528×378 μm^2 rectangle. The detector scanning system also comprises a (PRIOR Scientific) motorized microscope stage controlled by Image-Pro software (Media Cybernetics). The software auto-focus option was used to scan the entire exposed area on the CR-39, storing contiguous images of the CR-39 surface to the computer hard disk. For CAI exposures an array of 36×48=1,728 microscope images were captured, while for pinhole case it was 4×6=24 images.

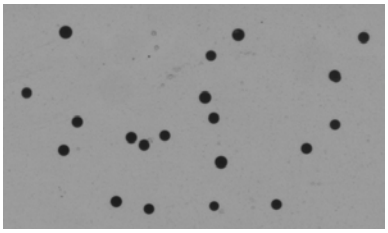

FIG 5. Optical micrograph of alpha-tracks on CR-39 with the dimension 226×133 μm^2.

An Image-Pro macro was written to automatically analyze all the stored images, and write a data file containing five measured parameters for each recognized dark candidate track. These parameters are: area, average brightness, roundness and (*x*,*y*) position. To discriminate between genuine α particle tracks and spurious dark features, within-polygon criteria were applied to scatter plots of (i) brightness vs. area, (i) roundness vs. area, and (iii) roundness vs. brightness, as shown in Fig. 6 (a-c). Genuine α particle tracks were selected by applying the logical AND of these three criteria, and the (*x*,*y*) positions of all selected tracks (representing the coded image) were written to a new file. The coded image was then processed by our convolution-based decoding algorithm. The first step in this algorithm is to pixelize the detector plane by two-dimensional binning of the track positions in a 39×39 histogram array. Standard CAI shifting and folding operations reduced this to a 20×20 fully-coded array. Cyclic convolution of this array with the defined mask pattern, followed by side-lobe subtraction and re-scaling produced the final de-coded image. The CAI decoding program is written in Visual Basic.

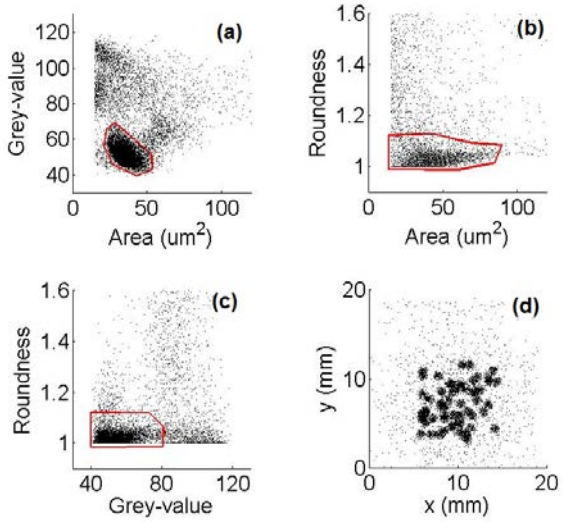

FIG 6. Scatter plots of measured parameters of dark features on CR-39 detector surface: (a) grey-value vs. area, (b) roundness vs. area, and (c) roundness vs. grey-value, with user-defined polygon for each. (d) Positions (x,y) of genuine alpha-particle tracks (for 1-spot source) selected by applying the logical AND of within-polygon criteria shown in a-c. This (x,y) data represents the coded image.

5. RESULTS AND DISCUSSIONS

Experiments with 1-spot, 2-spot and ridge sources were performed with both a CAI mask and a pinhole having the same angular resolution. Table 1 presents the number of recognized alpha-particle tracks and SNR values for each exposure.

TABLE 1. TRACK NUMBER AND SNR FOR CAI AND PINHOLE SYSTEM FROM EXPERIMENTAL RESULTS

Experiment	No. of tracks (pinhole)	No. of tracks (CAI)	Exp. SNR (pinhole)	Exp. SNR (CAI)	Theory SNR (CAI)
1-point circular source	142	8,086	6.2	26.6	38.0
2-point circular source	317	16,648	7.4	18.8	33.5
Ridge source	129	8,040	3.9	13.3	19.3

For CAI decoded images, the SNR was calculated by application of Eqn. (3). Since every pixel in the image effectively has a different signal-to-noise ratio, the values given in column 5 of Table 1 are those for the brightest pixel (n_p) in the image. Then with σ being the calculated standard deviation of pixel values outside of the illuminated region(s): SNR $= n_p/\sqrt{n_p + \sigma^2}$. This formula represents contributions from self-noise and sidelobe noise. The theoretical SNR values given in column 6 of Table 1 are calculated from Eqn. (4) using the total track number N in the reconstructed image and n_p the brightest pixel value. For pinhole images, only self-noise is present, and in accordance with Eqn. (6): SNR $= \sqrt{n_p}$.

For the 1-spot CAI mask exposure, the total number of α particle tracks was about 8000, and the coded image (as a scatter plot of tracks on the detector surface) is shown in Fig. 6 (d). The de-coded image derived from this data is shown in Fig. 7 (a2). The corresponding pinhole image for 1-spot, as shown in Fig. 7 (a1), has 142 tracks. Both images show the disc shape of the source but the CAI image reproduces it more faithfully, and as shown in Table 1, the CAI image has a superior SNR of 26.6 by comparison with 6.2 for the pinhole.

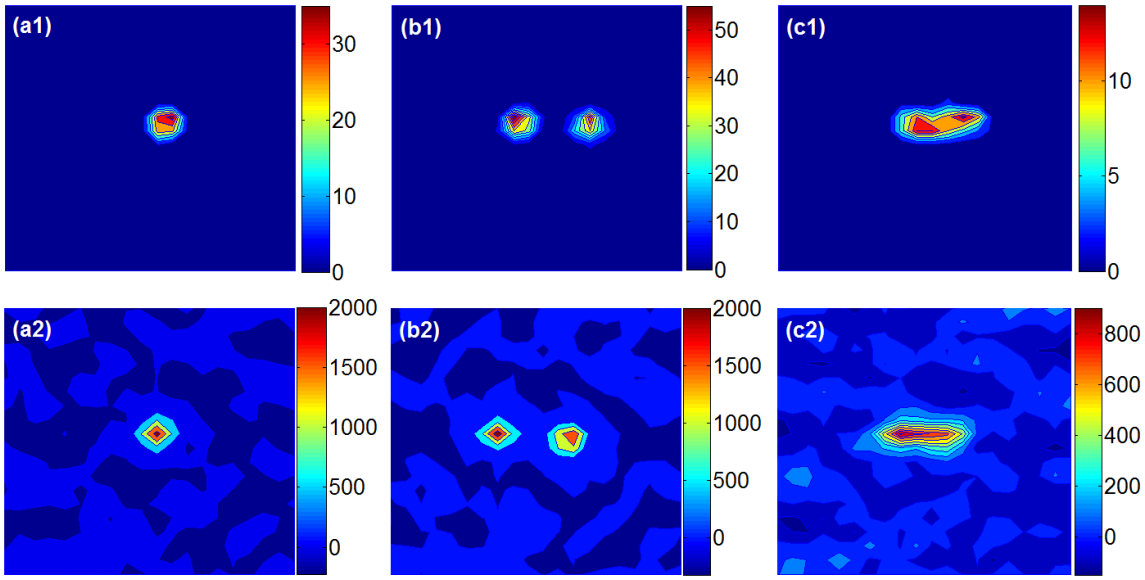

FIG 7. Reconstructed image from experimental track data for different source shapes with pinhole (top row) and 20×20 CAI mask (bottom row). All images are of 10 cm side (in the source plane). 1-point source for pinhole (a1) and mask (a2); 2-point source for pinhole (b1) and mask (b2); ridge source for pinhole (c1) and mask (c2).

For the 2-spot images, the detectors were exposed for 13 hours (twice the duration of the 1-spot exposures). Figure 7 (b1), for pinhole, shows two separated regions with no background; however the number of tracks in each spot differs significantly. With the same source, exposure times, and distances, the track counts per spot are 130 and 155. So they are respectively one standard deviation above and below their mean. This is a reflection of the large self-noise associated with the low-brightness pinhole image. By comparison, Fig. 7 (b2) shows the CAI reconstructed 2-spot image is much brighter and has a SNR value of 18.8 (a factor of 2.5 higher than that for the pinhole image). Here the number of counts in each spot is 5,656 and 5,759 respectively.

Lastly, Figs. 7 (c1) and 7 (c2) show the pinhole/CAI comparison for the ridge source. Again the CAI system produces a much brighter and more faithful image of the source, as reflected in the considerably larger SNR for the CAI vs. pinhole image: 13.3 and 3.9, respectively. However, despite the better SNR exhibited by the CAI, the values are below the theoretical SNR values predicted by equation (4).

One factor which degrades the SNR in the experimental situation is the background of spurious tracks due to microscopic flaws and scratches on the CR-39. This roughly uniform background is evident in the 1-spot coded image in Fig. 6 (d). A second factor is the spread in emitted alpha-particle energies, from 4.6 to 7.7 MeV, from members of the ^{226}Ra decay chain. This spread in alpha-particle energies necessarily produces a spread in etched track diameters and average grey-values, which complicates track-recognition and discrimination between genuine alpha-particle tracks and spurious tracks. As an indication of such problems: a total of 32,774 tracks were recognized and counted for the combined 26 hours of CAI exposure time (see Table 1), whereas the expected number (based on the activity calculation) is 4×9,740=38,960. Therefore the recognized number of tracks is about 16% lower than the expected value. Uncertainty in the ^{226}Ra source activity calibration may account for part of this difference. However, a 20% reduction would result from none of the highest energy alpha-particles (7.7 MeV from ^{214}Po), which produce the smallest tracks, being counted. More work aimed at optimizing detector etching conditions and image processing for track recognition would alleviate such problems. However, the present measurements are sufficient to validate the CAI technique with Singer set based masks before proceeding to image fusion protons from the plasma focus device.

6. MONTE CARLO SIMULATIONS

In order to check the correctness of the theoretical analysis and the decoding algorithm, a Monte Carlo program was written to simulate the experimental geometries described in the preceding sections. For example, for the 1-spot exposure, source points were generated pseudo-randomly and uniformly across a disc of the same radius (4.5 mm) as the alpha source. The directions of emitted rays were then generated isotropically within a 1º cone, fully illuminating the CAI mask. Rays impinging on the mask plane at the position of an open hole were transmitted to detector plane and the (x,y) position written to a file, while rays encountering opaque regions of the mask were terminated. In this way a coded image file is produced which is the equivalent of the experimental coded image file. The image decoding was then performed with the same program as for the experimental data. The number of rays emitted from the simulated source is the equivalent of the experimental exposures (as determined by the detector track count). SNR values in these images were calculated in the same way as for the experimental images.

In these simulations, the single pinhole and Singer set mask were compared for the three source geometries. In the absence of background noise, the result of pinhole system shows zero background but weak precision (Fig. 8-a1), whereas the coded aperture demonstrates better precision with the much higher particle number which is proportional to the number of holes (Fig. 8 (b1)). From the 1.38×10^6 radiated particles emitted within the 1° cone, about 143 particles will pass through the pinhole, whereas for the CAI maskS_{400}^{57} about 8,150 (57 times more than the pinhole) particles reach the detector.

From Table 2 it can be seen that the SNR for the 1-spot source shows an improvement by factor of 6.8, from 7.0 for pinhole to 47.7 for CAI. The 2-spot source is simulated as two 1-spot sources separated by 24 mm distance (center to center). Figure 8 (a2) and 8 (b2) show the simulation results for the pinhole and mask, respectively. The SNR for pinhole and CAI are 7.1 and 44.8 respectively; a factor of 6.3 improvement. Finally for the ridge source, the centres of random uniform disc sources were distributed randomly along a line of 2.4 cm length. Figure 8 (c1) shows the simulated pinhole image and it can be seen that the height and width of the imaged ridge varies irregularly along its length. By contrast the simulated CAI image shown in Fig. 8 (c2) reproduces the shape of the ridge far better. As the ridge source is the most extended of the three sources, the SNR for both pinhole and CAI mask are lower than the other two sources; being 4.7 for the pinhole and 22.9 for CAI mask. In this case the SNR for CAI mask is a factor of 4.9 better than that of the pinhole.

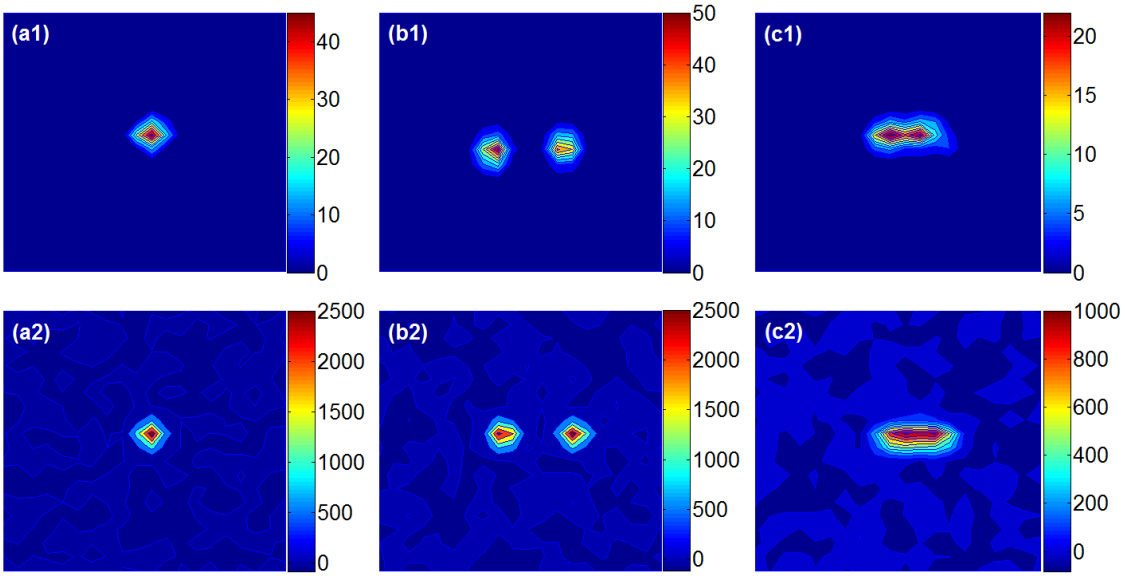

Figure 8. Reconstructed images from Monte Carlo simulation generated data for different source shapes with pinhole (top row) and 20×20 CAI mask (bottom row). All images are of 10 cm side (in the source plane). 1-point source for pinhole (a1) and mask (a2); 2-point source for pinhole (b1) and mask (b2); ridge source for pinhole (c1) and mask (c2).

TABLE 2. TRACK NUMBER AND SNR FOR CAI AND PINHOLE SYSTEM FROM MONTE CARLO SIMULATIONS

Simulation	No. of tracks (pinhole)	No. of tracks (CAI)	Sim. SNR (pinhole)	Sim. SNR (CAI)	Theory SNR (CAI)
1-point circular source	149	8,127	7.0	47.7	44.9
2-point circular source	292	16,299	7.1	44.8	40.9
Ridge source	144	8,051	4.7	22.9	21.1

7. CONCLUSION

In this study, a coded aperture mask based on a Singer Cyclic Difference Set has been used to image different alpha source shapes. A 20×20 pixel mask with 57 holes was fabricated and arranged within a vacuum enclosure to view a ^{226}Ra source. The position of the source was adjusted using a linear translator, enabling us to experimentally synthesize different source shapes, such as: 1-spot, 2-spot and ridge sources. The polymer nuclear track detector material CR-39 was used to register the ~5 to 8 MeV alpha particles passing through the coded mask. The detectors were then etched and scanned; and the acquired images were processed to select genuine alpha-particle tracks and produce a list of track positions – representing the coded image. A convolution procedure was then applied to obtain the final decoded images. For the purpose of comparison, exposures were also performed for each of the three source shapes, and for the same duration, using a pinhole of the same angular resolution as the CAI mask. It is observed from the final images that the CAI system has superior SNR and fidelity by comparison with pinhole images. The SNR values obtained for the CAI images are, however, below the values predicted from Eqn. (4). We consider this reduction in SNR to be largely due to the difficulty (in terms of automated image processing) in discriminating between spurious track-like features and the small tracks formed by the most energetic ^{214}Po alpha particles from the source.

Monte Carlo simulations of the CAI system were performed to validate our theoretical analysis and decoding algorithm/program. The SNR values obtained for the decoded images from simulation are in good agreement with predicted values from Eqn. (4). They also confirm that for moderately extended sources, a CAI system employing a Singer set mask with open fractions $\rho < 0.5$ achieves better SNR than a Hadamard mask. Moreover, a point which is of considerable practical importance is that the lower open fraction Singer set masks have an inherently stronger structure than the 50% Hadamard masks. This is a consequence of having fewer weakly supported opaque pixels. For imaging of *single* shots in pulsed fusion devices such as the plasma focus, the SNR enhancement obtainable with the CAI technique should permit definite structures to be observed and quantitative comparisons to be made with other diagnostic signals; which would be barely possible for the much dimmer pinhole images. In future work, we will present and analyze the first images of the plasma focus fusion source obtained using the CAI technique.

ACKNOWLEDGMENT

The authors would like to thank Dr. Daniel Lim Jye Suenn for his help in laser-machining the CAI mask. One of the authors, Alireza Talebitaher, would like to thank NIE/NTU for the provision of a research scholarship.

REFERENCES

[1] SPRINGHAM, S.V., LEE, S., MOO, S.P., “Deuterium Plasma Focus Measurements using Solid State Nuclear Track Detectors”, Braz. J. Phys. 32 (2002) 172–178.

[2] MERTZ, L., YOUNG, N.O., “Fresnel transformations of images”, (Proc. Int. Conf. on Opt. Instrum. Techniques, 1961), (HABELL, K.J., Ed) Chapman and Hall, London (1961) 305–310.

[3] DICKE, R.H., “Scatter-hole cameras for X rays and gamma rays”, Astrophys. J. 153 (1968) L101–L106.

[4] ABLES, J.G., “Fourier transform photography: a new method for X ray astronomy”, Proc. Astron. Soc. Australia 1 (1968) 172–173.
[5] FENIMORE, E.E., CANNON, T.M., "Coded aperture imaging with uniformly redundant arrays", Appl. Optics 17 (1978) 337–347.
[6] FENIMORE E.E., "Coded aperture imaging: predicted performance of uniformly redundant arrays", Appl. Optics 17 (1978) 3562–3570.
[7] S. R. Gottesman and E.E. Fenimore, "New family of binary arrays for coded aperture imaging", Appl. Optics 28 (1989) 4344–4352.
[8] CAROLI, E., *et al*., “Coded Aperture Imaging in X and Gamma Ray Astronomy”, Space Science Review 45 (1987) 349–403.
[9] SKINNER, G.K., “Coded-mask imaging in gamma-ray astronomy - separating the real and imaginary parts of a complex subject”, arXiv:astro-ph/0302354v1, 22nd Moriond Astrophysics Meeting, Vietnam-2003.
[10] ACCORSI, R., GASPARINI, F., LANZA, R.C., “Optimal coded aperture patterns for improved SNR in nuclear medicine imaging”, Nucl. Instrum. Methods Phys. Res. A. 474 (2001) 273–284.
[11] CUSANNO, F., *et al*., “High-resolution, high sensitivity detectors for molecular imaging with radionuclides: The coded aperture option”, Nucl. Instrum. Methods Phys. Res. A 569 (2006) 193–196.
[12] CHEN, Y.W., KISHIMOTO, K., "Tomographic resolution of uniformly redundant arrays coded aperture", Rev. Sci. Instrum. 74 (2003) 2232–2235.
[13] GARIBALDI, F., *et al*., “Small Animal Imaging by Single Photon Emission Using Pinhole and Coded Aperture Collimation”, IEEE Trans. Nuclear Science 52 (2005) 573–579.
[14] ZHANG, L., LANZA R.C., “CAFNA, coded aperture fast neutron analysis for contraband detection: Preliminary results”, IEEE Trans. Nuclear Science 46 (1999) 1913–1915.
[15] ACCORSI, R., LANZA R.C., “Coded Aperture Fast Neutron Analysis: Latest Design Advances”, 16th Intl. Conf. Appl. of Accel. Res. & Indust., Conf. Proc. 576 (2001) 491–494.
[16] CHEN, Y.W., *et al*., “Measurement of D-D burn region using proton penumbral coded aperture imaging”, Optics Communications, 73 (1989) 337–341.
[17] JAGER, U., *et al*., “Energy spectra and space resolved measurement of fusion reaction proton from plasma focus devices”, Rev. Sci. Instrum. 56 (1985) 77–79.
[18] BARRERA, C.A., MORSE, E.C., “Image reconstruction algorithms for inertial confinement fusion neutron imaging”, Rev. Sci. Instr. 77 (2006) 10E716.
[19] GROH, G., HAYAT, G.S., STROKE, G.W., “X ray and γ-Ray Imaging with Multiple-Pinhole Cameras Using a posteriori Image Synthesis”, Appl. Optics. 11 (1972) 931–933.
[20] BROWN, C., “Multiplex imaging with multiple-pinhole cameras”, J. Appl. Phys., 45 (1974) 1806–1811.
[21] SINGER, J., “A theorem in finite projective geometry and some applications to number theory”, Trans. Amer. Math. Soc. 43 (1938) 377–385.
[22] BAUMERT, L.D., “Cyclic Difference Sets”, in *Lecture Notes in Mathematics*, 182, Springer, New York, 1971.
[23] HALL M., *Combinatorial Theory*. Blaisdell Publishing Co. [Ginn & Co.], London, 1967.
[24] BAUMERT, L.D., HALL, M., “A new construction for Hadamard matrices”, Bull. Amer. Math. Soc. 71 (1965) 169–170.

[25] IN'T ZAND J.J.M., HEISE, J., JAGER, R., "The optimum open fraction of coded apertures. With an application to the wide field X ray cameras of SAX", Astron. Astrophys. 288 (1994) 665–674.
[26] NIKEZIC, D., YU, K.N., "Formation and growth of tracks in nuclear track materials", Mater. Sci. & Eng. R 46 (2004) 51–123.
[27] SPRINGHAM, S.V., *et al*., "Ferrofluidic masking of solid state nuclear track detectors during etching", Radiat. Meas. 44 (2009) 173–175.
[28] FLEISHER R.L., "Radon: Overview of properties, origin, and transport," in *Radon Measurements by Etched Track Detectors*, S.A Durrani *et al*., Ed. Singapore: World Scientific Publishing, 1997.
[29] DURRANI, S.A., BULL, R.K. "*Solid State Nuclear Track Detection: Principles, Methods and Applications*." Pergamon Press, Oxford, 1987.
[30] SEGUIN F.H., DECIANTIS, J.L., FEERJE J.A., KUREBAYASHI, S., LI, C.K., *et al*., "D^3He-proton emission imaging for inertial-confinement-fusion experiments", Rev. Sci. Instrum. 75 (2004) 3520–3525.
[31] NIKEZIC, D., YU, K.N., "Computer program TRACK_TEST for calculating parameters and plotting profiles for etch pits in nuclear track materials", Computer Phys. Comm. 174 (2006) 160–165.

CREATION OF A TESTBED AT ICTP BASED ON A REPETITIVE DENSE PLASMA FOCUS DEVICE FOR APPLICATIONS IN RADIATION MATERIAL SCIENCES AS WELL AS IN NUCLEAR MEDICINE AND FOR TRAINING OF YOUNG RESEARCHERS

C. TUNIZ[*], V.A. GRIBKOV[*,**,***], M.L. CRESPO[*], A. CHICUTIN[*], R. MIKLASZEWSKI[**], V.N. PIMENOV[***], E.V. DEMINA[***]

[*] The Abdus Salam International Centre for Theoretical Physics, Trieste, Italy
[**] Institute of Plasma Physics and Laser Microfusion, Poland
[***] A.A. Baikov Institute of Metallurgy and Material Science, Moscow, Russian Federation

Abstract

During the Project fulfillment we have elaborated a design of the Dense Plasma Focus (DPF) device "Bora" with the medium value of the stored energy (about 5 kJ). We have manufactured it and put into operation. Diagnostic equipment was prepared and tested. Key characteristics of the device were measured. With this device works in three main directions were provided according to the Agreement in the frame of the IAEA Co-ordinated Research Project "Investigations of Materials under High Repetition and Intense Fusion-Relevant Pulses": 1) scientific researches and applications of DPF in various fields, 2) training of junior physicists from developing countries, and 3) study courses for young researchers. The first field covers physics of dense magnetized plasmas (in cooperation with several laboratories of RF and Poland), radiation material science, dynamic quality control (initiated and partly sponsored by the "Pirelli Tyre" Company), and works related to flash neutron medicine. In particular we have investigated interaction of nitrogen hot plasma and fast ions with stainless steel. Subsequently results of damages produced by these streams were analyzed. The X ray "instant" image of the rotating fan has been obtained to demonstrate opportunities afforded by the DPF in dynamic defectoscopy. MCNP calculations of neutron interaction with different moderators and living cells having a goal to elaborate a single-shot neutron treatment of cancer were provided. In the second area we have organized the International Workshop on Dense Magnetized Plasma and Plasma Diagnostics with the help of IAEA. About 30 participants and lecturers took part in these events. An important element of this workshop was a practical training of the junior physicists at the "Bora" facility. Two young researchers from Ukraine and Poland are passing study courses at the device.

1. INTRODUCTION

The Multidisciplinary Laboratory (MLab) of the Abdus Salam International Centre for Theoretical Physics (ICTP) starts its theoretical and experimental activity in the field of Dense Magnetized Plasmas several years ago. It was decided to create a "reference" laboratory with equipment based on the most sophisticated elements. Besides the ICTP these researches was also sponsored by several laboratories and institutions from Italy, Poland, Singapore and Russian Federation. In the course of these works a new installation of the Dense Plasma Focus (DPF) type named "Bora" was designed and manufactured.

With this device three main directions of activity were provided according to the Agreement in the frame of the International Atomic Energy Agency Co-ordinated Research Project (IAEA CRP) "Investigations of Materials under High Repetition and Intense Fusion-Relevant Pulses": 1) scientific researches and applications of DPF in various fields, 2) training of junior physicists from developing countries, and 3) study courses for young scientists.

The first field covers physics of dense magnetized plasmas (in cooperation with several laboratories of RF and Poland), researches in the area of radiation material science, application of DPF for the goals of dynamic quality control (initiated and partly sponsored by the "Pirelli Tyre" Company), and works related to flash neutron medicine.

In particular we have investigated interaction of nitrogen hot plasma and fast ions with stainless steel. Then the irradiated samples were analyzed, and main characteristic features of damages produced by these streams were obtained.

The X ray “instant” image of the rotating fan has been obtained by means of just a single DPF “shot”. These works were provided to demonstrate opportunities afforded by the DPF in dynamic defectoscopy.

We provided MCNP calculations of neutron interaction with different moderators and live cells. These calculations have a goal to elaborate a single-shot neutron treatment of cancer.

In the second area we have organized the International Workshop on Dense Magnetized Plasma and Plasma Diagnostics with the help of IAEA. About 30 participants and lecturers took part in these events. An important element of these workshops was a practical training of the junior physicists at the “Bora” facility.

Two young researchers from Ukraine and Poland are passing study courses at the device during last 3 years.

2. APPARATUS

2.1. The “Bora” device

The “Bora” device (a detailed description of the facility is available at [1]) belongs to a class of Z-pinch devices known as Dense Plasma Focus (DPF). It was manufactured on a base of modern high voltage high current technology, the most important elements of which are low inductance capacitors, pseudosparks or thyratrons with cold cathode of the type TDI1-150/k25 (which means 150 kA, 25 kV of switchable current) and special type of DPF chambers produced by the All-Russia Research Institute of Automatics, where all elements (metallic and ceramic parts) are connected by welding.

It has a medium size bank consisting of 4 capacitors produced by the AEROVOX Corp., U.S.A., with parameters presented in Table 1.

TABLE 1. MAIN PARAMETERS OF THE CAPACITOR

Capacitance	6.10 μF
Rated voltage	60 kV
Equivalent series inductance	30 nH (max.)
Maximal energy at rated voltage	10,980 Joules
Weight	70 kg (app.)

Taking into consideration that our charger Spellman, U.K., is able to charge the capacitor maximum up to almost 20 kV this 4-capacitor bank has in reality its maximal storage ~ 5 kJ.

However due to the characteristics (the discharge energy must be not higher than 3 kJ) of the DPF chambers available at the moment at the MLab we used our bank on the level not exceeding the above-mentioned figure.

This device operates with deuterium as a working gas and, consequently, produces fusion neutrons of 2.5 MeV energy with parameters: maximal total yield per shot – $(3\text{-}4)\times10^8$, pulse duration – about 10 ns. Simultaneously this DPF facility generates soft ($E_{hv} \approx 0.1\text{-}3.0$ keV), medium ($E_{hv} \approx 3.0\text{-}10.0$ keV) and hard ($E_{hv} > 10$ keV) X ray flashes. The pulse of the hard component with photon energy in the range 40-200 keV has the overall yield up a few J and pulse duration ~ 10 ns. The "Bora" facility is able to work with other gases. It has been tested with nitrogen and hydrogen to the moment.

Besides X rays and neutrons the device produces powerful streams of fast ions and electrons (energy ~ 100 keV) and hot plasma (temperature $\leq$ 1 keV) ensuring a power flux density on the target placed either in cathode or in anode parts of the DPF chamber in the range up to 10^{10}-10^{12} W/cm^2. Such high values make this compact device a very attractive instrument for different applications. We implement it for testing of materials perspective for use in the mainstream fusion reactors of both types (with magnetic and inertial plasma confinement), for applying it in a single-shot dynamic quality control of machines and their parts during operation. We prepared this device also for various experiments in biology and medicine. General view of the "Bora" device is presented in Fig. 1.

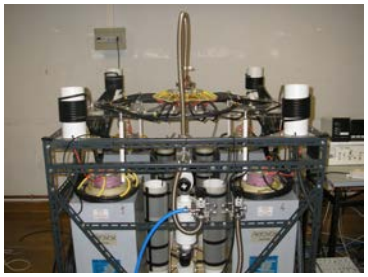

FIG. 1. General view of the "Bora" facility.

During these our works we used two types of the DPF chambers. The first chamber is optimized for production of hard X rays (for works in the field of dynamic quality control (see Fig. 2) whereas the other one is designed for the experiments in the area of radiation material sciences (Fig. 3).

FIG. 2. DPF chamber with the insert in the anode centre made of tungsten for production of hard X rays.

a) b)

FIG. 3. DPF chamber (a) designed for experiments in radiation material science and its various parts (b) intended for samples' holding and for diagnostics of the irradiation process.

2.2. Diagnostics

This device is equipped at present moment with a Rogowski coil, 4 magnetic probes, photomultiplier tube with scintillator (PMT+S), silver activation counter and the 4-channel LeCroy oscilloscope of 500 MHz bandwidth (see Fig. 4).

Typical oscilloscope trace of the discharge of 3 capacitors with a good “peculiarity” on them taken by 3 magnetic probes is shown in Fig. 5.

In the experiments provided in co-operation with ACS Ltd., Warsaw, Poland, where a special technique based on CCD detectors having temporal resolution 0.3 ns and a conventional PMT+S were applied, precision information on temporal evolution of hard X rays and neutrons generated by “Bora” was obtained (see Fig. 6). It appeared that typical durations for hard X ray pulses are about 4 ns at the full width at half maximum (FWHM) whereas for the neutron pulses the FWHM is about 8 ns correspondingly.

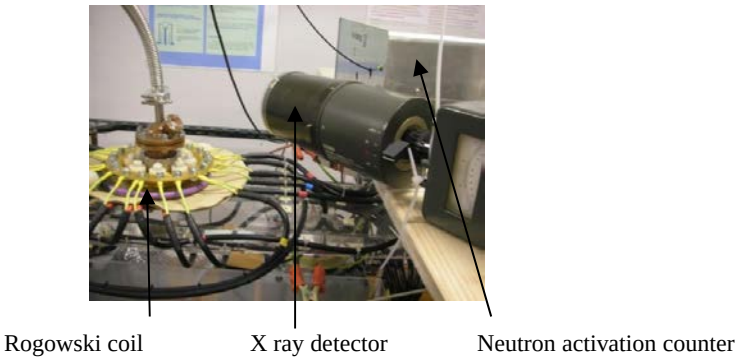

FIG. 4. Diagnostic equipment: Rogowski coil, X ray detector and neutron activation counter.

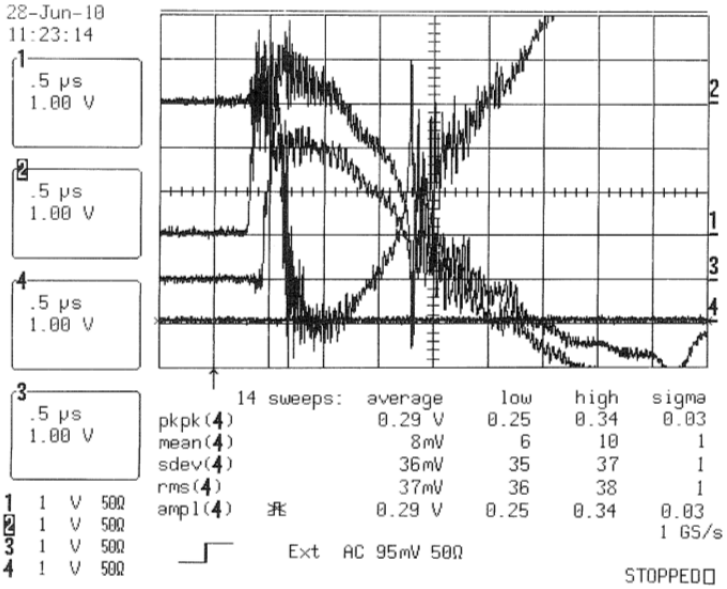

FIG. 5. Oscilloscope traces of magnetic field derivatives taken by 3 magnetic probes placed near 3 capacitors. One may see that a quarter of the discharge period of the device is about 1.25 µs.

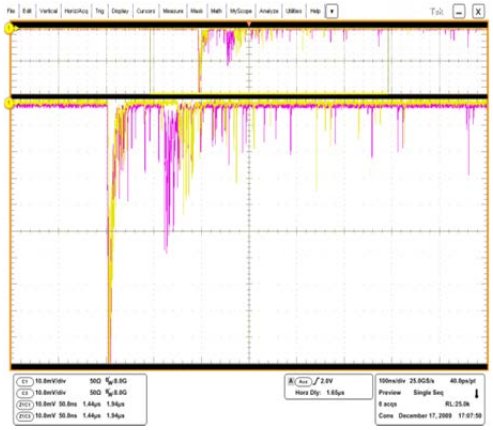

FIG. 6. Oscilloscope traces taken by two PMTs placed at different distances from the DPF chamber.

3. EXPERIMENTS IN RADIATION MATERIAL SCIENCES

It is known [2, 3] that irradiation of materials by powerful streams of fast ions and hot plasma inside the Dense Plasma Focus (DPF) device results in changes of phase-structure state of surface layer (SL) and gives an opportunity to modify its physics-chemical, mechanical and some other characteristics. Implantation of the working gas ions may takes place with and without SL melting at the power flux densities $\geq 10^8$ W/cm^2 and ~ 10^7 W/cm^2 correspondingly that attains by variation of a distance from samples to an anode. In both dissimilar cases its structure and properties will be different.

Implantation of ions of different elements is one of the modern methods of modification of SL [4, 5] with an aim of improvements its properties. We provide our experiments [6] in the field of radiation material sciences during the second week of the mutual IAEA-ICTP Workshop on Dense Magnetized Plasma and Applications, which took place in Trieste in November 2011. This second week was devoted to practical hands-on experimentation with a Dense Plasma Focus (DPF) device "Bora" at the Multidisciplinary Laboratory (MLAB), Trieste, Italy. During this week the device was used for experimental sessions devoted to diagnostics of its own operability, characterization of different types of radiation generated by it as well as for demonstration of some possible applications of these radiation pulses in a number of fields.

In particular the experiments were aimed to radiation tests of specimens of materials, which are the candidate ones for use in the main-stream fusion facilities. The results of irradiation of samples of the above types produced in the "Bora" device by streams of hot plasma and fast ions during this experimental session were examined with optical microscopy by methods elaborated in the A.A. Baikov Institute of Metallurgy and Material Sciences (IMET), Russ. Ac. Sci., Moscow, RF. It was done at the ICTP MLAB. In further analytical works micro-structure and some other parameters of the irradiated samples were investigated by means of an X ray structure and element analysis, electron microscopy and other methods. For these irradiation experiments we used a sample of low-activated austenitic steel of the type EP838.

Beside Fe it contains (in weight %) 12 Cr, 14 Mn, 4 Ni (plus Al, Mo). A sample was manufactured as a rectangular plate having thickness 1 mm and polished from both sides (see Fig. 7). In the DPF "Bora" we used nitrogen as a working gas in these tests.

This sample was placed in front of the anode of DPF at the cathode part of the discharge chamber. Thus it was irradiated mainly by hot nitrogen plasma streams having speed of about (2-3) $\times 10^7$ cm/s and by a beam of fast nitrogen ions having energy ~ 100 keV.

Distance between the anode and the specimen was 5 cm. We produced 50 shots with the "Bora" device. Power flux density of both the above-mentioned streams on the target's surface was ranged 10^8 - 10^9 W/cm^2.

In Fig. 7 (a) and (b) one may clearly see two zones differing one from another: a zone 1 which is quite large and occupies almost the whole area of the specimen. This area was irradiated mainly by a plasma stream. There is also a zone 2, where we have mutual action of a plasma stream and a beam of fast ions.

Subsequent optical and electron microscopy of a region near the border of these zones (Fig. 7 c, d, e, f and g) show the microscopic difference between damage characters in these zones. One may observe craters and waves as the main damage features in a zone 2.

In fact the damage is characterized in these cases by pores, bubbles and cracks of the size of several tens of μm. X ray diffractometry has shown that during irradiation an implantation of nitrogen atoms into austenitic lattice noticeably increases a parameter of the gamma-phase (Table 2).

An increase in the solid solution of concentration of nitrogen, which is an effective stabilizer of gamma-phase, compensates a certain loss of manganese. Ferritic and martensitic phases inside the SL were not observed. After high-temperature irradiation with subsequent fast cooling this matrix solution has a structure of the perfect gamma-phase. Martensitic phases presented in virgin samples are converted into austenite by a diffusionless transformation. Table 3 presents nitride phases created in the SL of the steel 10Cr12Mn14Ni4AlMo due to chemical activity of nitrogen atoms in relation to steel's components.

TABLE 2. PARAMETERS OF THE FCC LATTICE OF AUSTENIC STELL IRRADIATED BY NITROGEN IONS AND PLASMA

No. of a sample	Sample's state	a, Å	V, Å^3
1	Before irradiation	3.6012	46.70
2	After irradiation by fast ions and plasma of nitrogen	3.6234	47.57

TABLE 3. TYPE AND QUANTITY OF NITRIDE PHASES IN SL OF THE ABOVE STEEL AFTER IRRADIATION

No. of a specimen	Nitride phase	Lattice type	Quantity, %
1	$FeN_{0,0880}$	fcc	8.5
2	$FeN_{0,0939}$	bcc	<2
3	Fe_4N	B1	<2
4	Fe_3N	hexagonal	<2
5	Fe_2N	orthorhombic	<2

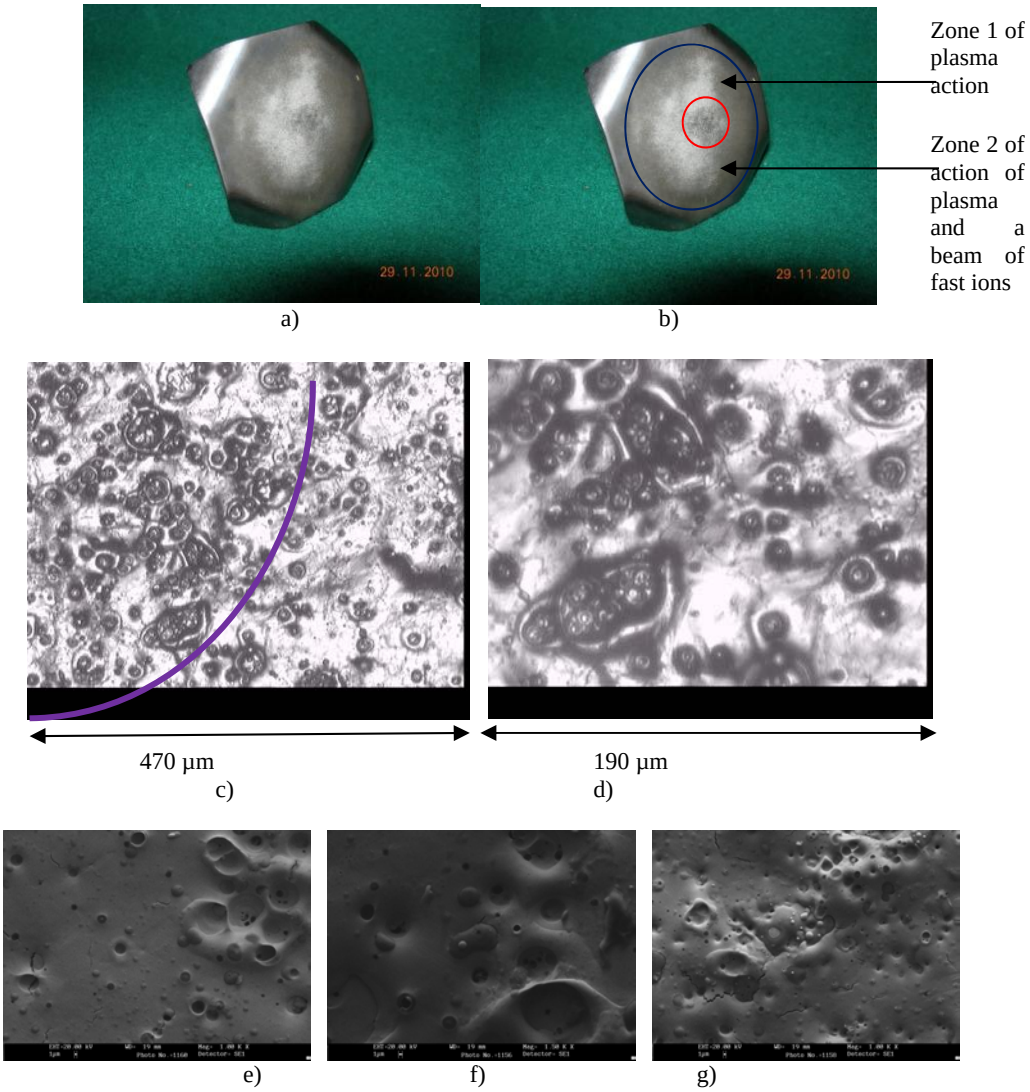

FIG. 7. Photo of the sample irradiated in the DPF chamber during the second ("experimental") week of the 1st ICTP-IAEA workshop on Dense Magnetized Plasma: a) – photo of the sample; b) same photo with demonstration of regions irradiated by plasma only (1) and by plasma and a beam of fast ions (2); c) optical microscopy of the region near the border of the first and second zones; d) optical microscopy of the region 2 taken with higher magnification; e), f), and g) – electron microscopy of the regions.

The above-mentioned features make usually in favor of an increase of hardness of the material. Tribological measurements will be our next step in these researches.

4. EXPERIMENTS WITH HARD X RAY RADIATION: DYNAMIC QUALITY CONTROL

We have made experiments in the field of the dynamic quality control. By this technique using just a single flash of DPF's hard X ray radiation we can take an X ray picture of machines and mechanisms during their operation. It is possible because of a very short X ray pulse generated by a DPF (about 4 ns as it is seen from the above Fig. 6). E.g. during such an interval of time a car wheel is turned on about 1 µm at the car speed of about 100 km/hour. We take two pictures of a fan made by thin plastic in its static position (7 shots with the same location of its blade) and in its dynamic (rotating) state (just a single shot) (see the experiment's arrangement in Fig. 8). The results are shown in Fig. 9.

The technique of such a kind is important because it can unveil (visualize) a crack in the element of the machine invisible in static position and manifestative at its rotation due to a centrifugal force.

Spatial resolution of an image Δx of a mechanism's detail (turbine's blade, car tire, piston of a car engine, etc.) taken *during its operation* by a flash of the hard X ray radiation generated in a DPF determined by:

- Pulse duration of X rays (ns)
- Size of the source of X rays (< 100 μ)
- Diffraction (wavelength, distance)
- Contrast degree of an object's detail to be visualized (spectrum of hard X rays).

Theoretically for DPF it could be $\Delta x \sim 1$ μm at a 10-cm distance for the rotational speed of about 6000 rpm at $\lambda \sim 0.1$ Å

5. BNCT WITH NANOSECOND NEUTRON PULSES

The use of short and powerful neutron pulses from DPF for the Boron Neutron Capture Therapy (BNCT) could potentially reduce the total dose absorbed by the patient. The induction of the synergetic effects within the cells by production a high concentration of secondary particles during a time interval short compared with the time duration of chemical reactions may result in a collective action of them. To verify it we introduced in our Monte Carlo Neutron Particle (MCNP) model (Geant4 code) the effects of the temporal profile of the beam (i.e. we intend to investigate whether there is a difference between pulsed and continuous irradiation). The simulation was planned to be developed in three fundamental steps: neutron source itself, modeling of the interaction of fast mono-energetic neutrons with a moderator used in BNCT, and interaction of the pulsed neutron beam with a live tissue.

Plasma Focus Device geometry simulated in Geant4 is shown in Fig. 10. The internal diameter of the spherical anode (blue) of the device's chamber is 60 mm. The external diameter of the spherical cathode (pink) of the device's chamber is 120 mm.

Fast neutrons (of 2.45 MeV or of 14 MeV) need to be moderated to the optimal neutron energy spectrum for BNCT. It is admitted that this optimal spectrum should be centered near 10 keV (epithermal neutrons). This particular energy (10 keV) is good for cancer therapy from three points of view – relatively long penetration depth of these neutrons into human body (a few cm), favorite neutron spectrum enriched by fast neutrons, and still a high cross-section of neutrons' absorption by boron nuclei (for applicability of BNCT). Below (see Fig. 11) we present geometry of our moderator's assembly

Moderating the neutrons to the optimal energy of 10 keV can be performed in two stages. The best results were achieved with iron and Fluental™ moderator materials. Fluental™ (69% AlF3/30% Al/1% LiF) is a neutron moderator material developed at VTT in Finland.

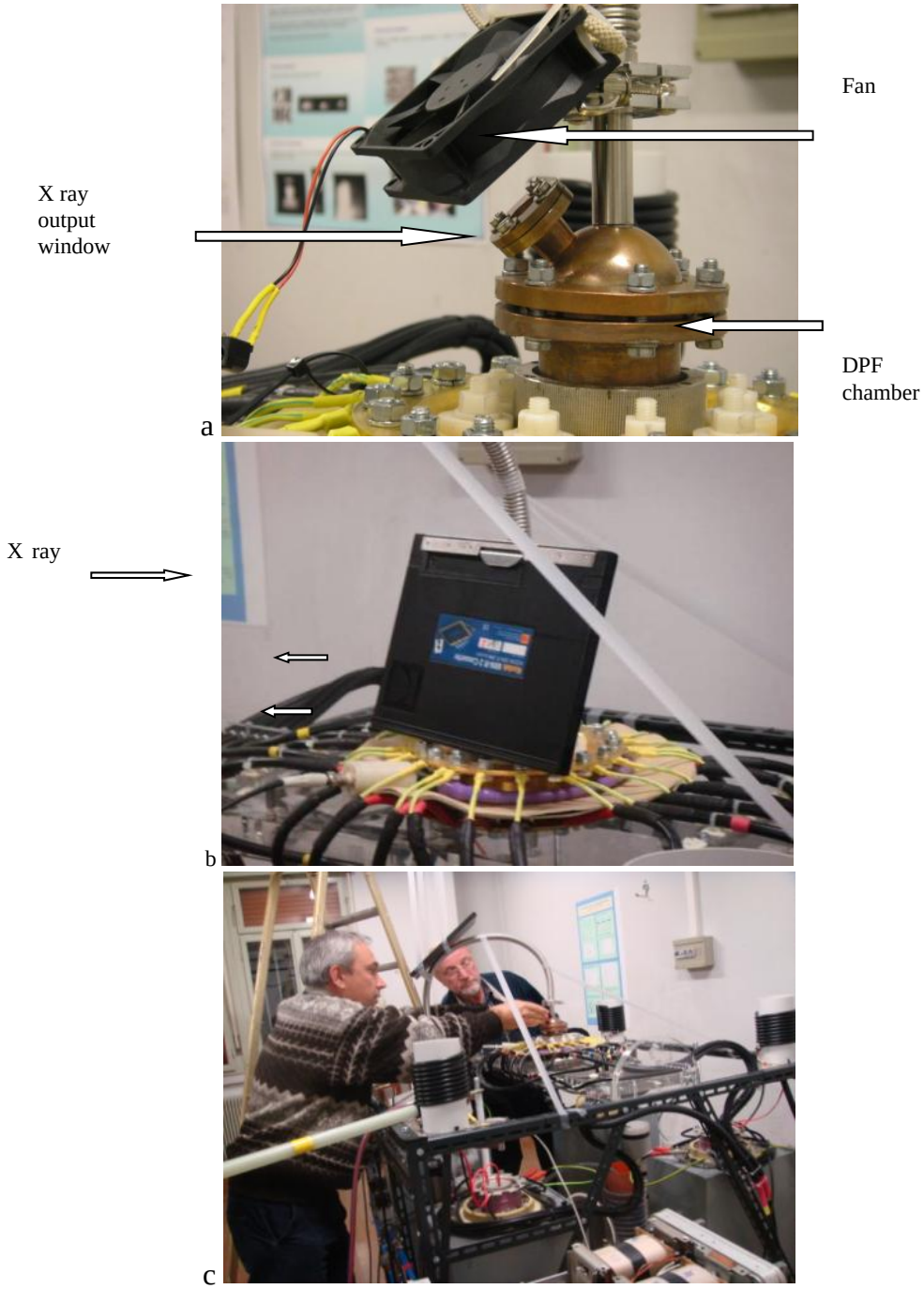

Fig. 8. Experiment in dynamic quality control made at different distances between the fan (a) and the X ray film (b and c); note that the longer distance the better resolution yet the worse sensitivity

For modelling of live tissue a closed packed structure of 14 spheres made from homogeneous material (see Fig. 12), whose composition was defined using the parameters of the Table 1 was used.

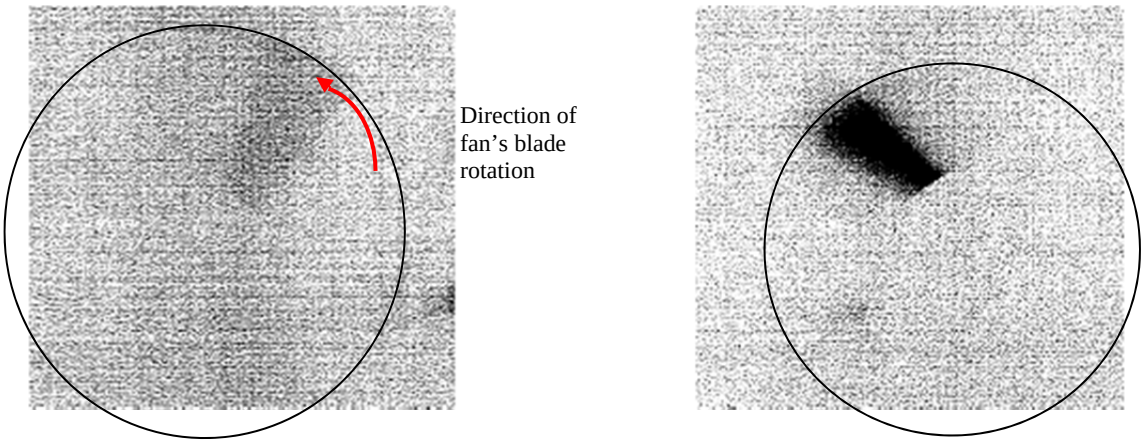

FIG. 9. X ray pictures of the fan's blade in dynamics (a), 1 shot of DPF, and in a static state (b), 7 shots of DPF.

It is easy to see that this blade of the fan at its rotation looks as if its image was obtained in a static state.

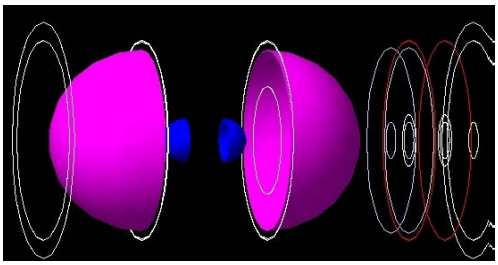

FIG. 10. Plasma Focus Device geometry simulated in Geant4

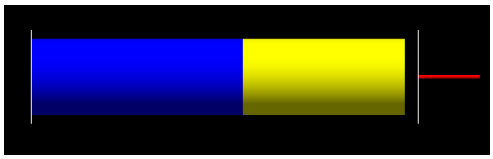

FIG. 11. Moderator's assembly: 1 and 4 – copper layers, 2 – Fluental™ material, 3 – iron, 5 – plasma column, producing neutrons inside the DPF discharge chamber.

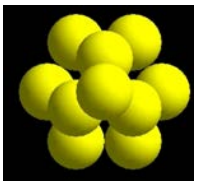

FIG. 12. Image of the cell cluster as simulated by G4. Dimension of the cell cluster is around 26 μm of diameter, arranged in order to minimize the space by each cell. The cells in the cluster were surrounding by water.

TABLE 4. COMPOSITION OF THE CELL MEDIUM.

	Hydrogen	Carbon	Nitrogen	Oxygen	Phosphorus	Boron
issue	59.59%	11.109%	4.039%	24.239%	1.009%	0.0029%

The arrangement of the cells in the cluster was optimized to use less space. Each cell had a diameter of 13 μm. The cell composition used in our model was that defined by the International Commission on Radiation Units and Measurements, but we included Boron with the concentration of 30 ppm of boron nuclei per tissue's molecules.

The pulsed simulated neutron spectrum was calculated with its initial time spread of 10 ns. Its moderated spectrum was found in general agreement with the predictions, given the amount of moderation material in front of the neutron source.

A preliminary tradeoff of the desired neutron spectrum with the optimal pulse spread was calculated. A moderate amount of Fluental (~ 5 mm) is able to moderate the initial spectrum and keep the pulse spread << 1 microsecond.

Similar results were obtained with a larger iron/fluental moderator, where a much larger moderation is obtained while keeping the neutron pulse within the time scale again less than 1 microsecond. The resulting spectrum was found to be much more thermal than the previous one. In these calculations we used a 50-ns neutron pulse. The final pulse shape width (FWHM) was found to be 200 nanoseconds, only a factor of 4 more than the initial neutron pulse width (see Fig. 13).

The resulting spectrum is then moderated by a large water sphere to simulate an isotropic flux as the one delivered to treated cells. The dose delivered to small cells was then preliminary evaluated.

First, we have found that the dose is distributed homogeneously among the cells within the cluster. Second, we found small differences in dose deposition between the cells of the cluster.

These differences arise mostly from the differences in a number of tracks through each cell; therefore the number of neutrons will be more important in determining the number of tracks through the cells rather than neutron energy.

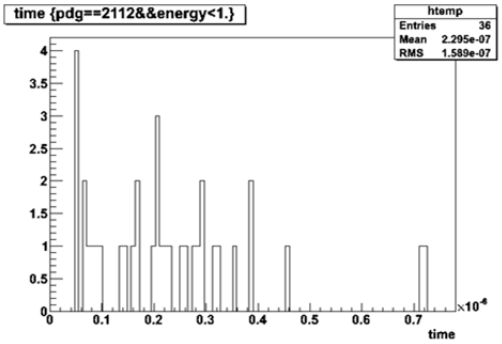

FIG. 13. Calculated temporal shape of a 50-ns pulse of 2.5-MeV neutrons after its moderation by means of the assembly shown in Fig. 11.

6. WORKSHOP ON DENSE MAGNETIZED PLASMA AND PLASMA DIAGNOSTICS

The main purpose of the workshop [7] was to train physicists, engineers and other scientists in topics related to the physics, state-of-the-art design, diagnostic methodologies and applications of dense magnetized plasma (DMP) devices. Other topics related to this field

were also covered, including plasma and particle accelerators, novel X ray sources and fusion energy. During the first 'theoretical' week of the workshop, the current status and performance of the modern diagnostic techniques based on X rays and other types of radiation for characterization of plasma parameters were discussed. In the first week, the programme also included a description of the development of new instrumentation and methodologies currently used for the diagnostics of DMP.

Several review reports on the mainstream nuclear fusion devices were presented, including devices like NIF (Lawrence Livermore National Laboratory, USA) and Z-machine (Sandia Laboratories, USA), DMP facilities of various sizes like MAGAPIE (Imperial College, UK), PF-1000 (Institute of Plasma Physics and Laser Microfusion, Poland), Poseidon (Stuttgart University, Germany) and 'Nanofocus' (Comisi´on Chilena de Energia Nuclear (CCEN), Chile), including contemporary diagnostics methods. These examples showed applications of different advanced tools in real full-scale experiments with fusion plasma.

The second week of the workshop was devoted to practical, hands-on experiments with the dense plasma focus (DPF) device 'Bora' based on modern technology that has recently been put into operation at the ICTP Multidisciplinary Laboratory (MLAB), Trieste, Italy. The ICTP device was used in experimental sessions devoted to the diagnostics of its functionality and characterization of different types of radiation generated, as well as for demonstration of selected applications, including dynamic quality control and radiation tests of materials of potential practical importance for large fusion facilities. In particular, the results of irradiation of the samples produced in the 'Bora' device by streams of hot plasma and fast ions during the experimental session were examined using optical microscopy by methods elaborated in the A.A. Baikov Institute of Metallurgy and Material Sciences (IMET), RF.

Presentation of the so-called 'Nanofocus' (2 kg weight), designed by the CCEN, Chile, was carried out during the workshop. Its design was explained and assembly of the device was demonstrated. The results of X ray and neutron measurements made with this miniature device were presented together with discussion of their possible applications. Special sessions of the second week were devoted to training students in computer modeling of MHD (magnetohydrodynamic) processes, which take place in DPF devices. It was performed by means of an original numerical code elaborated on recently by researchers in Singapore and Malaysia.

The main goal of these types of activities was to demonstrate feasibility and attainability of such works in small laboratories and to help in providing cost-effective solutions for the DMP instrumentation needed for research and training in developing countries. The workshop also provided the basic concepts and techniques necessary to work on leading edge technologies such as radiation material sciences, radiation biology and nuclear medicine.The combination of basic theoretical education in plasma diagnostics with information on complex applications in full-scale advanced experiments, practical training in design of medium/small-sized DMP devices, applications of computer modeling of corresponding processes taking place in the plasma followed by experimental implementation in real devices was done for the first time, and looks very promising for the future joint ICTP/IAEA activities.

According to the feedback received from the participants after their return to their home countries, one can conclude that the workshop:

- Exposed scientists and engineers to advanced design methodology in modern DMPs, plasma diagnostics and DMP applications.
- Encouraged scientists and engineers from developing countries to use cost-effective DMP devices to support research, education and development activities and enhanced their capabilities in this field.
- Promoted networking of researchers in developing countries in advanced DMP devices' design under north– south cooperation.
- Addressed the issue of lack of expertise in DMP/DPF design and related fields in developing countries.

Scientists in developing countries have rather limited access to large plasma sources, which are available in advanced research centres in developed countries. Since various types of small plasma facilities of relatively low cost, modern design/instrumentation with a reliable operation became available for research and applications over the last few years, there is a need to present recent advances in plasma diagnostic techniques based on X ray spectroscopy, including their applications for diagnostics of fusion plasmas.

The meeting also created an opportunity for scientists from developing countries to initiate collaboration with the advanced laboratories represented by the workshop's lecturers and tutors.

The complete programme and most of the lecture notes of the workshop can be downloaded from [8]. The main topics covered during the workshop were as follows:

Current status and basic results obtained with the mainstream fusion facilities, modern particle and plasma accelerators and DMP devices of different sizes; DMP physics: experiments, modeling and simulation; classical and recent results of dense magnetized plasma physics investigations (plasma dynamics, fast particle generation, beam interaction with plasma and solid targets, etc); DMP applications in science and technology Dr S. H. Glenzer (Lawrence Livermore National Laboratory, USA) presented recent results obtained at the largest laser device ever built—National Ignition Facility (NIF)—in the autumn of 2010.

In two lectures, 'Plasma focus' by Dr S. Lee (INTI International University, Malaysia and Institute for Plasma Focus Studies, Australia) and 'Insights from plasma focus numerical experiments: scaling properties to scaling laws' by Dr S. Lee and S. H. Saw (Nanyang Technological University, Singapore), results on recent extensive and systematic numerical experiments mainly in the frame of MHD model, provided under an approximation that the DPF plasma is ideal, and at steady state being in equilibrium at any moment, were presented.

In his lecture 'Z-pinch, concept, experiment. The physics of wire-array Z-pinches' Dr G. Hall (Imperial College, UK) presented the main conceptual ideas connected with the fulfillment of inertial confinement fusion by means of a technique based on high-voltage high-current generators which are less expensive/sophisticated compared with laser fusion facilities of the NIF type. He also discussed a correlation of experiments produced in the

mainstream devices like Z-machine and in a low-scale ‘university’ sized setup like MAGPIE of the Imperial College.

Very close to the themes discussed in the previous lecture was a report of Dr J. Cittenden (Imperial College, UK) ‘Computer modeling of MHD processes’. It represented a collection of contemporary numerical tools elaborated to simulate processes taking place in a DMP at modern devices and in astrophysical phenomena. Particular attention was paid to comparison of these simulations with results obtained on Z-machine and MAGPIE.

Dr. G. de Ninno (Elettra, Trieste, Italy) presented a lecture ‘Theory and general properties of X ray FEL’s’ devoted to the free-electron built by Synchrotron Trieste.

Dr. M. Scholz (Institute of Plasma Physics and Laser Microfusion, IPPLM, Poland) devoted his report to the following main points of the programme of the PF-1000 facility—the largest DPF device (bank energy E = 1 MJ) currently in operation with deuterium working gas at the IPPLM: (1) the understanding of the long time scale dynamics, linked to the necessity of developing realistic scaling laws for the design of large energy devices, and evaluating their range of applicability, and (2) the understanding of the short time scale dynamics, including the intense anomalous effect accompanying the neutron production, and more recently, the very late phase of the implosion.

Dr. V. Krauz (Russian Research Centre ‘Kurchatov Institute’, Moscow) presented a report ‘Plasma-Focus PF-3’. In this lecture the following topics were presented: history of DPF research, Filippov-type PF - main features, Plasma Focus PF-3 facility: design and parameters, PF-3 as a source of soft X rays (SXR), plasma current sheath (PCS) dynamics, new approaches in PF studies: astrophysics phenomena simulation, experiments with liners, experiments with dust, and production of nanoparticles and nanofilms.

In the report ‘Summary of results from POSEJDON Plasma-Focus: diagnostics and scaling of fusion-produced neutrons in PF experiments’ Dr H. Schmidt (International Centre for DMP, Poland, and University of Stuttgart, Germany) discussed neutron-based analytical methods using the largest DPF devices in operation at Stuttgart University.

Dr. I. Garkusha (Kharkov Institute of Physics and Technology—KIPT, Institute of Plasma Physics, Ukraine) presented a report, ‘Quasi steady plasma accelerators (QSPA): physics and applications’. This lecture was devoted to one of the important classes of plasma accelerators where duration of the process (discharge) essentially exceeds the time of flight of the plasma particles in the accelerating channel. He examined the physics of steady-state plasma flows and the principles of the QSPA design and operation. He also discussed contemporary experimental devices, QSPA Kh-50 plasma accelerator and MPC Magneto-Plasma Compressor, which are currently in operation at KIPT and dynamics of dense plasma streams generated by QSPA and MPC as well as some examples of their applications.

In his two reports, ‘Similarities and differences in plasma focus devices from 1MJ to less than 1 J’ and ‘How to build a small PF,’ Dr L. Soto (CCEN, Chile) discussed various aspects of DPF characteristics in a wide range of bank energy, emphasizing miniature DPF devices. An important part of the lectures was devoted to design and construction of the nanofocus and in particular to sophisticated methods of measurements of radiations at the very low intensity of these devices.

In his lecture ‘Energy pumped to the pinch and its influence on X ray and neutron emission from the Mather type Plasma Focus,’ Dr M. Zakaullah (Quid-I-Azam University, Pakistan) presented a valuable picture of dependence of the neutron and X ray emission on energy obtained by the pinch column.

In the first of two reports ‘Localized structures in the plasma focus: a review’ and ‘Relaxation phenomena in the plasma focus’ presented by Dr. S. K.H. Auluck (Bhabha Atomic Research Center, India), a survey of experimental and theoretical results on the formation of filaments, ‘blobs’, micropinches, ‘fractal structures’ and localized ion sources observed in DMP was presented. In the second lecture, Dr. Auluck presented a universal, device independent model of neutron emission from DPF and Z pinches which was provided by applying Turner’s relaxation theory (Turner L. 1986 Hall effects on magnetic relaxation IEEE Trans. Plasma Sci. PS14 849) to magnetic configurations created in DPF.

Plasma parameters defined by X ray spectrometry techniques; status and advances in passive and active spectroscopy techniques for plasma diagnostics; new X ray optics and detectors for diagnosis of fusion plasmas.

In the first of his lectures, ‘Introduction to spectroscopy’, Dr H. J. Kunze (Ruhr Universitat Bochum, Germany) presented a broad picture of spectroscopic methods available at the moment for experimentalists to determine the main plasma parameters. In conclusion he presented schemes of the main types of X ray spectrometers based on flat and bent crystals and discussed their applicability for different tasks. The second lecture of Dr. Kunze, ‘Thomson scattering’, was devoted to a well-known method of determination of electron and ion temperatures as well as plasma density using scattering of laser light inside a plasma. In his second lecture, ‘Plasma diagnostics by X ray scattering’, Dr S. Glenzer presented a very modern method for diagnostics of very dense plasmas produced during implosion of pellets in the experiments on laser fusion.

Dr. M. J. Sadowski (The Andrzej Soltan Institute for Nuclear Studies (IPJ), Poland) presented a lecture, ‘Diagnostics of charged particles emitted from DMP experiments’, where diagnostics of accelerated primary ions and electrons and diagnostics of charged products of fusion reactions were discussed.

Design of DMP devices (Z- and X-pinches, exploding wires and wire arrays, capillary discharges, etc); DPF: technologies, architectures and design were the main part of the activity during the second week of the Workshop. At the examples of ‘Bora’ and nanofocus devices (ICTP MLAB and CCEN correspondingly) all problems connected with design, assembling, operation, optimization and their applications were discussed thoroughly by Dr. V.A. Gribkov, Dr L. Soto, Dr. M. Chernyshova and Dr. E. Demina. This work also included real experiments with the devices, their applications, and discussion of safety measures and radiation hygiene for such devices as well.

Some difficulties arising at the application of diagnostics in real plasma objects and complementary use of plasma diagnostic techniques In the final lecture presented by Dr. V.A. Gribkov, many problems connected with DMP devices’ constructions and exploitation as well as with use of diagnostics techniques were discussed.

The ICTP has a long tradition of supporting events related to plasma physics and plasma diagnostics. This workshop included presentations by experienced lecturers, who not

only helped participants understand plasma properties at fusion devices, but also demonstrated applications of novel techniques for fusion, astrophysical plasmas and radiation materials science. ICTP hosted the first IAEA Research Coordination Meeting of the Coordinated Research Project (CRP) on the Integrated Approach to Dense Magnetized Plasmas Applications in Nuclear Fusion Technology (April 2008). However, this workshop was the first time such a combination of theoretical and practical activities with the involvement of the participants was provided. In the future, similar workshops will be organized biennially. A training course on "Dense magnetized plasma as a source of ionizing radiations, their diagnostics and applications" will be held at ICTP in October 2012.

7. CONCLUSION

The new Dense Plasma Focus device is operational at the Mlab of the Abdus Salam International Centre for Theoretical Physics. It has a minimal set of diagnostic tools. Scientific researches provided with this device covered radiation material science, dynamical quality control of machine and mechanisms during its operation. Numerical modeling done by means MCNP code Geant 4 for a number of geometries shows good perspectives for nanosecond neutron therapy of cancer. International Workshops provided by the Laboratory is a very useful event combining theoretical lecturing with practical training with "Bora" facility.

REFERENCES

[1] http://mlab.ictp.it/uploads/C1/cK/C1cKba2XDKJNeoN26x5GmA/Dense-Plasma-Focus-BoraICTP.pdf.

[2] PIMENOV, V.N., GRIBKOV, V.A., *et al.*, "Influence of powerful pulses of hydrogen plasma upon materials in PF - 1000 device", Nukleonika **47** (2002) 155–162.

[3] PIMENOV, V.N., DYOMINA, E.V., *et al.*, "Damage of structural materials for fusion devices under pulsed ion and high temperature plasma beams", J. of Nucl. Mater. **307-311** Part 1 (2002) 95–99.

[4] POGREBNIAK, A.D., TIURIN, Yu.N., "Modification of material properties and film deposition with a help of plasma streams",Uspekhi fizicheskikh nauk **175** (2005) No. 5, 515–544, *in Russian.*

[5] LI, Z.G., HE, J.L., *et al.*, "Electronic structure of Yb2.75C60", Physical Review B **68** (2003) 165417.

[6] GRIBKOV, V.A., PIMENOV, V.N., ROSCHUPKIN, V.V., *et al.*, "Irradiation of austenitic steel 10Cr12Mn14Ni4AlMo and titanium alloy Ti-Al-V by pulsed streams of fast nitrogen ions and plasma in Dense Plasma Focus", Proc. of the International Conference PLASMA-2011, Warsaw, Sept. 12-16, 2011 (O-8.4) (accepted for publication in Nukleonika).

[7] V.A. GRIBKOV, V.A., MANK, G., MARKOWICZ, A., MIKLASZEWSKI, R., TUNIZ, C., AND CRESPO, M.L., "ICTP-IAEA Workshop on Dense Magnetized Plasma and Plasma Diagnostics: an executive summary", Nucl. Fusion **51** (2011) 127001 (4pp) doi:10.1088/0029-5515/51/12/127001.

[8] Available at: http://cdsagenda5.ictp.it/full display.php?email=0&ida=a09172.

DENSE PLASMA SOURCE DEVELOPMENT FOR FUSION APPLICATION

A.V. VORONIN[*], V.K. GUSEV[*], YA. A. GERASIMENKO[**], E.V. DEMINA[***], S.V. KOBYAKOV[**], G.S. KURSKIEV[*], V.B. MINAEV[*], A.N. NOVOKHATSKY[*], YU.V. PETROV[*], V.N. PIMENOV[***], N.V. SAKHAROV[*], I.P. SCHERBAKOV[*], S.YU. TOLSTYAKOV[*]

[*] Ioffe Physical-Technical Institute of the Russian Academy of Sciences, St. Petersburg, Russian Federation
[**] St. Petersburg State Polytechnical University, St. Petersburg, Russia Federation
[***] A.A. Baikov Institute of Metallurgy and Material Science RAS, Moscow, Russia Federation

Abstract

The parameters of the plasma gun generating a fully ionized plasma jet with a high kinetic energy were improved. The modified gun produces fully ionised clean hydrogen jet with total number of accelerated particles $(1\text{-}5)\times10^{19}$, the flow velocity 100-250 km/s and the pulse duration 10-15 μs. The jet with kinetic proton energy up to 300 eV may be used as a fuelling tool for tokamak Globus-M-like plasmas. Undisruptive fuelling the spherical tokamak Globus-M plasma core with the help of the developed plasma gun was achieved. A moderate density rise (up to 40%) in the central plasma region without plasma disruption was obtained. Preliminary surface investigations of the fusion reactor materials irradiated by the jet at power density 1 MW/cm^2 were performed.

1. INTRODUCTION

One of the main problems of tokamak-reactor is fuel feeding the reactor plasma. This is important because fusion power increases square with raising the plasma density. For hot plasma average free path of neutrals is several cm when they pass from periphery to center of plasma column. That makes traditional fuelling methods inefficient, such as external gas puffing and pellet injection. For reactor the source has to generate a number of particles $10^{20} \div 10^{23}$, for density $>10^{22}$m^{-3}, flow velocity up to 1000 km/s. In addition fuelling system has to inject clean or low impurity fuel. Therefore development of intensive jet may allow controlling the ignition, burning, mitigation of the discharge and test of fusion grade materials. Such as, plasma startup in tokamak with the help of the plasma jet may perform faster heating of the discharge as compared to gas puffing with ECR-preionization. High pressure jet injection before disruption may mitigate the discharge and avoid uncontrollable energy release on the first wall of the reactor.

General task of the present research is developing a plasma jet injection technique to allow central fuel penetration to ITER-like plasma core. Local tasks are: a) plasma parameter control in tokamak Globus-M with intensive jet without discharge degradation; b) investigation of fusion grade materials irradiated by the jet.

The project includes: i) jet injection in plasma core - which may led to fast density increase; local enhancement of plasma density can cause transport barriers improving plasma confinement in this region. ii) jet injection at ELM-event - one can initiate weaker instabilities at the plasma edge and may avoid strong energy losses from confined plasma; transition to regime with favorable ELM: high frequency, low amplitude could be realized; iii) test of construction materials under high energy plasma jet - could be also possible.

Latest gun modifications were directed on increasing of kinetic energy of the jet (density and/or velocity), reduction of impurities and improving of the jet parameter reproducibility.

2. EXPERIMENTAL FACILITIES

Plasma gun with fast gas feeding the accelerator has been developed (Fig.1) [1]. The source consists of two stages. The first - gas generating stage contains titanium grains loaded with hydrogen. An electric discharge passing through the grains releases high-pressure hydrogen. Neutral hydrogen passing through a specially designed grid fills the accelerator electrode gap to a high pressure in a few tens of microseconds. The second - plasma generating stage is a system of coaxial electrodes. Electric discharge fired through the gas between the coaxial electrodes provides gas ionisation and plasma acceleration as in the classical “Marshall gun scenario”.

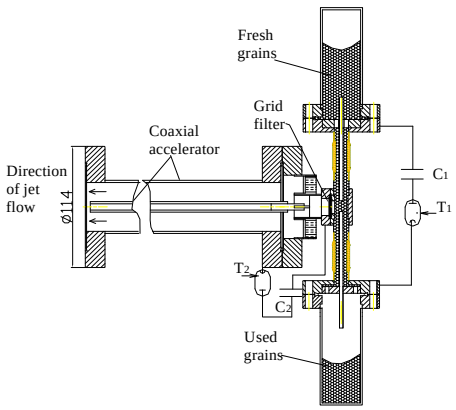

FIG. 1. Coaxial plasma gun with fast gas feeding the accelerator.

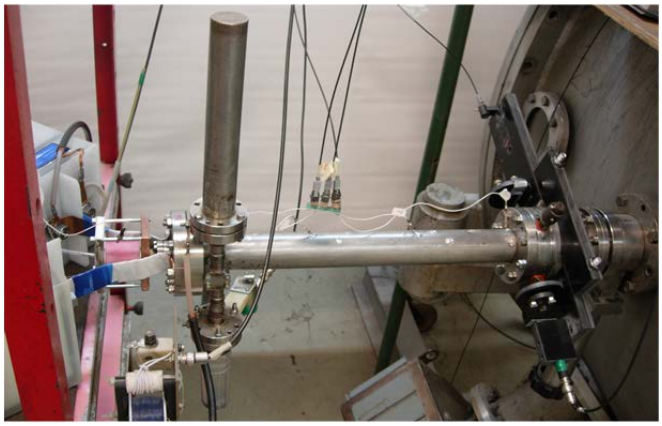

FIG. 2. View of the gun at the test bench.

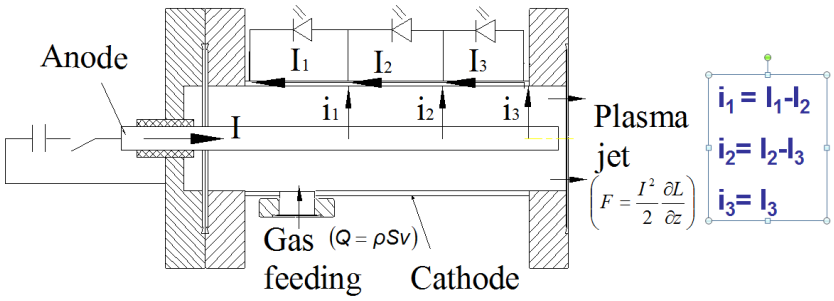

FIG. 3. Coaxial accelerator equipped with light emitting diodes.

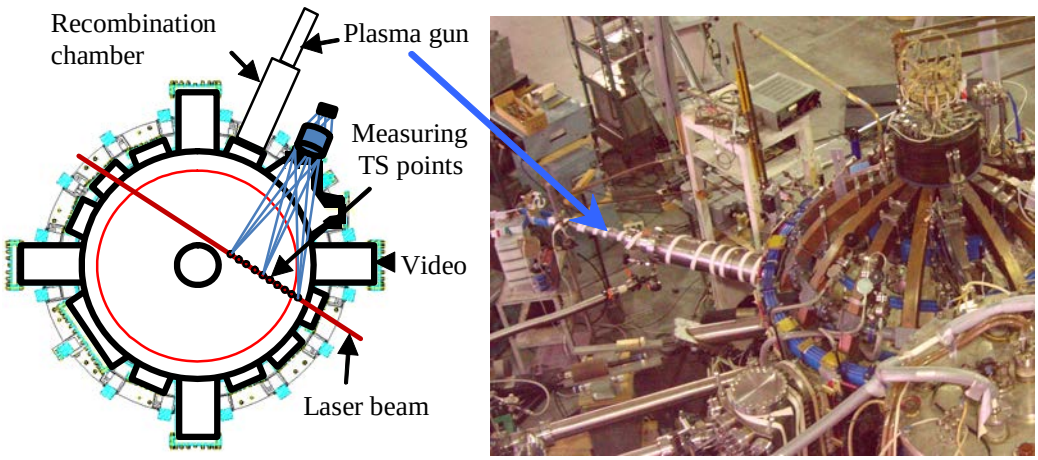

FIG. 4. Top view of plasma fuelling experiment at the Globus-Mg diodes

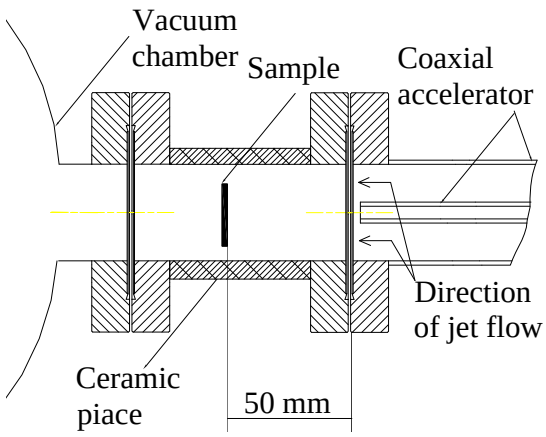

FIG. 5. Pure hydrogen jet irradiated sample located perpendicular to the gun axes generating stage is a system of coaxial electrodes. Electric discharge fired through the gas between the coaxial electrodes provides gas ionisation and plasma acceleration as in the classical "Marshall gun scenario".

The gun permits to combine necessary merit of the fuel injector – high density and speed of the jet with high purity of the substance. The modified gun produces fully ionised clean hydrogen jet with density reaching 4×10^{22} m^{-3}, total number of accelerated particles $(1\text{-}5)\times10^{19}$, the flow velocity 100-250 km/s and the pulse duration 10-15 μs.

General view of the gun connected to the vacuum chamber at the test bench is presented in Fig.2. At the exit of accelerator the spectrometer registered plasma jet radiation and the laser interferometer measured the plasma density. The frame camera (Bifo Company K008) observed propagation of visible jet radiation. The streak-camera (also Bifo Company K008), sweeping image of the jet propagation along the narrow slit away from the gun muzzle recorded the jet velocity. The pressure gauge (PMI-10) adapted to a pulsed regime investigated the dynamics of gas feeding of accelerator. Light emitted diodes (LED) observed dynamic of current bridge in coaxial plasma accelerator (Fig.3). LEDs placed along outer electrode of the accelerator and registered current distribution along the muzzle. Currents I_1, I_2, I_3 produced a voltage drop along outer electrode and changed the glow intensities of LEDs

according to the amplitude of current bridges i_1, i_2, i_3 and the time which takes for the bridges to pass the three domains under study. The LED glows were transferred through the optical fiber to integrated photodetectors placed far from a source of electromagnetic noise. The photodetectors converted light signals to electrical ones, which were transmitted to a computer through an ADC.

Investigations of the jet dynamics in the plasma discharge of Globus-M spherical tokamak has been performed (Fig.4). The jet was injected through 1.5 or 0.5 m recombination chamber to perform time-of-flight recombination into the neutral flux and avoid interaction with tokamak magnetic field up to 0.4 T. Video camera (Olympus i-speed 2) monitored the jet radiation during injection. Upgraded for 10 spatial points, a multi-pulse TS system measured density and temperature distribution across the plasma column. The frame camera (RedLake MotionPro HS-3) observed jet propagation in the Globus-M vacuum chamber. The streak-camera measured the jet propagation speed in plasma core of Globus-M. Pure hydrogen jet irradiated stainless steels and tungsten. Perpendicular to the gun axes samples were located (Fig.5). The jet with pulse duration 10-15 μs, plasma density $2\times10^{22}m^{-3}$ and proton energy 100 - 300 eV irradiated samples.

3. RESULTS

Investigation showed that only compact current bridge, accelerated between coaxial electrodes is able to produce high kinetic energy plasma jet. That means the working gas should feed the accelerator during time as short as possible. Dynamic of the gas feeding the coaxial accelerator has been investigated (Fig.6). The highest pressure (speed) of gas feeding the accelerator was observed when TiH grains released hydrogen and passing through 40 μm grid filter. This speed was increased up to 10^{19} atoms in 50 μs. Time dependence of current distribution along muzzle at low and high kinetic energy jet has been investigated (Fig.7) [2]. Investigation showed that only movable current bridge may produce clean and high kinetic energy jet. The gun generated low energy jet if the current was mainly localised near inlet and/or outlet gun edge. Contrary, when the current was running along the muzzle (LED signals are delayed one to another) high energy was generated. Measured by the calorimeter the kinetic energy of the jet was increased by several tens of times. The spectrometer at the exit from the accelerator did not record any radiation. This indicates that the pure hydrogen plasma jet was fully ionized. The plasma density reached the highest density at the exit, as followed from interferometer data. The jet velocity reached 200–250 km/s.

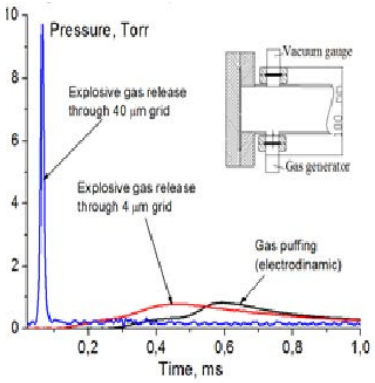

FIG. 6. Dynamics of gas feeding the accelerator with different type of gas generator.

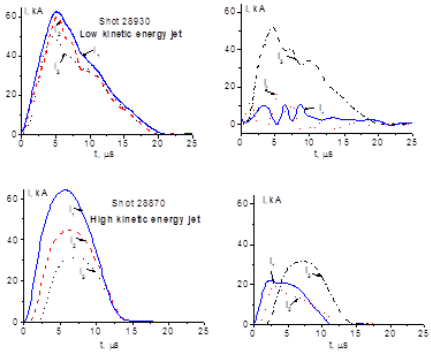

FIG. 7. Time dependence of current distribution along muzzle at low and high kinetic energy jet.

The jet has sharp boundary and small divergence, as it was observed by the frame camera (Fig.8) [3]. Sweeping image of the jet propagating along the narrow slit away from the gun muzzle showed that the plasma jet consists of several fractions, each of them propagating with its own velocity from 100 to 250 km/s according to different slopes of the strips (Fig.9).

Observations of the jet propagation in the Globus-M vacuum chamber with frame camera were performed (Fig.10). The jet hits central solenoid in few microseconds after reaching the gun port. The jet has small divergence.

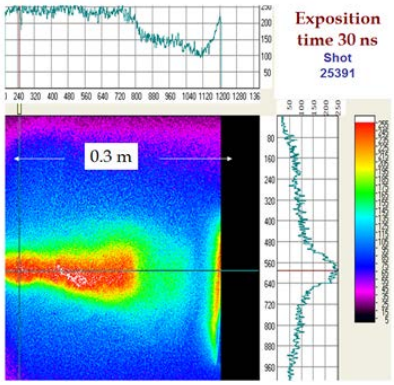

FIG. 8. The jet observed with a frame camera.

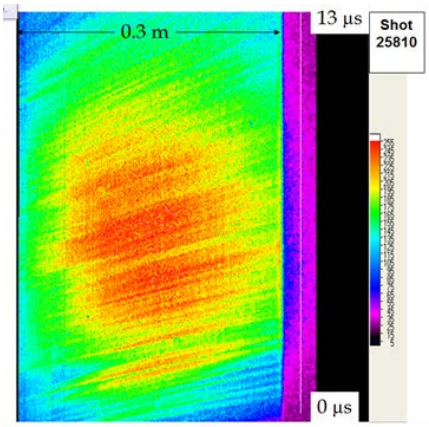

FIG. 9. Sweeping image of the jet propagating along the narrow slit away from the gun muzzle; the vertical axis is the time from the injection start; the horizontal axis is the distance from the gun port; the inclined stripes correspond to the separate fractions of the jet, and their slope defines the velocity of each fraction.

Jet propagation across toroidal magnetic field of Globus-M was investigated (Fig.11) [3]. Presence of components with different velocities confirmed measurements made with streak camera. Deviation of the jets increases with magnetic field rising. The components with higher speeds deviate for lower angles. Investigations of the jet dynamics in the plasma column of Globus-M spherical tokamak were carried out. The jet propagation speed in plasma core of Globus-M by a streak-camera was measured (Fig.13) [4]. The jet consists of several components, each of them propagating with its own speed ($\leq$ 30 km/s). The flux penetrates far inside separatrix.

The video-frame of the jet injected in the target plasma with fragments of the superimposed magnetic lines was analyzed (Fig. 12). [5-7]. Spreading the jet along the magnetic field lines was observed. This could be the possible diagnostic method for q profile measurements.

Strong jet penetration inside column at high jet energy was observed (Fig.14) [8-11]. The tokamak plasma density increases 2 -3 times. The temperature decreases 7 times. The discharge survives during only a few milliseconds after such injection. At lower jet energy the discharge survived until the end of the tokamak shot (Fig.15). In this case the density raised about 25 % and temperature didn't change in the range of accuracy of measurements.

Jet penetration in plasma column after H-mode initiated with NBI was investigated (Fig.16). After injection the density increases and temperature decreases by 40 %. The discharge lives many milliseconds after injection.

No disturbing jet injection demonstrated significance of fast density profile controlling in experiments with H-mode (Fig.17). Injection after H-mode switching was performed. H-mode didn't disappear–that means there were low plasma perturbations. Plasma density was rapidly increased. Following for the density raise ELM frequency also rapidly was increased. Transition to regime with favorable ELM-mode-high frequency and low amplitude was observed. After injection new distribution of stationary density with high gradient near periphery was created. Injection confirms dependence of frequency of periphery instabilities on density.

Pure hydrogen jet irradiated several fusion reactor materials [12]. Modification of the ferrite steel surface under irradiation of the jet was observed (Fig.18). Topographical structure has central symmetry $\approx$ 15 mm in diameter with deep relief. Actually the wave relief arises at power density > 1 MW/cm^2. The surface has no structural defects such as bobbles, craters, pores, microcracks. Such defects usually happen at higher fluxes 10-100 MW/cm^2 typical for plasma focus with pulse duration 0.1 – 1 μs. Only some open bubbles large diameter ~ 50 μm were observed. These results confirm both the better perspectives of 10Cr9WVTa steel like Eurofer97 as comparison with austenite steels for fusion application and the fact that the gun produces power density flux > 1 MW/cm^2. Preliminary experiment on W-irradiation with such plasma jet was performed (Fig. 19). Experiment showed that the jet modifies tungsten surface of the specimen. This tool may help for selection and development of appropriate type of tungsten as a construction material for ITER and DEMO.

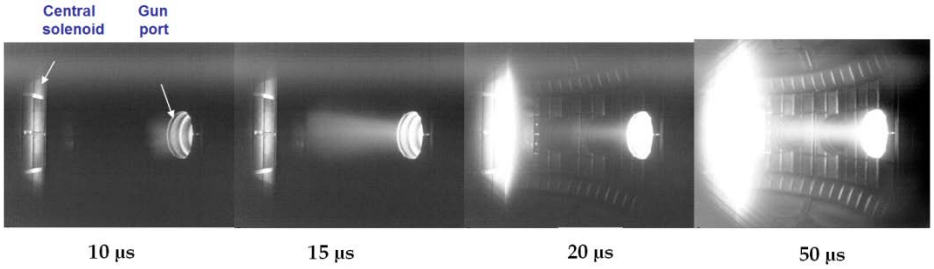

FIG. 10. Jet propagation in the Globus-M vacuum chamber; opening of the exposition was coincided with beginning of the accelerated current; distance between gun muzzle edge and central solenoid was about 1 m.

FIG. 11. Jet propagation across toroidal magnetic field of Globus-M; exposition time 5 ms; initial jet velocities 100 - 200 km/s.

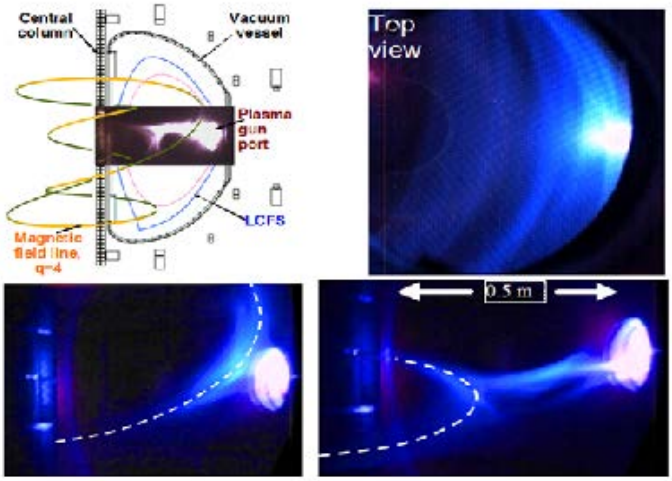

FIG. 12. The video-frames of the jet injected in the Globus-M target plasma with fragments of the superimposed magnetic lines.

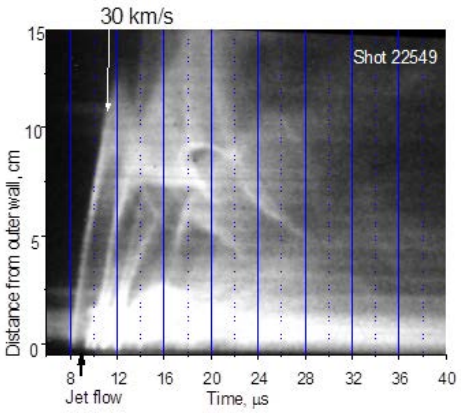

FIG. 13. Sweeping image of the jet propagating in plasma core of Globus-M; initial velocity of jet near the muzzle edge ≤ 120 km/s.

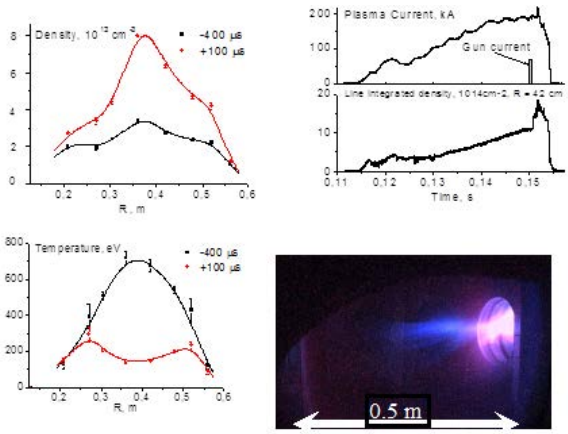

FIG. 14. Strong jet penetration inside plasma column at high jet energy.

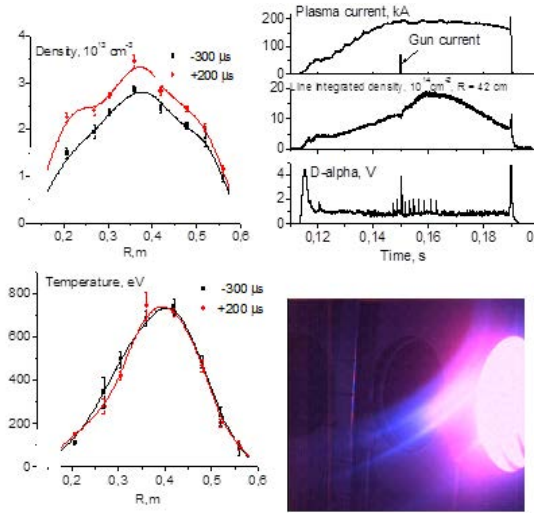

FIG. 15. Weak jet penetration inside plasma column at lower jet energy.

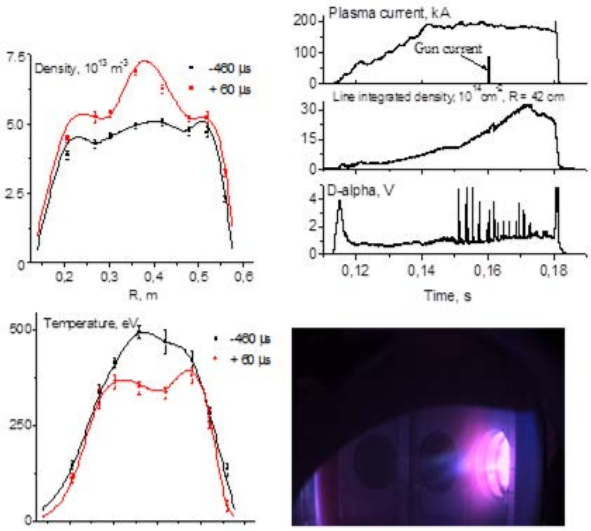

FIG. 16. Jet penetration in plasma column after H-mode initiated with NBI

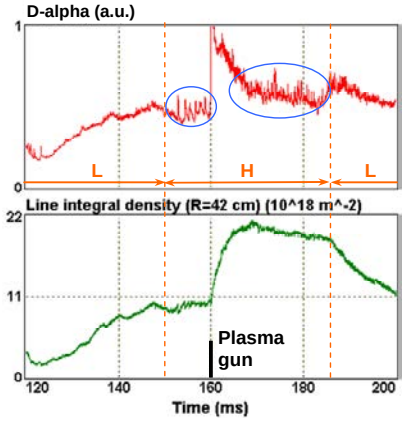

FIG. 17. No disturbing jet injection during H-mode and ELM switching.

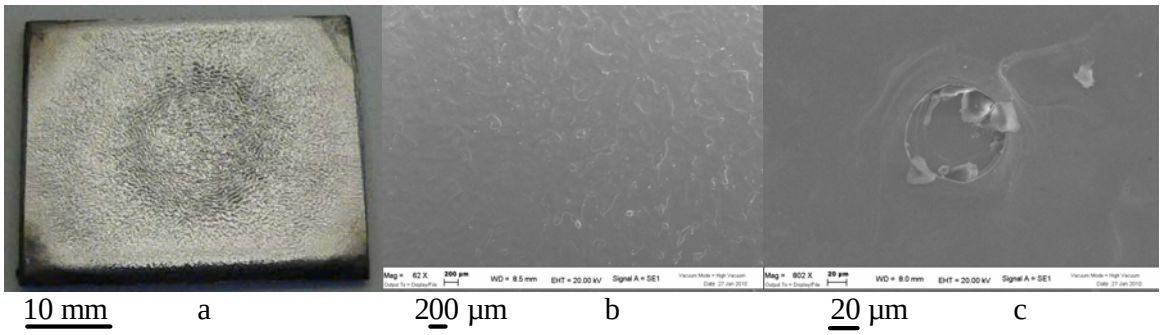

FIG. 18. Photos of the ferrite steel 10Cr9WV surface irradiated by pulse hydrogen plasma jet for different space resolution: a-sample 24x30 mm, 15 shots; b – SEM, 200 µm; c – SEM, 20 µm.

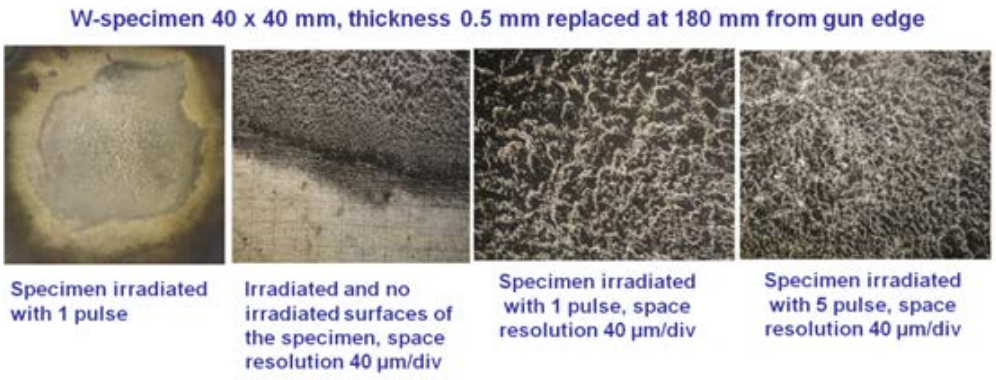

FIG. 19. Photos of the tungsten surface irradiated by pulse hydrogen plasma jet for different space resolutions and number of shots.

4. CONCLUSIONS

The parameters of accelerator generating a pure plasma jet with a high kinetic energy were improved, such as: size and polarity of electrodes, gas flow direction, time delay between gas feeding the accelerator and its ionization. The achieved results approve a perspective of upgraded plasma gun in fusion application. The gun producing clean hydrogen jet with density up to 4×10^{22} m^{-3} and kinetic proton energy up to 300 eV may be injected in Globus-M-like plasmas.

Undisruptive fuelling of core plasma with the help of the developed plasma gun was achieved. The jet may penetrate in central region of the plasma column without discharge degradation. A moderate density rise (up to 40%) in the central plasma region without plasma disruption was achieved.

Surface influence of the jet flux with the power density 1 MW/cm^2 on fusion reactor materials was demonstrated. Pure hydrogen jet irradiated steels and tungsten. A modification of the surface under irradiation of the jet was observed. The results confirmed the better perspectives of ferrite steel as comparison with austenite steels for fusion application. The jet was able to modify tungsten surface of the specimen. This tool may help for selection and development of appropriate type of tungsten as a construction material for ITER and DEMO.

REFERENCES

[1] VORONIN, A.V., et al, Dense plasma source development and jet injection in Globus-M, Nukleonika 53 3 (2008) 103.

[2] VORONIN, A.V., GUSEV, V. K., KOBYAKOV, S. V., Dynamics of a Current Bridge in a Coaxial Plasma Accelerator Technical Physics, 56 7 (2011) 963.

[3] VORONIN, A.V., et al, "Two stage plasma gun as the fuelling tool of Globus-M tokamak". (Proc. 35th EPS Conference on Plasma Phys., Greec, Hersonissos, 9 - 13 June, 2008), ECA 32D, P-2.104.

[4] VORONIN, A.V., et al, "Double pulse plasma gun for parameter controlling of Globus-M". (Proc. 36th EPS Conference on Plasma Physics, Bulgaria, Sofia June 29 - July 3, 2009), P5.157.

[5] PETROV, Yu.V., VORONIN, A.V., et al, "Central Fueling of Globus-M Plasma with the Help of Coaxial Plasma Gun", (Proc. 22nd IAEA Fusion Energy Conference, Switzerland, Geneva, 13-18 October, 2008), EX/P5-8.

[6] GUSEV, V.K., VORONIN, A.V., et al, "Experimental study of electron component dynamics during injection of plasma jet and neutral beam into spherical tokamak Globus-M". (Proc. 37th EPS Conference on Plasma Physics, Ireland, 21th – 25th June 2010), P5.137.

[7] GUSEV, V.K., VORONIN, A.V., et al, "Overview of Results obtained at the Globus-M Spherical Tokamak". (Proc. 22nd IAEA Fusion Energy Conference, Switzerland, Geneva 13-18 October, 2008), OV/5-4.

[8] GUSEV, V.K., VORONIN, A.V., et al, Overview of results obtained at the Globus-M spherical tokamak, Nuclear Fusion, 49 10 (2009) 1.

[9] TOLSTYAKOV, S.Yu., VORONIN, A.V., et al, "Kinetic measurements of plasma electron component dynamics in the Globus-M tokamak during plasma gun injection experiment". (Proc. 35th EPS Conference on Plasma Phys., Grees, Hersonissos, 9 - 13 June, 2008), ECA 32D, P-2.108.

[10] GUSEV, V.K., VORONIN, A.V., et al, "Investigation of Beam- and Wave- Plasma Interaction in the Globus-M Spherical Tokamak". (Proc. 23rd IAEA Fusion Energy Conference, Korea, Daejon, 11-16 October 2010), Rep. EXW/P7-08.

[11] GUSEV, V.K., VORONIN, A.V., et al, Investigation of Beam and Wave Plasma Interaction in the Globus-M Spherical Tokamak, Nuclear Fusion **51** 10 (2011).

[12] VORONIN, A.V., et al, "Plasma gun with super fast gas feeding in fusion research". (Proc. 37th EPS Conference on Plasma Physics, Ireland, 21th – 25th June 2010), P5.192.

APPLICATION OF X-PINCH PLASMA AS X RAY SOURCE FOR BACKLIGHTING HIGH DENSITY Z-PINCH PLASMA

X. WANG

Department of Electrical Engineering
Tsinghua University, Beijing, Republic of China

Abstract

The characteristics of X ray emission from an X-pinch powered by pulsed power generator PPG-1 (400kA, 100 ns) were investigated with photoconducting detectors (PCDs) and pinhole camera. It was shown that the X-pinch is an intensive and subnanosecond-pulse X ray point source that is very suitable to be used as X ray source for backlighting of wire-array Z-pinch plasma. The evolution of two-wire Z-pinch plasma in its initial stage was "viewed" by X ray backlighting method using PPG-1 X-pinch as X ray source. The backlighting images show clearly that all the processes are similar to those occurring in the initial stages of a cylindrical wire-array Z-pinch, including the electric explosion of single wires characterized by the dense wire cores surrounded by the low-density coronal plasma, the expansion of the exploding wire, the sausage instability (m=0) in the coronal plasma around each wire, the motion of the coronal plasma as well as the wire core toward to the symmetrical axis, the formation of the precursor plasma column with a twist structure something like that of higher mode instability, especially the kink instability (m=1). The quantitative measurement of mass density in the plasma around Z-pinch wires was performed based on a step-wedges having known thickness. The mass ablation rate and expansion rate of wire core were obtained. For the purpose of using X-pinch as X ray source for phase-contrast imaging of small and soft biological object, a movable table-top X-pinch device (2m×1m×1.5m) was constructed and tested. It was shown that the X ray emission from the X-pinch was observed even with a current as low as 60 kA when thinner wires were used as X-pinch load. The characteristics of the X ray emission from the table-top X-pinch are similar to those from PPG-1 X-pinch.

1. INTRODUCTION

Z-pinch produces dense magnetized plasma in a similar way to plasma focus. In the Z-pinch system the plasma is produced by applying a high voltage pulse across an anode-cathode gap of cylindrical geometry that is either pre-filled with an annular and hollow gas shell produced by using a supersonic nozzle or bridged by an array of wires (typically made of a high-Z metal such as tungsten). The plasma is imploded by the azimuthal magnetic field produced by the axially flowing pulsed discharge current. During compression and stagnation, the kinetic energy is converted to thermal energy and radiation, and a hot and dense core is formed at the center. Typical densities and temperatures at the pinch core are 10^{18}-10^{22} cm^{-3} and 0.1-1 keV, respectively. Highly stripped ions are formed during the thermalization phase, and the plasma emits mostly in the X ray regime [1].

The Z-pinch was developed originally to try heating plasmas to thermonuclear temperatures. However, the discouraging results due to MHD instabilities in the late 1950s made people not to consider Z-pinch as a candidate of nuclear fusion [2]. In 1997 a breakthrough was achieved by Sandia Laboratories in PBFA-Z project which got promising parameters of 1.8 MJ X ray energy with an efficiency of 16% from electrical energy to X ray and 290 TW X ray pulsed power [3,4]. The improvement on Z-pinch load was thought to be responsible for this breakthrough. A wire-array load made using hundreds fine wires provides a high degree of initial symmetry of the load and current distribution, leading to a lower "seed level" of MHD instabilities. The breakthrough has sparked current worldwide interest in Z-pinch-driven nuclear fusion [5].

The detailed physics of the wire-array Z-pinch is still under intensive investigation. Among the most important issues are the transition from metallic wires to plasma at the start of the current pulse and the mechanism responsible for inhomogeneity in mass distribution during the initial phase of the implosion. Investigation of these two issues requires use of soft X ray backlighting with high spatial and temporal resolution.

An X pinch is made using two fine wires that cross and touch at a single point forming an “X” shape. When a high current flows through the wires, they explode and form plasma that implodes and forms a dense and hot plasma region at the crossing point, called X-pinch. As an intensive soft X ray point source that is micrometers in size and subnanoseconds in pulse width, X-pinch is expected to be suitable for backlighting Z-pinch plasma [6-7].

Partly supported by IAEA under contact Nos.14509/(R0, R1, R2, R3) during the period of implementing the CRP from September of 2007 to May of 2012, the research on using the X-pinch driven by PPG-1 (Pulsed Power Generator 1) as X ray source to backlight the initial phase of wire-array Z-pinch was conducted and a table-top X-pinch driven by PPG-2 (Pulsed Power Generator 2) was constructed.

2. EXPERIMENTAL SETUP

2.1. Experimental facility

The experimental facility is a load section powered by a pulsed power generator (PPG 1) [8]. PPG-1 is shown in figure 1 and consists of a 1.2 MV Marx generator, a 1.25 Ω pulsed forming line (PFL), a V/N switch, a 1.25 Ω pulsed transmission line (PTL). It is capable of delivering a voltage pulse, up to 500 kV in amplitude and 100 ns in pulse width (FWHM), through a 1.25Ω pulse transmission line to the load section.

FIG. 1. Pulsed power generator 1 (PPG-1).

As shown in figure 2, the load section is a coaxial configuration. A plexiglass diaphragm is inserted in between the PTL and the load section to isolate the water inside the PTL from the vacuum inside the load section. Both X-pinch and wire-array Z-pinch were put inside the load section. As the object to be backlighted, a two-wire Z-pinch was installed in between the anode and cathode. As X ray backlighting sources, one or two X-pinches each made of two crossing wires were installed in the places of current-return rods. Figure 3 shows the voltage applied to the load section and the load current.

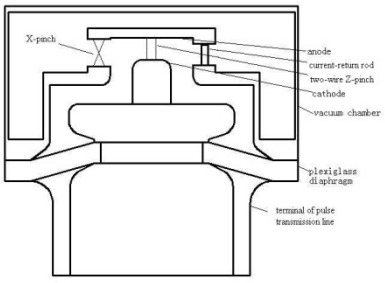

FIG. 2. Sketch of the load section.

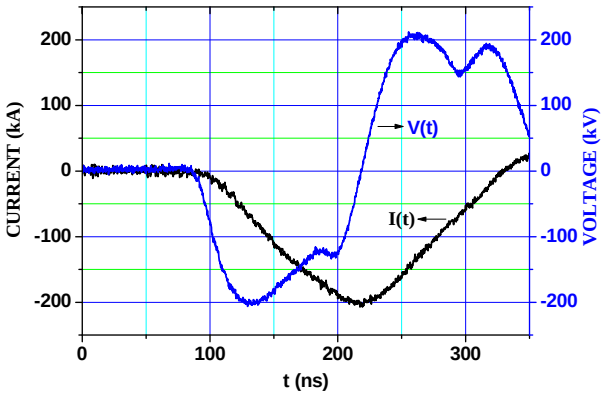

FIG. 3. Voltage applied to the load section and the load current.

2.2. Diagnostics

2.2.1. Photoconducting detector

The time-resolved X ray emission from X-pinch was measured with three X ray photoconducting detectors (PCDs) each using a diamond (3mm×1mm×1mm) as X ray sensor, as shown in figure 4. The PCDs from AASC (Alameda Applied Science Corporation) were calibrated to be with a flat sensitivity of 5×10^4 A/W in a range of 1~ 5 keV at a biasing voltage of 100 V. Since the X ray pulse from X-pinch is subnanosecond in pulse width, an extremely fast digitizing oscilloscope (Lecroy SDA6020) with a bandwidth of 6 GHz and a sampling rate of 20 GS/s was used.

Different filters were used for different PCDs and thus the X rays with different cut-off photon energy were measured. PCD1 was covered by a 50-μm thick Be filter for measuring X rays with hν>1.5 keV, PCD2 by a 12.5-μm thick Ti filter for X rays with hν>2.5 keV, and PCD3 by a 20-μm Al filter for X rays with hν>4 keV.

FIG. 4. Photoconducting detector.

2.2.2. Pinhole camera

The pattern of the X rays from X-pinch was recorded on X ray sensitive film (KODAK: BioMax-MS) by using an 8-μm aperture pinhole camera. The distances from X-pinch to the pinhole and from the pinhole to the film are 80 mm and 440 mm, respectively, which correspond to a geometric magnification of 5.5.

2.2.3. Step wedges

Quantitative density measurements of the plasma formed around exploded wires of Z-pinch were carried out by comparing the absorption of backlighter X rays by the wire-generated plasmas with that by a step wedges having known step thickness. The step wedges are made from Tungsten or Molybdenum, the same material as that of the Z-pinch wires. By a magnetron sputtering method, eight Tungsten or Molybdenum layers with a thickness of 0.016μm, 0.029μm, 0.072μm, 0.170μm, 0.304μm, 0.519μm, 0.855μm, 1.101μm were deposited on the right edge of an Al foil substrate that is 6.5mm in thickness and 30 mm in diameter. Figure 5 shows the Al foil substrate together with the step wedge (left) and the X ray exposed film covered by the step wedges (right). Al foil substrate together with the step wedge serves as the X ray filter placed in front of the X ray film recording backlighting image, as shown in figure 6.

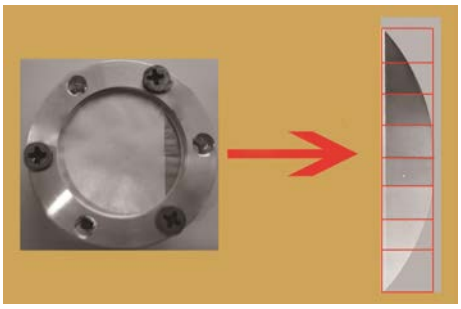

FIG. 5. Al foil substrate together with the step wedge (left) and the X ray exposed film covered by the step wedges (right).

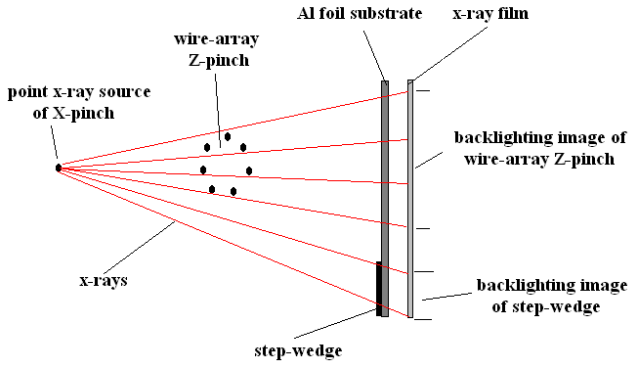

FIG. 6. Experimental arrangement of X ray backlighting of wire-array Z-pinch with the step wedges.

3. RESULTS FROM EXPERIMENTS ON PPG-1 X-PINCH

3.1. Characteristics of X ray emission

3.1.1. Results from measurements using PCDs

As the mass of X-pinch load increases, the delay time from the beginning of the load current to the appearance of the X ray pulse increases. In the case of using two 25-μm Mo wires as X-pinch load, the X ray pulse appears at an instant far ahead the time of current maximum, as shown in figure 7 (a), which means the load mass is too small for 200 kA current. If we change 25-μm Mo wires to 50-μm Mo wires, the X ray pulse appears at the time of current maximum, as shown in figure 7 (b), which means the load mass is matched to the load current.

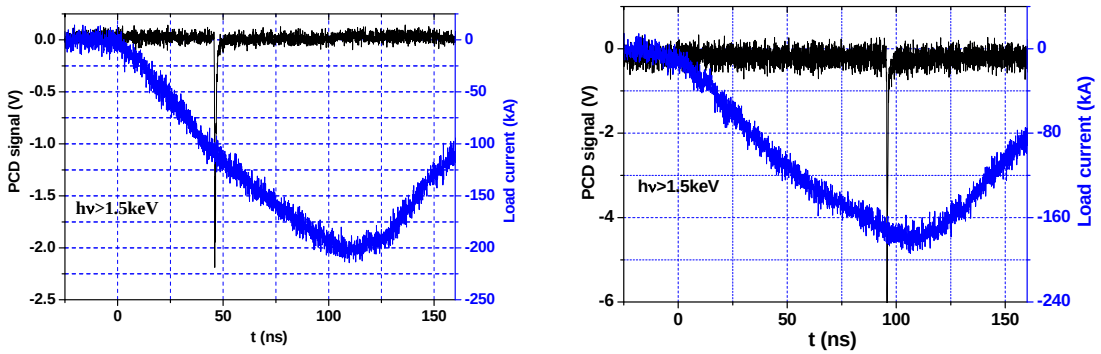

(a) two 25-μm Mo wires *(b) two 50-μm Mo wires*

FIG. 7. X ray pulse and load current for different X-pinch load.

The waveform expansion shows that the X ray pulse consists of either one subnanosecond peaks, as is shown in figure 8(a), or two subnanosecond peaks with a time interval of about 0.5 ns, as is shown in figure 8(b).

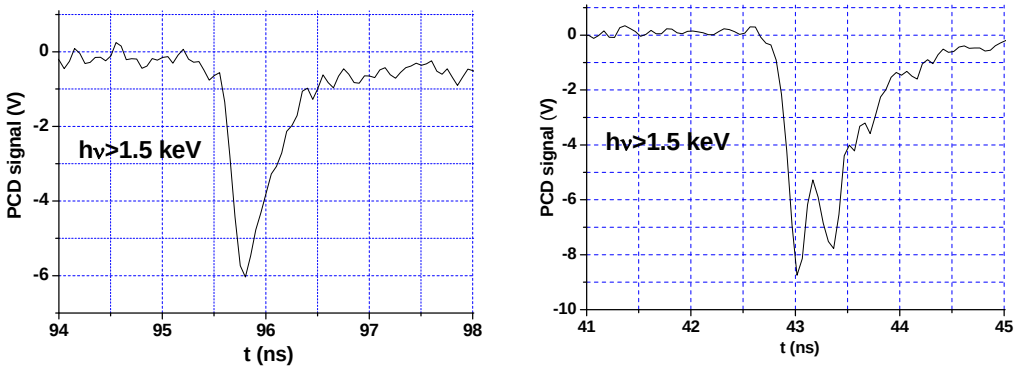

(a) one peak *(b) two peaks*

FIG. 8. Waveform expansion of the X ray pulse.

Figure 9 are the waveforms of the X ray pulses output from the three PSDs installed at the positions with a same distance from the X-pinch and aiming at the X-pinch from different direction. By comparing these waveforms, it was concluded that the X ray emission is isotropic.

Since a filter was put in front of PCD, only the X rays with photon energies above a minimum value named as cut-off photon energy could be measured. Figure 10 shows the waveforms of the X ray pulses measured with three PCDs covered by different filters and thus with different cut-off photon energy. It can be seen that as the cut-off photon energy determined by the filter rises, the signal of the X ray pulse rapidly decreases.

By integrating the X ray pulse over time, the total energy of the X ray emission was obtained. Under the same experimental conditions, the total energy of the X ray emission changes from shot to shot. As the cut-off photon energy rises, the total energy of the X ray emission rapidly decreases. Table 1 is the result from one shot. The total energy of X rays with photon energies higher than 1.5keV was averaged to be 0.35J for X-pinch made using two 25-μm Mo wires and 0.42J for X-pinch made using two 50-μm Mo wires.

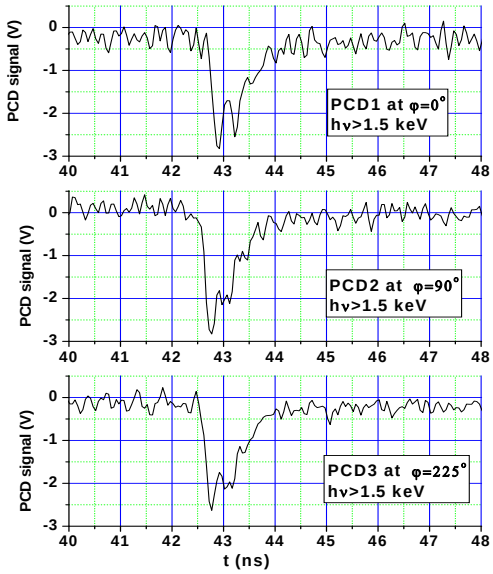

FIG. 9. Waveform of the X ray pulse from one shot measured at different positions.

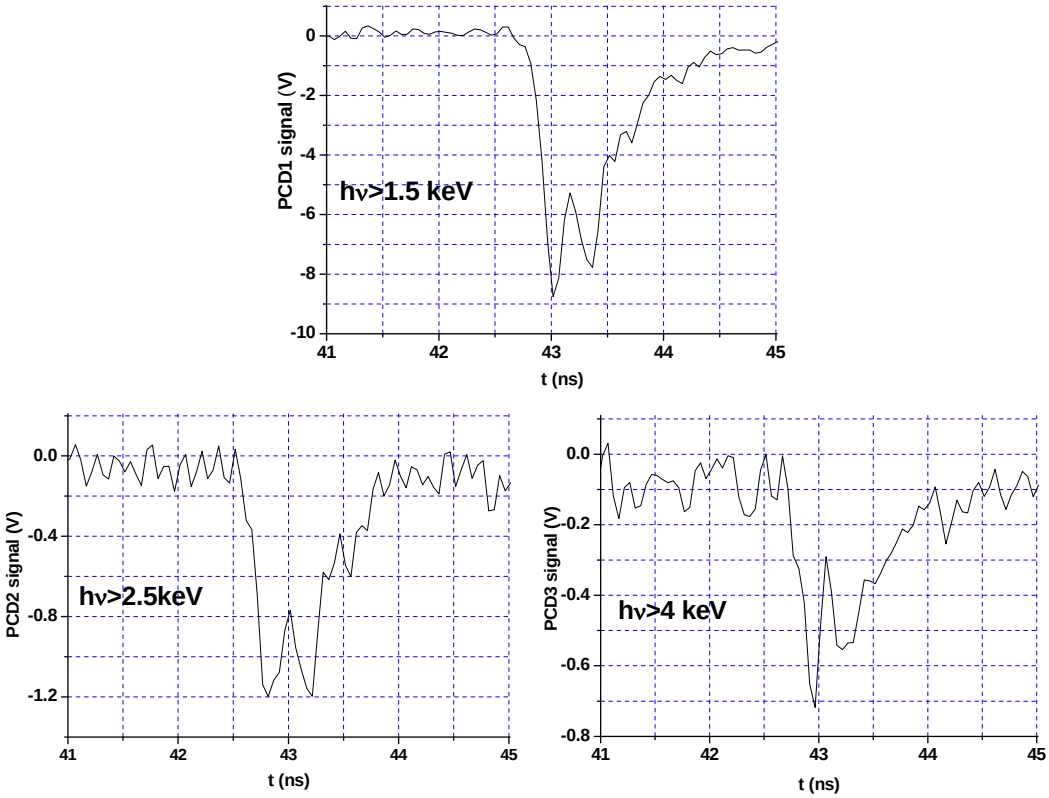

FIG. 10. Waveform of the X ray pulse measured with PCDs covered by different filters.

TABLE 1. TOTAL ENERGY OF X RAYS WITH DIFFERENT CUT-OFF PHOTON ENERGY

Photon energy (keV)	>1.5	>2.5	>4.0
X ray energy (J)	0.70	0.11	0.07

3.1.2. Results from measurements using pinhole camera

Depending on the load current and the X-pinch load, the size of the radiation region varies from 100 μm to a 5 μm. It was found from the pinhole pictures that there are usually two point source of X ray emission, which is consistent with the X ray pulse with two peaks. These two point sources, with a distance of tens micrometers, are located near the crossing point along the axis of X-pinch load. Figure 11 is the typical pinhole pictures for X-pinch made using two 25-μm Mo wires. As the cut-off photon energy rises from 1.5 keV to 4 keV, the source size changes from 50 μm to 5μm.

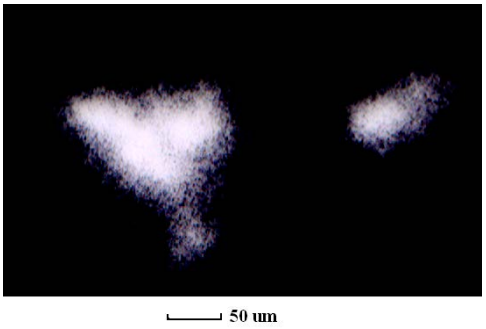

(a) hν > 1.5 keV

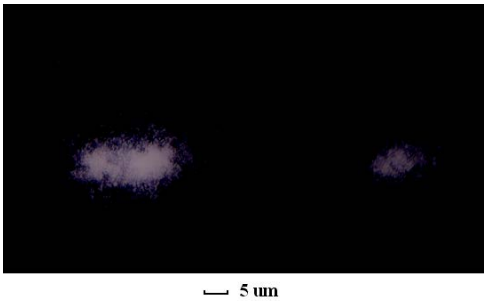

(b) hν > 4 keV

FIG. 11. Typical pinhole pictures for X-pinch made using two 25-μm Mo wires.

For some shots it can be two nearly overlapping X ray sources, as shown in figure 12 that is a pinhole picture of hν > 4 keV for X-pinch made using two 50-μm Mo wires.

FIG. 12. Two nearly overlapping X ray sources for X-pinch made using two 50-μm Mo wires.

3.2 Evolution of two-wire Z-pinch plasma viewed with X ray backlighting

3.2.1 Experimental arrangements

Figure 13 illustrates the experimental arrangement schematically. The experiments were performed on PPG-1. Two Mo wires of 50 μm in diameter, 10 mm long and 2 mm spacing between wires were used as Z-pinch load that connect the anode and the cathode at the output of PPG-1. The total current passing through this two-wire Z-pinch load is in the range of 250-275 kA, corresponding to 125-138 kA per wire. Being used as the X ray source for backlighting, one or two X-pinches each consisting of two 13-μm Mo wires were installed in the places of the current-return rods.

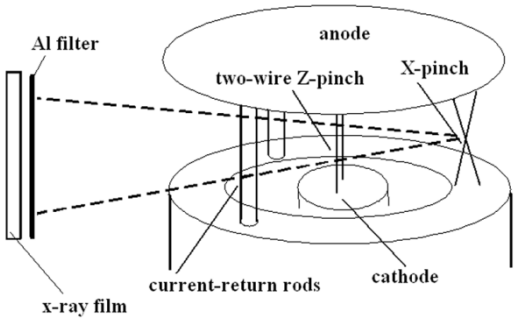

FIG. 13. Experimental arrangement for backlighting of Z-pinch using X-pinch as X ray source.

The X ray sensitive film (KODAK: BioMax-MS) was covered with a 13-μm Al filter to cut off the photons with energy lower than 3 keV and put at a position of 810 mm away from the Z-pinch. With these geometrical arrangements, the magnification for the Z-pinch image is 14.5. Three diamond photoconducting detectors (PCDs) covered with different filters were used to measure the X ray pulse of different cut-off photon energy from the X-pinch and one X ray pinhole camera was used to record the pattern of the X ray source. The signals from the Rogowski coil and from the PCDs were fed to a fast digitizing oscilloscope (Lecroy SDA6020) with a bandwidth of 6 GHz and a sampling rate of 20 GS/s.

3.2.2. Reasons for choosing two-wire Z-pinch

Two-wire Z-pinch load is the simplest linear wire-array in which there is also the tendency for the current-carrying plasma to be magnetically drawn away from the wires toward the centroid of the current, even though the geometry is not cylindrical. Therefore, the results are relevant to the experiments on cylindrical wire-array Z-pinches. The advantages of using a linear wire-array are no image distortions due to the plane of the array being oriented perpendicular to the lines-of-sight of the backlighter (X-pinch) and no overlapping images of the wires in front and behind.

3.2.3. Results and discussions

Figure 14 shows two typical X ray backlighting images of two-wire z-pinch. The time at which the image was taken was determined by the relative time of backlighter X ray pulse to the onset of the current flowing through the Z-pinch.

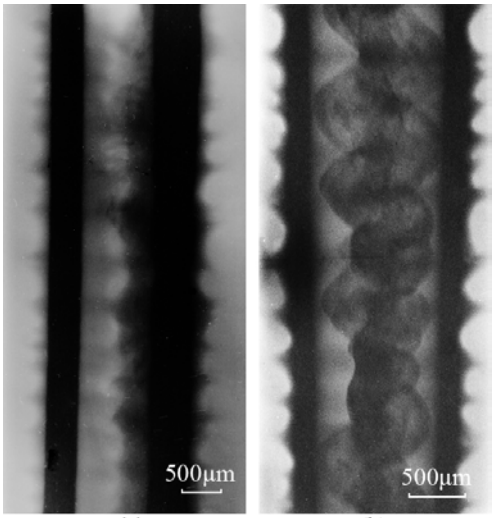

FIG. 14. X ray backlighting images of two-wire z-pinch; a) 61 ns and 155 kA and b) 86 ns and 215 kA.

All the processes similar to those occurring in the initial stages of a cylindrical wire-array Z-pinch could be observed in figure 14(a), including the electric explosion of single wire, the expansion of the exploding wire, MRT (m=0) stability in the coronal plasma, the coronal plasma as well as the wire core moving toward to the current centroid. From figure 14(a) we could see that individual dense wire core is surrounded by low-density coronal plasma produced by the breakdown in the desorbed gases and metallic vapor from the wire surface as a result of the Joule heating, which is a physical picture typical to the electric explosion of single wire. The coronal plasma as well as the wire cores expanded rapidly and the diameters of these two wire cores were measured to be 410 μm and 580 μm, respectively, indicating an expansion by a factor 8 to 12 in consideration of the wires being 50 μm in diameter before the wire explosion. It was noted that the wires expand differently even with using the same wire, which may leads to an asymmetry in the plasma shell merged by individual wire plasmas from a wire-array. Induced by self-magnetic pinch forces as the current increases, MRT stability (m = 0) was observed in the coronal plasma that was highly nonuniform axially. The instability pattern around each wire shows a quasiperiodic structure and the wavelength of this structure is about 400 μm. It was easy to find that more coronal plasma is in between the two wires than that in the other side of each wire, which means the coronal plasma was swept away from the wire to the current centroid by the global magnetic field. To our surprise, the dense wire cores also moved much toward to the current centroid at the time as early as 61 ns and the distance between the two wires was shortened to 1.4 mm from the original distance of 2 mm.

Figures 14(b) is a backlighting image taken at the time of 86 ns when a current of 215 kA was flowing through the two-wire Z-pinch. The big difference of figure 14(b) from figure 13(a) is that massive coronal plasma swept from the two wires was accumulated at the current centroid and forms so called “precursor plasma”. The axial nonuniform structure in the coronal plasma around the each wire due to m=0 MRT instability leads to, in turn, a nonuniform sweeping of the plasma from the wire and a nonuniform precursor plasma with a twist structure something like that of higher mode MRT instability. In addition, these two wire cores were pulled closer with a distance of about 1.2 mm by a stronger global magnetic force due to a higher current and a longer action time than that of figure 14(a).

An important phenomenon was observed on some of the X ray backlighting images and one example was shown in figure 15 that was taken at the time of 80 ns when a current of 210 kA was flowing through the two-wire Z-pinch. At the bottom of the precursor plasma column a bend was observed. As we know, there are two types of plasma instability, the sausage instability (m=0) and the kink instability (m=1), those are easier to develop in the pinched plasma column. The kink distortion consists of a perturbation in the form of a bend or kink in the plasma column. Thus, we attribute this bend in the precursor plasma column to the kink instability.

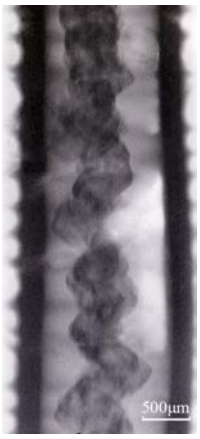

FIG. 15. Kink instability observed at the bottom of the precursor plasma column.

3.3. Quantitative density measurement

Based on the quantitative density measurements with the step wedges, some important parameters such as the mass ablation rate (MAR) of the plasma from the wire and the core expansion rate (CER) of the wire for two-wire Z-pinch were obtained. The results were shown in figure 16(a) for Z-pinch made using two 30-μm Mo wires and figure 16(b) Z-pinch made using two 50-μm Mo wires.

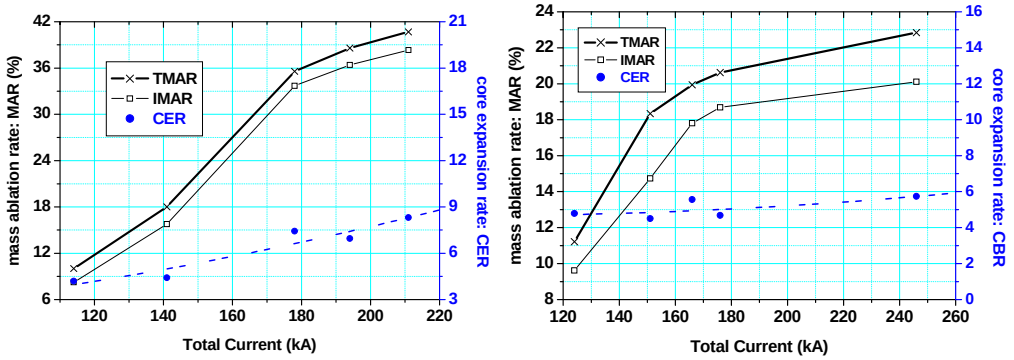

FIG. 16. Mass ablation rate and core expansion rate for two-wire Z-pinch; a) Results for Z-pinch made using two 30-μm Mo wires; b) Results for Z-pinch made using two 50-μm Mo wires.

Here we defined two mass ablation rates, total mass ablation rate (TMAR) and inner mass ablation rate (IMAR). IMAR is for the plasma in the area between two wires of the Z-pinch. As the current rises, both the mass ablation rate and the expansion rate increase. However, there is a turning point at about 180 kA after which the mass ablation rate increases

slowly. For Z-pinch made of two 30-μm Mo wires when the current rises to 210 kA, the ablation rate and the expansion rate are about 40% and 8.4, respectively. For Z-pinch made of two 50-μm Mo wires when the current rises to 250 kA, the ablation rate and the expansion rate are about 24 % and 5.8, respectively. It is important to find that IMAR is close to TMAR, which means most of the plasma around the wires were swept away and accumulated in between two wires by the global magnetic field.

4. PRELIMINARY RESULTS FROM RESEARCH ON TABLE-TOP X-PINCH

4.1. Introduction

Phase-contrast radiography is different from the conventional radiography. While the conventional radiography relies on X ray absorption as the sole source of contrast and ignores another source of contrast, *i.e.*, phase information, phase-contrast radiography records phase variations of X rays passing through an object and offers improved contrast sensitivity, especially when imaging weakly absorbing samples [9]. In 1996 Wilkins demonstrated a simplified scheme for phase-contrast imaging based on an X ray source having high spatial coherence expressed by $d_{\perp}=\lambda l/\sigma$, where l is the source to observation distance, σ is the source size, λ is the wavelength of X ray [10]. Thus, high spatial coherence may be achieved by using a source having small size or by observing the beam at a large distance from the source. In general, the smaller σ and the longer l, the better, provided that the flux from the source is sufficient.

Microfocus X ray tubes are often used for phase-contrast imaging due to their small size of X ray source, but microfocus X ray tubes have a shortcoming, *i.e.*, the radiation intensity is very low, leading to a very long exposure time. For example, the exposure time for taking an image of a small aquarium goldfish (fantail) is as long as 110 minutes [10]. Synchrotrons are excellent sources for phase-contrast imaging, but they are extremely expensive and not available everywhere. As shown in 17, X-pinch has proved to be an ideal X ray source for phase-contrast imaging of small and totally soft biological object such as a mosquito that is weakly X ray absorbing and may not be clearly imaged by conventional X ray radiography [11]. It is desirable to have a table-top X-pinch device that can be easily moved everywhere to take phase-contrast images for biological and clinical purpose.

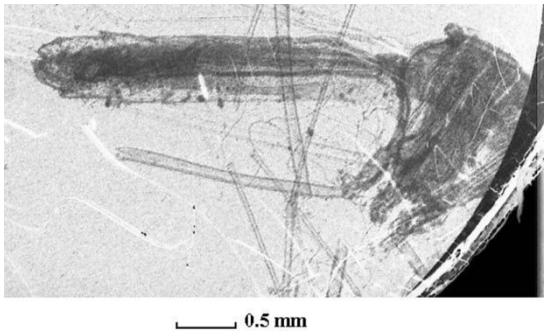

FIG.17. Phase contrast image of a mosquito taken with X-pinch as X ray source.

4.2. Table-top X-pinch device

A table-top X-pinch device was designed, constructed and tested. The table-top X-pinch device is almost the same in construction as the PPG-1 X-pinch device, but much smaller in capacity and size. As is shown in figure 18(b), the whole X-pinch device, with a size of 2m×1m×1.5m, was put on a platform under which there are four wheels and thus it can easily

be moved by a single person. It is powered by a pulsed power generator (PPG-2). PPG-2 is shown in figure 18(a) and consists of a 360 kV Marx generator, a 1.25 Ω pulsed forming line (PFL), a V/N switch, a 1.25 Ω pulsed transmission line (PTL). It is capable of delivering a voltage pulse, up to 150 kV in amplitude and 60 ns in pulse width (FWHM), through a 1.25Ω pulse transmission line to the load section.

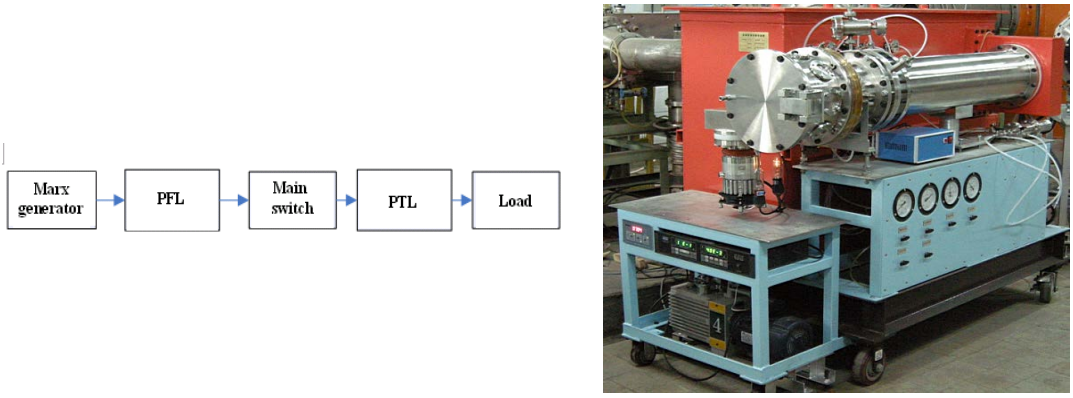

a) Construction *b) Photo*

FIG.18. Table-top X-pinch device.

4.3. Preliminary experimental results

The load current was almost unchanged for X-pinches made using different wires (5μm, 8μm, 10μm and 13μm Wu wire, 13μm and 25μm Mo wire), which means that the impedance of the wires is much lower than the total impedance of the load section. When the above mentioned wires were used as two-wire X-pinch load, X ray pulses from the X-pinches were always observed. Figure 19 are the typical waveforms of the load current together with the X ray pulse from X-pinch measured with PCD. From figure 19 it can be seen that the time delay of the X ray emission relative to the beginning of the load current increases as the mass of the two-wire load increases. It is easy to understand that for a given current, a longer time is needed to compress a higher density of plasma to a temperature high enough to emit X rays.

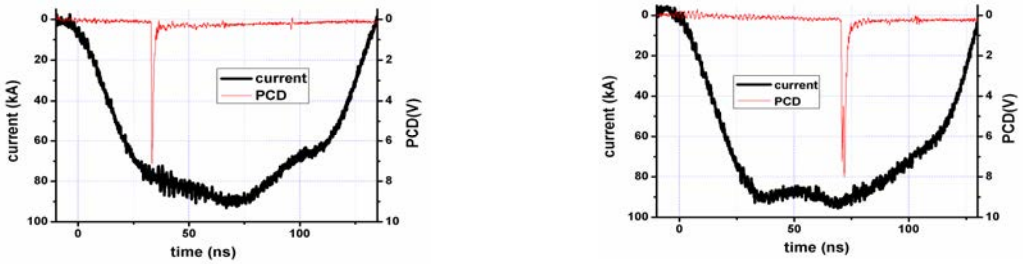

a) Two 13-μm Mo wires for X-pinch *b) Two 25-μm Mo wires for X-pinch*

Fig. 19. Typical waveforms of the load current together with the X ray pulse from X-pinch.

The same as that from the X-pinch powered by PPG-1, the X ray pulse from the table-top X-pinch consists of single peak or two overlapping peaks of subnanosecond pulse width. Figu re 20 are the typical waveforms of the X ray pulse. By the integration of the X ray pulse over time, the total energy of the X ray emission can be obtained. It was found that this total energy changes significantly from shot to shot and is in the range of 0.1J ~ 1J for X rays of hν > 1.5 keV.

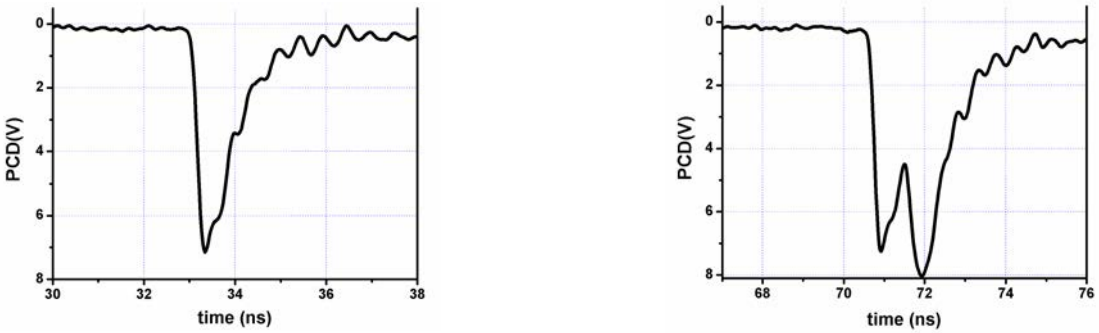

a) single peak *b) two overlapping peaks*

FIG. 20. Typical waveforms of the X ray pulse from X-pinch.

The amplitude of the X ray pulse measured with PCD2 for hν > 1.5 keV is much higher than that measured with PCD1 for hν > 2.5 keV, as shown in figure 21, which indicates that the major part of the X rays are with photon energy lower than 2.5 keV.

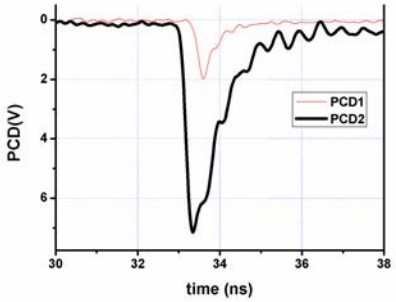

FIG. 21. Comparison between the X ray pulse of hν > 1.5 keV and that of hν > 2.5 keV.

For a relatively small mass of the X-pinch load such as two 8-μm W wires, when the load current rises from 60 kA to 82 kA and finally to 90 kA, the X ray emission usually changes from one pulse, figure 22(a), to two pulses with a time interval of about 50 ns, figure 22(b), and finally to two pulses with a time interval of about 10 ns, figure 22(c).

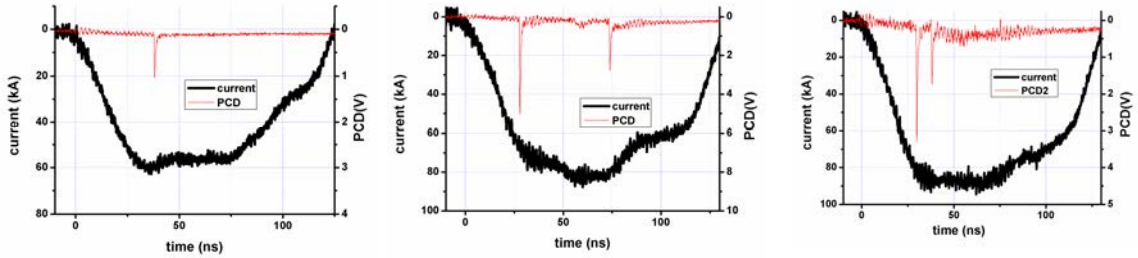

FIG. 22.Two X ray pulses when the load current is high enough compared to the mass of X-pinch load.

As we know, there are two possibilities for an X-pinch to emit X rays. The first one is the result of plasma pinch in which plasma is compressed to a high density and temperature. The second one is beam-target emission. Beam-target emission was described as the following. Due to plasma instabilities, the pinched plasma column collapses and breaks, leading to an abrupt change in the plasma current and a huge induced voltage proportional to di/dt. The electrons from the collapsed plasma column are accelerated to a high speed by the induced voltage and bombard on the targets, the ions in the collapsed plasma column.

As a result of the bombardments, a second X ray emission so called bremsstrahlung follows the first one, the X ray emission from the pinched plasma. Since the time interval between the pinched plasma emission and beam-target emission should be shorter than a few nanoseconds, the second X ray pulse shown in figure 21(b) and (c) is attributed to the second pinch of the plasma rather than beam-target emission.

5. CONCLUSIONS

The characteristics of the X ray emission from the X-pinch powered by PPG-1 were obtained. It was shown that X-pinch is a subnanosecond pulsed X ray point source very suitable for backlighting wire-array Z-pinch plasma.

The evolution of two-wire Z-pinch plasma was investigated by X ray backlighting using X-pinches as the X ray sources. The backlighting images show clearly the processes similar to those occurring in the initial stages of a cylindrical wire-array Z-pinch, including the electric explosion of single wires characterized by the dense wire cores surrounded by the low-density coronal plasma, the expansion of the exploding wire, the sausage instability (m=0) in the coronal plasma around each wire, the motion of the coronal plasma as well as the wire core toward to the current centroid, the formation of the precursor plasma column with a twist structure something like that of higher mode instability, especially the kink instability (m=1).

Based on the quantitative density measurements with the step wedges, some important parameters such as the ablation rate of the plasma from the wire and the expansion rate of the wire core for two-wire Z-pinch were obtained. It is important to find that the ablation rate for the area between two wires is close to the total ablation rate, which means most of the plasma around the wires were swept away and accumulated in between two wires by the global magnetic field.

Based on a compact (2m×1m×1.5m) pulsed current generator (~ 100 kA, 60ns), a table-top X-pinch device was constructed and tested. The load current was almost unchanged for X-pinches made using different wires (5μm, 8μm, 10μm and 13μm Wu wire, 13μm and 25μm Mo wire), which means that the impedance of the wires is much lower than the total impedance of the load section. When the above mentioned wires were used as two-wire load, X ray pulses from X-pinch were always observed. As the mass of the two-wire load increases, the time delay of the X ray emission relative to the beginning of the load current increases. As was expected, the X ray pulse consists of single peak or two overlapping peaks of subnanosecond pulse width. Two X ray pulses with a time interval on the order of 10 ns were often observed for a small mass load when the load current is high enough. The appearance of the second X ray pulse is attributed to the second pinch of the plasma.

ACKNOWLEDGEMENTS

The authors would like to thank the Natural Science Foundation of China for supporting the research under contract 10635050 and to thank International Atomic Energy Agency for partly supporting the research under contract No. 12509/(R0, R1, R2, R3).

REFERENCES

[1] LIBERMANN, M. A., *et al.*, Physics of high-density Z-pinch plasmas, Springer-Verlag, New York (1999).

[2] HUSSEY, W., *et al.*, Scaling of (MHD) instabilities in the imploding plasma liners, J. Appl. Phys. 51 3 (1980) 1452.

[3] SANFORD, T. W. L., *et al.*, Improved Symmetry greatly increases X ray power from wire-array z-pinches, Phys. Rev. Lett. 77 25 (1996) 5063.

[4] DEENEY, C., *et al*, Enhancement of X ray power from a z pinch using nested-wire Arrays, Phys. Rev. Lett. 81 22 (1998) 4883.

[5] RAMIREZ, J. J., The X-1 Z-pinch driver, IEEE Trans. Plasma Science 25 2 (1997) 155.

[6] KALANTAR, D. H., *et al.*, The X-pinch as a point source of X rays for backlighting, Rev. Sci. Instrum. 66 1 (1995) 779.

[7] LEBEDEV, S. V., *et al*, X ray backlighting of wire array Z-pinch implosions using X-pinch, Rev. Sci. Instrum. 72 1 (2001) 671.

[8] ZOU, X., *et al.*, Pulsed power generator for X-pinch, Laser Part. Beams 24 4 (2006), 503.

[9] FITZGERALD, R., Phase-sensitive X ray imaging, Phys. Today 53 7 (2000) 23.

[10] WILKINS, S., *et al*, Phase-contrast imaging using polychromatic hard X rays, Nature 384 (1996) 335.

[11] LIU, R., *et al.*, Phase-contrast imaging of soft biological object using X-pinch as X ray source, Europhys. Lett. 83 2 (2008) 25002.

LIST OF PARTICIPANTS

Blagoev, A.B.	Sofia University, Sofia, Bulgaria Email : blagoev@phys.uni-sofia.bg
Demina, E.V.	A.A. Baikov institute of metallurgy and material science, RAS., 119991 Moscow Russian Federation Email: elenadyom@mail.ru
Dubrovsky, A.V.	Moscow Physical Society. Moscow, Russian Federation Email: adubrov@mail.ru
Garkusha, I.E.	Institute of Plasma Physics of the NSC KIPT 61108, Kharkov, Ukraine Email: garkusha@ipp.kharkov.ua
Jednoróg, S.	Institute of Plasma Physics and Laser Microfusion ul. Hery 23, 01-497 Warsaw, Poland Email: jednorog@ifpilm.waw.pl
Kubes, P.	Czech Technical University in Prague Faculty of Electrical Engineering Czech Republic Email: kubes@fel.cvut.cz
Laas, T.	Institute of Mathematics and Natural Sciences Tallinn University, Estonia Email: tonu.laas@tlu.ee
Scholz, M.	International Centre for Dense Magnetized Plasmas ul. Hery 23, 01-497 Warsaw, Poland Email: marek@ifpilm.waw.pl
Sprinngham, S.V.	National Institute of Education, Nanyang Technological University, 1 Nanyang Walk, Singapore-637616 Email: stuart.springham@nie.edu.sg
Tuniz, C.	The Abdus Salam International Centre for Theoretical Physics, Strada Costiera 11, 34151 Trieste, Italy Email: ctuniz@ictp.it
Voronin, A.V.	Ioffe Physical-Technical Institute of the Russian Academy of Sciences, St. Petersburg, Russian Federation Email: voronin.mhd@mail.ioffe.ru
Wang, X.	Department of Electrical Engineering Tsinghua University, Beijing, China Email: wangxx@tsinghua.edu.cn

IAEA
International Atomic Energy Agency

Where to order IAEA publications

In the following countries IAEA publications may be purchased from the sources listed below, or from major local booksellers. Payment may be made in local currency or with UNESCO coupons.

AUSTRALIA
DA Information Services, 648 Whitehorse Road, MITCHAM 3132
Telephone: +61 3 9210 7777 • Fax: +61 3 9210 7788
Email: service@dadirect.com.au • Web site: http://www.dadirect.com.au

BELGIUM
Jean de Lannoy, avenue du Roi 202, B-1190 Brussels
Telephone: +32 2 538 43 08 • Fax: +32 2 538 08 41
Email: jean.de.lannoy@infoboard.be • Web site: http://www.jean-de-lannoy.be

CANADA
Bernan Associates, 4501 Forbes Blvd, Suite 200, Lanham, MD 20706-4346, USA
Telephone: 1-800-865-3457 • Fax: 1-800-865-3450
Email: customercare@bernan.com • Web site: http://www.bernan.com

Renouf Publishing Company Ltd., 1-5369 Canotek Rd., Ottawa, Ontario, K1J 9J3
Telephone: +613 745 2665 • Fax: +613 745 7660
Email: order.dept@renoufbooks.com • Web site: http://www.renoufbooks.com

CHINA
IAEA Publications in Chinese: China Nuclear Energy Industry Corporation, Translation Section, P.O. Box 2103, Beijing

CZECH REPUBLIC
Suweco CZ, S.R.O., Klecakova 347, 180 21 Praha 9
Telephone: +420 26603 5364 • Fax: +420 28482 1646
Email: nakup@suweco.cz • Web site: http://www.suweco.cz

FINLAND
Akateeminen Kirjakauppa, PO BOX 128 (Keskuskatu 1), FIN-00101 Helsinki
Telephone: +358 9 121 41 • Fax: +358 9 121 4450
Email: akatilaus@akateeminen.com • Web site: http://www.akateeminen.com

FRANCE
Form-Edit, 5, rue Janssen, P.O. Box 25, F-75921 Paris Cedex 19
Telephone: +33 1 42 01 49 49 • Fax: +33 1 42 01 90 90
Email: formedit@formedit.fr • Web site: http://www. formedit.fr

Lavoisier SAS, 145 rue de Provigny, 94236 Cachan Cedex
Telephone: + 33 1 47 40 67 02 • Fax +33 1 47 40 67 02
Email: romuald.verrier@lavoisier.fr • Web site: http://www.lavoisier.fr

GERMANY
UNO-Verlag, Vertriebs- und Verlags GmbH, Am Hofgarten 10, D-53113 Bonn
Telephone: + 49 228 94 90 20 • Fax: +49 228 94 90 20 or +49 228 94 90 222
Email: bestellung@uno-verlag.de • Web site: http://www.uno-verlag.de

HUNGARY
Librotrade Ltd., Book Import, P.O. Box 126, H-1656 Budapest
Telephone: +36 1 257 7777 • Fax: +36 1 257 7472 • Email: books@librotrade.hu

INDIA
Allied Publishers Group, 1st Floor, Dubash House, 15, J. N. Heredia Marg, Ballard Estate, Mumbai 400 001,
Telephone: +91 22 22617926/27 • Fax: +91 22 22617928
Email: alliedpl@vsnl.com • Web site: http://www.alliedpublishers.com

Bookwell, 2/72, Nirankari Colony, Delhi 110009
Telephone: +91 11 23268786, +91 11 23257264 • Fax: +91 11 23281315
Email: bookwell@vsnl.net

ITALY
Libreria Scientifica Dott. Lucio di Biasio “AEIOU”, Via Coronelli 6, I-20146 Milan
Telephone: +39 02 48 95 45 52 or 48 95 45 62 • Fax: +39 02 48 95 45 48
Email: info@libreriaaeiou.eu • Website: www.libreriaaeiou.eu

JAPAN
Maruzen Company Ltd, 1-9-18, Kaigan, Minato-ku, Tokyo, 105-0022
Telephone: +81 3 6367 6079 • Fax: +81 3 6367 6207
Email: journal@maruzen.co.jp • Web site: http://www.maruzen.co.jp

REPUBLIC OF KOREA
KINS Inc., Information Business Dept. Samho Bldg. 2nd Floor, 275-1 Yang Jae-dong SeoCho-G, Seoul 137-130
Telephone: +02 589 1740 • Fax: +02 589 1746 • Web site: http://www.kins.re.kr

NETHERLANDS
De Lindeboom Internationale Publicaties B.V., M.A. de Ruyterstraat 20A, NL-7482 BZ Haaksbergen
Telephone: +31 (0) 53 5740004 • Fax: +31 (0) 53 5729296
Email: books@delindeboom.com • Web site: http://www.delindeboom.com

Martinus Nijhoff International, Koraalrood 50, P.O. Box 1853, 2700 CZ Zoetermeer
Telephone: +31 793 684 400 • Fax: +31 793 615 698
Email: info@nijhoff.nl • Web site: http://www.nijhoff.nl

Swets and Zeitlinger b.v., P.O. Box 830, 2160 SZ Lisse
Telephone: +31 252 435 111 • Fax: +31 252 415 888
Email: infoho@swets.nl • Web site: http://www.swets.nl

NEW ZEALAND
DA Information Services, 648 Whitehorse Road, MITCHAM 3132, Australia
Telephone: +61 3 9210 7777 • Fax: +61 3 9210 7788
Email: service@dadirect.com.au • Web site: http://www.dadirect.com.au

SLOVENIA
Cankarjeva Zalozba d.d., Kopitarjeva 2, SI-1512 Ljubljana
Telephone: +386 1 432 31 44 • Fax: +386 1 230 14 35
Email: import.books@cankarjeva-z.si • Web site: http://www.cankarjeva-z.si/uvoz

SPAIN
Díaz de Santos, S.A., c/ Juan Bravo, 3A, E-28006 Madrid
Telephone: +34 91 781 94 80 • Fax: +34 91 575 55 63
Email: compras@diazdesantos.es, carmela@diazdesantos.es, barcelona@diazdesantos.es, julio@diazdesantos.es
Web site: http://www.diazdesantos.es

UNITED KINGDOM
The Stationery Office Ltd, International Sales Agency, PO Box 29, Norwich, NR3 1 GN
Telephone (orders): +44 870 600 5552 • (enquiries): +44 207 873 8372 • Fax: +44 207 873 8203
Email (orders): book.orders@tso.co.uk • (enquiries): book.enquiries@tso.co.uk • Web site: http://www.tso.co.uk

On-line orders
DELTA Int. Book Wholesalers Ltd., 39 Alexandra Road, Addlestone, Surrey, KT15 2PQ
Email: info@profbooks.com • Web site: http://www.profbooks.com

Books on the Environment
Earthprint Ltd., P.O. Box 119, Stevenage SG1 4TP
Telephone: +44 1438748111 • Fax: +44 1438748844
Email: orders@earthprint.com • Web site: http://www.earthprint.com

UNITED NATIONS
Dept. I004, Room DC2-0853, First Avenue at 46th Street, New York, N.Y. 10017, USA
(UN) Telephone: +800 253-9646 or +212 963-8302 • Fax: +212 963-3489
Email: publications@un.org • Web site: http://www.un.org

UNITED STATES OF AMERICA
Bernan Associates, 4501 Forbes Blvd., Suite 200, Lanham, MD 20706-4346
Telephone: 1-800-865-3457 • Fax: 1-800-865-3450
Email: customercare@bernan.com · Web site: http://www.bernan.com

Renouf Publishing Company Ltd., 812 Proctor Ave., Ogdensburg, NY, 13669
Telephone: +888 551 7470 (toll-free) • Fax: +888 568 8546 (toll-free)
Email: order.dept@renoufbooks.com • Web site: http://www.renoufbooks.com

Orders and requests for information may also be addressed directly to:

Marketing and Sales Unit, International Atomic Energy Agency
Vienna International Centre, PO Box 100, 1400 Vienna, Austria
Telephone: +43 1 2600 22529 (or 22530) • Fax: +43 1 2600 29302
Email: sales.publications@iaea.org • Web site: http://www.iaea.org/books

INTERNATIONAL ATOMIC ENERGY AGENCY
VIENNA
ISBN 978–92–0–142810–3
ISSN 1011–4289